Transactions of the ASME®

Transactions of the ASME, Journal of Turbomachinery (ISSN 0889-504X) is published quarterly (Jan., Apr., July, Oct.) for $100 per year by The American Society of Mechanical Engineers, 345 East 47th Street, New York, NY 10017. Second-class postage paid at New York, NY and additional mailing offices. POSTMASTER: Send address change to The Journal of Turbomachinery, c/o The AMERICAN SOCIETY OF MECHANICAL ENGINEERS, 22 Law Drive, Box 2300, Fairfield, NJ 07007-2300."

CHANGES OF ADDRESS must be received at Society headquarters seven weeks before they are to be effective. Please send old label and new address.

PRICES: To members, $29.00, annually; to nonmembers, $100.00. Add $15.00 for postage to countries outside the United States and Canada.

INDEXED by Applied Mechanics Reviews and Engineering Information, Inc.

Journal of Turbomachinery

Published Quarterly by The American Society of Mechanical Engineers

VOLUME 111 • NUMBER 2 • APRIL 1989

TECHNICAL PAPERS

ANNOUNCEMENTS

Surface Heat Transfer Fluctuations on a Turbine Rotor Blade Due to Upstream Shock Wave Passing

A. B. Johnson[1]

M. J. Rigby[2]

M. L. G. Oldfield

R. W. Ainsworth

Oxford University,
Oxford, United Kingdom

M. J. Oliver
Rolls Royce,
Derby, United Kingdom

A theoretical model to explain observed rapid large-scale surface heat transfer rate fluctuations associated with the impingement of nozzle guide vane trailing edge shock waves on a transonic turbine rotor blade is described. Experiments were carried out in the Oxford Isentropic Light Piston Cascade Tunnel using an upstream rotating bar system to simulate the shock wave passing. High-frequency surface heat transfer and pressure measurements gave rapidly varying, large, transient signals, which schlieren photography showed to be associated with the impingement of passing shock waves on the surface. Heat transfer rates varying from three times the mean value to negative quantities were measured. A simple first-order perturbation analysis of the boundary layer equations shows that the transient adiabatic heating and cooling of the boundary layer by passing shock waves and rarefactions can give rise to high-temperature gradients near the surface. This in turn leads to large conductive heat transfer rate fluctuations. The application of this theory to measured fluctuating pressure signals gave predictions of fluctuating heat transfer rates that are in good agreement with those measured. It is felt that the underlying physical mechanisms for shock-induced heat transfer fluctuations have been identified. Further work will be necessary to confirm them in rotating experiments.

Introduction

The true environment in the gas turbine aeroengine is unsteady, even though most design practice is based on time-averaged processes. Much interest is now being shown in examining the effects of this unsteady environment.

This paper shows that large, short-duration positive and negative pulses of heat transfer rate on the surface of a gas turbine rotor blade can be produced by the periodic impingement of shock waves from the upstream nozzle guide vanes, and that these pulses can be predicted by a compression/heat conduction theory.

The unsteady interaction between the moving rotor and upstream stator of a high-pressure turbine stage can cause major fluctuations in both the aerodynamics of the rotor passage flow and the heat transfer rate to the surface of the rotor blades. At low speeds these fluctuations are mainly due to the stator potential field and downstream wakes, and have been studied in large, low-speed rotating turbines such as used by Hodson (1985) and Joslyn and Dring (1983). Increasingly, modern high work turbine stages have transonic flow in the nozzle guide vane passages, with associated trailing edge shock waves. These shock waves form a major source of unsteady disturbance passing through the rotor passage. Doorly and Oldfield (1985a, 1985b, 1985c) showed that the NGV shock waves and wakes could be simulated by passing bars in front of a stationary instrumented cascade at the correct relative bar Mach number, $M_{brel} = 0.98$, appropriate to the profile studied. They also showed that the passing wakes and shock waves could temporarily trip the rotor blade boundary layer, causing large increases in the surface heat transfer rate. Figure 1 from Doorly and Oldfield (1985b) shows that with widely spaced wakes the passage of a shock wave gave rise to a relatively small direct effect (A), but caused a short-lived separation at the leading edge, which in turn collapsed to form a turbulent spot (B) ahead of the main wake effect (C). In this case the simulated NGV shock waves were weak. Subsequently, Ashworth et al. (1985) and Schultz et al. (1986) reported further time-resolved heat transfer measurements using the same shock and wake simulation technique. This used a different, transonic, rotor blade profile and a higher M_{brel} of 1.16, which simulated stronger NGV trailing edge shock waves. Figure 2, from Schultz et al. (1986), shows massive pulses of heat transfer (clipped by the instrumentation), which were associated with shock wave passing. Somewhat surprisingly, pulses of negative heat transfer can be seen in Fig. 1.

The results presented here were obtained using the same blade profile and rotating bar simulation as in Ashworth et al. (1985), but at a 10 deg lower flow incidence angle, as in Schultz et al. (1986), and at a bar relative Mach number of 1.13 in order to simulate slightly different engine design conditions. They show similar transient peaks and troughs of heat transfer rate (Figs. 5–9). In Ashworth et al. (1985) and Schultz

[1]Present address: Schlumberger Cambridge Research Limited, Cambridge, United Kingdom.

[2]Present address: Rolls-Royce, Derby, United Kingdom.

Contributed by the International Gas Turbine Institute and presented at the 33rd International Gas Turbine and Aeroengine Congress and Exhibition, Amsterdam, The Netherlands, June 5–9, 1988. Manuscript received by the International Gas Turbine Institute September 25, 1987. Paper No 88-GT-172.

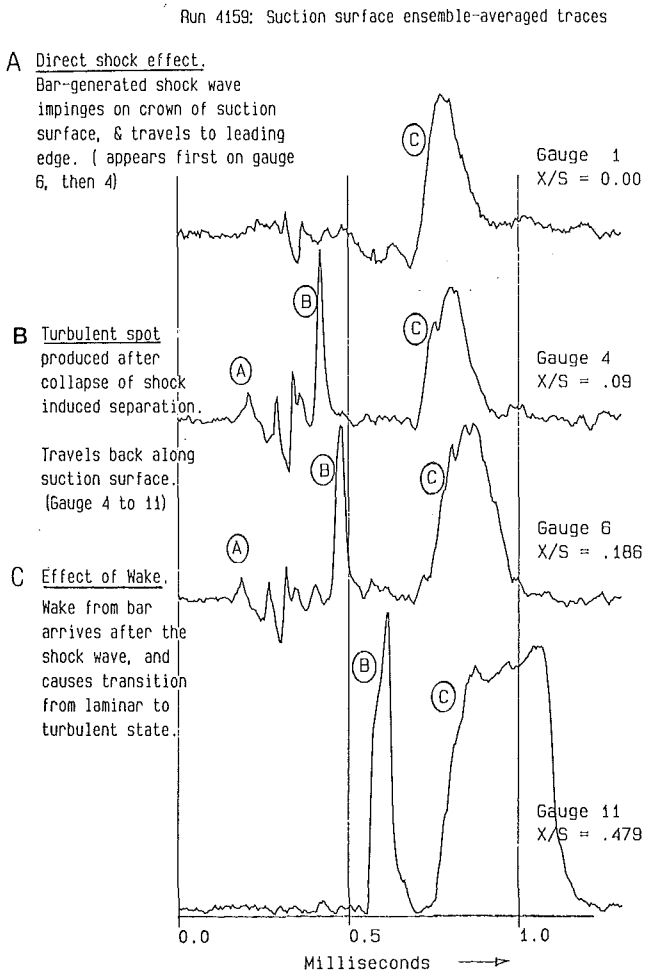

Fig. 1 Summary of effects of isolated wakes and shock waves on heat transfer rate measured on a just sonic rotor profile with M_{brel} = 0.98 (from Doorly and Oldfield, 1985b)

et al. (1986) these effects were thought to be due to transient separation induced by the passing shock waves. While this is a possible mechanism, it is difficult to see how a separation could cause the reversals of the heat transfer rate seen in Fig. 2.

As will be shown in this paper, there is another mechanism involving compression heating leading to thermal conduction in the boundary layer close to the wall, which can be used to predict the large heat transfer fluctuations from measured time-resolved blade surface pressures. These short-time fluctuations appear to add to those due to the passage of the wakes following the shock waves.

Of course, these bar passing experiments do not model any rotational or three-dimensional effects seen in a fully rotating turbine stage. However, it should be possible to detect these large fluctuations of surface heat transfer in the short-duration fully rotating turbine experiments conducted by Epstein et al.

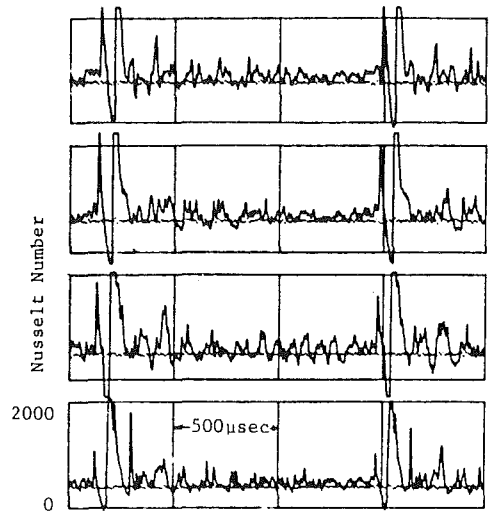

Fig. 2 Large heat transfer fluctuations measured by Schultz et al. (1986) due to passing shock waves and wakes. Transonic rotor profile and conditions as in this paper. M_{brel} = 1.16.

(1984) (which uses turbine blading of the same profile as the present work), Dunn (1986), Dunn et al. (1986a, 1986b), and Ainsworth et al. (1988).

It is important to note that Dunn (1986) also showed negative fluctuations in measured heat flux, which he considered was due either to a flow phenomenon or to instrumentation noise.

Shock Wave Simulation

The experimental shock wave simulation was carried out in the Isentropic Light Piston Tunnel at Oxford (Schultz et al., 1977). The tunnel was used in the configuration described by Doorly and Oldfield (1985) with the six-passage linear transonic rotor cascade used by Schultz et al. (1986). The experimental flow conditions are given in Table 1.

The moving shock waves and wakes that would have been generated in a turbine by an upstream nozzle guide vane ring were simulated by using a rotating bar wake generator, previously described by Doorly and Oldfield (1985a). A set of 1.6-mm-dia bars mounted on a 250-mm-dia rotating disk pass through a plane 15 mm upstream of the leading edge of the cascade, as shown in Fig. 3. Two configurations of the shock wave generator system were tested. With 16 bars mounted on the disk an equivalent NGV/rotor pitch ratio of 1.73 was attained, which gives engine similarity, or with two bars mounted on the disk it was possible to study the effects of isolated NGV wakes.

In addition to a trailing wake, each bar will produce two shock waves, a bow shock, which will stand off the front of the bar, and a recompression shock, which will be produced downstream of the bar as shown by Schultz et al. (1986) and Shapiro (1954). An expansion wave will be produced between the two shock waves. The majority of tests were carried out with the bar speed set to give a bar Mach number of 1.13

Nomenclature

c = specific heat capacity
k = thermal conductivity
M_{brel} = Mach number of rotating bar (midspan) relative to inlet flow
P = static pressure
$\dot{q}$ = heat transfer rate
T = temperature
u = velocity component parallel to surface
v = velocity component perpendicular to surface
α = thermal diffusivity = $k/\rho c$
γ = ratio of specific heats
δ = 99 percent boundary layer thickness
ρ = density

Subscripts

0 = mean time level
1 = first-order perturbation
g = gas property
s = substrate surface property
u = unsteady change

Table 1 Experimental flow conditions

Inlet Mach No.	0.38	
Exit Mach No.	1.18	
Bar relative Mach No.: design	1.13	
	low (no bar shocks) 0.73	
Reynolds No. (based on true chord and isentropic exit conditions)	1.0×10^6	
Inlet angle	48 deg	
Blade chord	41 mm	
Blade axial chord	34 mm	
	Heat transfer tests	Pressure tests
Total temperature	460 K	300 K
Initial blade temperature	290 K	290 K
Total pressure	290 kPa	170 kPa
Bar generator rotational speed	21,800 rpm	17,000 rpm

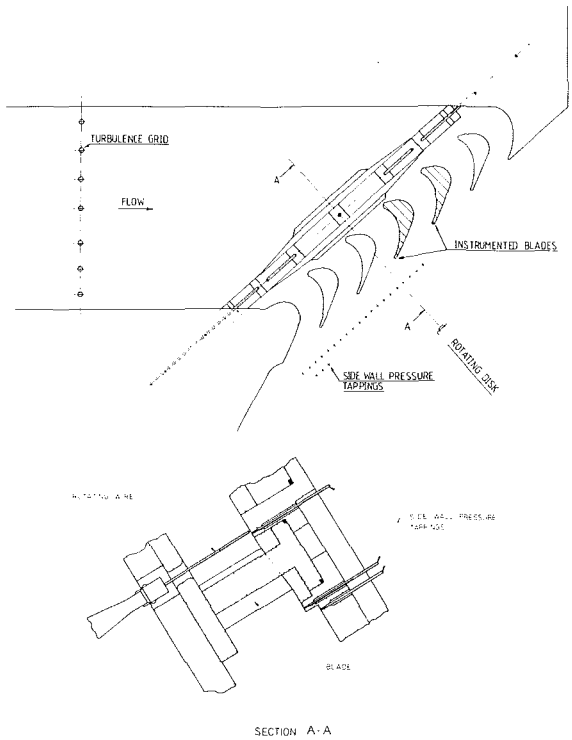

Fig. 3(a) Arrangement of rotating bar wake generator and cascade

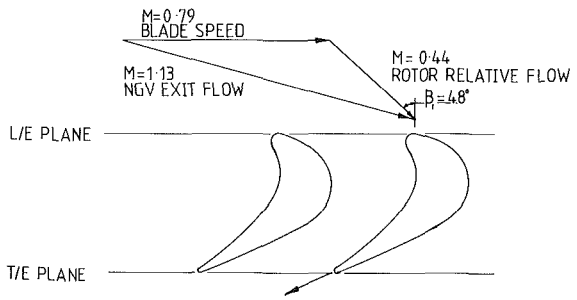

Fig. 3(b) Velocity triangles at inlet for the steady nominal design case at midspan

relative to the upstream flow. This was appropriate to the engine design case, although some work was done with an M_{brel} of 0.73 so that the effects of wakes could be studied without the presence of shock waves.

Flow behavior was measured using platinum thin-film heat transfer gages (Schultz and Jones, 1973) mounted on Macor machinable glass blades, coupled with high-speed electrical analogues (Oldfield et al., 1982) giving a system bandwidth of

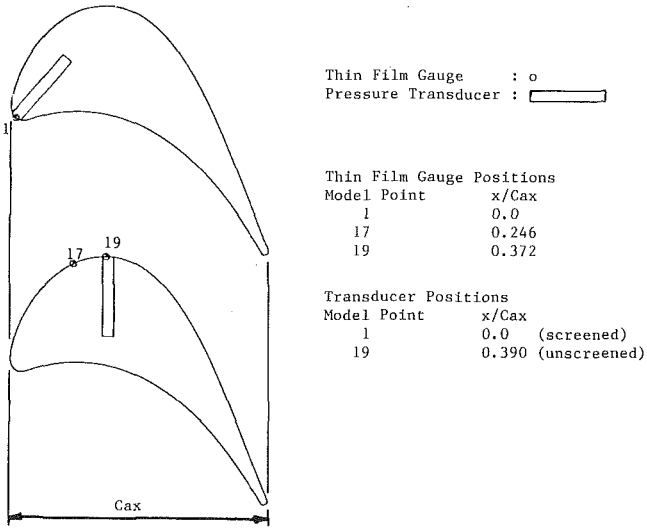

Fig. 4 Positions of thin-film heat transfer gages and Kulite pressure transducers

80 kHz. The fluctuating surface pressures were measured with Kulite (XCQ-062-050D) wide-bandwidth pressure transducers. The data were recorded on a digital transient recorder at a sampling rate of 500 kHz. The positions of the heat transfer gages and the pressure transducers are shown in Fig. 4.

From Table 1 it can be seen that the heat transfer rate measurements were made with an upstream gas total temperature of 460 K, while the pressure measurements were taken with a gas total temperature of 300 K; the total pressures and wake generator speeds were changed to keep the Reynolds number and Mach number constant. The time base on the 300 K pressure data presented here has been adjusted to allow direct comparison with the 460 K heat transfer data.

Heat Transfer Rate Measurements

Heat transfer rate measurements are presented in Figs. 5–9 for thin-film gage model points 17 and 19 on the suction surface instrumented blade, and the leading edge model point 1 on the pressure surface instrumented blade. The locations of these model points correspond to the positions of the pressure transducers, which are discussed below. The positions of both the heat transfer gages and the pressure transducers referred to in this paper are shown in Fig. 4. Other gages and transducers are omitted for clarity.

Figure 5(*i*) shows the heat transfer measurements observed on model point 19 in the 16-bar configuration, which corresponds to the engine conditions. Unfortunately, the overlaying of successive bar passing events prevents an analysis of individual shock wave and wake passing. In order to achieve a better understanding, the experiment was repeated with two bars in the rotating disk. The heat transfer trace for model point 19 with two bars is shown in Fig. 6(*i*). It can now be seen that as the bar passes the blade, very large changes occur in the measured heat transfer rate. The peaks observed appear to be associated with the shock waves from the bar. The first peak coincides with the bow shock, while the second peak coincides with the recompression shock. Between the two peaks, the rate of heat transfer falls dramatically toward zero. These changes in heat transfer rate are even more dramatic on model point 17, which is upstream of the crown of the blade (Fig. 7). Here, the second peak rises to over four times the mean level, while between the two peaks the heat transfer rate falls to less than zero. This phenomenon of negative heat transfer was also observed by Schultz et al. (1986). The smaller rise in

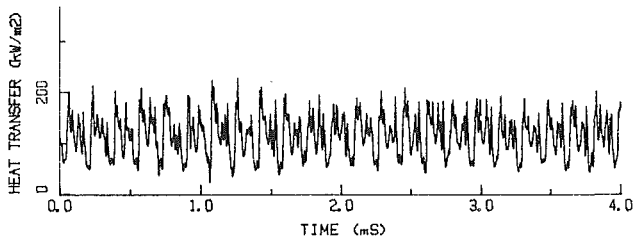

Fig. 5(*i*) Unsteady heat transfer rate measured at MP 19 at design condition; M_{brel} = 1.13; 16 bars

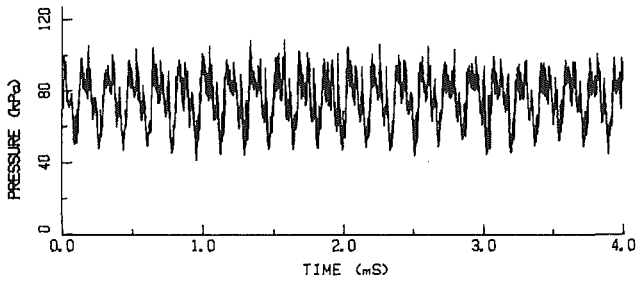

Fig. 5(*ii*) Unsteady surface pressure measured at MP 19 at design condition; M_{brel} = 1.13; 16 bars

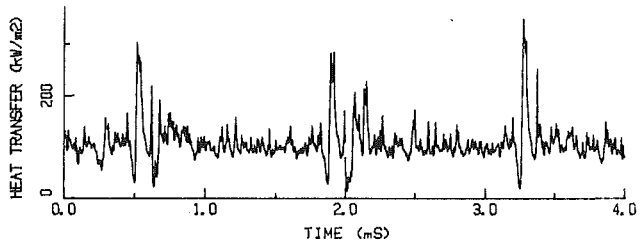

Fig. 6(*i*) Unsteady heat transfer rate measured at MP 19; M_{brel} = 1.13; 2 bars

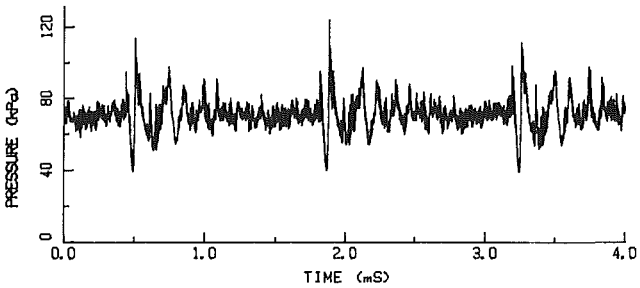

Fig. 6(*ii*) Unsteady surface pressure measured at MP 19; M_{brel} = 1.13, 2 bars

heat transfer following these peaks is attributable to the passage of the wake.

These large peaks and troughs in the measured heat transfer rate are definitely not due to oscillation or transient overshoot in the instrumentation used. Careful measurements of the analogues described by Oldfield et al. (1982) and the second-order filters used show that the system gain rolls off smoothly with frequency with a −3 dB bandwidth at 85 kHz (nominally 100 kHz). The phase shifts of the system contribute to a time delay of 3–4 μs, nearly constant with frequency, which does not significantly affect the results here.

Figure 8(*i*) shows the heat transfer trace for model point 19 taken with a subsonic M_{brel} = 0.73 and shows the effects of wakes alone. This enables the events occurring as a result of shock activity to be distinguished from those due to the wake passing. Figure 9(*i*) shows the heat transfer traces obtained on

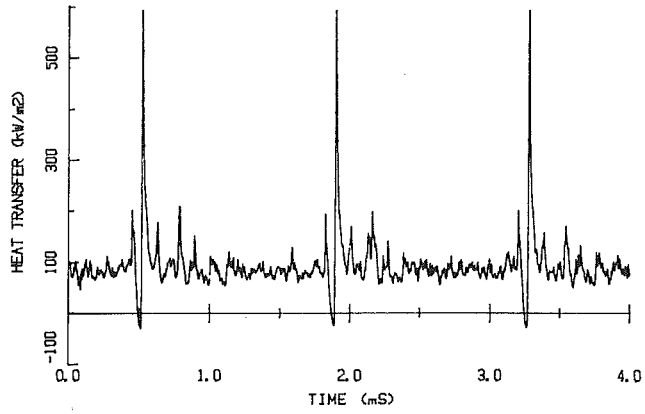

Fig. 7 Unsteady heat transfer rate measured at MP 17; M_{brel} = 1.13, 2 bars

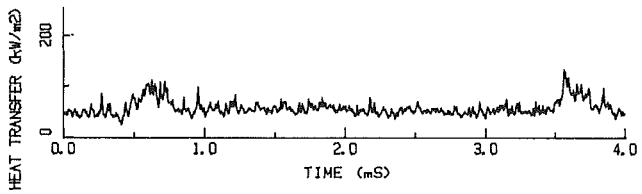

Fig. 8(*i*) Unsteady heat transfer rate measured at MP 19; M_{brel} = 0.73; 2 bars

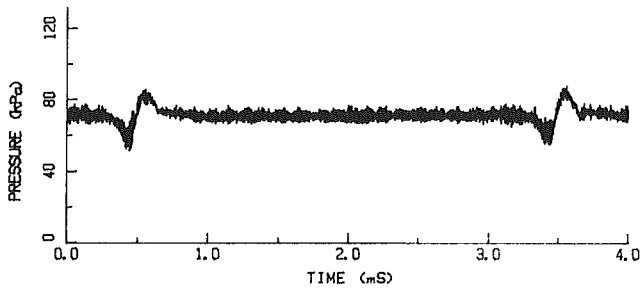

Fig. 8(*ii*) Unsteady surface pressure measured at MP 19; M_{brel} = 0.73, 2 bars

model point 1, a leading edge gage. The measured heat transfer rate fluctuations associated with the shock wave passing are considerably smaller than those measured on the suction surface gages. This is thought to be due to the shock front being perpendicular to the surface at the leading edge, while it is parallel near the suction surface.

However, it is interesting to note that the moving leading edge separation mechanism seen in Doorly and Oldfield (1985a), Fig. 1, also exists on this profile, albeit on the pressure surface, as can be seen in Fig. 7 of Schultz et al. (1986). This produced large pressure surface heat transfer rate fluctuations. As this paper is concerned with direct shock interaction, the pressure surface is not considered here in detail.

Unsteady Pressure Measurements

The unsteady pressure–time signals corresponding to the heat transfer rate traces in Figs. 5(*i*), 6(*i*), 8(*i*), and 9(*i*) are shown in Figs. 5(*ii*), 6(*ii*), 8(*ii*), and 9(*ii*), the data being taken at model points 1 and 19, as shown in Fig. 4. Two types of pressure transducer were used. According to the manufacturer, the diaphragm in the first pressure transducer, model point 1, has a natural frequency of 600 kHz, but a protective screen limits the frequency response to about 20 kHz, and so results taken, Fig. 9(*ii*), showed no evidence of transducer ringing. The diaphragm on the second transducer, model point 19, was

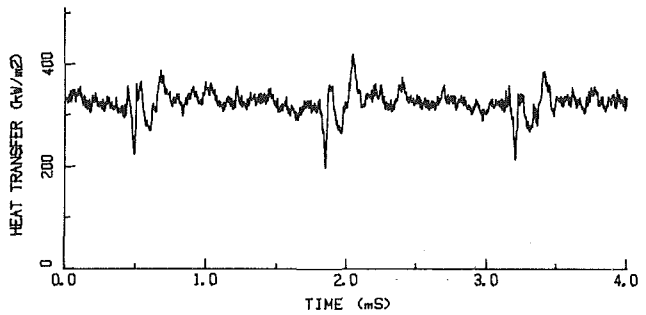

Fig. 9(*i*) Unsteady heat transfer rate measured at MP 1 leading edge; M_{brel} = 1.13, 2 bars

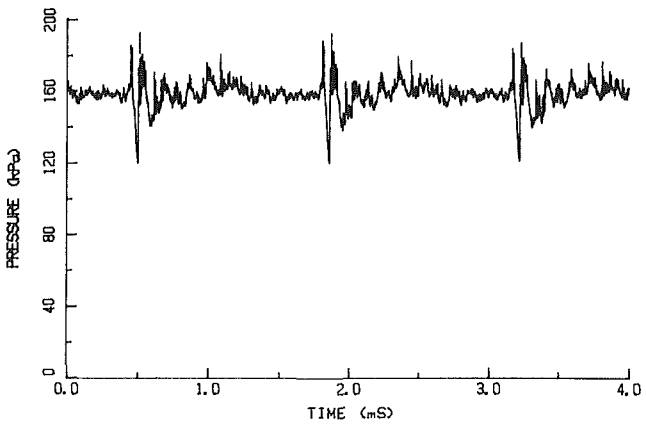

Fig. 9(*ii*) Unsteady surface pressure measured at MP 1 leading edge; M_{brel} = 1.13, 2 bars

unscreened but coated with RTV to give it durability. This is said to reduce the natural frequency to approximately 150 kHz. The data taken with this configuration showed clear evidence of ringing at 150 kHz, Fig. 8(*ii*), but this frequency is far higher than that characteristic of the large pulses in pressure due to the shock wave passing.

The data taken at model point 19 in the 16-bar configuration are shown in Fig. 5(*ii*). As with the heat transfer rate data taken in this configuration it is difficult to identify any specific phenomena, the data showing periodic fluctuations with a peak-to-peak amplitude of approximately 0.7 times the mean pressure level.

The two bar data taken at the same point, Fig. 6(*ii*), show very clear periodicity with a series of large rapid peaks and troughs in static pressure. The highest peak is approximately 1.7 times the mean level with the lowest trough slightly over half the mean level. It should also be noted that these fluctuations, although reduced in amplitude, continue almost until the disturbances associated with the next bar occur. These very rapid fluctuation are associated with the passing of unsteady shock waves, since when the tunnel was run with M_{brel} = 0.73, Fig. 8(*ii*), they were absent.

A re-examination of the 16-bar data shows that many of the phenomena present in the two-bar data can be identified here. The time signature for these data, Fig. 5(*ii*), has the same large positive and negative fluctuations as the two-bar results, but they are of a lower amplitude.

Pressure data were also recorded at the leading edge of the blade, Fig. 9(*ii*). The transducer mounted here was fitted with the protective screen and therefore had a reduced bandwidth. In spite of this, many of the same phenomena can be identified, with large fluctuations having a peak-to-peak amplitude of approximately half of the mean pressure level. These pulses die away slowly in a similar manner to those at model point 19.

Schlieren Photography Results

Schlieren photography, using the mirrored backwall system described in Doorly et al. (1985c), was used to visualize the positions of the wakes and shock waves in the cascade passages. The photographic results, taken at known times, were used to track the propagation and reflection of the unsteady shock waves across the passage. A brief summary of these results has previously been published by Schultz et al. (1986). An example of the results for both 16-bar and two-bar tests is shown in Fig. 10.

Analysis of the 16-bar data is not easy, as it is very difficult to isolate the effects of individual bars. This can be seen in Fig. 10(*i*) where there appears to be a continuous wake across the cascade, although the NGV/rotor pitch ratio was 1.73.

In the two-bar data, Fig. 10(*ii*), the bow shock can be identified propagating across the lower passage, and the recompression shock can be seen hitting the crown of the suction surface, while the wake can be seen entering the upper passage. The results also showed the existence of shock waves still present in the passage from the passing of the previous bar when the next bar arrives, although the simulated NGV/rotor passage ratio was 13.8.

Discussion of Experimental Results

The experimental data for both heat transfer rate and surface pressure are characterized by large positive and negative fluctuations from the mean. Careful analysis of the data shows that the largest positive spikes in both pressure and heat transfer rate occur when the schlieren data show the recompression shock wave from the bar hitting and being reflected from the surface of the blade. It should also be noted that the large drop in heat transfer rate, and negative heat transfer in some cases, occurs between the passing of the bow shock and the recompression wave, where an expansion wave would be expected. There are a number of other rapid peaks in heat transfer rate, clearly identifiable in the two-bar heat transfer rate data. Each one can be associated with a rapid rise in the measured pressure, and, in the schlieren results, with shock waves that have been reflected one or more times from the surface of the blades.

There is therefore an identifiable association between the peaks and troughs in the pressure and heat transfer signals with the passing of shock waves and expansion waves.

There is clear evidence that these shock wave associated pulses in both the heat transfer rate and pressure continue, although with a reduced amplitude, until the arrival of the next bar. This is also clear in the schlieren photographs, where shock waves can be identified in the passage long after the bar shock waves have passed.

Theoretical Model

The model used to explain the high-frequency surface heat transfer rate fluctuations considers the boundary layer behavior in very close proximity to the wall. The flow is assumed to be subsonic and the effect of an incident shock wave, with the shock front parallel to the surface, is to vary the pressure rapidly in this region.

This rapid pressure variation heats the boundary layer gas quickly by adiabatic compression. The large temperature gradients thus generated at the wall give rise to high rates of conductive heat transfer. It will be demonstrated that in the short time during which the shock wave passes through the boundary layer and reflects, conduction occurs only very close to the wall. It is then shown that this conductivity-dominated process can be used to predict the rapid heat transfer rate variations from measured surface pressure time signatures.

A simplified view of the process is shown in Fig. 11. A parallel or near-parallel unsteady shock wave from an upstream

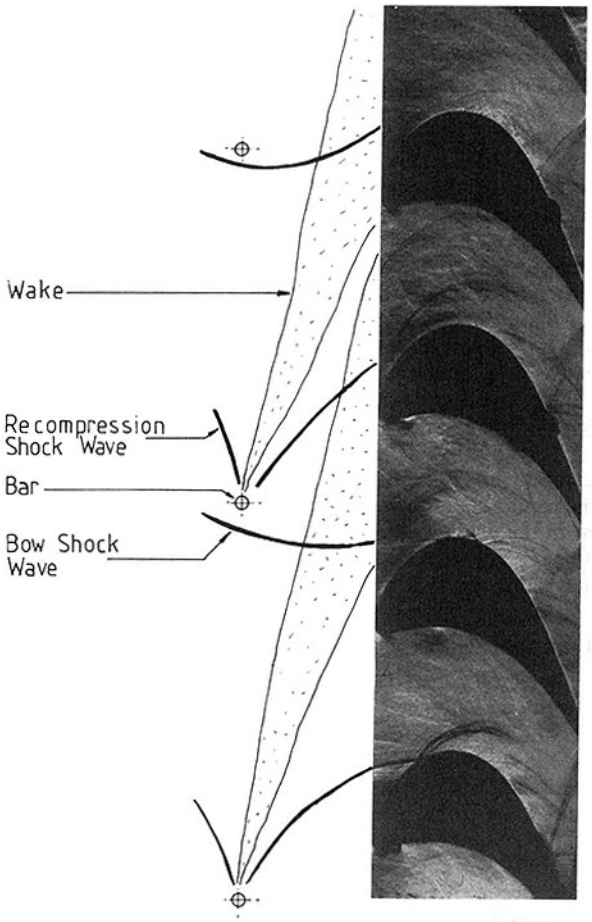

Fig. 10(*i*) Schlieren photograph of cascade flow design condition; 16 bars; approximate bar positions shown; $M_{brel} = 1.16$

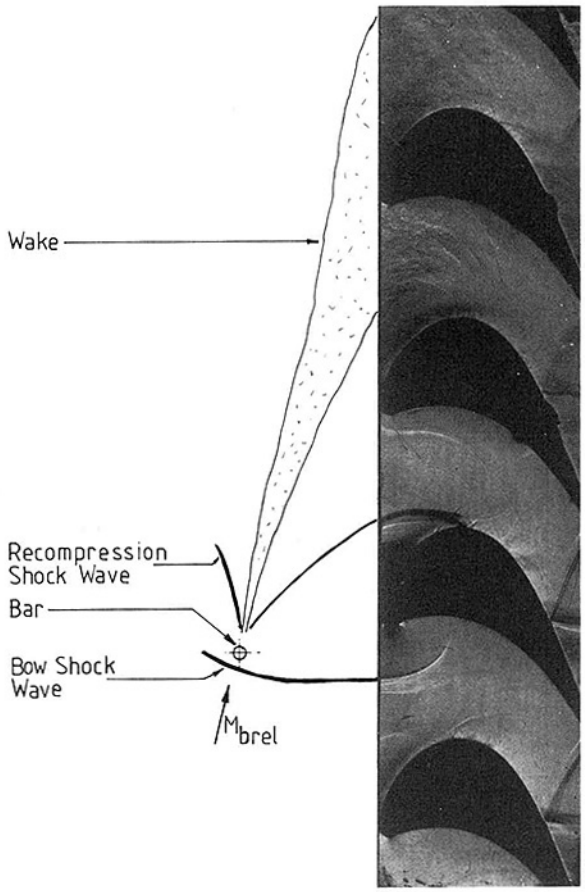

Fig. 10(*ii*) Schlieren photograph of cascade flow; 2 bars; approximate bar positions shown; $M_{brel} = 1.16$

blade or bar passes through the boundary layer and reflects from the surface. The increase of surface pressure and temperature occurs in a very short time, and can be modeled as a step in time. Although the compression due to the incident and reflected shock waves is not strictly isentropic, for the weak shock waves associated with turbine blade interactions, the isentropic approximation

$$\frac{T_1}{T_0} = \left(\frac{P_1}{P_0}\right)^{\frac{\gamma-1}{\gamma}} \tag{1}$$

can be used. For a shock wave Mach number of 1.13, giving a reflected shock pressure rise of 1.8, normal reflected shock wave heating gives $T_1/T_0 = 1.08396$, while isentropic compression gives $T_1/T_0 = 1.08327$, a difference of only 0.06 percent.

Now, consider the effect on the boundary layer equations of this sudden compression. For simplicity the incompressible boundary equations will be used, and only the first-order perturbations about the mean values will be considered. Schlichting (1979) derives a set of unsteady perturbation equations by assuming that all flow variables can be expanded as a power series in some small number ϵ. Here only the first-order equations are considered.

As only the temperatures are of interest here, we need only consider the first-order perturbation of the energy equation

$$\frac{\partial T_1}{\partial t} + u_0\frac{\partial T_1}{\partial x} + u_1\frac{\partial T_0}{\partial x} + v_0\frac{\partial T_1}{\partial y} + v_1\frac{\partial T_0}{\partial y} = \frac{\alpha\partial^2 T_1}{\partial y^2} \tag{2}$$

Near the wall, where y is small, with near-parallel shock waves and a near-constant-temperature wall, the $u_0\dfrac{\partial T_1}{\partial x}$ and $u_1\dfrac{\partial T_0}{\partial x}$ terms are small. Since v_0 and v_1 are zero at the wall, we can assume that they are of the order of y^n for some value $n > 1$. Then $v_0\dfrac{\partial T_1}{\partial y}$ and $v_1\dfrac{\partial T_0}{\partial y}$ are of the order of $y^{(n-1)}$ and are negligible compared with $\alpha\dfrac{\partial^2 T_1}{\partial y^2}$, which is of the order y^{-2} for small y. Neglecting these four terms the energy equation collapses to the one-dimensional unsteady heat conduction equation

$$\frac{\partial^2 T}{\partial y^2} = \frac{1}{\alpha}\frac{\partial T}{\partial t} \tag{3}$$

Now consider the effect of a step increase of the gas temperature superposed on the steady-state temperature field. Consider a steady boundary layer temperature distribution $T_0(y)$ (Fig. 12). The boundary layer is then heated by a step T_g at $t = 0$, while the temperature of the surface remains at $T_0(0)$. Cooling of the boundary layer by conduction to the wall then occurs and the temperature falls by $T_2(y, t)$. The new temperature of the boundary layer will be

$$T(y, t) = T_0(y) + T_g - T_2(y, t) \tag{4}$$

The unsteady heat transfer rate $\dot{q}_u$ ($+ve$ to the wall) is therefore given as

$$\dot{q}_u(y, t) = \frac{k\partial}{\partial y}\left(T_g - T_2(y, t)\right) = -\frac{k\partial T_2}{\partial y} \tag{5}$$

The boundary condition is applied

$$T(0,t) = T_0(0) \text{ or } T_2(0, t) = T_g$$

Equation (3) can be solved using Laplace transforms to give

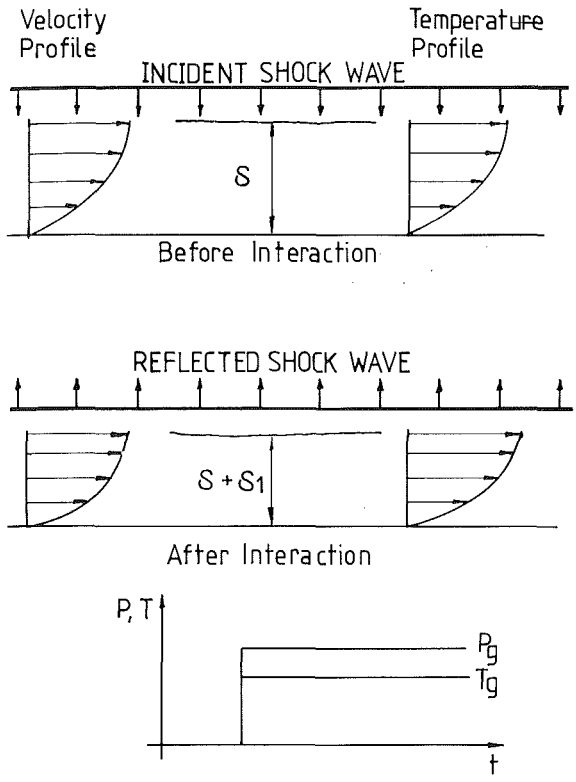

Fig. 11 Effect of incident and reflected shock waves on boundary layer, showing compression of boundary layer and change in velocity and temperature profiles; increase in pressure and temperature of boundary layer resulting in step change

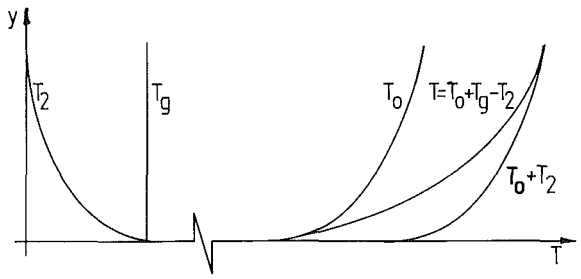

Fig. 12 Boundary layer temperature profile following step gas temperature change

$$T_2(y, t) = T_g \text{erfc}\left(\frac{y}{2\sqrt{(\alpha t)}}\right) \tag{6}$$

which can be substituted into equation (5) to give

$$\dot{q}_u(y, t) = kT_g \frac{\partial}{\partial y} \text{erf}\left(\frac{y}{2\sqrt{(\alpha t)}}\right) \tag{7}$$

The methods described above are familiar from the theory of one-dimensional unsteady heat transfer in solids (Schultz and Jones, 1973; Carslaw and Jaeger, 1959).

Equation (6) can be used to calculate the penetration depth into the boundary layer of a thermal wave in a given time. This gives the curves in Fig. 13, for various values of T_2/T_g, or different amplitudes of the thermal wave. The calculations are presented for air at the conditions relevant to the surface of the blades used in the experiment

$T = 306.6$ K
$P = 1.348$ bar
$\rho = 1.5345$ kg m^{-3}

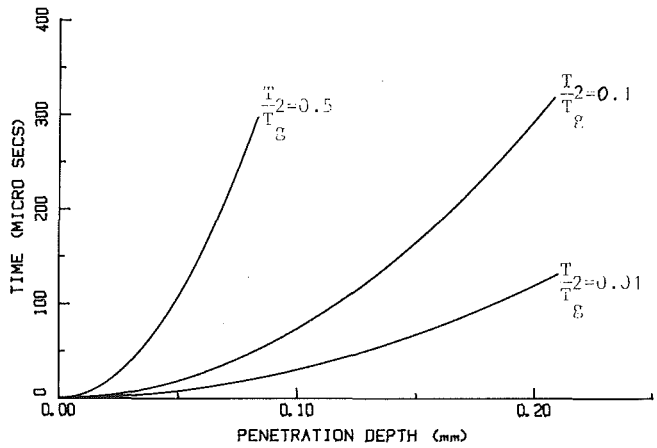

Fig. 13 Boundary layer penetration depth for various amplitudes of the thermal wave, T_2/T_g, for a step in T_g

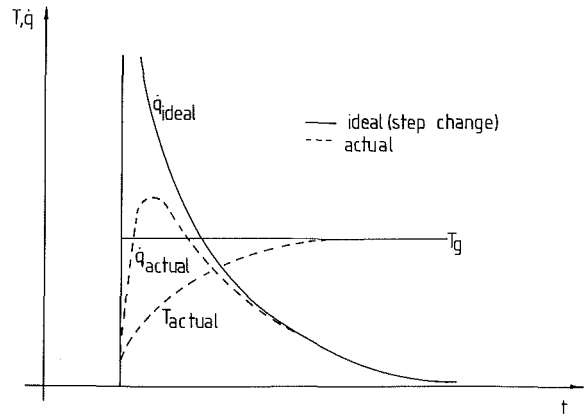

Fig. 14 Comparison between ideal and actual effect of step change in surface gas temperature for temperature and surface heat transfer rate

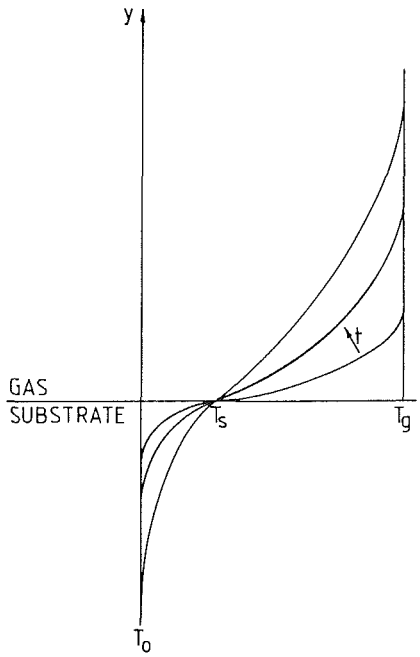

Fig. 15 Changes in substrate and gas temperature profiles following a step change in gas temperature

$$c = 1006 \quad \text{J kg}^{-1}\text{K}^{-1}$$
$$k = 0.0257 \quad \text{W m}^{-1}\text{K}^{-1}$$
$$\sqrt{(\rho ck)} = 6.279 \quad \text{W m}^{-2}\text{K}^{-1}\text{s}^{-1/2}$$

For a typical blade with a boundary layer thickness of 0.5 mm and an incident shock wave velocity of 450 m/s, the compression process takes less than 2.5 μs, so the step onset model is valid.

The duration of the measured high-frequency heat transfer rate pulses is of the order of 60 μs (Fig. 7). This will give a penetration depth for the $T_2/T_g = 0.1$ of approximately 0.1 mm. This is small compared to the predicted thickness of the boundary layer of order 1 mm, and so the earlier assumption of the effect being confined to the lower region of the boundary layer is valid. As the velocities in the boundary layer close to the wall are low, the use of incompressible boundary layer equations (2) is justified within the limits of the approximate model given here.

Equation (7) can be solved to give the heat transfer rate at the surface ($y = 0$) for a step compression

$$\dot{q}_u(0, t) = \frac{T_2\sqrt{(\rho ck)_{\text{gas}}}}{\sqrt{(\pi t)}} \tag{8}$$

This is presented graphically in Fig. 14.

This gives an infinite heat transfer rate at time $t = 0$. In practice, the finite but small rise time in T_g reduces this to a high peak in heat transfer rate as shown by dashed lines.

Of course, this analysis also holds for the heat transfer generated by steep expansion waves, which can cause large negative changes in heat transfer rate.

This analysis gives a possible physical mechanism for the observed fluctuations in heat transfer rate, and it will now be shown how these may be predicted from the measured surface pressure fluctuations, Figs. 5(*ii*), 6(*ii*), 8(*ii*), and 9(*ii*).

The analysis so far has assumed that the wall temperature does not vary with time. In practice the heat transfer rate is measured by thin-film thermometers mounted on the surface of the blade, and the thermal properties of the surface substrate must be allowed for.

A region is considered where the temperature of the gas and the wall is at a steady temperature T. If rapid compression heating occurs then the gas temperature away from the wall will rise by $T_g(t)$ and at the wall by $T_s(t)$ (Fig. 15), if radiation and convective effects are neglected. It can be shown that in Laplace transform coordinates

$$\dot{q}_u = \sqrt{(\rho ck)_{\text{gas}}}(\bar{T}_g - \bar{T}_s)\sqrt{s} \tag{9}$$

But

$$\dot{q}_u = \sqrt{(\rho ck)_{\text{substrate}}}\bar{T}_s\sqrt{s} \tag{10}$$

Dividing equation (9) by (10) and taking the inverse transform

$$\frac{T_g - T_s}{T_s} = \frac{\sqrt{(\rho ck)_{\text{substrate}}}}{\sqrt{(\rho ck)_{\text{gas}}}} \tag{11}$$

Equation (11) can be rearranged to give

$$T_s = \frac{\sqrt{(\rho ck)_{\text{gas}}}}{\sqrt{(\rho ck)_{\text{gas}}} + \sqrt{(\rho ck)_{\text{substrate}}}} T_g \tag{12}$$

Thus we see that the changes in surface temperature follow the changes in gas temperature.

Thus

$$\dot{q}_u = \frac{\sqrt{(\rho ck)_s}\sqrt{(\rho ck)_g}}{\sqrt{(\rho ck)_s} + \sqrt{(\rho ck)_g}} \bar{T}_g\sqrt{s} \tag{13}$$

$$= \sqrt{(\rho ck)_{\text{equiv}}}\bar{T}_g\sqrt{s} \tag{14}$$

For the Macor machinable glass blades used in this experiment, $\sqrt{(\rho ck)_s} = 2060$ $\text{Wm}^{-2}\text{K}^{-1}\text{s}^{-1/2}$ and so $\sqrt{(\rho ck)_{\text{equiv}}} = 6.26$ $\text{Wm}^{-2}\text{K}^{-1}\text{s}^{-1/2}$, a correction of only 0.3 percent on $\sqrt{(\rho ck)_g}$. For a metal blade this will be even less. Computational solutions of equation (14) are well known (Schultz and Jones, 1973; Oldfield et al., 1978) from the theory of thin-film heat transfer gages, and it is possible using the digitized pressure signal to compute changes in T_g and hence in the unsteady heat transfer rate.

The above analysis predicts the unsteady heat transfer rate assuming that the only effect of the pressure fluctuations is to change the temperature of the gas near the surface. There will, however, be a density change, which will manifest itself as a change in the thickness of the boundary layer.

Consider the steady-state heat transfer rate

$$\dot{q}_0 = k\frac{dT}{dy} \tag{15}$$

When an incident shock wave reflects from the surface (Fig. 11), the boundary layer is compressed in the y direction along with the embedded temperature field $T(y)$. This increases the gradient dT/dy. It is possible to predict the modulating heat transfer rate $\dot{q}_m$ caused by the compression and heating of the boundary layer under the influence of the pressure fluctuation associated with the shock wave passing by using

$$\dot{q}_m = k\frac{dT}{dy_m} = k\left(\frac{T}{T_0}\right)\frac{dT_0}{dy}\left(\frac{\rho}{\rho_0}\right)$$
$$= k\frac{dT_0}{dy}\left(\frac{p}{p_0}\right) = q_0\left(\frac{p}{p_0}\right) \tag{16}$$

The relevant conductivity k is that at the blade surface temperature, and this too will be affected by the heating

$$k = 0.0047 + (7\times10^{-5}T) \quad \text{Wm}^{-1}\text{K}^{-1} \tag{17}$$

In practice, for gas temperature fluctuations of the order of 40 K about a surface mean of 300 K, the short-term surface temperature fluctuations are only of the order of 0.12 K and the effects on conductivity can be neglected. It should be emphasized that the predictive models given in this section are effectively a linearized first-order approximation to the Navier–Stokes energy equation, which enables relevant mechanisms to be identified. Somewhat surprisingly, as will be shown, this simple theory is remarkably effective in predicting the experimental heat transfer results.

Comparison Between Experimental and Theoretical Data

In practice the measured pressure signals are in the form of discrete digitized samples, and numerical solutions of equation (4) using experimental temperatures suffer from the effects of digitization noise. This was reduced by using a zero phase Hamming window digital low pass filter (Rabiner and Gold, 1975) with a 30 kHz, −3 dB bandwidth, to produce a smoothed pressure trace stored as real values rather than integers, to reduce quantization errors (Fig. 16). This filter has the advantage that it introduces no phase or time shifts in the data,

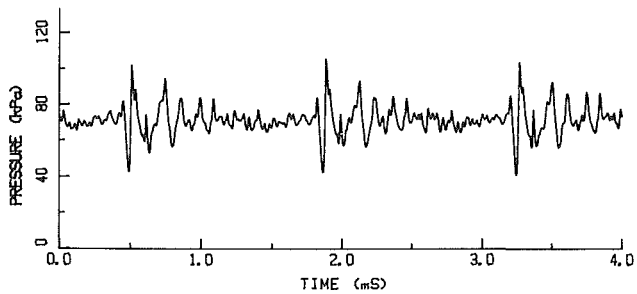

Fig. 16 Unsteady surface pressure measured at MP 19 (Fig. 6(*ii*)). Filtered with 30 kHz low pass Hamming window filter; 2 bars.

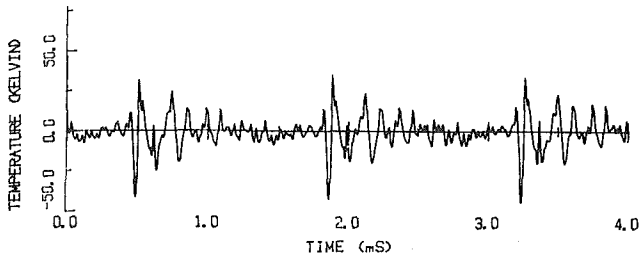

Fig. 17 Predicted gas temperature fluctuation T_g due to pressure variations in Fig. 16

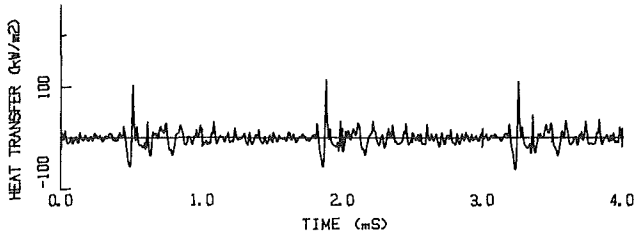

Fig. 18(*a*) Surface heat transfer rate fluctuations predicted from pressure data at MP 19 due to compressive heating (equation (18))

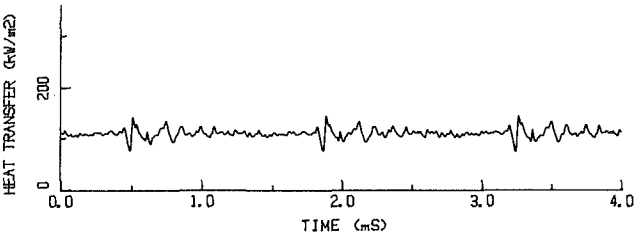

Fig. 18(*b*) Unsteady surface heat transfer rate levels predicted from pressure data at MP 19 due to modulation of boundary layer thickness (equation (18))

and exhibits no ringing or overshoot on pulse or square wave input signals. The choice of the low 30 kHz cutoff has the added benefit of removing any ringing and overshoots due to either the heat transfer instrumentation or pressure transducers. It should be noted that the recovery shock follows the expansion wave around the bar and is stronger than would be expected for $M_{brel} = 1.13$. This smoothed pressure signature was used point by point to predict $T_g(t)$ (Fig. 17), which was in turn used to predict the unsteady heat transfer rate (equation (14)) neglecting the change in thickness of the boundary layer (Fig. 18*a*), using a numerical ramp approximation convolution from Oldfield et al. (1978)

$$\dot{q}(t) = \dot{q}(m\tau) = \frac{2\sqrt{\rho ck}}{\sqrt{\pi\tau}} \sum_{n=0}^{m} (T_{n+1} + T_{n-1} - 2T_n)(m-n)^{0.5} \tag{18}$$

Equation (16) was then used to calculate the predicted unsteady heat transfer rate (Fig. 18*b*), due to the modulation of $T_0(y)$ by the fluctuating pressure. The total effect is shown in Fig. 19.

As the pressure signals used in the predictions were filtered using a high-frequency cutoff filter, making a direct comparison with the wide-bandwidth heat transfer rate measurements would be invalid. To make the comparison between the predicted and measured data legitimate, the measured data were filtered with the same Hamming window filter used for the pressure signals.

Considering the two-bar data for model point 19 first (Figs. 19 and 20), for the predicted and measured data, respectively,

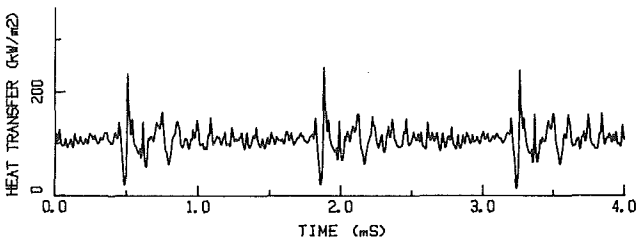

Fig. 19 Predicted unsteady surface heat transfer rate calculated from unsteady surface pressure data (Fig. 6(*ii*)) measured at MP 19, M_{brel} = 1.13, 2 bars. This is the sum of Figs. 18(*a*) and 18(*b*).

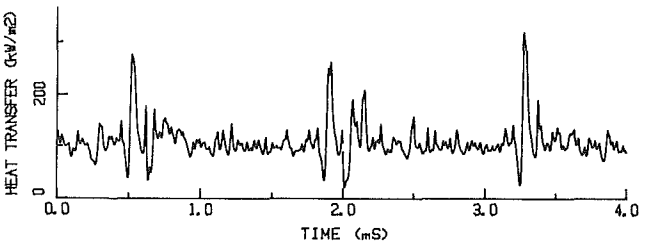

Fig. 20 Unsteady heat transfer rate (Fig. 6(*i*)) measured at MP 19, M_{brel} = 1.13; 2 bars; filtered to 30 kHz

it can be seen that the amplitude of the large peak and the deep trough have been predicted well and other shock wave associated spikes are similar in both figures. The duration of the peak in heat transfer rate is however underpredicted. It is possible that the shock wave causing the peak also induces a transient separation, which amplifies and broadens the observed peak. In the measured data there is a drop in heat transfer rate after the incidence of the reflected shock wave, followed by an increase in heat transfer rate. This increase is associated with the passing of the wake, and is not modeled from the pressure fluctuation. This wake effect is demonstrated in the $M_{brel} = 0.73$ data (Figs. 21 and 22), where the predicted data show a drop in heat transfer rate followed by a rise of the same amplitude and duration, while the measured data show a slight drop followed by a more significant and longer rise. The 16-bar data (Fig. 23) agree well with the prediction (Fig. 24). The amplitude of the fluctuations is very close, while many of the individual flow phenomena can be clearly identified in both traces.

The data taken at the leading edge and those predicted from the relevant pressure signal are shown in Figs. 25 and 26. The two peaks in heat transfer rate associated with the shock wave and the drop caused by the expansion wave between them are well predicted. The later peak in the measured data caused by the wake is not modeled, and so does not appear in the predicted data.

Conclusions

Short-duration, positive and negative pulses of heat transfer rate on the surface of a turbine blade have been observed in a shock wave passing simulation experiment. It was shown that these can be due to the reflection of shock waves attached to the trailing edge of an upstream nozzle guide vane. A simple theoretical model enables these pulses to be predicted from surface pressure fluctuations.

Five mechanisms leading to unsteady fluctuations in rotor blade surface heat transfer rate have now been identified in the program of wake and shock wave passing simulation in the Oxford Isentropic Light Piston Cascade Tunnel:

(*i*) Nonperiodic boundary layer transition associated with turbulent spots due to boundary layer instabilities and free-stream turbulence.

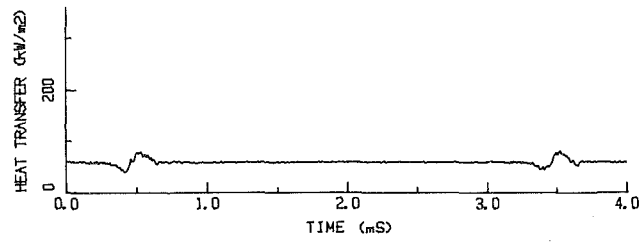

Fig. 21 Predicted unsteady surface heat transfer rate calculated from unsteady surface pressure data (Fig. 8(*ii*)) measured at MP 19; low M_{brel} = 0.73; 2 bars

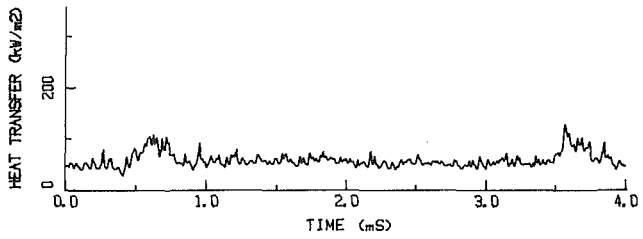

Fig. 22 Unsteady heat transfer rate (Fig. 8(*i*)) measured at MP 19; low M_{brel} = 0.73; 2 bars; filtered to 30 kHz bandwidth

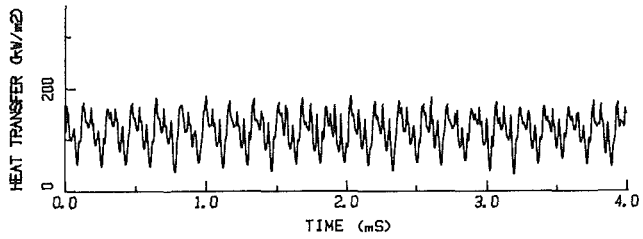

Fig. 23 Predicted unsteady surface heat transfer rate calculated from unsteady surface pressure data (Fig. 5(*ii*)) measured at MP 19 at design condition; M_{brel} = 1.13; 16 bars

(*ii*) Periodic tripping of the boundary layer by the upstream NGV wakes leading to large unsteady increases of heat transfer rate.

(*iii*) Transient separations on either surface excited by the passage of NGV shock waves past the blade leading edge. These separations convect along the surface and subsequently collapse to form a moving turbulent band of increased heat transfer rate.

(*iv*) Rapid adiabatic compressive heating and cooling of the boundary layer by reflected NGV shock and expansion waves leading to short-duration pulses of heat conduction between the blade surface and the gas immediately next to the surface.

(*v*) Compression and expansion of the embedded time mean temperature gradient profile in the boundary layer giving rise to modulations of the heat transfer rate by the surface pressures.

The final mechanism, at least in terms of the Binear heat conduction theory proposed here, will not lead to any change in the mean heat transfer rate to the turbine blade surface. However, the observed fluctuations (Fig. 7) in heat transfer rate have peak-to-peak amplitudes of up to five times the mean level. Consequently, the unsteady temperature gradients in the blade near the surface will be up to five times the mean gradient. This may make a significant contribution to destructive thermal fatigue in the surfaces of thermal barrier coatings (TBC) or ceramic blades, where the blade surface material has a lower thermal conductivity and thermal product $\sqrt{(\rho ck)}$ than a metal surface.

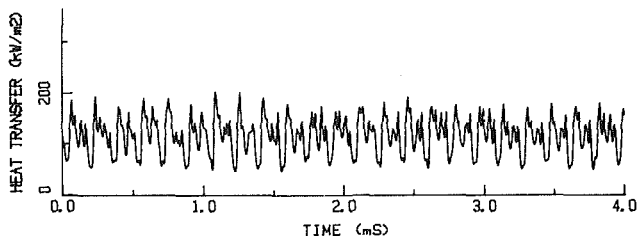

Fig. 24 Unsteady heat transfer rate (Fig. 5(*ii*)) measured at MP 19 at design condition; M_{brel} = 1.13; 16 bars; filtered to 30 kHz bandwidth

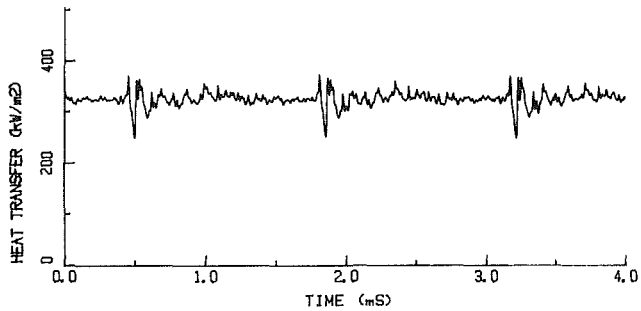

Fig. 25 Predicted unsteady surface heat transfer rate calculated from unsteady surface pressure data (Fig. 9(*ii*)) measured at MP 1; leading edge; M_{brel} = 1.13; 2 bars

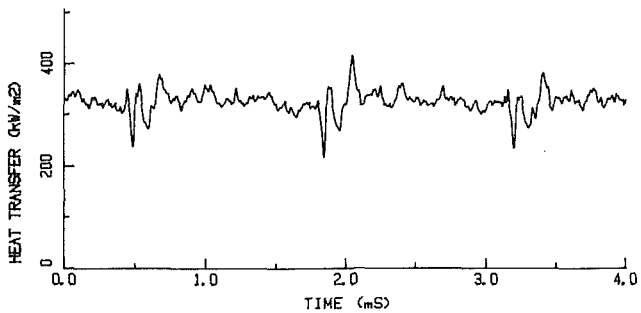

Fig. 26 Unsteady heat transfer rate (Fig. 9(*i*)) measured at MP 1 leading edge; M_{brel} = 1.13; 2 bars; filtered to 30 kHz bandwidth

Although all five unsteady heat transfer mechanisms listed above are more easily identified in the two-bar, widely spaced NGV simulation, they can nevertheless be seen in the 16-bar case. It is likely that they will be identified in rotating stage experiments, as wide-bandwidth heat transfer and pressure measurements from rotating turbine blades become available.

Further work needs to be undertaken in order to refine the models identified here and to confirm that they are applicable to the stator–rotor interaction in rotating turbomachinery. The authors await with interest detailed time-resolved heat transfer measurements from the fully rotating experiments mentioned in the introduction.

Acknowledgments

The authors are deeply grateful to the late Professor D. L. Schultz for his organizational help and advice, without which this work would not have taken place.

The authors gratefully acknowledge the support of Rolls-Royce plc and the U.S. Air Force (Wright Aeronautical Laboratories, Aero-Propulsion Laboratory, Air Force Systems Command, Wright-Patterson AFB, Ohio, Contract No. F33615-84-C-2475) for this work and the kind permission of Rolls-Royce plc to publish this paper.

The work of K. J. Grindrod, J. L. Allen, T. Norman, and

others in the Oxford Turbomachinery Group is also gratefully acknowledged.

References

Ainsworth, R. W., Schultz, D. L., Davies, M. R. D., Forth, C. J. P., Oldfield, M. L.G., Hilditch, M. A., and Sheard, A. G., 1988, "A Transient Facility for the Study of the Thermofluidynamics of a Full Stage Turbine Under Engine Representative Conditions," ASME Paper No. 88-GT-xx.

Ashworth, D. A., LaGraff, J. E., Schultz, D. L., and Grindrod, K. J., 1985, "Unsteady Aerodynamics and Heat Trnasfer Processes in a Transonic Turbine Stage," ASME *Journal of Engineering for Gas Turbines and Power*, Vol. 107, pp. 1022–1030.

Carslaw, H. S., and Jaeger, J. C., 1959, *Conduction of Heat in Solids*, 2nd ed., Oxford University Press, United Kingdom.

Doorly, D. J., and Oldfield, M. L. G., 1985a, "Simulation of the Effects of Shock Wave Passing on a Turbine Rotor Blade," ASME *Journal of Engineering for Gas Turbines and Power*, Vol. 107, pp. 998–1006.

Doorly, D. J., and Oldfield, M. L. G., 1985b, "Simulation of Wake Passing in a Stationary Turbine Rotor Cascade," *J. Propulsion and Power*, Vol. 1, No. 4, p. 316.

Doorly, D. J., Oldfield, M. L. G., and Scrivener, C. T. J., 1985, "Wake Passing in a Turbine Rotor Cascade," presented at the AGARD Symposium on Heat Transfer and Film Cooling in Gas Turbines, AGARD PEP CP-390.

Dunn, M. G., 1986, "Heat-Flux Measurements for the Rotor of a Full-Stage Turbine: Part I—Time Averaged Results," ASME JOURNAL OF TURBOMACHINERY, Vol. 108, pp. 90–97.

Dunn, M. G., George, W. K., Rae, W. J., Woodward, S. H., Moller, J. C., and Seymour, P. J., 1986a, "Heat-Flux Measurements for the Rotor of a Full-Stage Turbine: Part II—Description of Analysis Technique and Typical Time Resolved Measurements," ASME JOURNAL OF TURBOMACHINERY, Vol. 108, pp. 98–107.

Dunn, M. G., Martin, H. L., and Stanek, M. J., 1986b, "Heat-Flux and Pressure Measurements and Comparison With Prediction for a Low Aspect Ratio Turbine Stage," ASME JOURNAL OF TURBOMACHINERY, Vol. 108, pp. 108–115.

Epstein, A. H., Guenette, G. R., and Norton, R. J. G., 1984, "The MIT Turbine Blowdown Facility," ASME Paper No. 84-GT-116.

Hodson, H. P., 1985, "Measurements of Wake-Generated Unsteadiness in Rotor Passages of Axial Flow Turbines," ASME *Journal of Engineering for Gas Turbines and Power*, Vol. 107, pp. 467–476.

Joslyn, H. D., Dring, R. P., and Sharma, O. P., 1983, "Unsteady Three-Dimensional Turbine Aerodynamics," ASME *Journal of Engineering for Power*, Vol. 105, pp. 322–331.

Oldfield, M. L. G., Jones, T. V., and Schultz, D. L., 1978, "On-Line Computer for Transient Turbine Cascade Instrumentation," *IEEE Transactions on Aerospace and Electronic Systems*, Vol. AES 14, pp. 738–749.

Oldfield, M. L. G., Burd, H. J., and Doe, N. G., 1982, "Design of Wide-Bandwidth Analogue Circuits for Heat Transfer Instrumentation in Transient Tunnels," in: *Heat and Mass Transfer in Rotating Machinery*, D. E. Metzger and N. H. Afgan, eds., Hemisphere Publ. Corp., New York.

Rabiner, L. R., and Gold, B., 1975, *Theory and Application of Digital Signal Processing*, Prentice-Hall, New York.

Schlichting, H., 1979, *Boundary Layer Theory*, 7th ed., McGraw-Hill, New York, p. 414.

Schultz, D. L., and Jones, T. V., 1973, "Heat Transfer Measurements in Short Duration Facilities," AGARD AG-165.

Schultz, D. L., Jones, T. V., Oldfield, M. L. G., and Daniels, L. C., 1977, "A New Transient Cascade Facility for the Measurement of Heat Transfer Rates," AGARD Conference Proceedings No. 229, *High-Temperature Problems in Gas Turbine Engines*.

Schultz, D. L., Ashworth, D. A., LaGraff, J. E., Rigby, M. J., and Johnson, A. B., 1986, "Wake and Shock Interactions in a Transonic Turbine Stage," AGARD Proceedings No. 401, Munich.

Shapiro, A. H., 1954, *The Dynamics and Thermodynamics of Compressible Flow*, Vol. II, Ronald, p. 884.

Heat Transfer, Pressure Drop, and Mass Flow Rate in Pin Fin Channels With Long and Short Trailing Edge Ejection Holes

S. C. Lau
Associate Professor.
Mem. ASME

J. C. Han
Professor.
Mem. ASME

T. Batten
Research Assistant.

Department of Mechanical Engineering,
Texas A&M University,
College Station, TX 77843-3123

Experiments have been conducted to study the turbulent heat transfer and friction characteristics in pin fin channels with small trailing edge ejection holes that are commonly found in modern internally cooled turbine airfoils. The main objective of the investigation is to examine the effects of varying the length and the configuration of the trailing edge ejection holes on the overall heat transfer, the overall pressure drop, the local pressure distribution, and the local mass flow rate distribution in the pin fin channel. The staggered pin fin array (L/D = *1.0*, X/D = S/D = *2.5*) *in the test channel has 15 rows of three pins. The diameter of the ejection holes is one-half the diameter of the pins. There are 30 or 23 ejection holes on one of the side walls of the test channel and six similar ejection holes at the radial flow exit. Experimental results are obtained for two trailing edge ejection hole lengths, four ejection hole configurations, and Reynolds numbers between 10,000 and 60,000. The results show that the overall heat transfer increases when the length of the trailing edge ejection holes is increased and when the trailing edge ejection holes are configured so that much of the cooling air is forced to flow farther downstream in the radial flow direction before exiting the pin fin channel through ejection holes. The overall Nusselt number can be correlated with an equation of the form* $Nu_D = a(Re_D)^b$, *where the values of the exponent* b *are about the same for all the test cases with trailing edge flow ejection. Results also show that the increase in the overall heat transfer is generally accompanied by an increase in the overall pressure drop (that is, an increase in the required pumping power), except that the overall heat transfer is lower and the overall pressure drop is higher when there is no radial flow ejection. In the cases with both radial and trailing edge flow ejection, about 15 to 20 percent of the flow exits through the tip bleed holes.*

Introduction

The tail region of a typical airfoil in modern gas turbine engines is cooled by forcing cooling air through an internal pin fin channel located near the trailing edge of the airfoil. The cooling air enters the pin fin channel at the base of the airfoil. Most of the cooling air exits the pin fin channel through small ejection holes along the trailing edge of the airfoil.

For aerospace applications, there are typically ten to fifteen rows of staggered pins of length-to-diameter ratio of about one in the pin fin cooling channel. In general, there are many ejection holes, whose diameter is small compared to the dimensions of the pin fin channel. In addition, there are small holes at the tip of the airfoil for the cooling air to exit the pin fin channel in the radial flow direction. To maximize the efficiency of a gas turbine engine and to ensure its safe operation, a designer needs to know the heat transfer and friction characteristics of air flow through such pin fin channels of various configurations.

Heat transfer for the flow of air straight through short pin fin channels has been studied by Brown et al. (1980), VanFossen (1982), Brigham and VanFossen (1984), Metzger and Haley (1982), Metzger et al. (1982, 1986), and Lau et al. (1985). Lau et al. (1987) conducted experiments to demonstrate that, when there was flow exiting a pin fin channel through lateral (trailing edge) ejection holes, the gradually decreasing mass flow in the channel and the turning of the air stream in the channel affected significantly the overall heat transfer from the pin fin channel. They presented results for various ejection hole/slot geometries, ratios of the ejection flow rate to the total mass flow rate between 0 and 100 percent, and Reynolds numbers between 6000 and 60,000.

The present experimental investigation is motivated by the need to understand better the effects of varying the length and the configuration of the ejection holes on the heat transfer, pressure drop, and mass flow distribution for the flow of cool-

Contributed by the International Gas Turbine Institute and presented at the 33rd International Gas Turbine and Aeroengine Congress and Exhibition, Amsterdam, The Netherlands, June 5-9, 1988. Manuscript received at ASME Headquarters February 11, 1988. Paper No. 88-GT-42.

ing air through pin fin channels in turbine airfoils with ejection holes along the trailing edges.

In the present investigation, the aforementioned pin fin cooling passages in modern turbine airfoils are modeled as a wide rectangular channel with a staggered array of short pin fins spanning the space between the two principal walls, and small ejection holes in one of the two side walls and at the straight (radial) flow exit. The overall heat transfer, the overall pressure drop across the pin fin channel, the local pressure distribution, and the mass flow rate distribution in the channel are obtained for various ejection hole configurations, long and short lateral (trailing edge) ejection holes, and Reynolds numbers typical of gas turbine airfoil applications.

Experimental Apparatus

The test apparatus was an open flow loop consisting of the test section, an entrance section, and an orifice flow meter. Clean, dry air was supplied from a building compressor rated at 1.0 MPa (150 psia) and 34.0 m^3/min. (1200 SCFM). Before entering the flow loop, the air passed through a large storage tank, a flow regulator, and control valves. Air exited the test apparatus into the air-conditioned laboratory.

The test section was a pin fin channel made entirely of copper. A schematic of the test section is shown in Fig. 1. The flow cross section of the test channel measured 6.35 mm (0.25 in.) by 5.56 cm (2.19 in.). The pins were 6.35 mm (0.25 in.) long and 6.35 mm (0.25 in.) in diameter (L/D = 1.0). They were staggered in the test channel with spacings of 2.5 times the pin diameter in both the straight (radial) flow and the lateral (trailing edge) flow directions (X/D = S/D = 2.5). There were three pins on each row and 15 rows of pins.

The top and bottom walls of the test section were both 6.35 mm (0.25 in.) thick. As shown in Fig. 1, one of the side walls was solid and the other had an array of 30, equally spaced, trailing edge ejection holes. These ejection holes were 3.18 mm (0.125 in.) in diameter and were located halfway between the top and bottom walls. The center of every other hole was aligned with the centers of the three pins on a pin row. The length of the ejection holes (which was also the thickness of the side wall with the ejection holes) was either 3.97 cm (1.56 in.) or 6.35 mm (0.25 in.), corresponding to length-to-diameter ratios L^*/d of 12.5 and 2.0.

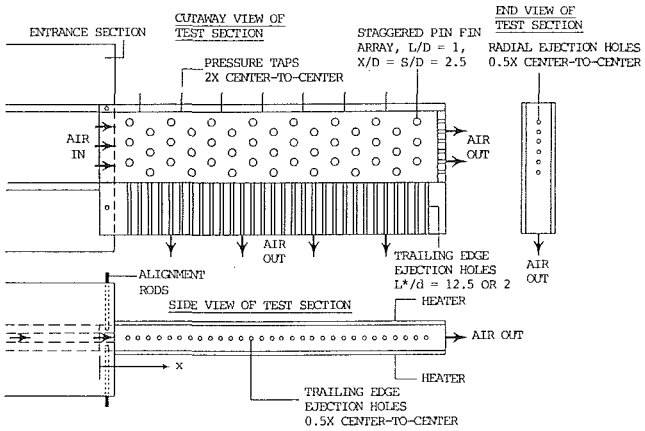

Fig. 1 Schematic of test section

Electric heaters (heater wires vulcanized between thin layers of fiberglass-reinforced silicone rubber) were attached to the exterior surfaces of the top and bottom walls to supply heat to the test section. The heaters, rated at 0.78 W/cm^2 (5.0 W/$in.^2$), covered the entire top and bottom surfaces of the test section.

The radial flow exit of the test channel was a 6.35 mm (0.25 in.) thick blockage with an array of six equally spaced holes 3.18 mm (0.125 in.) in diameter. As in the case of the trailing edge ejection holes, these holes were located halfway between the top and bottom walls. In one of the test section geometries studied, the radial flow exit blockage was removed, and the wide open cross section of the radial flow exit was identical to the inlet flow cross section.

The test section was fabricated with precision. All of its dimensions were accurate to within ±0.05 mm (±0.002 in.). The pins were press fitted into holes drilled through the top and bottom walls of the test channel. Solder sealed the gap between the holes and the pins and was used to assemble the channel walls and the radial flow exit blockage.

The entrance section was made of 6.35 mm (0.25 in.) thick acrylic sheets and reinforced on the outside with 2.54 cm (1.0 in.) thick hard wood. The entrance channel had the same flow

Nomenclature

a = coefficient in equation (10)
A = total heat transfer area, including surfaces exposed to air flow in pin fin channel and in ejection holes, m^2
A_j = cross-sectional area of trailing edge ejection holes, m^2
A_{min} = area of minimum flow cross section in pin fin channel, m^2
b = exponent in equation (10)
C_D = discharge coefficient
c_p = specific heat of air at average bulk temperature, J/kg/K
d = diameter of trailing edge ejection holes, m
D = diameter of pins, m
f = overall friction factor, equation (5)
k = thermal conductivity of air at average bulk temperature, W/m/K
L = length of pins, m
L^* = length of trailing edge ejection holes, m
$\dot{m}$ = total mass flow rate of air, kg/s
$\dot{m}_j$ = rate of mass flow through trailing edge ejection holes, kg/s
$\dot{m}_x$ = radial mass flow rate, kg/s
n = total number of trailing edge and radial ejection holes
N = number of pin rows
Nu_D = Nusselt number, equation (1)
p_{exit} = ejection hole exit pressure, N/m^2
p_{local} = local pressure in pin fin channel, N/m^2
P_j = normalized local pressure, equation (6)
$\dot{q}_{in}$ = total power input to heaters, W
$\dot{q}_{loss}$ = rate of heat loss through insulation, W
Re_D = Reynolds number, equation (4)
S = pin spacing in trailing edge flow direction, m
$\bar{T}_w$ = average channel wall temperature, K
T_{bi} = inlet bulk temperature, K
T_{bo} = outlet bulk temperature, equation (3), K
u_{max} = velocity of air at minimum flow cross section in pin fin channel, m/s
x = distance from channel entrance, m
X = pin spacing in radial flow direction, m
ΔT_{lm} = log mean temperature difference, equation (2), K
μ = dynamic viscosity of air at average bulk temperature, N•s/m^2
ρ = density of air at average bulk temperature, kg/m^3

Table 1 Test section configurations

Test Case	L*/d	Exit Hole Configuration: Radial Flow Exit	Exit Hole Configuration: Trailing Edge Ejection Flow Exit
1	2.0	Wide Open	Blocked*
2	2.0	6 Holes	30 Holes
3	2.0	Blocked*	30 Holes
4	2.0	6 Holes	23 Holes**
5	2.0	Blocked*	23 Holes**
6	12.5	6 Holes	30 Holes
7	12.5	Blocked*	30 Holes
8	12.5	6 Holes	23 Holes**
9	12.5	Blocked*	23 Holes**

* Holes were plugged with wooden dowels and sealed with silicone rubber sealant.
** First seven even-numbered holes from the test section entrance were plugged with wooden dowels and sealed with silicone rubber sealant.

cross section as that of the test channel and was 30.5 cm (12.0 in.) long to ensure that the flow of air was fully developed at the inlet of the test pin fin channel. At the upstream end of the entrance channel, air was supplied through a standard 5.08 cm (2 in.) pipe elbow attached to the top of the entrance channel.

As shown in Fig. 1, the test section was mated to the entrance channel by inserting 1.27 cm (0.5 in.) of the test section into an inset at the downstream end of the entrance section. Four long rods of 3.18 mm (0.125 in.) in diameter were inserted through aligned holes drilled through the hard wood and the top and bottom walls on both sides of the flow channel to hold the test section in place. These rods did not block the flow entrance, as shown in Fig. 1. Silicone rubber sealant prevented air leakage at the joint.

The test section and the entrance section were heavily insulated. At the radial flow and trailing edge ejection flow exits, there were openings in the fiberglass insulation for the air to leave the test section and for maintaining the two exits at atmospheric pressure.

Instrumentation

The rate of mass flow through the test section was measured with a calibrated 5.08 cm (2.0 in.) orifice flow meter with a square-edged 2.54 cm (1.0 in.) orifice and flange taps. The pressure drop across the orifice and the pressure upstream of the orifice with respect to the atmospheric pressure were measured with mercury and oil manometers.

Twenty-eight 36-gage copper-constantan thermocouples with Teflon insulation measured the channel wall temperatures. Twenty-four of the thermocouples were installed in a regular inline 6 × 4 array of small holes in the top wall. The spacings between adjacent holes were 5.08 cm (2.0 in.) and 2.54 cm (1.0 in.) in the radial and trailing edge flow directions, respectively. Four other thermocouples were embedded in the bottom wall to check for symmetry in heating the top and bottom walls. To ensure good contact between each thermocouple junction and the channel wall, the thermocouple was held in place with epoxy in shallow grooves on the outside surface of the wall, with the thermocouple junction in contact with the bottom of the hole. The hole was then filled with paint made of pure silver.

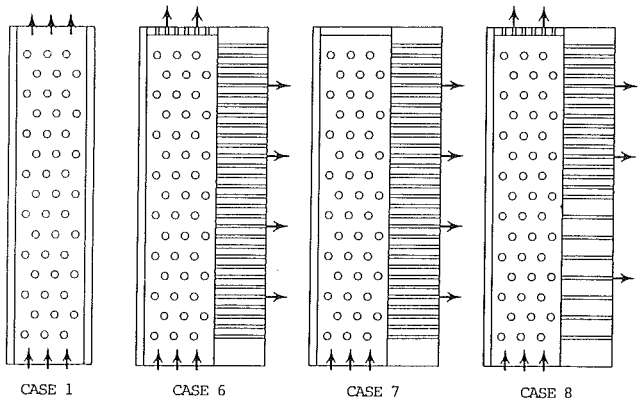

Fig. 2 Four typical ejection hole configurations

Two thermocouples measured the inlet air temperatures; four other thermocouples measured the air temperatures at the radial flow exit and the trailing edge ejection exit; and two thermocouples measured the room temperature.

The outputs of all 36 thermocouples were recorded with an Omega Model OM-205 data logger. The total power input to the two heaters was controlled with a variable transformer. The voltage drop across the heaters and the current through the heaters were measured with two Hewlett Packard Model 3478A 5 1/2-digit TRMS multimeters.

Eight static pressure taps were installed on the test channel, one immediately upstream of the test section and seven along the solid side wall halfway between adjacent odd-numbered and even-numbered pin rows (at x/X = 2.0, 4.0, 6.0, . . . , 12.0, and 14.0). The overall pressure drop across the test section and the local pressures along the solid side wall with respect to the ejection hole exit pressure were measured with one of several oil or mercury manometers, depending on the measurement range.

Experimental Procedure

Experiments were conducted for Reynolds numbers between 10,000 and 60,000, two trailing edge ejection hole length-to-diameter ratios of 2.0 and 12.5, and four exit hole configurations, as shown in Table 1. Four of the test section exit hole configurations are illustrated in Fig. 2.

A typical experiment lasted two hours. After compressed air flowed through the test section at a predetermined rate, the test section was heated. Power input to the heaters was adjusted by monitoring the typical temperatures in the channel walls until the wall–inlet temperature difference was about 25°C (45°F). The system attained steady state in about an hour and a half, during which the atmospheric pressure, the pressure drop across the orifice, and the power input to the heaters were monitored periodically.

After the system attained steady state, the atmospheric pressure, the pressure drop across the orifice, and the gage pressures upstream of the orifice and at taps on the test section were recorded. A printout of all the thermocouple readings was then obtained and the power input to the heaters recorded.

Preliminary experiments were conducted to determine the heat loss through the insulation. Before each of the test runs, the system was checked for possible air leakage. For most of the test section configurations studied, it was necessary to plug some of the ejection holes with wooden dowels and seal them with silicon rubber sealant before the test run.

The same test section was used for the long trailing edge ejection hole study and the short ejection hole study. After completion of the long ejection hole test runs (test cases 6

through 9), a 3.33 cm (1.31 in.) wide section of the side wall with the trailing edge ejection holes was cut off on a mill. The test section was then used in the short ejection hole experiments (test cases 1 through 5).

Reduction of Data

The overall Nusselt number is calculated as

$$\mathrm{Nu}_D = \{[(\dot{q}_{in} - \dot{q}_{\mathrm{loss}})/A]/\Delta T_{lm}\}(D/k) \tag{1}$$

where $\dot{q}_{in}$ is the total power input to the two heaters and is the product of the measured voltage and current. The rate of heat loss, $\dot{q}_{\mathrm{loss}}$, to the surroundings is determined from the relationship between the steady-state power input to the heaters under no flow conditions and the heater-room temperature difference, which is obtained from preliminary experiments. The total heat transfer area A includes the exposed surface areas of the top and bottom walls, the pins, the side walls, the radial flow exit blockage, and the ejection holes. The values of A are different for the various test section configurations and, thus, the various cases studied.

The log mean temperature difference, ΔT_{lm}, is defined as

$$\Delta T_{lm} = [(\bar{T}_w - T_{bi}) - (\bar{T}_w - T_{bo})] / \{\ln[(\bar{T}_w - T_{bi})/(\bar{T}_w - T_{bo})]\} \tag{2}$$

where the average wall temperature $\bar{T}_w$ is the overall average of the measured wall temperatures, and the nominal outlet air temperature T_{bo} is evaluated as

$$T_{bo} = T_{bi} + (\dot{q}_{in} - \dot{q}_{\mathrm{loss}})/(\dot{m}c_p) \tag{3}$$

For all of the test runs, the calculated nominal outlet air temperature is comparable to the average of the measured outlet air temperatures.

The Reynolds number is defined in terms of the pin diameter and the air velocity at the minimum flow cross section in the pin fin channel

$$\mathrm{Re}_D = \rho u_{\max} D/\mu = \dot{m}D/(A_{\min}\mu) \tag{4}$$

The total pressure drop across the test section and the local pressure in the test section with respect to the ejection hole exit pressure (equal to the atmospheric pressure in the experiments) are normalized by the dynamic pressure based on $u_{\max}$. The former is defined as the overall friction factor f. Thus

$$f = (p_{\mathrm{inlet}} - p_{\mathrm{exit}})/[(1/2)\rho u_{\max}^2 N] = 2(p_{\mathrm{inlet}} - p_{\mathrm{exit}})\rho(A_{\min}/\dot{m})^2/N \tag{5}$$

where N is the number of pin rows in the test section. The normalized relative local pressure is defined as

$$p_j = (p_{\mathrm{local}} - p_{\mathrm{exit}})/[(1/2)\rho u_{\max}^2 N] = 2(p_{\mathrm{local}} - p_{\mathrm{exit}})\rho(A_{\min}/\dot{m})^2/N \tag{6}$$

The rate of mass flow through each trailing edge ejection hole is estimated as

$$\dot{m}_j = C_D A_j [2\rho(p_{\mathrm{local}} - p_{\mathrm{exit}})]^{1/2} \tag{7}$$

where C_D is a discharge coefficient and A_j is the flow cross-sectional area of the ejection hole. The sum of the rates of mass flow through all the ejection holes is equal to the rate of total mass flow through the pin fin channel, $\dot{m}$. If the value of C_D does not change significantly from one ejection hole to another, it can be shown that

$$\dot{m}_j/\dot{m} = (P_j)^{1/2} \Big/ \left[\sum_{i=1}^{n} (P_i^{1/2})\right] \tag{8}$$

The ratio of the radial mass flow rate to the total mass flow rate is then given as

$$\dot{m}_x/\dot{m} = 1 - \sum_{i=1}^{j} \dot{m}_i/\dot{m} \tag{9}$$

where $\Sigma\dot{m}_i/\dot{m}$ is the sum of the rates of mass flow through the trailing edge ejection holes located upstream of the station at which the value of $\dot{m}_x/\dot{m}$ is to be calculated.

In all of the above equations, the properties of the flowing air are evaluated at the average bulk temperature.

The pressure drop across the orifice in the flow meter never fluctuated more than 1.5 percent during any of the test runs. Since the orifice flow meter is rated at ±1.0 percent accuracy, the uncertainty of the total mass flow rate through the test section is estimated to be less than ±1.8 percent. Based on the tolerance of all the dimensions of the test section, the uncertainties of A and D are estimated to be both ±0.8 percent. Using equation (4), estimated uncertainties of ±2.0 percent for the properties of air, and the uncertainty estimation method of Kline and McClintock (1953), the maximum uncertainty of the calculated Reynolds number is ±2.9 percent.

The total power input to the heaters varied by no more than ±4.0 percent during any experiment. The estimated rate of heat loss through the insulation is always less than 3.0 percent of the total power input to the heaters (much less for high Reynolds number runs). Even if the estimated heat loss rate (based on the results of preliminary experiments under no flow conditions) were accurate to only ±30 percent, the uncertainty of $\dot{q}_{\mathrm{loss}}$ would still be less than ±1.0 percent. Therefore, the uncertainty of the actual power input to the heaters is about ±5.0 percent. Using equation (1), a conservatively estimated uncertainty of ±8.0 percent for the evaluation of the log mean temperature difference results in an uncertainty of ±9.7 percent in the calculated overall Nusselt number.

Similarly, with the method of Kline and McClintock (1953), the normalized pressure drops have an uncertainty of ±4.7 percent.

Presentation of Results

In Figs. 3 through 5, the overall Nusselt number is plotted as a function of the flow Reynolds number for the various cases studied. In each of the test cases, data are obtained for at least five different Reynolds numbers ranging from about 10,000 to 60,000.

Attention is first focused on the heat transfer results of test case 1 in Fig. 3. In test case 1, the cooling air is forced to flow straight (radially) through the pin fin channel and there is no lateral (trailing edge) ejection of the cooling air. Also shown in Fig. 3, for comparison, are the Nusselt number–Reynolds number correlations based on the published data of Metzger et al. (1982) and Lau et al. (1987).

In Fig. 3, it is evident that all the data points of test case 1 fall on a straight line. Thus, the Nusselt number is a power function of Reynolds number (that is, $\mathrm{Nu}_D = a(\mathrm{Re}_D)^b$, where a and b are constants). The slope of the curve fit line, however, is very different from those based on the correlations from the aforementioned earlier studies. At Re = 10,000 and 60,000, the present data of test case 1 are about 11.5 percent higher and 34 percent lower, respectively, than those of Metzger et al. (1982).

The deviation of the present data from the earlier correlations is believed to be due to the geometry of the test section in the present investigation being very different from those in the two earlier studies. Although the staggered pin arrangement of L/D = 1.0 and X/D = S/D = 2.5 is the same in all three studies, the test section of Metzger et al. (1982) had ten rows of ten pins and a 25:1 flow cross section; that of test case G in Lau et al. (1987) had eight rows of four pins and an 11.25:1 flow cross section. The test section in the present investigation has 15 rows of three pins and a 8.75:1 flow cross section. It appears that, for the same pin configuration, varying the channel geometry significantly affects the heat transfer characteristics of the flow of air in a pin fin channel. The low overall heat transfer coefficient in test case 1 over most of the Reynolds

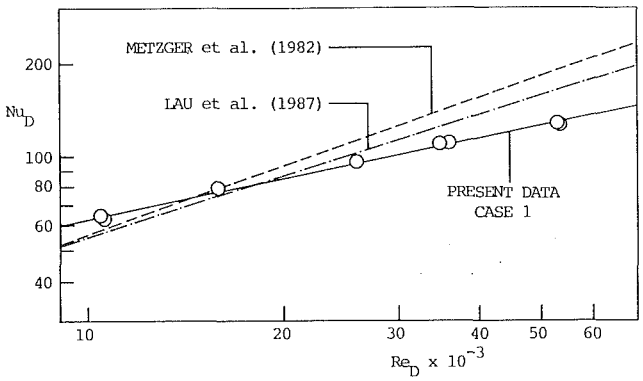

Fig. 3 Overall heat transfer, case 1

number range of interest is attributed largely to the large number of pin rows (15 rows) used in the present investigation. Metzger et al. (1982) demonstrated that the row-averaged Nusselt number decreases with increasing distance from the channel entrance after an initial increase.

To ensure that the deviation of the data in test case 1 from the results of the previous studies was not due to human errors, three of the five original test runs were repeated. Before the additional test runs were carried out, the test apparatus was taken apart and reassembled, the thermocouples and all instrumentations were inspected, and all joints along the flow loop were checked for air leakage. Furthermore, the three additional tests were conducted with power input different from that in the earlier runs.

The results of the three additional test runs are plotted with those of the original test runs. Figure 3 shows that the additional test data are consistent with data from the original five test runs.

Hole Geometry Effect. The heat transfer results of test cases 2 through 5 and test cases 6 through 9 are presented separately in Figs. 4(*a*) and 4(*b*). In test cases 2 through 5, the length-to-diameter ratio of the trailing edge ejection holes, L^*/d, is 2.0. In test cases 6 through 9, the corresponding ratio is 12.5. Test cases 2 through 5 and 6 through 9 differ in the configuration of the radial flow exit blockage (six tip bleed holes or no radial flow exit) and the configuration of the trailing edge ejection holes (30 equally spaced holes or 23 holes with the eight holes near the channel entrance spaced twice the distance between adjacent holes farther away from the channel entrance).

In Fig. 4(*a*), all the data fall on parallel straight lines. The deviation of a few of the data points from the straight lines is within the uncertainty of the data. These lines are all lower and have a steeper slope than that of the curve fit line through the data of test case 1, which is included in the figure for comparison. The gradual convergence of the curve fit line for test case 1 (for radial flow only) and the parallel curve fit lines for other test cases (for flow through both trailing edge ejection holes and holes at the radial flow exit) with increasing Reynolds number is similar to the trend exhibited in the results of Lau et al. (1987).

When all the cooling air is forced to exit through the trailing edge ejection holes (test case 3), the overall Nusselt number is about 6 percent lower than that in test case 2, in which the cooling air exits the test channel through both trailing edge and radial flow ejection holes. Lau et al. (1987) showed that the overall heat transfer in a pin fin channel decreases with increasing ejection ratio (defined as the rate of mass flow through the trailing edge ejection holes divided by the rate of the total mass flow through the channel). It is clear that the trend of the results of the present investigation also shows that, with only a portion of the total mass flow through the

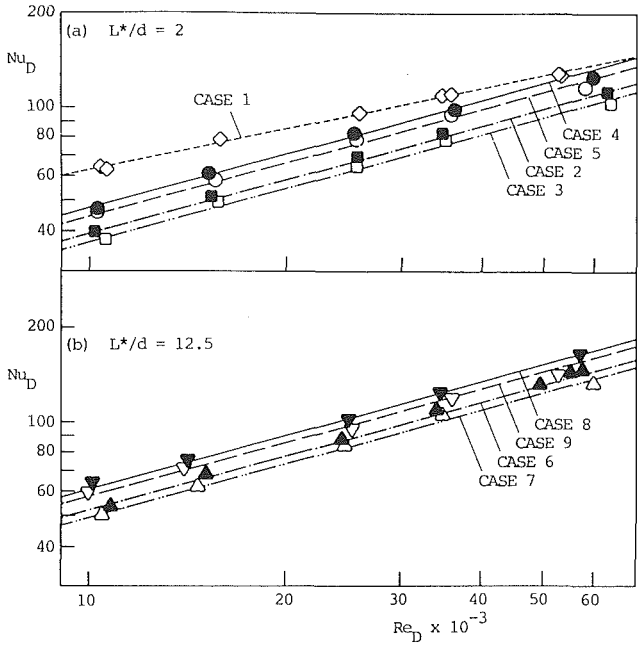

Fig. 4 Overall heat transfer: (*a*) $L^*/d = 2$; (*b*) $L^*/d = 12.5$

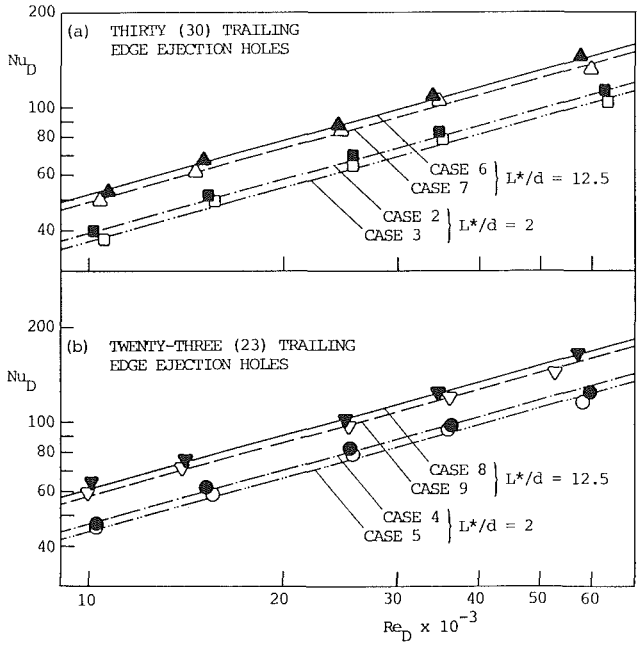

Fig. 5 Overall heat transfer: (*a*) 30 trailing edge ejection holes; (*b*) 23 trailing edge ejection holes

trailing edge ejection holes, the overall heat transfer is higher than that in the corresponding case of total mass flow through the trailing edge ejection holes (that is, no radial flow ejection).

Since the Nusselt numbers in test cases 2 and 3 differ only slightly, the ejection ratio in test case 2 is believed to be quite large. That is, the portion of the total air flow through the radial flow exit in test case 2 is relatively small. It will be shown shortly that the ejection ratio in test case 2 is about 0.85, regardless of the flow Reynolds number, over the range of Reynolds number studied. Since a fluid finds the path of least resistance, most of the flow exits the test channel through the trailing edge ejection holes. During test runs, the velocities of the air flow through the holes near the channel entrance were much higher than those through holes farther from the channel entrance.

Table 2 Values of coefficient and exponent in equation (10)

Test Case	a	b
1	1.1586	0.4335
2	0.2184	0.5642
3	0.2056	0.5642
4	0.2643	0.5642
5	0.2497	0.5642
6	0.2908	0.5642
7	0.2761	0.5642
8	0.3378	0.5642
9	0.3201	0.5642

When seven of the thirty trailing edge ejection holes near the channel entrance are plugged with wooden dowels, more air must flow farther downstream in the radial flow direction before exiting the test channel. The test results show that the overall heat transfer in test case 4 with seven ejection holes blocked is about 21 percent higher than that in test case 2. When there is no radial flow exit (test case 5), the Nusselt number is again lowered by about 6 percent. Thus, the Nusselt number for test case 5 is also about 21 percent higher than that for test case 3. It can be concluded that the pin fin channel geometry that forces more cooling air to flow farther downstream in the radial flow direction before exiting the test section provides better overall cooling of the test channel.

Figure 4(*b*) shows that the results of test cases 6 through 9 are very similar to those in Fig. 4(*a*). The data points fall on parallel straight lines, with the same slope as the curve fit lines in Fig. 4(*a*). At any given Reynolds number, the Nusselt numbers in test cases 7 and 9 are about 5 percent lower than those in test cases 6 and 8, respectively. Again, the effect of no radial flow exit is the lowering of the overall heat transfer of the pin fin channel. When seven of the trailing edge ejection holes near the channel entrance are blocked (test cases 8 and 9), the Nusselt number is increased by about 16 percent.

Hole Length Effect. To examine the effect of varying the length of the trailing edge ejection holes on the overall heat transfer, the experimental results of test cases 2, 3, 6, and 7 and test cases 4, 5, 8, and 9 are replotted separately in Figs. 5(*a*) and 5(*b*). In both figures, the long ejection hole data are higher than the corresponding short ejection hole data. When the cooling air flows through all 30 equally spaced trailing edge ejection holes on the test channel, the long ejection hole data (test cases 6 and 7) are about 33 to 34 percent higher than the corresponding short ejection hole data (test cases 2 and 3). Increasing the length of the ejection holes forces the cooling air to flow through long holes of small diameter at high speeds, which enhances the overall heat transfer of the channel.

In Fig. 5(*b*), the long and short ejection hole data are presented for test cases 4, 5, 8, and 9. In these cases, seven of the thirty trailing edge ejection holes near the pin fin channel entrance are blocked. Again, the Nusselt numbers for the long ejection hole cases are higher than those for the corresponding short ejection hole cases. It will become evident shortly, however, that the pumping power must be increased with the increase in the ejection hole length and the aforementioned trailing edge ejection hole arrangement (typically with fewer ejection holes near the channel entrance and more holes farther away from the entrance).

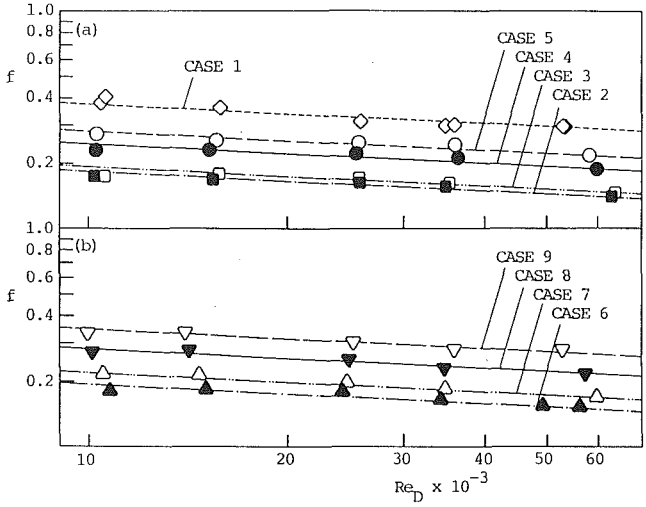

Fig. 6 Overall friction factor

Since all the heat transfer data fall on straight lines, they can be correlated with the equation

$$\mathrm{Nu_D} = a(\mathrm{Re_D})^b \tag{10}$$

In test case 1, the values of the coefficient a and the exponent b are 1.1586 and 0.4335, respectively. Since all the data of test cases 2 through 9 follow parallel straight lines, the values of the exponent b are the same in all of the cases. Table 2 lists the values of the coefficient a and the exponent b for all the cases studied.

Overall Pressure Drop and Local Pressure. In Fig. 6, the overall friction factors for all the test cases are plotted versus the Reynolds number. The results for the $L^*/d = 2.0$ cases (test cases 1 through 5) are displayed on the top half of Fig. 6; those for the $L^*/d = 12.5$ cases (test cases 6 through 9) are presented on the bottom half of the figure. In general, the overall friction factor decreases slightly with increasing Reynolds number. In test case 1, there is no trailing edge ejection hole. The cooling air is forced to flow past the 15 rows of pins and exit through the wide opened radial flow exit. The experimental results show that the pressure drop across the test channel in test case 1 is higher than that in all other cases.

Comparing the results for test cases 2 through 5 shows that blocking the radial flow exit and/or blocking some of the trailing edge ejection holes near the channel entrance increase(s) the overall channel pressure drop. The $L^*/d = 12.5$ data (test cases 6 through 9) exhibit similar trends, as the overall friction factor is the lowest for test case 6 and the highest for test case 9. When straight lines are fitted through the data points in Fig. 6, the lines through the points for test cases 2 through 9 are all about parallel.

When the overall friction factors for the $L^*/d = 2.0$ cases are compared with those for the corresponding $L^*/d = 12.5$ cases (for the same ejection hole configuration), the short ejection hole data are always the lower. Thus, increasing the length of the trailing edge ejection holes also increases the overall channel pressure drop.

From Figs. 4 and 6, it is evident that the increase in the overall heat transfer is generally accompanied by an increase in the overall pressure drop (that is, an increase in the required pumping power), except that the overall heat transfer is lower and the overall pressure drop is higher when the radial flow exit is blocked.

Typical local pressure data are presented in Figs. 7(*a*) and 7(*b*). The normalized local pressure (defined in equation (6)) is plotted as a function of the dimensionless distance from the channel entrance, x/X, for Re $\cong$ 25,000, and for the $L^*/d =$

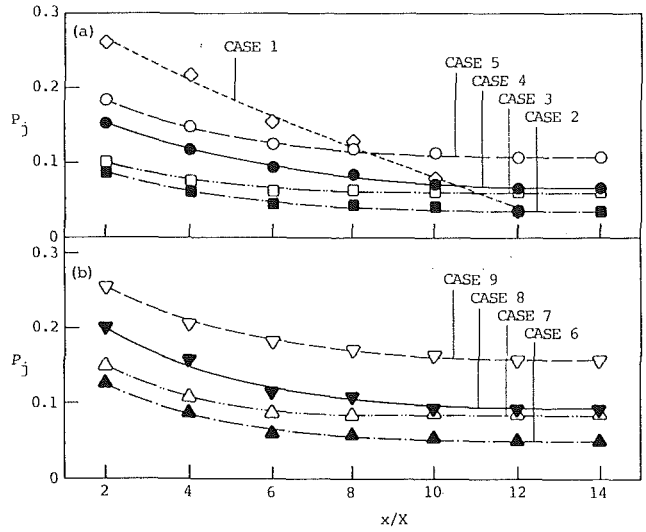

Fig. 7 Local pressure drop, $Re_D \cong 25{,}000$: (*a*) cases 1 through 5; (*b*) cases 6 through 9

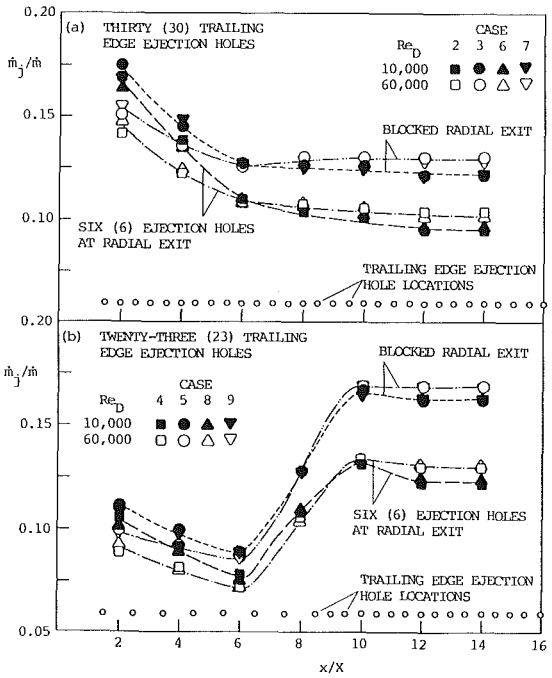

Fig. 8 Trailing edge ejection mass flow rate per two pin rows

2.0 cases and the $L^*/d = 12.5$ cases, respectively. The seven pressure taps are installed along the solid side wall at $x/X =$ 2.0, 4.0, 6.0, . . . , 12.0, and 14.0 (every two times the pin spacing in the radial flow direction) midway between adjacent pin rows at $x/X = 1.5, 2.5, 3.5, \ldots, 14.5$, and 15.5.

In all test cases, the local pressure decreases monotonically with increasing distance from the channel entrance. The slopes of the pressure distributions increase gradually with increasing values of x/X. In test case 1, with no trailing edge ejection flow, the local pressure decreases much faster than all other test cases with increasing values of x/X.

The local pressure distributions in Figs. 7(*a*) and 7(*b*) show that the local pressures are higher when all of the cooling air is forced to exit through the trailing edge ejection holes (by blocking the radial flow exit) and/or when more of the cooling air is forced to flow downstream in the radial flow direction before exiting the channel through the trailing edge ejection holes (by blocking some of the trailing edge ejection holes near the channel entrance). Comparing the local pressure distributions in Figs. 7(*a*) and 7(*b*) shows that the local pressures in the channel are higher in the long ejection hole cases than in the corresponding short ejection hole cases.

The local pressure distributions for other Reynolds numbers are similar to those shown in Fig. 7. The normalized local pressures are generally higher at low Reynolds numbers and lower at high Reynolds numbers.

Local Mass Flow Rate. *The ratio of the rate of mass flow* through a trailing edge ejection hole to the total mass flow rate, $\dot{m}_j/\dot{m}$, is calculated with equation (8) from the measured relative local pressure. The local pressure is measured at seven pressure taps on the solid side wall of the channel. Subsequent pressure measurement experiments using an acrylic geometrically similar test section (twice the size of the copper test section) with many pressure taps show that there is negligible pressure drop in the lateral (trailing edge) flow direction in the test pin fin channel. The supplementary pressure experiments also show that the local pressure drops monotonically in the radial flow direction as shown in Fig. 7.

In Figs. 8(*a*) and 8(*b*), the rate of mass flow through trailing edge ejection holes per two pin rows is plotted versus the distance from the channel entrance, in the cases of 30 and 23 trailing edge ejection holes, respectively. Results are presented for $Re_D \cong 10{,}000$ (darkened symbols) and $Re_D \cong 60{,}000$ (open symbols).

Figure 8(*a*) shows that the rate of mass flow through trailing edge ejection holes (per two pin rows) is generally high near the channel entrance and low further away from the channel entrance. The ejection mass flow rate is higher when the radial flow exit is blocked (test cases 3 and 7) than when a portion of the flowing air is allowed to exit radially through six tip bleed holes (test cases 2 and 6). The effect of varying the flow Reynolds number is that, at higher Reynolds numbers, the ejection mass flow rate is lower near the channel entrance and higher farther away from the channel entrance. The inertia of the flowing air at higher Reynolds numbers pushes more of the air to flow downstream in the radial direction before exiting the pin fin channel through trailing edge ejection holes and/or radial ejection holes.

Increasing the length of the trailing edge ejection holes from $L^*/d = 2.0$ to $L^*/d = 12.5$ does not appear to affect the distribution of the trailing edge ejection mass flow rate significantly. Thus, smooth curves are drawn through data points for the corresponding long and short ejection hole cases.

When seven of the trailing edge ejection holes near the channel entrance are blocked, the mass flow rates through the trailing edge ejection holes farther away from the entrance increase signficantly, as shown in Fig. 8(*b*). The effects of blocking the radial flow exit and varying the flow Reynolds number and the length of the trailing edge ejection holes on the mass flow rate distribution are similar to those in the previous cases with ejection flow through all 30 ejection holes.

Figure 9 shows the local distributions of the ratio of the radial mass flow rate to the total mass flow rate, $\dot{m}_x/\dot{m}$, for $Re_D \cong 10{,}000$, 25,000, and 60,000. In the evaluation of $\dot{m}_x/\dot{m}$, the rates of mass flow through four (or two when seven of the trailing edge ejection holes are blocked) trailing edge ejection holes on two adjacent odd-numbered and even-numbered pin rows are assumed to be the same. The radial mass flow rate at any radial station, x/X, is then calculated with equation (9). Since the difference between the radial mass flow rate distributions for the long and short ejection hole cases is insignificant, a single symbol is used for corresponding long and short ejection hole cases.

The $\dot{m}_x/\dot{m}$ distributions in Fig. 9 show that the radial mass flow rate remains high in the pin fin channel when seven of the trailing edge ejection holes near the channel entrance are blocked and/or when there are six ejection holes at the radial

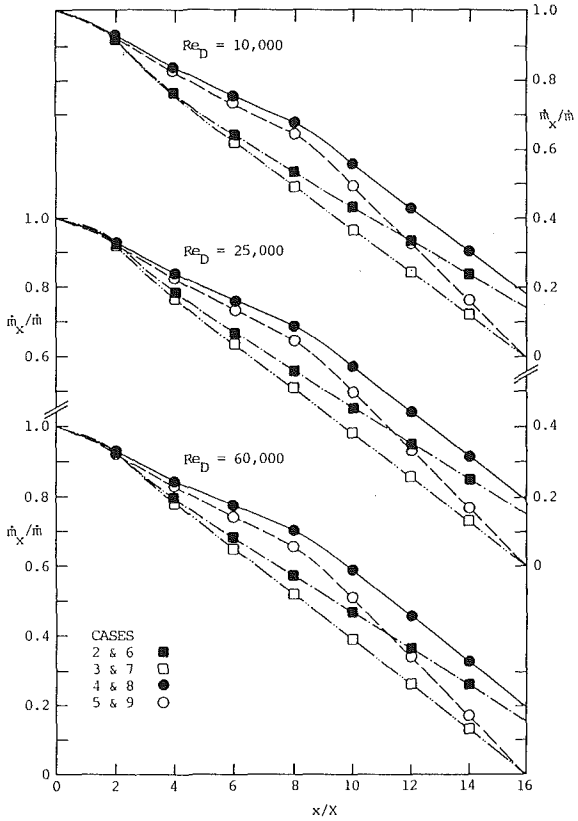

Fig. 9 Radial mass flow rate in pin fin channel

flow exit. When air is allowed to exit through all 36 trailing edge and radial ejection holes (test cases 2 and 6), about 15 percent of the flow exits through the radial ejection holes. That is, the ejection ratio is about 0.85.

In cases 4 and 8, with seven of the trailing edge ejection holes blocked, about 18 to 20 percent of the flow exits through the radial ejection holes. Thus, the ejection ratio is about 0.82 to 0.80. The blocking of some of trailing edge ejection holes forces more flow to exit through the radial ejection holes.

With increasing flow Reynolds number, slightly more flow exits through the radial ejection holes, in the cases with the radial flow exit open (test cases 2, 4, 6, and 8). Otherwise, the effect of varying the flow Reynolds number on the radial mass flow rate distribution is small.

The distributions of the radial mass flow for the corresponding long and short trailing edge ejection hole cases are almost identical. The heat transfer in the pin fin channel only should remain about the same in corresponding long and short ejection hole cases. Since the overall heat transfer in the long ejection hole cases is higher than that in the corresponding short ejection hole cases (Fig. 5), it can be concluded that the higher overall heat transfer is the result of the higher heat transfer coefficient for the air flow through the long trailing edge ejection holes.

Concluding Remarks

An experimental investigation studied the effect of varying the ejection hole length and configuration on the heat transfer, the pressure drop, and the local mass flow rate for the flow of air through a pin fin channel with lateral ejection holes. The following conclusions are drawn:

1 When there is trailing edge flow ejection, the overall heat transfer is lower than that in the case of only radial flow through the pin fin channel. Published data on straight flow through pin fin channels overpredict the overall heat transfer in pin fin channels with trailing edge flow ejection.

2 The overall heat transfer increases when the trailing edge ejection holes are configured so that much of the cooling air is forced to flow downstream in the radial direction before exiting the channel through trailing edge ejection holes or tip bleed holes.

3 When the trailing edge ejection holes are long, the overall heat transfer is higher than that in the corresponding short ejection hole case. Since the distributions of the local mass flow rate in the pin fin channel in corresponding long and short ejection hole cases are about the same, the heat transfer coefficient in the long trailing edge ejection holes must be higher than that in the pin fin channel.

4 The increase in the overall heat transfer is generally accompanied by an increase in the overall pressure drop (that is, an increase in the required pumping power), except that the heat transfer is lower and the pressure drop is higher when there is no radial flow ejection.

5 The Nusselt number–Reynolds number relationship can be correlated well with the equation $Nu_D = a(Re_D)^b$. The exponent b in the equation is almost a constant in all of the cases studied except when there is no trailing edge flow ejection.

6 The overall friction factor decreases slightly with increasing Reynolds number over the range of Reynolds number studied.

7 In the case of flow ejection through six tip bleed holes and 30 (or 23) trailing edge ejection holes, about 15 to 20 percent of the flow exits through the tip bleed holes.

Acknowledgments

This research was supported by the National Science Foundation (Grant No. CBT-8713833).

References

Brigham, B. A., and VanFossen, G. J., 1984, "Length to Diameter Ratio and Row Number Effects in Short Pin Fin Heat Transfer," ASME *Journal of Engineering for Gas Turbines and Power*, Vol. 106, pp. 241–245.

Brown, A., Mandjikas, R., and Mudyiwa, J. M., 1980, "Blade Trailing Edge Heat Transfer," ASME Paper No. 80-GT-45.

Kline, S. J., and McClintock, F. A., 1953, "Describing Uncertainties in Single-Sample Experiments," *Mechanical Engineering*, Vol. 75, pp. 3–8.

Metzger, D. E., and Haley, S. W., 1982, "Heat Transfer Experiments and Flow Visualization for Arrays of Short Pin Fins," ASME Paper No. 82-GT-138.

Metzger, D. E., Berry, R. A., and Bronson, J. P., 1982, "Developing Heat in Rectangular Ducts With Staggered Arrays of Short Pin Fins," ASME *Journal of Heat Transfer*, Vol. 104, pp. 700–706.

Metzger, D. E., Shepard, W. B., and Haley, S. W., 1986, "Row Resolved Heat Transfer Variations in Pin-Fin Arrays Including Effects of Nonuniform Arrays and Flow Convergence," ASME Paper No. 86-GT-132.

Lau, S. C., Kim, Y. S., and Han, J. C., 1985, "Effects of Pin Configuration and Entrance Length on Local Endwall Heat/Mass Transfer in a Pin Fin Channel," ASME Paper No. 85-WA/HT-62.

Lau, S. C., Kim, Y. S., and Han, J. C., 1987, "Effect of Lateral Flow Ejection on Turbulent Heat Transfer in Pin Fin Channels," presented at the ASME/AIChE National Heat Transfer Conference, Pittsburgh, PA, Aug.

VanFossen, G. J., 1982, "Heat-Transfer Coefficients for Staggered Arrays of Short Pin Fins," ASME *Journal of Engineering for Power*, Vol. 104, pp. 268–274.

The Two-Dimensional Behavior of Film Cooling Jets on Concave Surfaces

S. G. Schwarz
Department of Mechanical Engineering,
Tulane University,
New Orleans, LA 70118

R. J. Goldstein
Department of Mechanical Engineering,
University of Minnesota,
Minneapolis, MN 55455

Local impermeable wall effectiveness is measured along a concave surface downstream of a row of film cooling jets. Three different injection hole diameters, two density ratios (0.95 and 2.0), and a wide range of blowing rates (0.3 to 2.7) are considered. Except close to injection, where normal momentum is strong, an increase in blowing rate results in improved film cooling performance. This is attributed to an increase in thermal mass (capacity) of coolant, tangential momentum of the jet, and blockage. Far downstream of injection, the normal and tangential momentum weaken, but blockage and large thermal mass at high injection rates still keep effectiveness high. Lateral mixing of the jets caused by the unstable concave mainflow results in film-cooling performance, which correlates well with the same parameter, which is influential in slot injection on a flat surface. Deviation from this two-dimensional behavior is found only at very low blowing rates and weak wall curvature.

Introduction

Film cooling is used extensively to protect gas turbine rotor blades from hot combustor gases. Although streamwise curvature has a very strong influence on the flows within a turbine cascade, only sporadic attention has been paid to it when considering film cooling. Fundamental work on boundary layer flows (e.g., Bradshaw, 1973) has shown that heat transfer coefficients and turbulence quantities are greatly affected by streamline curvature. The presence of centrifugal forces and a cross-stream pressure gradient can greatly affect the trajectory of a jet along a curved wall, drastically improving or degrading film cooling effectiveness.

The injection parameters (density ratio, blowing ratio, and momentum flux ratio) influence film cooling effectiveness. Their role with flat surface geometries has been the subject of much study. In curved flows, not as much information is available. Ito et al. (1978) examined curvature effects for flow in a turbine cascade. Ko et al. (1984) considered a constant-radius-of-curvature convex surface. Later Xu et al. (1986) turned their attention to a concave surface.

Increased injection beyond a very low momentum flux ratio (usually less than 0.5) on flat or convex surfaces results in a reduction in effectiveness. The jets tend to lift off the wall (Ito, 1976; Pedersen et al., 1977). Liftoff is precipitated by the normal momentum of the jets. Additionally the convex wall curves away from the jet. Film cooling on a concave surface is quite different. Except very near the injection holes, an increase in blowing rate improves the laterally averaged and centerline effectivenesses on a concave surface (Ito et al., 1978; Ko et al., 1986).

It was also found that the jets spread more effectively on a concave surface than a convex (Ko et al., 1986). Studies on flat surfaces show boundary layer size influences lateral spreading (Goldstein et al., 1984; Kadotani and Goldstein, 1979).

Kacker and Whitelaw (1967) found that a fourfold increase in boundary layer thickness causes the impermeable wall effectiveness to decrease by no more than 5 percent over a wide range of blowing rates for slot injection on a flat surface. The magnitudes of the effectivenesses compared well with Seban's (1960) adiabatic wall effectivenesses for a similar slot design. Seban found a reduction of no more than 8 percent with a tenfold increase in boundary layer thickness. Chin et al. (1958) found similarly small variations with a different slot design.

For single-hole injection, Goldstein et al. (1970) found that local (centerline) effectiveness can be reduced significantly when δ_0^*/D is doubled. Later, Kadotani and Goldstein (1979) found similar decreases when looking at ejection through a row of holes. Conversely, they found that midline ($z = z_D/2$) effectiveness can double with a twofold increase in δ_0^*/D. Injection into a thick boundary layer slows the jet down, causing more spreading, thereby flattening lateral profiles of local effectiveness. The interesting result is that the laterally averaged effectiveness is relatively unaffected by the change in δ_0^*. Thus, on flat surfaces, lateral spreading is tied to the size and condition of the mainstream boundary layer at the point of injection while the overall performance is not.

Extending this conclusion to flows affected by curvature, differences between boundary layers on concave and convex surfaces may be the cause of the differences in lateral spreading found by Ko et al. (1986). Taylor–Goertler cells have been

Contributed by the International Gas Turbine Institute and presented at the 33rd International Gas Turbine and Aeroengine Congress and Exhibition, Amsterdam, The Netherlands, June 5–9, 1988. Manuscript received by the International Gas Turbine Institute January 1988. Paper No 88-GT-161.

observed by Tani (1962) along concave walls. These corkscrew-like flow patterns travel downstream near the concave wall. There are generally several of them. The cells, of diameter about the size of the boundary layer thickness, randomly move above in the spanwise direction, sometimes disappearing and reappearing (Barlow and Johnston, 1985a, 1985b). These vortices could also promote spreading on a concave surface.

Boundary layer size, incorporated in both the momentum thickness Reynolds number and the strength of curvature (defined as the displacement thickness divided by the radius of curvature), has been known to affect heat transfer rates on curved surfaces (cf. Simon and Moffat, 1981).

There have been no direct studies of the influence of the boundary layer on film cooling effectiveness for curved flows. Lander et al. (1972) and Ito et al. (1978), however, found that altering the Reynolds number based on chord length in turbine cascade experiments has little influence on the laterally averaged effectiveness. Although no values for displacement thicknesses at these Reynolds numbers were given, Reynolds number independence implies displacement thickness independence. This is what has been found by others on flat surfaces.

The present study focuses on the influence of strength of curvature ($2r/D$) on the impermeable wall effectiveness. As discussed previously, curved and flat wall studies indicate that δ_0^*/D and the condition of the mainstream boundary layer both have little influence on the laterally averaged, impermeable wall, or adiabatic wall film-cooling effectiveness. Thus, the role of $2r/D$ in film cooling can be determined by designing a system that will vary the parameters at constant δ_0^*/r. This was done by fixing both the radius of curvature and the boundary displacement thickness at the point of injection for all cases studied; $2r/D$ was varied by using different injection hole diameters.

Blowing rate plays a very important role in film cooling. In the present work a wide range of blowing rates (0.3 to 2.7) is studied at two density ratios (0.95, simulating isothermal injection, and 2.00, simulating more typical turbine density ratios) for three strengths of curvature ($2r/D$ of about -60, -90, and -120).

Apparatus and Procedure

The experimental apparatus (described in detail by Schwarz, 1986) was designed to determine the film-cooling effectiveness along a concave surface at various locations downstream of injection through a row of holes. A foreign gas injection technique similar to that described by Pedersen et al. (1977) was used. A wind tunnel and a curved test section were constructed to perform this task; they are two of five major components of the total experimental system. The others are the secondary injection, sampling, and data acquisition and reduction systems (Fig. 1).

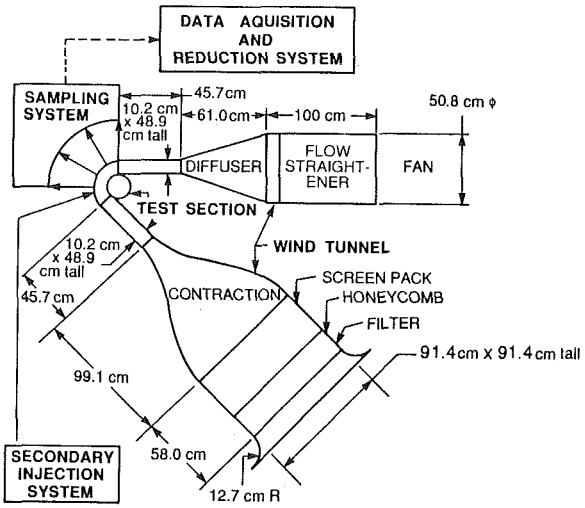

Fig. 1 Experimental apparatus—schematic

The secondary injection system combines desired amounts of air and foreign tracer gas (either Freon-12 or helium). This mixture is injected into the air mainstream through a row of holes. The sampling system is used to draw off samples of the injected gas slowly at the concave wall at various locations downstream of injection. The samples are held in containers until they can be taken for analysis using a gas chromatograph.

The foreign gas concentrations by the wall and in the secondary flow, along with property data and the measured flow rate and velocity enable calculations of the blowing rate, density ratio, and local impermeable wall effectivenesses to within 1.4, 0.1, and 5.7 percent, respectively (Schwartz, 1986).

The concave working surface goes through a bend of 135 deg (see Fig. 1). It is 48.9 cm high and spaced 10.2 cm from the opposite convex wall. The surface has a radius of curvature ($-$) 20.32 cm. Upstream of the curved test section is a 48.9

Nomenclature

C_2 = concentration of tracer in injected gas
C_{iw} = concentration of tracer adjacent to impermeable wall
D = injection hole diameter
I = momentum flux ratio = $(\rho_2 U_2^2/\rho_\infty U_\infty^{*2}$
M = blowing rate = $\rho_2 U_2/\rho_\infty U_\infty$
n_D = number of injection holes
r = radius of curvature of wall (negative for concave wall) = 203.2 mm in present study
Re_2 = Reynolds number of secondary flow = $\rho_2 U_2 D/\mu_2$ or $\rho_2 U_2 s/\mu_2$
s = equivalent slot thickness of row of injection holes ($Z_D s = \pi/4)D^2$)
U_{av} = average streamwise fluid velocity in wind tunnel
U_2 = average velocity of secondary gas through the injection holes
U_∞ = mainflow velocity at the outside edge of the boundary layer at point of injection
x = streamwise distance from downstream edge of injection hole
y = distance from concave wall
z = lateral distance from injection hole centerline
z_D = lateral spacing of injection holes center to center, three dimensional in present study
α = angle of jet axis to tangent to wall = 35 deg in present study
δ_0^* = boundary layer displacement thickness at the point of injection
η = local impermeable wall effectiveness = C_{iw}/C_2
$\bar{\eta}$ = laterally averaged impermeable wall effectiveness
θ_0 = boundary layer momentum thickness at the point of injection
μ_2 = dynamic viscosity of the secondary gas
μ_∞ = dynamic viscosity of the mainstream gas; air in present study
ξ = slot injection parameter applied to concave flows in present study $[x/Ms]$ $[\mathrm{Re}_2(\mu_2/\mu_\infty)] - 1/4$
ρ_2 = density of the secondary injection gas
ρ_∞ = density of the mainstream gas

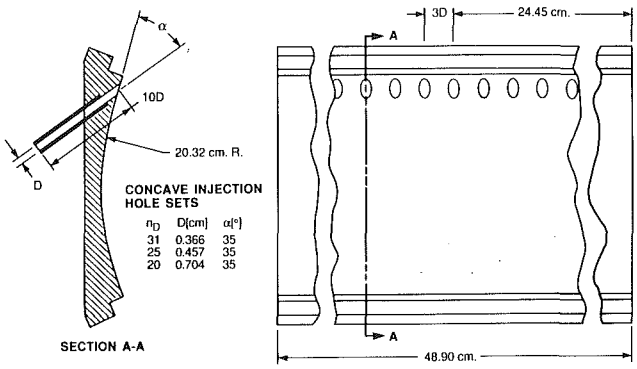

Fig. 2 Concave injection plate

Table 1 Nominal operating conditions

T_∞	24°C
U_{av}	40 m/s
U_∞	32 m/s
δ_0^*	0.41 cm
θ_0	0.29 cm
ρ_2/ρ_∞	0.95 or 2.0
M	0.3 to 2.7
$2r/D$	−59, −89, or −111

cm by 10.2 cm by 45.72 cm long duct, which connects to the tunnel contraction section. A similar duct connects the downstream end of the curved test section to the wide angle diffuser.

The concave working surface is milled out of three aluminum plates to a radius of 20.32 cm, each contributing 45 deg to the total 135 deg curve. The first plate (Fig. 2), which can be removed and replaced with others like it, contains the injection holes. Each of three injection plates has holes drilled through it at an angle of 35 deg to the working surface. Stainless steel tubes of either 0.366 cm, 0.457 cm, or 0.704 cm inner diameter are epoxied into these holes and serve to define the film cooling jets. The tubes are all ten (inner) diameters long. The center line of the injection hole is located at 42.5 deg after the onset of the curvature. The holes are spaced three (inner) diameters apart center to center. The three different hole diameters allow the effects of $2r/D$ and δ_0^*/D on the film cooling effectiveness to be considered.

The nominal operating conditions are listed in Table 1.

Measurement of local velocities used to calculate the displacement and momentum thicknesses at the point of injection was accomplished with a gooseneck pitot probe inserted through the concave wall (see Schwarz, 1986 for a photograph of the probe).

Tests for two dimensionality of the flow in the measurement region of the test section were performed by measuring the local velocities within the boundary layer at various lateral locations both at the injection location and just upstream of the onset of curvature. Boundary layer displacement and momentum thickness varied by no more than 3 percent laterally.

Over most of the range where impermeable wall concentrations were measured, the streamwise pressure gradient was negligible. The gas sampling taps downstream of injection were used to measure the static pressure along the concave wall. Streamwise variation was found to be less than 1 mm H_2O except at the final tap just before the curved portion of the test section ends, where effects of recovery from curvature become significant.

Results

The local impermeable wall effectiveness for helium-tracer injection on a concave surfce for $2r/D = -58$ is displayed in Figs. 3 and 4 for blowing rates of 0.64 and 2.45, respectively. The centerline effectiveness (at $z = 0$) at blowing rates less than unity (Fig. 3) is relatively high just after injection, and

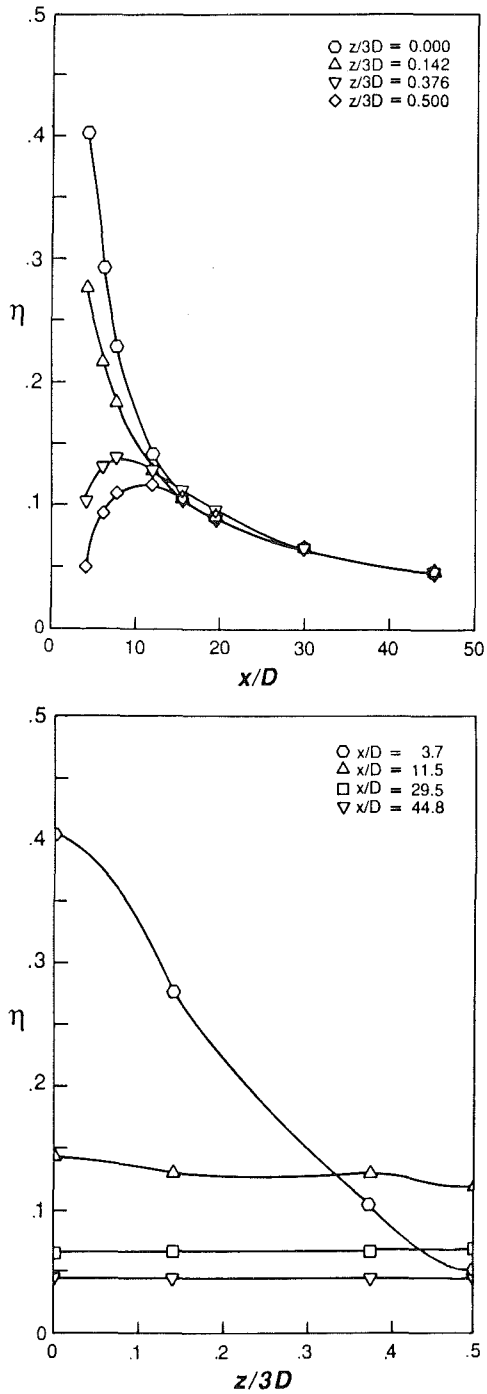

Fig. 3 Film cooling of a concave surface: local effectiveness; $2r/D = -58$, $\delta_0^*/D = 0.58$, $\rho_2/\rho_\infty = 0.95$, $M = 0.64$

trails off as the jet progresses downstream. The jets at low blowing rates remain on the surfce as they leave the injection holes. The performance degrades quickly as the jet mixes with the main flow.

For $M > 1.5$ (Fig. 4) the jets lift off the surfce immediately after injection, as evidenced by the low centerline effectiveness there. The large normal momentum of the jets at high blowing rates is the cause. Moving downstream, the effectiveness increases rapidly to a maximum at between ten and twenty diameters from injection. This improvement is caused by the surface curving upward toward the jets as the jets spread out by turbulent mixing. Performance then trails off due to dilution of the jet by the mainflow, but much more gradually than at the lower blowing rates because of the larger momentum.

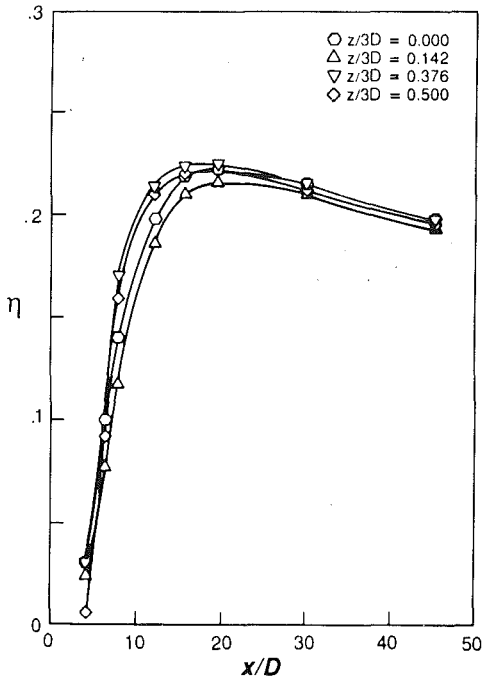

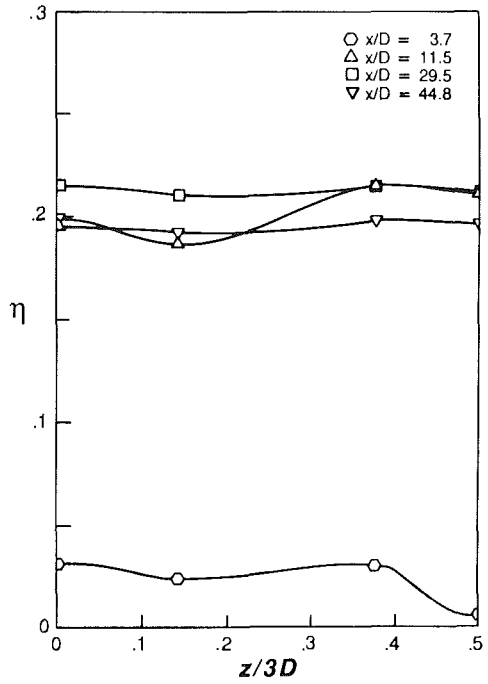

Fig. 4 Film cooling of a concave surface: local effectiveness; $2r/D = -58$, $\delta_0^*/D = 0.58$, $\rho_2/\rho_\infty = 0.95$, $M = 2.45$

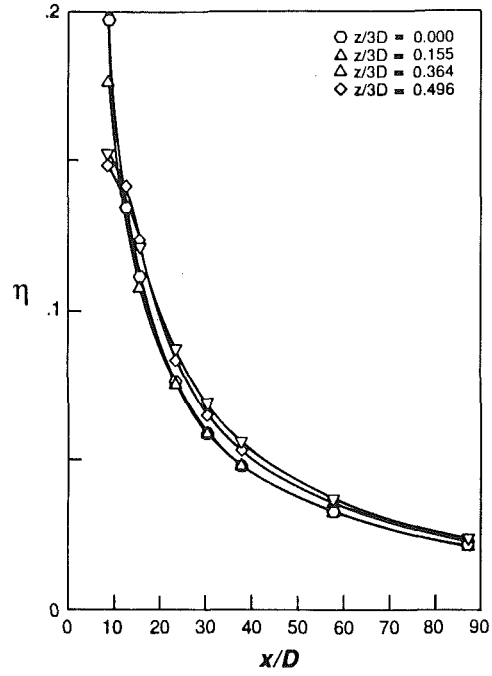

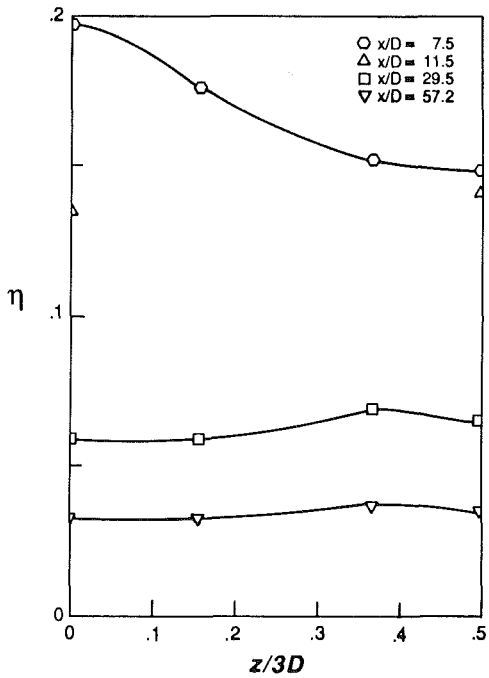

Fig. 5 Film cooling of a concave surface: local effectiveness; $2r/D = -111$, $\delta_0^*/D = 1.12$, $\rho_2/\rho_\infty = 0.95$, $M = 0.63$

The lateral variation in local effectiveness is small in virtually every situation (Figs. 4 and 5). The only exception is found at very low blowing rates, for the largest set of holes studied ($\delta_0^*/D = 0.58$), up to 15 diameters from injection (Fig. 3). Kadotani and Goldstein (1979) observed that on a flat wall, the larger the boundary layer displacement thickness in relation to hole diameter, the more effectively the jet would spread laterally. This also is observed on a concave surface (cf. the lateral profiles of local effectiveness in Figs. 3 and 5 for $\delta_0^*/D = 0.58$ and $\delta_0^*/D = 1.12$, respectively). It should be noted, however, that since the hole diameter is varied in the present study, the relative strength of curvature ($2r/D$) also changes. This may also have an effect on spreading, Schwarz (1986) found that when film-cooling concave and convex surfaces, the lateral profiles of local effectiveness are flatter on the concave than the convex surface. This indicates that there is a potential influence of strength of concave curvature on spreading.

Photographs of the jets (Fig. 6) injected along the concave surface verify that lateral mixing is quite strong. At a low blowing rate of 0.4, the overhead, stop-action views of the jet reveal significant lateral motion. The location of each jet varies widely, as is evidenced from two photos taken at random times using a strobe for lighting. Sometimes two adjacent jets attach to each other. Taylor-Goertler cells, observed by Tani (1962) and visualized by Barlow and Johnston (1985a, 1985b) are concave instabilities, which may be one cause of this enhanced lateral mixing. This lateral mixing at low blowing rate flattens the lateral profile of local effectiveness.

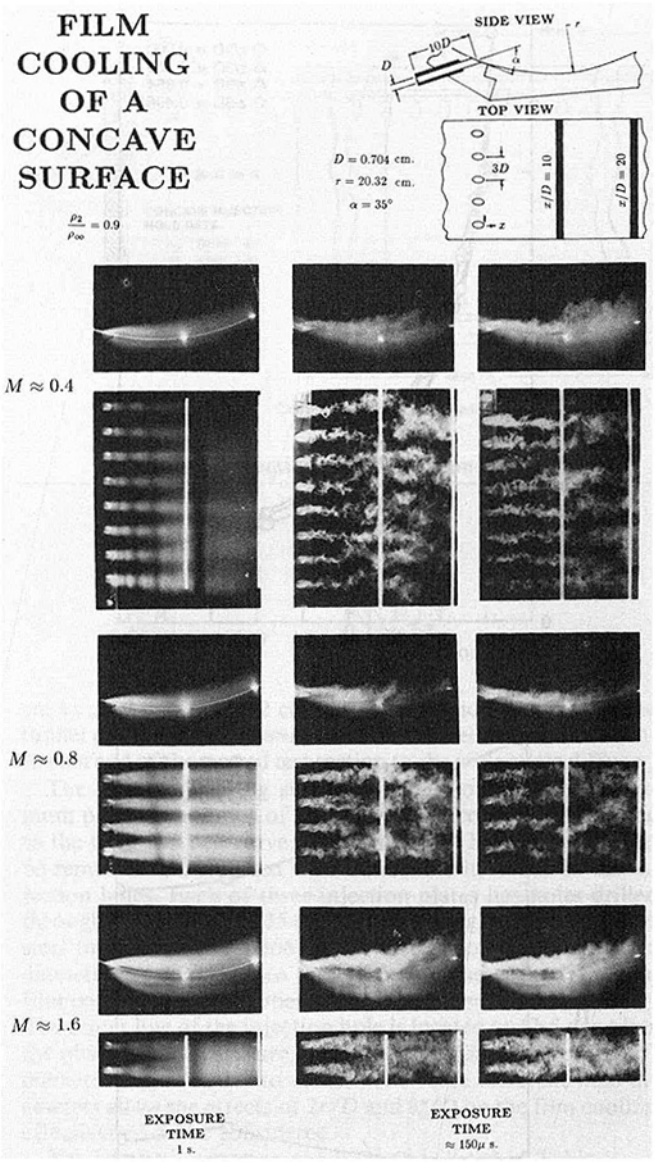

Fig. 6 Film cooling of a concave surface: flow visualization

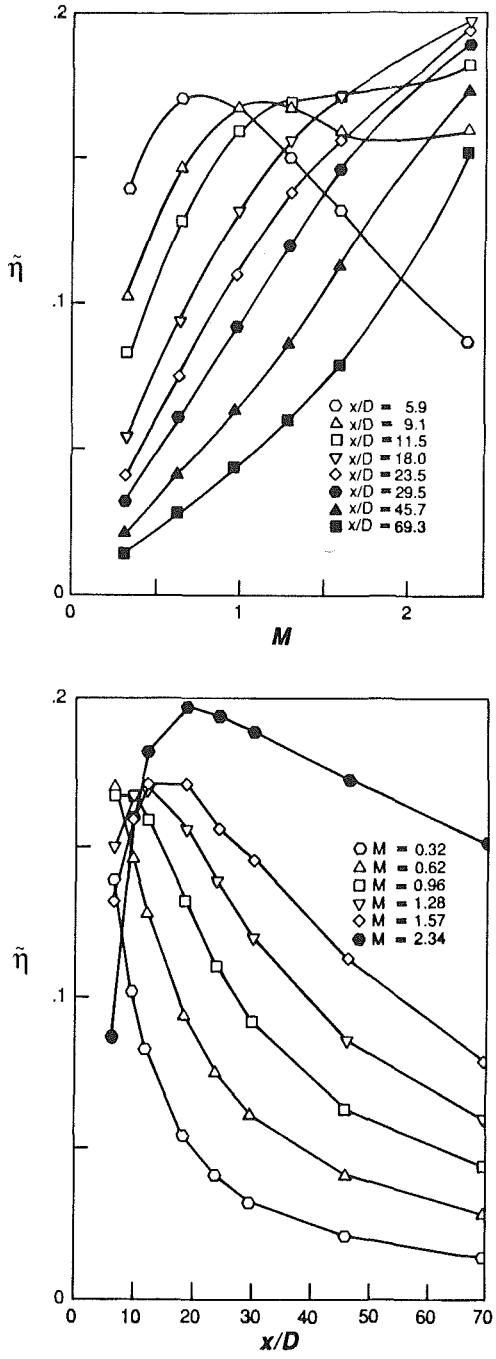

Fig. 7 Film cooling of a concave surface: laterally averaged effectiveness; $2r/D = -89$, $\delta_0^*/D = 0.90$, $\rho_2/\rho_\infty = 0.95$

At high blowing rate (Fig. 6), the lateral sway of the jets is not quite as dramatic; however, it is still evident. The jets attach to each other for longer streamwise distances than is seen for $M = 0.4$. The added mass in the jets increases the tendency for blockage. Time-averaged photos also reveal that the jets exhibit significant lateral spread. At a blowing rate of 1.6, there is no distinction between the jets ten diameters past injection.

The lateral profiles of local effectiveness were integrated and averaged using a cubic spline. The results are plotted in Fig. 7 for $2r/D = -89$. (All three relative strengths of curvature exhibit similar trends.)

Just downstream of injection, an increase in blowing rate beyond a certain point causes a decrease in effectiveness. We call the injection rate at which this maximum performance occurs the optimum blowing rate. Large momentum normal to the concave surface at high blowing rates promotes jet liftoff. Farther downstream, however, normal momentum weakens, but the strong tangential momentum moves the spreading jet closer to the wall. Also, the larger mass of the jet at high blowing rates promotes blockage of the mainstream. Thus, in the range of blowing rates studied, for $x/D > 12$ no maximum effectiveness is indicated.

When considering how blowing rate affects film cooling performance on a concave surface one must examine the competing influences of the normal and tangential momenta of the jet. The question of which predominates may depend upon two factors: injection angle and streamwise location. Injection angle affects both momentum flux components. If sin α is large compared to cos α, the optimum blowing rate might be lower for a given x/D. For tangential or near injection, liftoff might not occur, and the effectiveness might be ever increasing with blowing rate at all x/D, even very near the injection holes.

The three blowing parameters, blowing rate, momentum flux ratio,and velocity ratio, all influence film-cooling performance, and it is not immediately apparent which would be best in correlating the data. Momentum flux ratio might at first seem to be the logical choice. However, varying degrees of

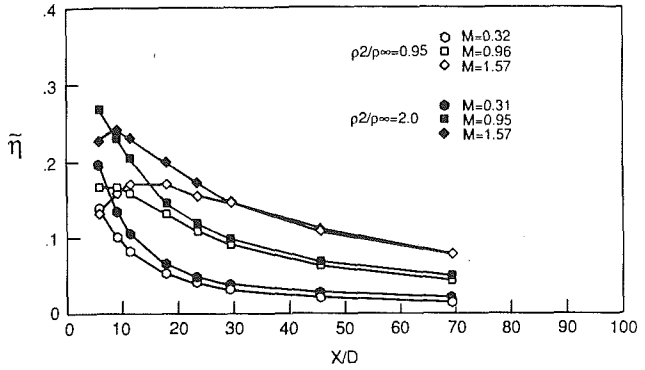

Fig. 8 Film cooling of a concave surface: laterally averaged effectiveness; blowing rate effects: $2r/D = -89$, $\delta_0^*/D = 0.90$, $\rho_2/\rho_\infty = 0.95$ and 2.0

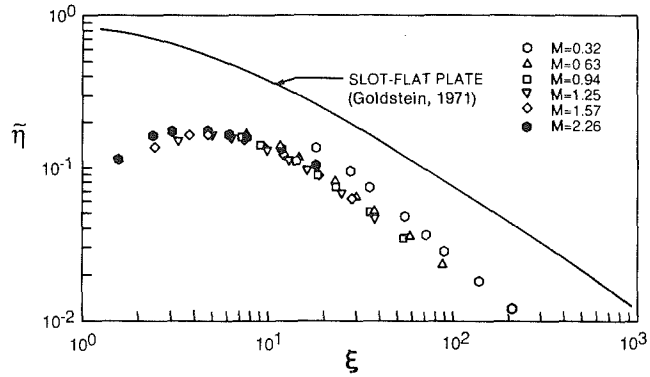

Fig. 9 Film cooling of a concave surface: laterally averaged effectiveness; slot-flat plate comparison: $2r/D = -111$, $\delta_0^*/D = 1.2$, $\rho_2/\rho_\infty = 0.95$

cancellation of the opposing effects of tangential and normal momentum limit momentum flux ratio's overall influence, especially for the 35 deg injection angle of the present study.

Increased blockage and thermal mass are the direct results of high blowing rate, and both improve effectiveness. Figure 8 shows that for a given blowing rate, different density ratios give similar effectiveness sufficiently far from injection. After the initial effects of the strong normal and tangential momentum of injection have worn off blowing rate becomes the correlating injection parameter on the concave surface.

This is also typical of injection through a slot along a flat plate. A number of analytical and experimental studies have shown that a parameter ξ, which depends directly upon blowing rate and streamwise location, can uniquely determine the effectiveness of flush slot geometries (Goldstein, 1971). In Fig. 9, a comparison is made of the results for $2r/D = -58$ (all others yield similar results) with the model of Kutateladze and Leonte'v modified by Goldstein (1971) for slot injection over a flat plate. Except for weak injection through the smallest set holes (weakest curvature), the laterally averaged effectiveness data for row-of-holes injection over a concave surface collapses to one curve when plotted against ξ. Performance is consistently lower than the flat plate predictions, however. The correlation with ξ for row-of-holes injection over a concave surface is due to the large lateral mixing, which promotes blockage of the mainflow from the wall and causes the discrete holes to behave like a slot.

Comparisons such as this have been made for one and two row-of-holes injection on a flat surface (Goldstein et al., 1985). Data for injection through a single row of holes do not correlate well with ξ. The larger the blowing rate, the farther below the slot correlation the performance falls. The poor performance was attributed to the mainflow's ability to travel around and under the jets, causing them to lift off the surface. But injection through two staggered rows of holes is quite different. Al-

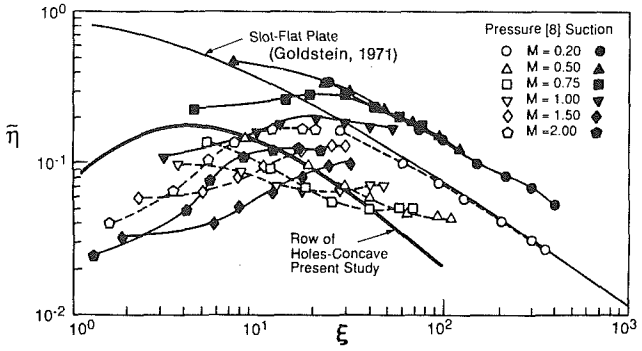

Fig. 10 Film cooling of curved surfaces: laterally averaged effectiveness, comparison of concave surface with turbine blade (Ito, 1976): $\rho_2/\rho_\infty = 0.95$

though at low values of ξ, the performance is lower than that for slot injection, the laterally averaged effectiveness correlates well with ξ. Better initial lateral coverage with two staggered rows of holes blocks the mainflow, preventing liftoff. The end result, then, is that better injection hole coverage increases blockage, improving performance, resulting in correlation with ξ. For the concave surface of the present study correlation with ξ is found with only one row of holes because of the lateral mixing and the absence of liftoff.

In view of the slotlike behavior of row-of-holes injection along a concave surface, it is interesting to examine the effectiveness results along the pressure side of the turbine blade of Ito et al. (1978). Data extracted from Ito (1976) are plotted with ξ in Fig. 10. Contrary to what was found on the constant curvature concave surface of the present study, along the pressure surface of the turbine blade, there is significant variation in effectiveness at any given ξ. Also, performance is better at large ξ and worse at small ξ when compared to the constant-radius-of-curvature concave surface of the present study.

The major differences between the pressure surface of Ito's turbine blade and the concave surface of the present study are that the turbine blade has variable curvature, and is initially convex before injection. Looking at the suction side of the same blade, which is convex throughout, a still larger variation in effectiveness is found at any given ξ (Fig. 10). Therefore, lateral mixing along the pressure side of the blades does have an effect, but not so as to create the good correlation with ξ seen in the present study. The initial convex curvature on the pressure side of the blade can influence the effectiveness significantly.

Note the transition between the effectiveness data from the surface of constant concave curvature to the convex-concave pressure surface and then to the convex suction surface. Correlation with ξ is very good for the fully concave wall and very poor for the fully convex (blade-suction) surface. In between is the convex-concave (blade-pressure) surface. At large ξ the performance is lowest for injection along the concave surface, highest on the suction surface, and somewhere in between for the pressure surface. The jets on the pressure surface of a turbine blade, then, are effected by both concave and convex surface characteristics. The performance is relatively high at large ξ, and relatively low at small ξ, and too variant at all ξ to be classified as "concave." The performance is strongly influenced by the curvature both upstream and downstream of injection.

Conclusion

An increase in blowing rate yields an improvement in film-cooling performance on a concave surface, except where liftoff occurs. Liftoff is significant only in a region just downstream of injection. It is dependent upon the relative strengths of the tangential and normal momenta of the jets. Strong tangential momentum impedes liftoff from a concave surface, while large

normal momentum promotes it. Very near the injection holes normal momentum is strong, and then falls off further downstream. Beyond the region where liftoff occurs, an increase in blowing rate results in better performance because of the large thermal mass of the coolant and the increased tendency for blockage of the mainflow.

The unstable flow along the concave wall promotes lateral mixing of the film cooling jets. As a result, lateral profiles of local effectiveness are very flat. Because lateral mixing is so great on the concave surface, the laterally averaged effectiveness correlates well with the parameter ξ, which is typically used for slot injection. The only situation where the effectiveness deviates from the correlation is at very low blowing rates for the weakest curvatures studied.

Effectiveness data for the pressure side of a turbine blade (Ito et al. 1978) do not exhibit the same behavior as data for the concave surfaces. Comparing pressure and suction surface data with those for the present concave surface, it is reasoned that the initial convex curvature on the pressure side of the blade strongly affects the film cooling performance there.

References

Barlow, R.S., and Johnston, J. P., 1985, "Structure of Turbulent Boundary Layers on a Concave Surface," Report MD-47, Thermosciences Division, Department of Mechanical Engineering, Stanford University, CA.

Barlow, R. S., and Johnston, J. P., 1985, "Roll Cells in Concave Turbulent Boundary Layers," film to accompany Report MD-47, Thermosciences Division, Department of Mechanical Engineering, Stanford University, CA.

Bradshaw, P., 1973, "Effects of Streamline Curvature on Turbulent Flow," AGARDOgraph #169.

Chin, J. H., Skirvin, S. C., Hayes, L.E., and Silver, A. H., 1958, "Adiabatic Wall Temperature Downstream of a Single, Tangential Injection Slot," ASME Paper No. 58-A-107.

Goldstein, R. J., 1971, "Film Cooling," *Advances in Heat Transfer*, Academic Press, New York.

Goldstein, R. J., Eckert, E. R. G., Chiang, H. D., and Elovic, E., 1985, "Effect of Surface Roughness on Film Cooling Performance," ASME *Journal of Engineering for Gas Turbines and Power*, Vol. 107, pp. 111–116.

Goldstein, R. J., Eckert, E. R. G., Eriksen, V. L., and Ramsey, J. W., 1970, "Film Cooling Following Injection Through Inclined Circular Tubes," *Israel J. Technology*, Vol. 8, pp. 145–155.

Ito, S., 1976, "Film Cooling and Aerodynamic Loss in a Turbine Cascade," Ph.D. Thesis, University of Minnesota, Minneapolis, MN.

Ito, S., Goldstein, R. J., and Eckert, E. R. G., 1978, "Film Cooling of a Gas Turbine Blade," ASME *Journal of Engineering for Power*, Vol. 100, pp. 476–481.

Kacker, S. C., and Whitelaw, J. H., 1967, "The Dependence of the Impervious Wall Effectiveness of a Two-Dimensional Wall-Jet on the Thickness of the Upper-Lip Boundary Layer," *Int. J. Heat Mass Transfer*, Vol. 10, pp. 1623–1624.

Kadotani, K., and Goldstein, R. J., 1979, "Effect of Mainstream Variables on Jets Issuing From a Row of Inclined Round Holes," ASME *Journal of Engineering for Power*, Vol. 101, pp. 298–304.

Ko, S-Y., Xu, J-Z., Yao, Y-Q., and Tsou, F. K., 1984, "Film Cooling Effectiveness and Turbulence Distribution of Discrete Holes on a Convex Surface," *Int. J. Heat Mass Transfer*, Vol. 27, pp. 1551–1557.

Ko, S.-Y., Yao, Y-Q., Xia, B., and Tsou, F. K., 1986, "Discrete-Hole Film Cooling Characteristics over Concave and Convex Surfaces," *Heat Transfer 1986, Proceedings of the Eight International Heat Transfer Conference*, Hemisphere Publishing Corp., New York, Vol. 3, pp. 1297–1301.

Lander, R. D., Fish, R. W., and Suo, M., 1972, "External Heat-Transfer Distribution on Film Cooled Turbine Vanes," *J. Aircraft*, Vol. 9, pp. 707–714.

Pedersen, D. R., Goldstein, R. J., and Eckert, E. R. G., 1977, "Film Cooling With Large Density Difference Between the Mainstream and the Secondary Fluid Measured by the Heat-Mass Transfer Analogy," ASME *Journal of Heat Transfer*, Vol. 99, pp. 620–527.

Schwarz, S. G., 1986, "Film Cooling of Curved Surface," Ph.D. Thesis, University of Minnesota, Minneapolis, MN.

Seban, R. A., 1960, "Effects of Initial Boundary-Layer Thickness on a Tangential Injection System," ASME *Journal of Heat Transfer*, Vol. 82, pp. 392–393.

Simon, T. W., and Moffat, R. J., 1981, "Turbulent Boundary Layer Heat Transfer Experiments: A Separate Effects Study on a Convexly-Curved Wall," ASME Paper No. 81-HT-78.

Tani, I., 1962, "Production of Longitudinal Vortices in the Boundary Layer Along a Concave Wall," *J. Geophysical Research*, Vol. 67, pp. 307–308.

M. K. Chyu
Department of Mechanical Engineering,
Carnegie Mellon University,
Pittsburgh, PA 15213

H. K. Moon
McDonnel Douglas Helicopter Company,
Mesa, AZ 85205

D. E. Metzger
Mechanical and Aerospace
Engineering Department,
Arizona State University,
Tempe, AZ 85287

Heat Transfer in the Tip Region of Grooved Turbine Blades

Local convective heat transfer at the tip region of grooved blades is experimentally investigated. The present study models the problem by flow over a shrouded, rectangular cavity, with the shroud moving opposite to the main flow direction. The naphthalene sublimation technique together with a computer-controlled measurement system provides detailed local transfer information on all the participating surfaces. The local heat transfer coefficient in the cavity is strongly influenced by the cavity aspect ratio, gap size, and leakage flow Reynolds number. Within the present study range, the effect of relative motion between the shroud and cavity on the heat transfer is found to be minor, particularly for the average heat transfer coefficient. With the same leakage flow rate, the average heat transfer coefficient over the entire tip area decreases with an increase in cavity depth. However, in terms of total heat transfer to the tip, an overly deep cavity is undesirable, because it provides larger surface area but only a small increase in flow resistance.

Introduction

In gas turbines, the blades of axial turbine stages rotate in close proximity to a stationary peripheral wall (sometimes termed an outer ring or stationary shroud). Differential expansion of the turbine wheel, blades, and the shroud causes variations in the size of the clearance gap between blade tip and stationary shroud. The necessity to tolerate this differential thermal expansion dictates that the clearance gap cannot be eliminated altogether, despite accurate engine machining (Hennecke, 1984). Pressure differences between the pressure and suction sides of a blade drive a flow through the clearance gap. This flow, often referred as the "tip leakage" flow, is detrimental to engine performance. A primary detrimental effect of tip leakage flow is the reduction of turbine stage efficiency. A second important effect concerns the convective heat transfer associated with the flow. The surface area at the blade tip in contact with the hot working gas represents an additional thermal loading on the blade, which, together with heat transfer to the suction and pressure side surface area, must be removed by the blade internal cooling flows (Metzger, 1983).

Limited information on turbine tip heat transfer and fluid flow has been reported to date (Lakshminarayana, 1970; Booth and Dodge, 1982; Wadia and Booth, 1982; Mayle and Metzger, 1982), and almost all of the published work dealing with clearance gap flows involves consideration only of plain flat blade tips. A strategy commonly employed to reduce tip flow and heat transfer is to groove a single rectangular cavity chordwise along the blade tip. The groove acts like the cell of a labyrinth seal to increase the pressure drop and thus reduce the flow for a given pressure differential across the tip. The reduction of the flow will also act to reduce heat transfer. However, grooving a blade tip also creates increase in the heat transfer area exposed to the leakage flow, and this effect is undesirable if the cooling of a blade tip is of concern. A schematic diagram representing the geometry of a grooved blade tip, viewed from a coordinate system fixed relative to the blade, is shown in Fig. 1. As seen in the figure, the outer shroud can be considered moving in the general direction from the suction side to the pressure side, with relative velocity equal to U_w. The leakage flow, as denoted by U in the figure, is driven by a pressure difference between the two sides of the blade and flows in the direction opposite to the shroud motion. With this general configuration in mind, the grooved tip problem can be categorized as fluid flow and heat transfer over a shrouded rectangular cavity.

Both fluid flow and heat transfer over unshrouded, rectangular cavities have been the subjects of extensive investigation for many years (Aung, 1983). The flow field over a cavity is characterized by flow separation and shear layer reattachment resulting in complex flow patterns with substantial effects on the friction drag and heat transfer. Most studies have relied on flow visualization techniques and/or heat and mass transfer data to obtain momentum and heat transfer information in cavity flow (Haugen and Dhanak, 1967; Yamamoto et al., 1979; Chyu and Goldstein, 1986). In all cases, the cavity problems studied have been considered as a flow system in which the cavity is open to a usually well-specified approaching flow over an otherwise smooth and stationary sur-

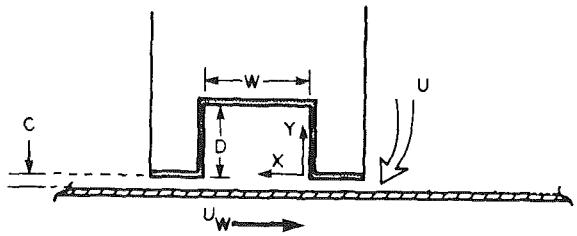

Fig. 1 Shrouded rectangular cavity

Contributed by the International Gas Turbine Institute and presented at the 33rd International Gas Turbine and Aeroengine Congress and Exhibition, Amsterdam, The Netherlands, June 5–9, 1988. Manuscript received by the International Gas Turbine Institute September 26, 1987. Paper No. 88-GT-246.

face. The approaching flow may be a wall boundary layer for external flow or a well-developed channel flow.

The grooved tip differs from the aforementioned unshrouded situation by virtue of the confined nature of the geometry as well as by the proximity of moving shroud. The degree of similarity between the heat transfer characteristics of the grooved tip and those of previous cavity studies have been unclear until recently. Metzger and Bunker (1985), using a time-dependent paint coating technique, studied heat transfer for flow through a confined narrow slot-type channel where one of the bounding walls contains a rectangular cavity. The effect of shroud motion is not included in this study. Details of heat transfer on surfaces are found to be largely dependent on the size of gap clearance and the cavity aspect ratio. A semi-empirical study by Mayle and Metzger (1982), using a plain tip geometry, has argued that the heat transfer from the blade tip is essentially unaffected by the relative motion between blade and shroud. Similar indication is also shown in a numerical study for turbulent flow over two-dimensional, shrouded, rectangular cavities by Chyu et al. (1986). To gain further understanding of the convective heat transfer in cavities with various degrees of relative shroud motion is the primary objective of this study.

In the present work, experimental results concerned with the local heat transfer characteristics on all surfaces of shrouded, rectangular cavities are reported. The varying parameters include the cavity depth-to-width ratio, D/W, gap clearance-to-cavity width ratio, C/W, relative shroud speed, U_w/U, and Reynolds number, $\mathrm{Re} = UC/\nu$. Values of these parameters are chosen to accommodate the range of interest in actual turbine applications. To facilitate good accuracy and experimental control, the naphthalene ($C_{10}H_8$) sublimation mass transfer technique is employed instead of direct heat transfer tests. The mass transfer results can be transformed into their counterparts in heat transfer through an analogy between the two transfer processes. More detailed description of the analogy has been given by Eckert (1976) and Goldstein et al. (1985). A brief discussion of the mass transfer system with associated data reduction procedure used in this study is given in the next section.

Data Reduction of Mass Transfer System

The mass transfer coefficient h_m is given by

$$h_m = \frac{\dot{m}}{\rho_{v,w} - \rho_i} \tag{1}$$

where $\dot{m}$ is the mass transfer flux of naphthalene from a surface, $\rho_{v,w}$ is the vapor concentration of naphthalene at the surface, and ρ_i is the vapor mass concentration at the inlet of gap passage. Equation (1) corresponds to the conventional definition of heat transfer coefficient

$$h = \frac{q}{T_w - T_i} \tag{2}$$

In the present study, ρ_i is considered to be zero and equation (1) becomes

$$h_m = \frac{\dot{m}}{\rho_{v,w}} \tag{3}$$

In addition, as the mass transfer system is essentially maintained isothermal, the naphthalene vapor pressure and vapor concentration at the surface are constant. This corresponds to a constant wall temperature boundary condition in a heat transfer study.

Local mass transfer from a naphthalene surface can be evaluated from the change in naphthalene thickness. The change of thickness due to sublimation is given by

$$dy = \frac{\dot{m} \cdot dt}{\rho_s} \tag{4}$$

where ρ_s is the density of solid naphthalene ($\approx 1.143 \times 10^3$ kg/m^3), and dy and dt represent the change in naphthalene thickness and the differential time duration, respectively. Note that dy and $\dot{m}$ are functions of the local coordinate of the subliming surface. Combining equations (3) and (4), and integrating over the test duration, yield the time-averaged, local mass transfer coefficient

$$h_m = \frac{\rho_s \cdot \Delta y}{\rho_{v,w} \cdot \Delta t} \tag{5}$$

The mass transfer Stanton number is defined by

$$\mathrm{St} = \frac{h_m}{U} \tag{6}$$

As it is often the case that the wall temperature varies slightly during test run, $\rho_{v,w}$ can be represented by the time-

Nomenclature

A = heat transfer surface area with cavity
A_o = heat transfer surface area without cavity
C = clearance height at gap
D = cavity or groove depth
D_h = hydraulic diameter
f = pressure loss coefficient $= \Delta pC/2L\rho U^2$
d = differential operator
h = heat transfer coefficient
h_m = naphthalene mass transfer coefficient
$\dot{m}$ = mass transfer flux of naphthalene from surface
p = pressure
$p_{v,w}$ = naphthalene vapor pressure at wall
q = heat flux from wall
Re = Reynolds number $= UC/\nu$
St = local mass transfer Stanton number from naphthalene surface $\mathrm{st} = h_m/U$
St_o = local mass transfer Stanton number from flat wall without cavity presence
St_{FO} = fully developed heat or mass transfer Stanton number
$\overline{\mathrm{St}}$ = area-averaged St
$\overline{\mathrm{St}}_o$ = area-averaged St_o
T_i = temperature at gap inlet
T_w = temperature at wall
t = time
U = mean flow velocity at gap
U_w = shroud moving velocity
W = cavity width
X = streamwise coordinate; downstream distance from cavity upstream wall, see Fig. 1
Y = coordinate normal to the streamwise direction, see Fig. 1
y = coordinate of change in naphthalene thickness
Δ = finite difference operator
μ = dynamic viscosity
ν = kinematic viscosity
ρ = density of fluid
ρ_s = density of solid naphthalene, $\approx 1.143 \times 10^3$ kg/m^3 in present study
$\rho_{v,w}$ = vapor mass concentration or density of naphthalene at wall
ρ_i = vapor mass concentration or density of naphthalene at gap inlet

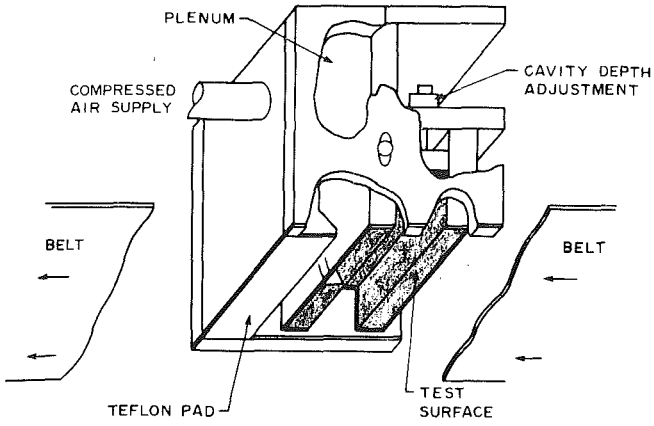

Fig. 2 Schematic view of test assembly

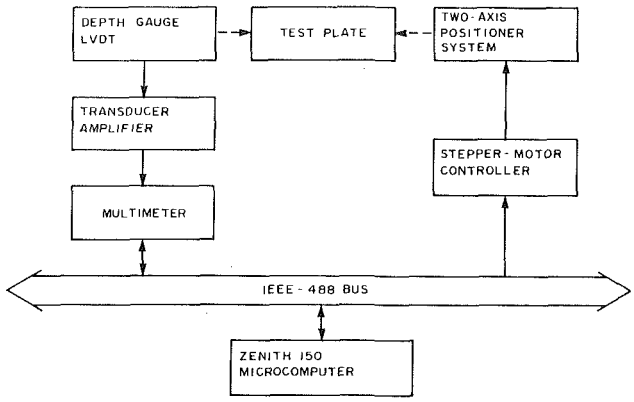

Fig. 3 Local mass transfer measurement system

averaged naphthalene concentration at the surface. This is obtained from numerical integration of the concentration determined at the measured surface temperature. A correlation proposed by Ambrose et al. (1975) is used to determine naphthalene vapor pressure; from this, $\rho_{v,w}$ is evaluated using the ideal gas law and the naphthalene surface temperature.

Experimental Apparatus and Procedure

Figure 2 displays a schematic view of the test section. The entire construction is made of aluminum tooling plates. The shaded area in the figure, representing a cavitylike grooved tip, is the mass transfer active surface cast with a thin layer of naphthalene, approximately 2 mm in thickness. The cavity width W is maintained constant at 32 mm (1.25 in) throughout the entire study. The desired values of C/W and D/W can be obtained accordingly, by fixing a pair of adjustable screws. A 16-mm-wide surface is extended both upstream and downstream of the cavity, forming the upstream gap and downstream gap, respectively. The cavity span normal to the streamwise direction is measured at 153 mm (6.0 in), which is approximately four times the streamwise width W. Under this condition, although some three-dimensional phenomena are expected, preliminary tests have shown that the mass transfer characteristics are quite two dimensional across at least 80 percent of the span. The moving shroud is modeled by a flat, seamless, Neoprene belt driven by a speed-adjustable, 0.56 kW (3/4 HP) d-c motor. The test assembly can be rotated in different orientation relative to the belt moving direction.

During a test run, the laboratory compressed air supply is first introduced to a plenum adjacent to the test cavity, then flows over the cavity, subsequently discharging to the surrounding atmosphere. The entire test assembly including plenum and cavity is placed above and contacts the moving belt, with the cavity opening facing downward. Between the test assembly and the moving belt, there are several teflon pads mounted on the contacting surface of the test assembly to reduce dynamic friction and to prevent air leakage. An additional teflon plate is placed underneath and against the belt, which effectively eliminates belt vibration as it moves over the test section. Preliminary tests at full anticipated belt speeds indicate that this design is very effective.

One of the most challenging aspects of the subliming mass transfer experiment is the surface profile measurement on the naphthalene surface. Mass transfer at a certain location is inferred from the change in naphthalene thickness at that location. In order to obtain the distribution of local mass transfer coefficient in the region of interest, the surface contour must be measured before and after each test run. Therefore, successful execution of local measurements in subliming mass transfer is critically dependent on precise positioning and accurate thickness change readings. In addition, to avoid errors

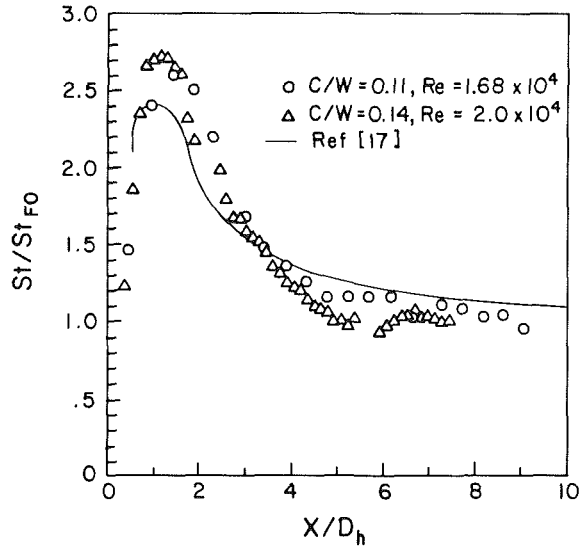

Fig. 4 Heat (mass) transfer in smooth channel

caused by the extraneous naphthalene sublimation and human fatigue during a lengthy measurement requires rapid data acquisition. A computer-controlled, automated data acquisition system has been designed and used to fulfill all of these requirements. A block diagram giving a schematic view of the entire system is shown in Fig. 3. It consists of a depth gage along with a signal conditioner, a digital multimeter, two-stepper-motor driven positioners, a motor controller, and a Zenith 150 microcomputer (IBM-PC compatible) as the measurement process controller. The Zenith microcomputer is also used for data storage and reduction. Details of the measurement system have been described in earlier studies (Goldstein et al., 1985; Chyu, 1986).

Results and Discussion

Most of the mass transfer results in this study are presented in form of Stanton number St, as discussed in the previous section. For all the test runs, the uncertainty in the local St is estimated to be 4 percent, and the repeatability is approximately equal to this value. Detailed uncertainty analysis for this study is given by Moon (1987). Prior to the actual tests for grooved-tip geometries, mass transfer from a flat surface in the absence of cavity has been measured to provide reference information. The flat channel experiments are performed using the same test section for cavity studies, with the cavity floor elevated to flush with the gap surfaces. Figure 4 shows the local Stanton number normalized by the corresponding fully developed value and presented as a function of the

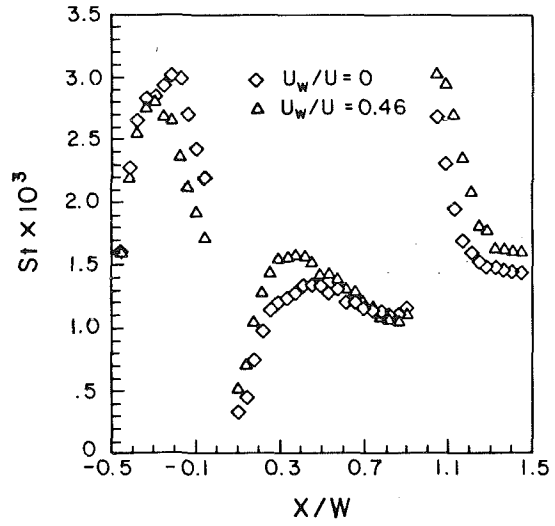

Fig. 5(a) $D/W = 0.1$

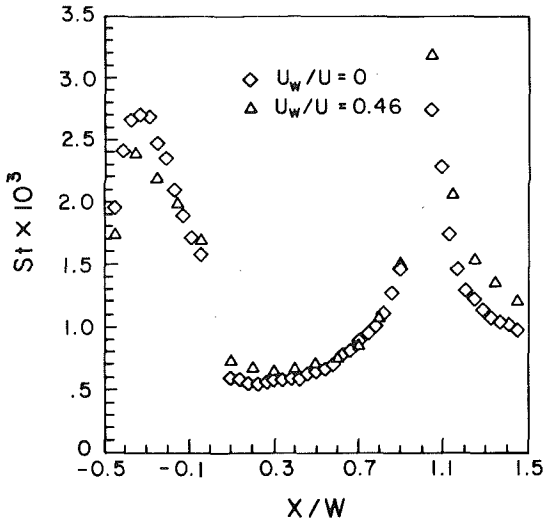

Fig. 5(b) $D/W = 0.5$

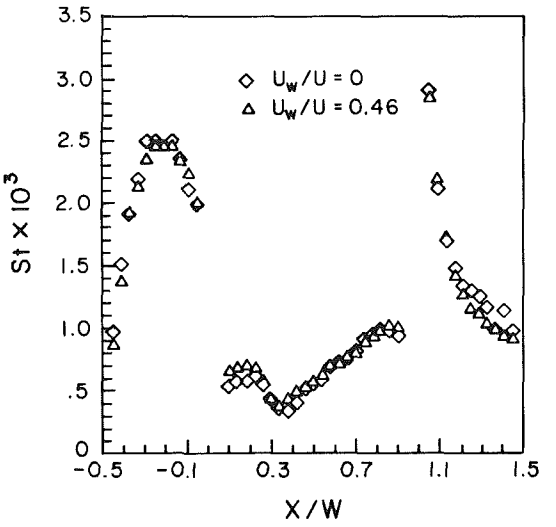

Fig. 5(c) $D/W = 1.0$

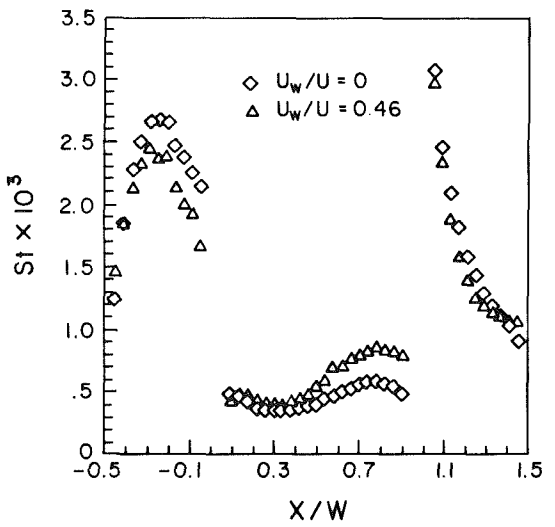

Fig. 5(d) $D/W = 1.5$

Fig. 5 St distribution in streamwise direction; $C/W = 0.14$, $Re = 2.0 \times 10^4$

distance in a unit of hydraulic diameter from the channel entrance. Due to the limited channel length, the average of St over the five most downstream locations of the test section is taken as the fully developed value for the present system, which is 0.96×10^{-3} for $Re = 1.68 \times 10^4$ ($C/W = 0.11$) and is 1.0×10^{-3} for $Re = 2.0 \times 10^4$ ($C/W = 0.14$), respectively. This approximation is justified as the St reaches a constant value at the midportion of the test channel. The data fluctuation near two thirds of the channel length from the gap entrance is thought to be due to a slight surface discontinuity between the elevated floor and the gap surface downstream. For comparison, the solid line represents the corresponding heat transfer results from Boetler (1948) for turbulent air flow with a sharp-angle entrance. The favorable comparison validates the present experimental system and provides confidence in data accuracy.

The effects of cavity aspect ratio (D/W) and shroud moving speed (U/U_w) on the local mass transfer distributions of the cavity floor and the surface upstream and downstream of the cavity are shown in Fig. 5. The figure consists of four subfigures 5(a) to 5(d), representing $Re = UC/\nu = 2.0 \times 10^4$, $C/W = 0.14$, and $D/W = 0.1$, 0.5, 1.0, and 1.5, $U_w/U = 0.0$ and 0.46. It is noted that very nonuniform St distributions exist for all the cases tested. On the surface upstream of the cavity (i.e., the upstream gap), St increases with streamwise location, reaches a local maximum near the midpoint of the surface, and then decreases toward downstream. The characteristic of this St distribution is virtually identical to that of heat transfer near a channel entrance preceded by a sudden contraction. A typical value of the maximum St is approximately twice that for a fully developed channel flow having the same Reynolds number. The maximum is considered to be caused by the reattachment effect of the separated flow in the region. This finding is in good agreement with the leakage-flow pattern near the gap entrance recently observed by Moore and Tilton (1988).

Mass transfer characteristics on the surface downstream of the cavity (i.e., downstream gap) are similar to that of a newly developing boundary layer with zero angle of incidence. In contrast to the upstream gap, the highest St occurs near the leading edge of the surface, and the St decreases along the streamwise direction. However, it is speculated that a second local maximum St may exist somewhere downstream of the leading edge provided that the gap size is sufficiently large; a recirculating region is expected to exist in the upstream portion of this surface. This second local maximum St has been

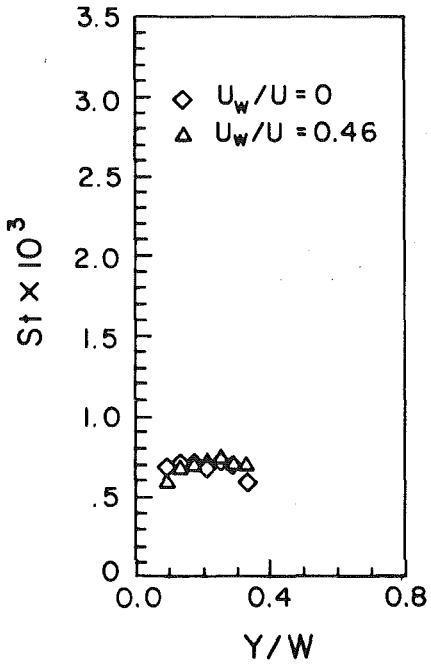

Fig. 6(a) Upstream wall

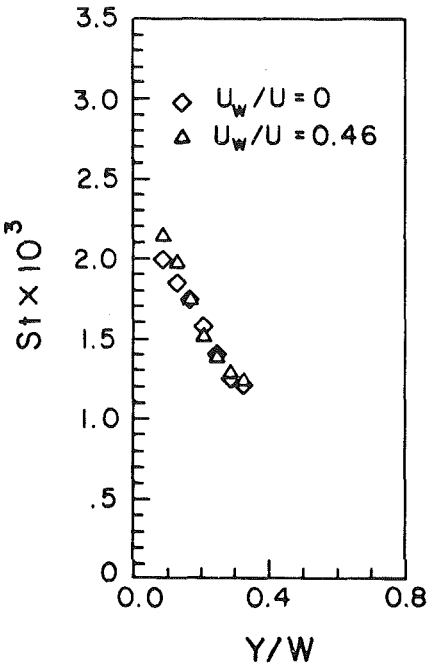

Fig. 6(b) Downstream wall

Fig. 6 St distribution on cavity side walls; $C/W = 0.14$, $D/W = 0.5$, $Re = 2.0 \times 10^4$

reported in the literature for cavity flow without shroud presence (Chyu and Goldstein, 1986). The presence of shroud restrains the development of the shear layer which initiates at the sharp corner of a cavity's upstream wall. This, in turn, results in a thinner shear layer with lower turbulence across the cavity as compared to the cases without shroud.

Values of St on the cavity floor are in general smaller than that on surfaces upstream and downstream of the cavity. In addition, as shown in Fig. 5, the nature of the cavity floor St distribution depends strongly on the cavity geometry, namely the cavity aspect ratio D/W. For shallow cavities, say $D/W = 0.1$, the shear layer separated from the upper corner of the cavity upstream wall should have reattached at the cavity floor. In the region near the reattachment point, generally accompanied with higher turbulence mixing, mass transfer coefficient reaches a local maximum. This effect is clearly observed in Fig. 5(a). For $D/W = 0.5$, according to a flow visualization study on unshrouded cavities (Yamamoto et al., 1979), the entire cavity will be largely filled with a recirculating vortex resulting in a streamwise, monotonically increasing trend of mass transfer on the cavity floor, as shown in Fig. 5(b). For even deeper cavities, $D/W = 1.0$ and 1.5, the values of cavity-floor St become smaller, and peculiar mass transfer characteristics exist, with more than one local maximum St being observed in Figs. 5(c) and 5(d). This is speculated to be attributable to the additional and strong degree of secondary-flow interactions near the cavity bottom.

For all the cases present in Fig. 5, the general trend of influence of relative shroud movement on the mass transfer from a grooved tip is found to be quite consistent. At each corresponding streamwise location, the mass transfer St on the surfaces of downstream gap and cavity floor is generally higher for $U_w/U = 0.46$ than that for stationary shroud situation (i.e., $U_w/U = 0$), while the reversed effect is observed on the surface of upstream gap. It is understandable that the shroud motion introduces more naphthalene-free air into the mainstream in the downstream portion of the test section; thus the bulk air flow in this region is less naphthalene-enriched than that without shroud motion. This in turn enhances the mass transfer. An opposite effect is expected for the upstream portion, resulting in a lower mass transfer driving potential. However, the difference in St affected by the different values of U_w/U is overall insignificant and, for majority of the data, the differences are in fact within the experimental uncertainty. The speculation raised by Mayle and Metzger (1982) that the relative shroud motion has a very minor effect on the flat blade-tip heat transfer is also applicable to heat transfer to a grooved tip, at least for the present study range. A recent numerical study by Chyu et al. (1987) on modeling the flow field and heat transfer in two-dimensional, shrouded cavities has reported similar results. For $U_w/U \leq 1$, the heat transfer in a cavity is mainly determined by the cavity geometry, and the relative shroud movement has virtually no effect. This implies that investigation of heat transfer in actual blade tips may be achieved by performing studies with a stationary model.

Mass transfer measurements are also made on cavity side walls, and Figs. 6 and 7 show typical results for the intermediate cases $D/W = 0.5$ and 1.0. The mass transfer from the cavity upstream wall (downstream-facing wall) is dominated by the vortex attached behind the wall and has the same order of magnitude of St as that on the upstream portion of cavity floor, which generally has low mass transfer rates. On the other hand, the fundamental mode of mass transfer mechanism for the cavity downstream wall (upstream-facing wall) is the impingement of the separated shear layer on the wall, in particular on the upper portion. As a result, the mass transfer coefficient is generally high near the top of the downstream wall. The influence of relative shroud movement on the mass transfer from the two side walls is also found to be insignificant. However, the influence seems to be stronger for a deeper cavity ($D/W = 1.0$) than for the shallower one ($D/W = 0.5$), and, as shown in Fig. 7, it has the opposite effect on the mass transfer between the upstream and downstream walls.

Results shown in Fig. 8 represent the area-averaged mass transfer coefficient and the overall mass transfer rate for

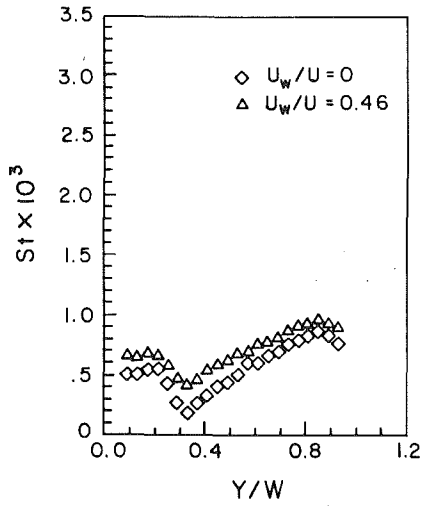

Fig. 7(*a*) Upstream wall

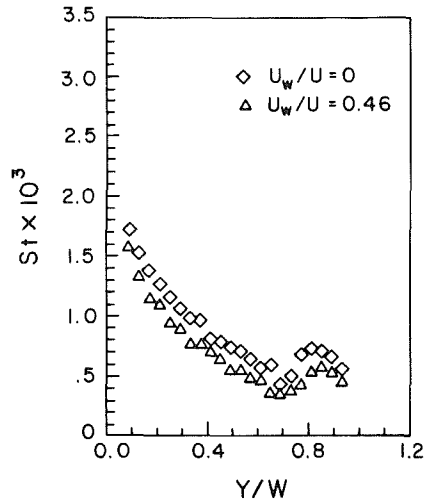

Fig. 7(*b*) Downstream wall

Fig. 7 St distribution on cavity side walls; $C/W = 0.14$, $D/W = 1.0$, $Re = 2.0 \times 10^4$

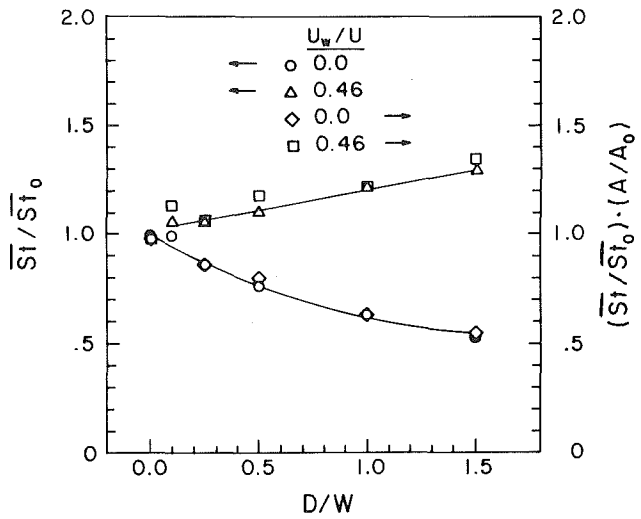

Fig. 8 Area-averaged mass transfer

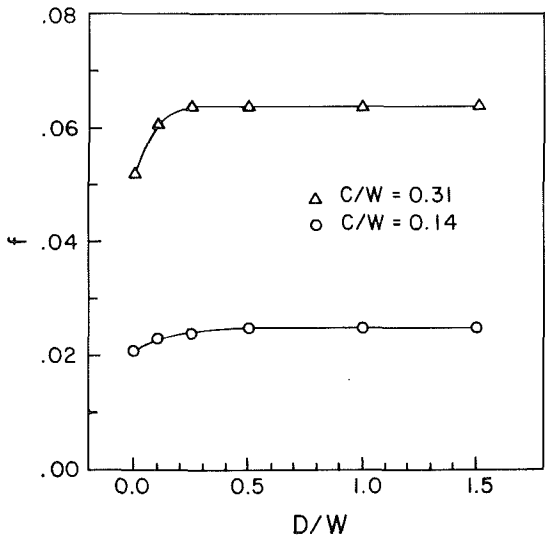

Fig. 9 Pressure loss coefficient

$Re = 2.0 \times 10^4$, $C/W = 0.14$. The area-averaged results are obtained using a numerical integration over the corresponding local data. The left scale in Fig. 8 is the Stanton number averaged over the entire mass transfer active region, $\overline{St}$, and normalized by the corresponding value of flat channel without cavity. The right scale gives the value of $(\overline{St}/\overline{St}_o) \times (A/A_o)$, representing the overall mass transfer rate normalized by its flat surface counterpart. A/A_0 is the ratio of the area of mass transfer active region with cavity to that without cavity; this ratio increases with an increase of D/W. As expected, the shroud motion has little influence on both results, with a less than 10 percent maximum variation caused by the difference in shroud movement. $\overline{St}$ decreases with an increase in the value of D/W; however, the value of normalized overall mass transfer rate is fairly constant for $D/W \leq 0.5$ but generally increases with D/W. This implies that, for a given mass flow rate through the gap, the deeper cavities experience higher overall mass transfer than the shallower ones, despite a lower mass transfer coefficient. Deepening a cavity causes additional mass transfer area on cavity side wall. It is a general speculation that deepening a cavity reduces the leakage flow rate, and thus also its associated convective heat transfer, for a given pressure differential across the cavity. Figure 9, showing the pressure loss coefficients calculated from the measured pressure differentials for the present tests, indicates that this is not always the case. Deepening the cavity beyond $D/W = 0.3$ does not result in further increases in pressure loss. The combined results shown in Figs. 8 and 9 suggest that it may be undesirable to groove a blade tip having a cavity aspect ratio D/W higher than 0.5. This result agrees with the conclusion reached by Metzger and Bunker (1985).

Another important parameter affecting the tip heat transfer is the size of gap clearance, namely C/W. Figure 10 shows the typical results for cavities with $D/W = 1.0$, $Re = 2.0 \times 10^4$, and $U_w/U = 0$. The general trend is that the larger the value of C/W, the higher the mass transfer coefficient. In addition to change in the magnitude of local St, the general characteristics of St distribution over the surfaces of upstream and downstream gap vary with different values of C/W. This variation may be understood by consideration of flow pattern in the gap, which, to a certain extent, is affected by the nature of sudden contraction as the fluids flow into the gap. Moreover, according to Chyu et al. (1987), the larger gap clearance permits the separated shear layer to grow thicker inducing higher turbulence level in the gap mainstream. The mass transfer on the downstream gap surface as well as on the cavity downstream wall is thus influenced by the characteristics of the shear layer. In view of the results shown

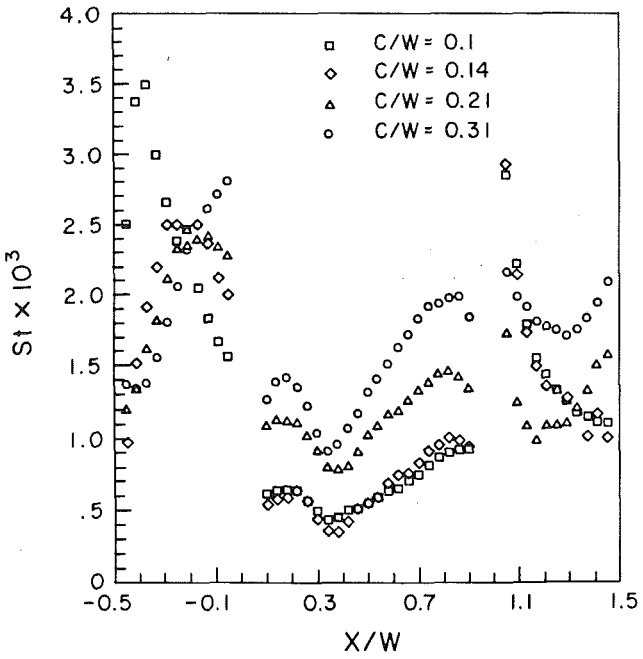

Fig. 10 Gap clearance effect on mass transfer; $D/W = 1.0$, $Re = 2.0 \times 10^4$, $U_w/U = 0.0$

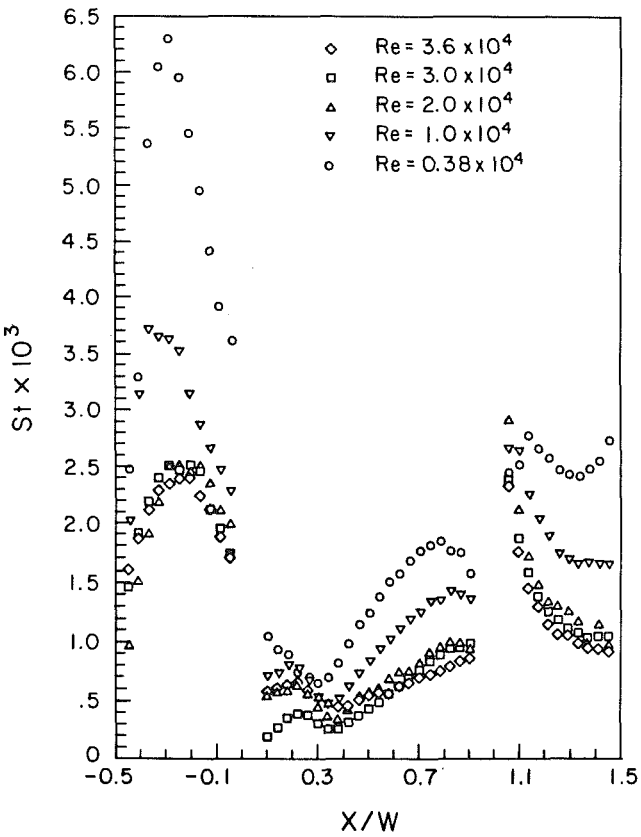

Fig. 11 Reynolds number effect on mass transfer; $C/W = 0.14$, $D/W = 1.0$, $U_w/U = 0.0$

in Fig. 10, a recirculating vortex may exist in the downstream gap for $C/W \geq 0.2$, as a local minimum of St observed in the midportion of the surface.

Figure 11 shows the Reynolds number effect on tip mass transfer. While fixing $D/W = 1.0$ and $C/W = 0.14$, Reynolds number, defined as $Re = UC/\nu$, varies from 0.38×10^4 to 3.6×10^4 by controlling the air flow from the laboratory compressor. Since the size of the clearance is physically the same in these cases, the only variable in fact is the gap mean velocity. As shown in Fig. 10, within the present test range, the local St generally decreases with an increase of Re. However, the trend is attenuated and even reversed when $Re \geq 3.6 \times 10^4$. This peculiar tendency can be plausibly explained by considering the flow compressibility. For $Re = 3.6 \times 10^4$, Mach number in the gap is approximately equal to 0.4, and it may be inappropriate to consider the flow incompressible, and the mass transfer increases as the compressibility effect dominates.

Attention is now turned to the correlation between the area-averaged mass transfer and the affecting parameters as previously discussed. Using the power regression fit, $\overline{St}$ is found to vary with -0.22 power of D/W, and the power index becomes -0.28 if the area-averaged $\overline{St}$ over the cavity floor is only of concern. The latter is in good agreement with results from previous studies; -0.22 by Metzger and Bunker (1985) and -0.27 by Yamamoto et al. (1979). It should be noted that, in the study by Yamamoto et al. (1979), only the cavity floor was heated and the cavity side walls were kept adiabatic, whereas the present mass transfer system is equivalent to the situation with the entire cavity surface maintained at an isothermal wall condition. As for the gap clearance dependency, $\overline{St}$ groups well with C/W to a 0.31 power, indicating a greater influence on tip heat transfer than the cavity aspect ratio D/W. The same conclusion has also been found by Metzger and Bunker (1985). The influence of Reynolds number on the entire tip mass (heat) transfer can be expressed at $\overline{St}$ proportional to $Re^{-0.36}$. In the study by Yamamoto et al. (1985), for unshrouded cavities, the Stanton number averaged over the cavity floor is found to vary as the -0.5 power of Reynolds number. The difference is probably attributable to the difference in the nature of cavity geometry, the boundary condition, and the testing range of Reynolds number.

Conclusions

Mass transfer with turbulent flow over shrouded, rectangular cavities has been experimentally investigated. The study models heat transfer at the tip region of grooved rotor blades. The naphthalene mass transfer technique with a high-precision surface measurement system has demonstrated itself as a viable method to study the local transfer information in great detail. The effects of cavity geometry, gap size, leakage flow Reynolds number, and relative shroud movement on the mass transfer of all cavity walls and surfaces upstream and downstream of cavity have been identified. The characteristic of the local mass transfer distribution on cavity floor is primarily determined by the cavity geometry, i.e., D/W. The area-averaged mass transfer Stanton number over the entire mass transfer area is dependent on D/W, C/W, and Re, with power indices of -0.22, 0.31, and -0.36, respectively. Results from the present investigation, similar to the findings from several related studies in the literature, have indicated that the effect of shroud movement on the tip heat transfer in most turbine applications is secondary. Also suggested is that an overly deep groove, i.e., $D/W \geq 0.5$, may be undesirable if the magnitude of total tip heat transfer is of concern.

References

Ambrose, D., Lawenson, I. J., and Sprake, C. H. S., 1975, "The Vapor Pressure of Naphthalene," *J. Chem. Thermo.*, Vol. 7, pp. 1173–1176.

Aung, W., 1983, "Separated Force Convection," *Proc. 1983 ASME/JSME Joint Thermal Eng. Conf.*, Honolulu, HI, Vol. 2, pp. 499–515.

Boetler, L. M. K., Young, G., and Iverson, H. W., 1948, "An Investigation of Aircraft Heaters XXVII—Distribution of Heat Transfer Rate in the Entrance Region of a Tube," NACA TN 1451.

Booth, T. C., Dodge, P. R., and Hepworth, H. K., 1982, "Rotor-Tip Leakage: Part I—Basic Methodology," ASME *Journal of Engineering for Power*, Vol. 104, pp. 154–161.

Chyu, M. K., 1986, "Influence of Roughness on the Local Mass Transfer From a Flat Surface," Ph.D. Thesis, University of Minnesota, Minneapolis, MN.

Chyu, M. K., and Goldstein, R. J., 1986, "Local Mass Transfer in Rectangular Cavities With Separated Turbulent Flow," *Proc. 8th Int. Heat Transfer Conf.*, Vol. 3, pp. 1065–1070.

Chyu, M. K., Metzger, D. E., and Hwan, C. L., 1987, "Heat Transfer in Shrouded Rectangular Cavities," *J. Thermophysics and Heat Transfer*, Vol. 1, pp. 247–252.

Eckert, E. R. G., 1976, "Analogies to Heat Transfer Processes," in: *Measurements in Heat Transfer*, E. R. G. Eckert and R. J. Goldstein, eds., Hemisphere Publishing Co., New York.

Goldstein, R. J., Chyu, M. K., and Hain, R. C., 1985, "Measurement of Local Mass Transfer on a Surface in the Region of the Base of a Protruding Cylinder With a Computer-Controlled Data Acquisition System," *Int. J. Heat and Mass Transfer*, Vol. 28, pp. 977–985.

Haugen, R. L., and Dhanak, A. M., 1967, "Heat Transfer in Turbulent Boundary-Layer Separation Over a Surface Cavity," ASME *Journal of Heat Transfer*, Vol. 89, pp. 335–340.

Hennecke, D. K., 1984, "Heat Transfer Problems in Aero-Engines," in: *Heat and Mass Transfer in Rotating Machinery*, D. E. Metzger and N. H. Afgan, eds., Hemisphere, Washington, D. C., pp. 353–379.

Lakshminarayana, B., 1970, "Methods for Predicting the Tip Clearance Effects in Axial Flow Turbomachinery," ASME *Journal of Basic Engineering*, Vol. 92, pp. 467–482.

Mayle, R. E., and Metzger, D. E., 1982, "Heat Transfer at the Tip of an Unshrouded Turbine Blade," *Proc. 7th International Heat Transfer Conference*, Vol. 3, pp. 87–92.

Metzger, D. E., and Mayle, R. E., 1983, "Heat Transfer Gas Turbine Engines," *Mech. Eng.*, Vol. 105, No. 6, pp. 44–52.

Metzger, D. E., and Bunker, R. S., 1985, "Cavity Heat Transfer on a Grooved Wall in a Narrow Flow Channel," ASME Paper No. 85-HT-57.

Moon, H. K., 1987, "Modeling and Measurement of Heat Transfer on Turbine Blade Tips," Ph.D. Thesis, Arizona State University, Tempe, AZ.

Moore, J., and Tilton, J. S., 1988, "Tip Leakage Flow in a Linear Turbine Cascade," ASME JOURNAL OF TURBOMACHINERY, Vol. 110, pp. 18–26.

Wadia, A. R., and Booth, T. C., 1982, "Rotor-Tip Leakage: Part II—Design Optimization Through Viscous Analysis and Experiment," ASME *Journal of Engineering for Power*, Vol. 104, pp. 162–169.

Yamamoto, H., Seki, N., and Fukusako, S., 1979, "Forced Convection Heat Transfer on Heated Bottom Surface of a Cavity," ASME *Journal of Heat Transfer*, Vol. 101, pp. 475–479.

Hydrodynamic Measurements of Jets in Crossflow for Gas Turbine Film Cooling Applications

J. R. Pietrzyk

D. G. Bogard

M. E. Crawford

Mechanical Engineering Department,
The University of Texas at Austin,
Austin, TX 78712

This paper presents the results of a detailed hydrodynamic study of a row of inclined jets issuing into a crossflow. Laser-Doppler anemometry was used to measure the vertical and streamwise components of velocity for three jet-to-mainstream velocity ratios: 0.25, 0.5, and 1.0. Mean velocity components and turbulent Reynolds normal and shear stress components were measured at locations in a vertical plane along the centerline of the jet from 1 diameter upstream to 30 diameters downstream of the jet. The results, which have application to film cooling, give a quantitative picture of the entire flow field, from the approaching flow upstream of the jet, through the interaction region of the jet and mainstream, to the relaxation region downstream where the flow field approaches that of a standard turbulent boundary layer. The data indicate the existence of a separation region in the hole from which the jet issues, causing high levels of turbulence and a relatively uniform mean velocity profile at the jet exit.

Introduction

A fundamental limitation to the development of improved film cooling for turbine blades is the lack of understanding of the fluid mechanisms affecting heat transfer during film cooling. Although there has been prolific research in the area of film cooling technology, much of this research has focused on the end product, i.e., the amount of heat transfer, while relatively few studies have attempted detailed descriptions of the flow field involved in the heat transport process. Comprehensive experimental measurements of jets-in-crossflow were made in this study to obtain a better understanding of the fundamental characteristics of this flow.

In previous studies of jets-in-crossflow, the most detailed measurements of the flow field have been made for a single jet issuing from a relatively long delivery pipe oriented normal to the mainstream. Although this is significantly different from the short length-to-diameter (L/D) inlet with the hole axis angled sharply downstream, generally used for film cooling, the flow field characteristics might be expected to be qualitatively the same. Crabb et al. (1981) used both laser-Doppler velocimetry (LDV) and X-sensor hot-wire anemometry to study a normal jet-in-crossflow with relatively high blowing ratios of $M = 1.15$ and 2.3, where M is the density–velocity product ratio of the jet to the mainstream. The jet issued from a pipe with $L/D = 30$. These investigators emphasized the importance of using LDV in the near field of the jet where the three-dimensionality, high turbulence, and reverse flow preclude the use of hot-wire techniques. Their measurements also indicated that the exit profile of the jet is highly distorted by the crossflow. For $M = 1.15$, measurements of the turbulent normal stresses showed a maximum at approximately 1/2 D downstream of the hole, which corresponded to a maximum in the mean streamwise velocity gradient located at $y/D = 2$.

The most detailed study of the turbulence characteristics of a jet-in-crossflow were made by Andreopoulos and Rodi (1984) for a normal jet issuing from a pipe with $L/D = 12$ and a smooth entrance. Using triple-sensor hot wires, measurements were made of all three velocity components. In this study, using a blowing ratio of $M = 0.5$, the crossflow was found to influence the pipe flow upstream of the exit, causing a highly nonuniform exit profile, which was skewed toward the back edge of the hole. The maximum turbulence level and uv shear stress levels occurred at locations from two to four diameters downstream of the jet and were coincident with maximum mean velocity gradients. The large velocity gradients in this region were due to a shear layer, which occurred on the lower edge of the jet because of a wake region below the jet.

Turbulence measurements for inclined jets have been limited to a few studies using single-sensor hot-wire probes. Since the accuracy of these probes is extremely poor in the highly turbulent, three-dimensional, and occasionally reversing flow field characteristic of jets-in-crossflow, these results should be regarded as qualitative descriptions of the flow turbulence. Kadotani and Goldstein (1979) and Yoshida and Goldstein (1984) used a row of jets introduced by pipes inclined at 35 deg to the surface and with $M = 0.35$ and $M = 0.50$, respectively. In both these studies mean and rms velocity measurements for the combined U and V components were presented for one streamwise position located one diameter downstream of the hole. At this point the maximum turbulence level was found to correspond with the lower edge of the injected flow where the mean velocity gradient was largest. Turbulence in-

Contributed by the International Gas Turbine Institute and presented at the 33rd International Gas Turbine and Aeroengine Congress and Exhibition, Amsterdam, The Netherlands, June 5–9, 1988. Manuscript received by the International Gas Turbine Institute January 1, 1988. Paper No 88-GT-174.

tensity was also measured by Jubran and Brown (1985) for holes inclined at 30 deg and with inlet pipe lengths of L/D = 15. Although two rows of holes were used, the second row was located x/D = 10 downstream of the first row, while the turbulence intensity measurements were made at x/D = 2.3 and 10. Results presented for blowing ratios of M = 0.2 and 1.0 were somewhat contradictory to the previous studies in that maximum turbulence levels were found at the point measured nearest to the wall (y/D = 0.1) rather than being coincident with the shear layer between the wake and the bottom edge of the jet.

In the present study, detailed measurements have been made of the mean and turbulence characteristics of jets-in-crossflow for hydrodynamic conditions typical of film-cooled turbine blades, but with a unity density ratio and a flat test surface. A short entrance of L/D = 3.5 was purposely used for the injected fluid to simulate actual film-cooled turbine blade configurations better, although this is significantly different from the pipe flow inlet configuration that has been used in past studies. An LDV was used to measure the distributions of streamwise and normal components of the mean and fluctuating velocity along with the uv shear stress over a range extending from one diameter upstream of the hole to 30 diameters downstream. Various sources of high turbulence were identified and the relaxation of the flow to essentially boundary layer characteristics was documented. A strong correspondence between the high turbulent normal and shear stresses with regions of high mean velocity gradients was also found.

Experimental Facility and Instrumentation

These experiments were carried out using a test plate installed in a recirculating low-speed wind tunnel. The test section, with dimensions 61 × 61 × 244 cm long, was preceded by a 6.25:1 contraction section with a bank of graduated screens and honeycomb upstream of the contraction. Air was used as the working fluid with the free-stream turbulence intensity in the test section measured at less than 0.5 percent at a velocitiy of 20 m/s. Air is injected into the mainstream through a row of 11 holes, 12.5 mm in diameter, in a flat plate. The holes are inclined at 35 deg and laterally spaced three diameters apart and are located 19 diameters downstream of the leading edge of the plate. Suction is used to remove the boundary layer at the test section inlet and a new boundary layer is initiated at the sharp leading edge of the plate. The length of the hole was made short relative to the diameter (L/D = 3.5) to simulate a typical film-cooled turbine blade geometry. Figure 1 shows a schematic of this arrangement. All 11 jets issue from a common plenum chamber located below the plate. Air to the plenum is supplied by a secondary flow loop containing a centrifugal fan and an orifice plate flowmeter. Different blowing ratios were obtained by varying the flow rate through the secondary flow loop while maintaining a constant mainstream velocity of 20 m/s.

Two-component velocity measurements were made with a TSI Inc. model 9100-10 LDV system. To allow measurements of the vertical velocity near the wall it was necessary to tilt the entire LDV 8 deg downward to prevent the lower beam from

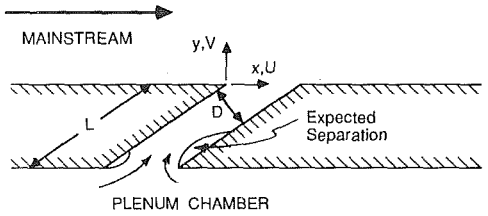

Fig. 1 Geometry of the 35 deg film cooling hole and coordinate system

intersecting the floor of the wind tunnel. As a result, the V component of velocity reported in this paper is composed primarily of the true vertical velocity, but also contains a small lateral velocity component. This tilt does not affect the measurement of the streamwise velocity component. The LDV was equipped with frequency shifting, which is necessary to distinguish reverse flow and also to avoid fringe bias errors in the measurement of the relatively small vertical velocity component. The diameter of the probe volume was reduced by a factor of 3.75 to d = 80 μm by passing the four transmitted beams through beam expansion optics. The receiving optics were modified to operate in a backscatter configuration offset 30 deg from the axis of the transmitted beams. As a result of this off-axis collection, the length of the probe volume was reduced by a factor of 5 to 1 = 160 μm. TSI counters were used for signal processing and an HP-1000 microcomputer system for data acquisition and anaysis. The HP-1000 system was also interfaced with the motion control system of the LDV traverse table to allow the computer to control the positioning of the table automatically. Velocity bias corrections, based on the residence time of a particle in the probe volume, were applied to the LDV data.

The mainstream and jets were independently seeded with 0.6 μm sugar particles generated by two TSI six-jet atomizers. To avoid bias due to different seed concentrations, the atomizers were adjusted to provide equal seed concentrations in the mainstream and jet flow. This condition was initially set and periodically checked by measuring the velocity and the data rate at various locations in the mainstream and in the jets. The seed concentration is proportional to the ratio of the data rate and the velocity. The jet air was obtained from the seeded mainstream, so the addition of a relatively small amount of seed was required to replace that which dropped out while passing through the secondary flow loop.

To obtain accurate measurements of the turbulence shear stress, essentially coincident measurements of the instantaneous streamwise and vertical components of velocity are necessary. A coincidence time window of 10 μs was used for these measurements, which allowed accurate measurements for flow fluctuations up to 50 kHz.

The time-averaged measurements presented in this paper were obtained using sample sizes of 1024 discrete coincident measurements. Measurement time for these samples varied from 10 s to 100 s. Precision uncertainties for these measurements were determined from repeatability tests and found to be ±0.5 percent for U and V, ±2 percent for u_{rms} and v_{rms}, ±15 percent for uv, where percentages are in terms of the free-stream velocity.

Nomenclature

D = hole diameter, Fig. 1
L = hole length, Fig. 1
M = density • velocity product ratio, jet-to-freestream
TL = turbulence level, two-dimensional
U = mean velocity, x direction
u_{rms} = rms velocity, x direction
uv = Reynolds uv shear stress
U_∞ = free-stream velocity
V = mean velocity, y direction
v_{rms} = rms velocity, y direction
x = streamwise distance, Fig. 1
y = distance from wall, Fig. 1
δ = boundary layer thickness, 99 percent velocity point
θ = boundary layer momentum thickness

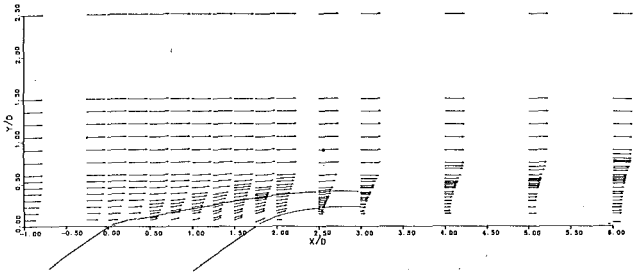

Fig. 2 Profiles of the normalized mean velocity vectors for the near-hole region of the jet exit and $M = 0.25$. Edges of the jet are defined by the interpolated mean streamlines.

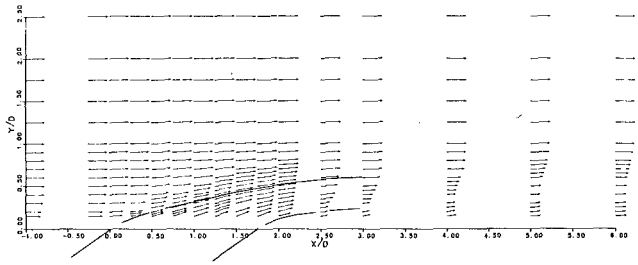

Fig. 3 Profiles of the normalized mean velocity vectors for the near-hole region of the jet exit and $M = 0.5$. Edges of the jet are defined by the interpolated mean streamlines.

Results and Discussion

Results are presented for two-component velocity measurements made along the centerline of the fourth jet and over a range from one diameter upstream of the jet to 30 diameters downstream. Three different blowing ratios were used with $M = 0.25$, 0.5, and 1.0, all with unity density ratio. These data will be discussed first in terms of the near-field mean flow and turbulence characteristics. Relaxation of the flow in the far field downstream of the hole will then be examined. Finally, results indicating the correspondence between mean velocity gradients and the turbulent normal and shear stresses will be presented.

For the following results the origin of the coordinate system is located on the wall at the leading edge of the jet. Because of the elliptical shape of the hole, the trailing edge is located at $x/D = 1.74$, where x is measured in the streamwise direction. The distance normal to the plate is denoted by y.

Mean Flow, Near Field. Profiles of mean velocity vectors for the three different blowing ratios are presented in Figs. 2, 3, and 4. The first two velocity profiles for each case were taken upstream of the hole at $x/D = -1.0$ and -0.25. The profile at $x/D = -1.0$ is the same for all three blowing ratios and indicates a boundary layer thickness of $\delta/D = 0.4$ ($\delta \approx$ 4.8 mm). Only a slight deceleration is noticeable at $x/D = -0.25$, but for $M = 1.0$ there was a significant negative V component at the nearest wall location, which might indicate the existence of a streamwise vortex caused by the obstruction of the jet.

Measurements taken nearest the exit of the hole indicate relatively flat velocity profiles as the jet exists the hole. The magnitudes of the velocity vectors just past the jet exit are larger than might be expected for the respective blowing ratios because of an acceleration as the jets were diverted downstream by the crossflow. The velocity profile was relatively uniform for $M = 0.5$, but slightly skewed downstream for $M = 0.25$ and upstream for $M = 1.0$. This is in contrast to the findings of earlier studies, where highly nonuniform profiles were found using normal jets (Andreopoulos and Rodi, 1984) at similar blowing ratios. The relatively uniform profiles found in the present study are probably due to the use of a short L/D delivery passage compared to the relatively long pipe inlets

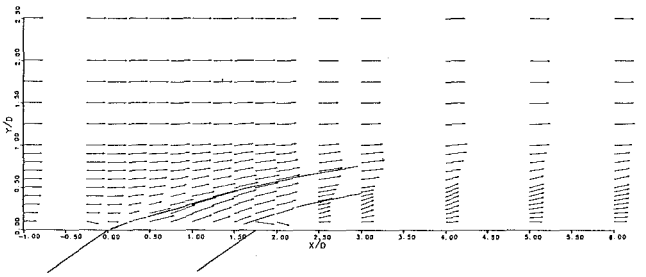

Fig. 4 Profiles of the normalized mean velocity vectors for the near-hole region of the jet exit and $M = 1.0$. Edges of the jet are defined by the interpolated mean streamlines.

used in previous studies. Furthermore, the sharp entrance to the inlet tube (see Fig. 1) is expected to cause a separation region on the downstream side of the tube, which would become more severe for higher tube velocities. Turbulence intensity measurements, to be discussed in the next section, confirmed this expectation. Consequently, the increased separation region within the delivery passage at higher blowing ratios would account for the skewing of the jet inlet profiles toward the leading edge of the hole for the large blowing ratio. Since the hole geometry and passage length used in this study have significant effects on the exit profile of the jet, it is important to reiterate that the present configuration is more representative of inlets actually used for film-cooled turbine blades.

Downstream of the hole a "wake region" was formed by the blockage of the jet for all three blowing ratios. In each case a strong shear layer was formed between the low speed fluid in the wake and the lower edge of the jet. For $M = 0.25$, a shear layer also developed between the mainstream and the relatively low-speed fluid at the top edge of the jet. These shear layers merged to form a continuous shear region across the jet for this lowest blowing ratio. The velocity in the wake region was found to increase substantially with increasing blowing ratio indicating a greater ingestion of mainstream fluid below the jet for higher blowing ratios. A lateral influx of mainstream fluid below the jet was also indicated for $M = 0.5$ by a negative velocity gradient near the wall evident in Fig. 3 for $x/D > 3$. This can only be accounted for by an influx of high-speed fluid into the lower part of the wake. A similar effect was seen for $M = 1.0$, but not for $M = 0.25$.

Turbulence Quantities, Near Field. Measurements of the two components of the fluctutating velocity, u_{rms} and v_{rms}, are presented in terms of a turbulence level (TL) defined as

$$TL = (u_{\text{rms}}^2 + v_{\text{rms}}^2)^{1/2}/U_\infty$$

where U_∞ is the free-stream velocity. Contours of TL were obtained by interpolating the data, and the results for the three blowing ratios are shown in Figs. 5, 6, and 7. In each case several distinct regions of high turbulence were identified at the exit of the hole and immediately downstream. These regions are most apparent at the largest blowing ratio, $M = 1.0$ (Fig. 7). The smallest region of high turbulence is at the upstream edge of the jet as it exists from the hole. The turbulence here is likely due to the remnants of the boundary layer that develops within the hole along the upstream side.

For blowing ratios of $M = 0.5$ and $M = 1.0$, larger regions of high turbulence were found above the downstream side of the hole. The larger extent of these regions of turbulence suggests the existence of a much fuller turbulent boundary layer along the downstream surface of the hole. These turbulence data represent additional evidence that a separation region exists on the downstream side of the hole, following the sharp entrance. Furthermore, this would account for the significantly

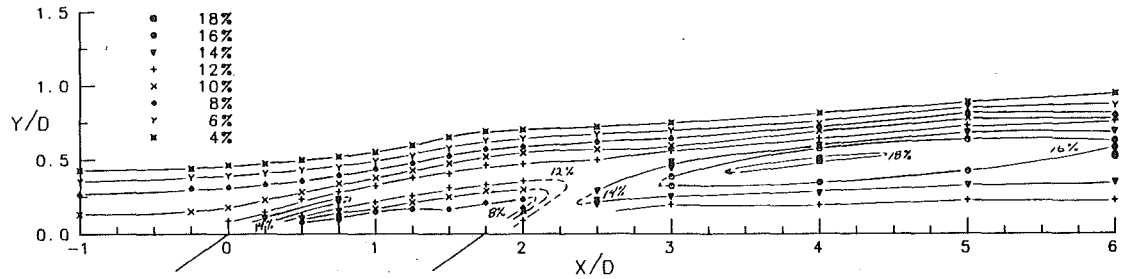

Fig. 5 Turbulence level, $(u^2_{rms} + v^2_{rms})^{1/2}/U_\infty$, contours for the near-hole region of the jet exit and $M = 0.25$

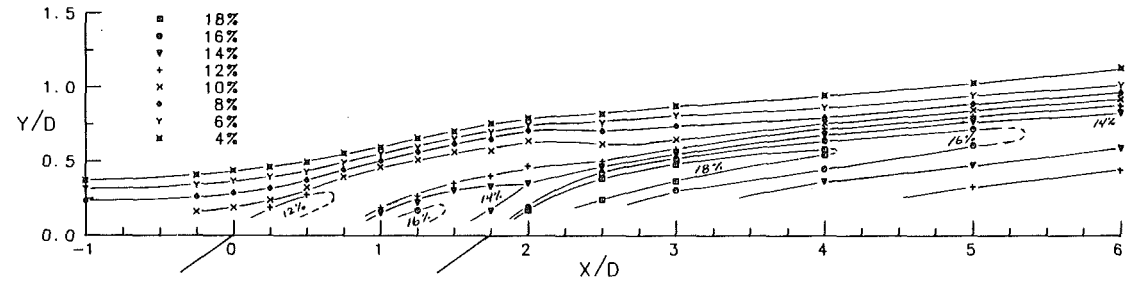

Fig. 6 Turbulence level, $(u^2_{rms} + v^2_{rms})^{1/2}/U_\infty$, contours for the near-hole region of the jet exit and $M = 0.5$

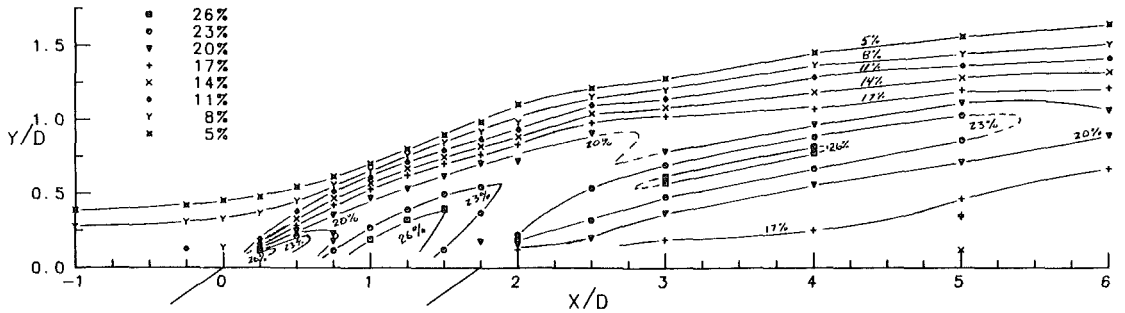

Fig. 7 Turbulence level, $(u^2_{rms} + v^2_{rms})^{1/2}/U_\infty$, contours for the near-hole region of the jet exit and $M = 1.0$

thicker boundary layer on this side of the hole. As discussed earlier, the size of this separated region is expected to decrease for decreasing blowing ratios, which would explain the decrease in the size of the turbulent region for $M = 0.5$ and the disappearance of this high turbulence region for $M = 0.25$.

In general, the highest level of turbulence was found along the bottom of the jet interface. Evidently this high turbulence is due to the shear layer that develops between the jet and the low-velocity wake below the jet. There was only a slight increase in the turbulence level in this region when the blowing ratio was increased from $M = 0.25$ to $M = 0.5$, but a dramatic increase from 18 percent to more than 26 percent occurred when the blowing ratio was increased to $M = 1.0$.

Comparing the above results to measurements by Yoshida and Goldstein (1984), at a location one diameter downstream of the hole for $M = 0.5$, shows there is a good agreement in the location of a maximum turbulence level at $y/D = 0.35$ in the shear layer below the jet. However, the maximum turbulence level of 12 percent was somewhat less than the 18 percent measured in this study. There are significant differences in the present results and those obtained by Jubran and Brown (1985) at a distance approximately two diameters downstream of the hole. As indicated in Fig. 7, for $M = 1.0$ and $x/D = 3.76$ the present measurements show a distinct peak in TL at $y/D = 0.7$, as opposed to maximum in the near-wall region ($y/D = 0.1$) measured by Jubran and Brown. A distinct peak in TL was also found in the present study for $M = 0.25$, but none was found by Jubran and Brown for $M = 0.2$.

Contours of the uv shear stress near the jet exit for the two lower blowing ratios, shown in Figs. 8 and 9, are very similar to the corresponding contours of TL shown previously. A small region of high uv at the upstream edge of the jet was found for both blowing ratios and is probably the remnants of the boundary layer that developed along the top side of the hole. At $M = 0.5$ a region of high turbulent shear stress exists above the downstream part of the jet exit, whereas at the lower blowing ratio of $M = 0.25$, the turbulent shear stress decreases at the jet exit. This is consistent with the contours of TL, and also indicates the existence of a separated region on the downstream side of the inlet tube, which is considerably reduced in size for the lower blowing ratio.

Maximum levels of uv shear stress were comparable for both blowing ratios and were found downstream of the jet at the interface between the jet fluid and the low velocitiy wake beneath the jet. Normalized with free-stream velocity, the peak value of $uv/U^2_\infty = -0.007$ is considerably larger than for a standard boundary layer flow, but consistent with the magnitude found in flows following separated regions such as the flow behind a backward-facing step (e.g., Chandrsuda and Bradshaw, 1981).

Downstream Development. The development of mean velocity profiles downstream of the jets was similar for all three

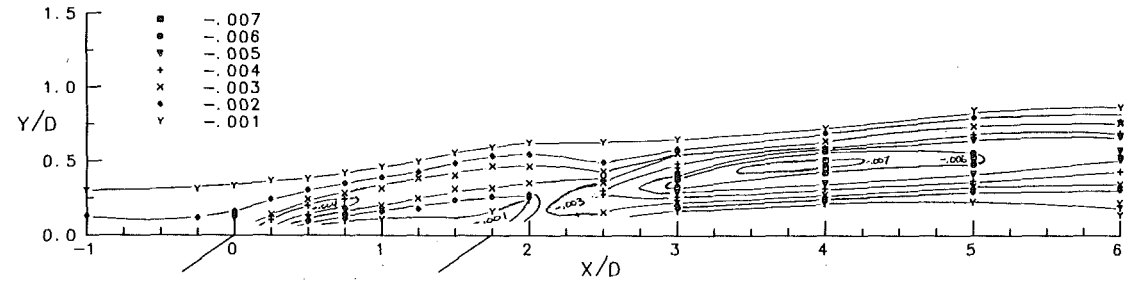

Fig. 8 Normalized shear stress, uv/V_∞^2, contours for the near-hole region of the jet exit and $M = 0.25$

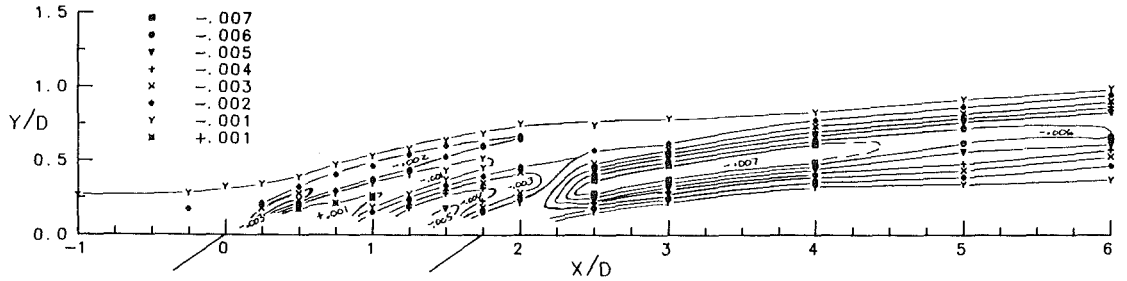

Fig. 9 Normalized shear stress, uv/V_∞^2, contours for the near-hole region of the jet exit and $M = 0.5$

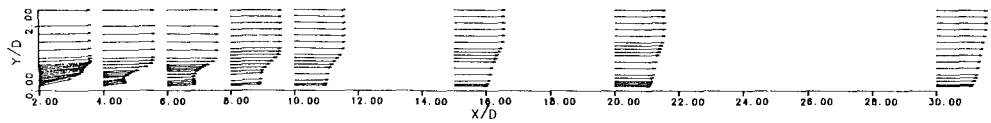

Fig. 10 Downstream development of the normalized mean velocity vectors along the jet centerline for $M = 0.5$

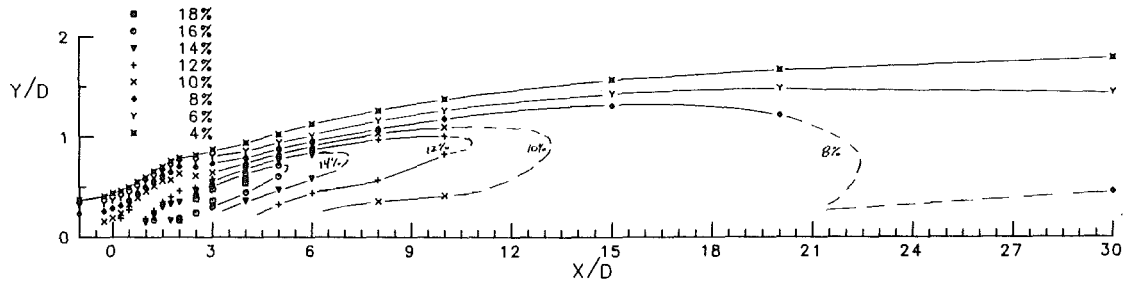

Fig. 11 Downstream development of the turbulence level, $(u_{rms}^2 + v_{rms}^2)^{1/2}/U_\infty$, for $M = 0.5$

blowing ratios, and representative results for $M = 0.5$ are shown in Fig. 10. These profiles show the shear layer that develops at the lower part of the jet is still apparent at $x/D = 10$, but has merged into the bottom wall boundary layer by $x/D = 30$. As shown in Table 1, boundary layer thickness measurements at $x/D = 30$ increased monotonically with increase in blowing ratio. However, the momentum thickness for $M = 0.5$ was substantially greater than for the higher and lower blowing ratios.

Contours of turbulence levels and uv shear stress downstream of the jet exit for $M = 0.5$ are given in Figs. 11 and 12, respectively. Note that the apparent trajectory of the jet in these figures is misleading because the vertical scales have been expanded for better resolution. Both turbulence quantities were found to decay rapidly by $x/D = 10$. Similar rapid decays in turbulence were found at the higher and lower blowing ratios. Moreover, despite the significantly higher turbulence levels for $M = 1.0$, turbulence levels for all three blowing ratios were essentially the same for $x/D > 10$, although the vertical extent of this turbulence was greater for higher blowing ratios. At $x/D = 30$ the turbulence levels and uv shear stress monotonically decreased moving away from the wall indicating that the flow has relaxed to a boundary layer flow.

Table 1 Boundary layer thickness at $x/D = 30$

M	δ/D	θ/D
0.25	1.2	0.12
0.5	1.9	0.19
1.0	2.5	0.15

Correspondence Between Turbulence Parameters and Mean Velocity Gradients. An important consideration from the standpoint of modeling is the degree of correspondence between turbulence parameters and mean velocity gradients. Using $M = 0.5$ as a representative blowing ratio, results for TL, uv, and dU/dy are presented for the region above and immediately behind the hole (Fig. 13), and for the development down-stream (Fig. 14). Each of the parameters in these figures has been normalized with the maximum measured value, which occurs at $x/D = 2.5$. Good agreement between the distribution of velocity gradients and the distribution of uv shear stress is immediately obvious from these two figures. The large positive shear generated at the top edge of the jet is evident from the profiles between $x/D = 0.5$ and $x/D = 2.0$, and the correspondence with uv was found to be excellent for this shear layer. Moreover, negative velocity gradients, which formed

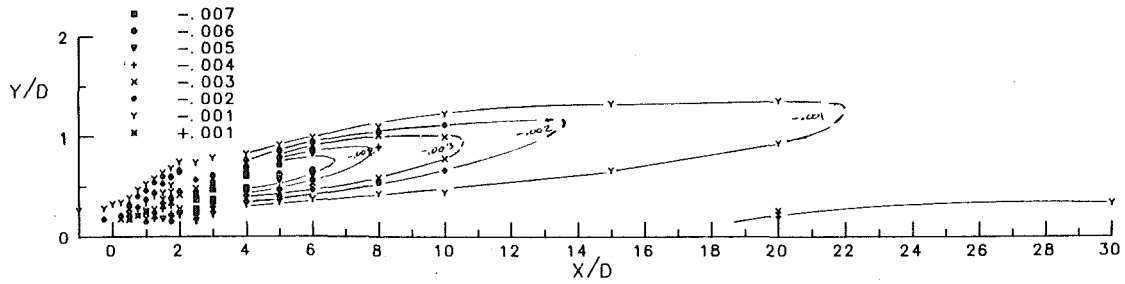

Fig. 12 Downstream development of the normalized shear stress, uv/U_∞^2, for $M = 0.5$

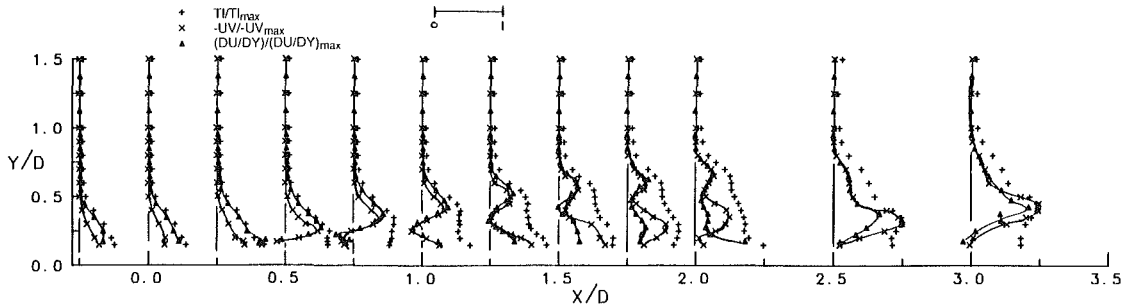

Fig. 13 Correspondence between the normalized turbulence quantities and the normalized mean velocity gradient for the near-hole region of the jet exit and $M = 0.5$

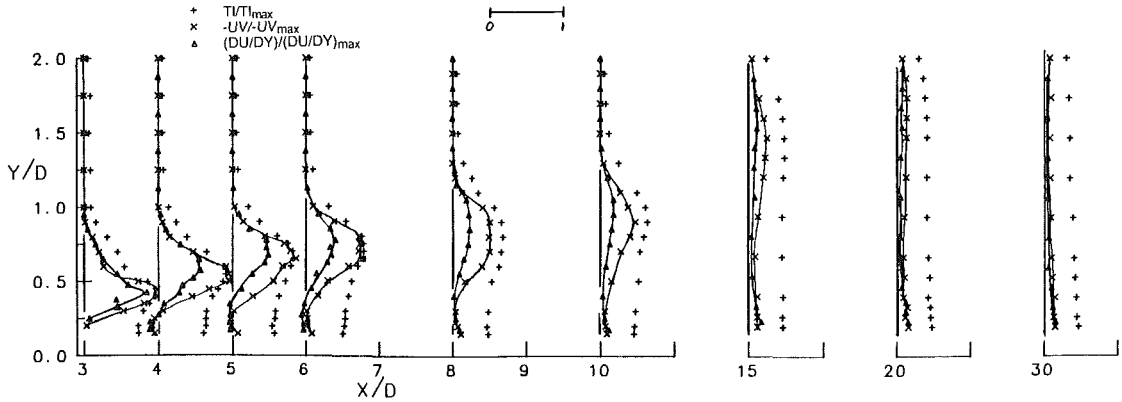

Fig. 14 Downstream development of the correspondence between the normalized turbulence quantities and the normalized mean velocity gradient for $M = 0.5$

below the top edge of the jet for $x/D = 0.5$ and 0.75, were found to correspond with peaks in positive uv shear stress. Note that the turbulence level remains high in this region where uv has a strong variation from negative to positive.

Immediately downstream of the back edge of the hole, at $x/D = 1.75$ and 2.0, a second uv peak appeared below the previous peak. Based on the contours of Fig. 9, it is apparent that this second peak is due to the remnants of the separated region within the inlet tube. These peaks in uv were associated with only mild peaks in velocity gradient.

At $x/D = 2.5$, the shear layer at the bottom of the jet dominates the flow. Good correspondence was found between the large velocity gradient and both the turbulence level and uv shear stress. As shown in Fig. 14, this good correspondence continues downstream although the magnitude of the velocity gradient decays faster than the uv shear stress. Beyond $x/D = 10$ the shear layer is no longer distinguishable.

Conclusions

The presence of a row of inclined jets issuing into a crossflow at a low blowing ratio ($M < 1$) causes a major disturbance to the hydrodynamic development of the turbulent boundary layer on the wall. All turbulence quantities are substantially enhanced in the region downstream of the jet. At ten diameters downstream, the presence of the jet is still clearly distinguishable in the profiles of the mean and fluctuating velocity components, but the flow is approaching normal wall boundary layer characteristics. The coincident occurrences of peaks in the mean velocity gradient and peaks in the turbulence quantities indicate that an eddy-viscosity model for the turbulence quantities may be applicable.

Computer simulation of jets-in-crossflow require that the flow field at the exit of the jet be specified. Previous studies indicate that a highly nonuniform velocity profile exists at the exit to jets issuing from long tubes. Measurements presented

here, for the more realistic geometry of jets issuing from short tubes, indicate that a uniform velocity profile may be a better representation of actual film-cooling conditions.

Acknowledgments

The authors gratefully acknowledge Garrett Turbine Engine Company for support of this research.

References

Andreopoulos, J., and Rodi, W., 1984, "Experimental Investigation of Jets in a Crossflow," *Journal of Fluid Mechanics*, Vol. 138, pp. 93–127.

Crabb, D., Durao, D. F. G., and Whitelaw, J. H., 1981, "A Round Jet Normal to a Crossflow," ASME *Journal of Fluids Engineering*, Vol. 103, pp. 142–152.

Chandrsuda, C., and Bradshaw, P., 1981, "Turbulence Structure of a Reattaching Mixing Layer," *Journal of Fluid Mechanics*, Vol. 110, pp. 171–194.

Jubran, B., and Brown, A., 1985, "Film Cooling From Two Rows of Holes Inclined in the Streamwise and Spanwise Directions," ASME *Journal of Engineering for Gas Turbines and Power*, Vol. 107, pp. 84–90.

Kadotani, K., and Goldstein, R. J., 1979,, "On the Nature of Jets Entering a Turbulent Flow, Part A. Jet–Mainstream Interaction," ASME *Journal of Engineering for Power*, Vol. 101, pp. 459–465.

Yoshida, T., and Goldstein, R. J., 1984, "On the Nature of Jets Issuing From a Row of Holes Into a Low Reynolds Number Mainstream Flow," ASME *Journal of Engineering for Gas Turbines and Power*, Vol. 106, pp. 612–618.

Cold Flow Turbine Rig Tests of the Original and Redesigned Compressor Turbines of an Industrial Gas Turbine Engine

I. S. Diakunchak

Gas and Steam Engineering,
Turbine & Generator Division,
Westinghouse Canada Inc.,
Hamilton, Ontario, Canada

This paper describes the results of cold flow turbine rig tests carried out on the original and redesigned compressor turbines of an industrial gas turbine engine. Some details of the aerodynamic design of the latest variant, a brief description of the advanced technology design methods used in this design, and a description of the test facility are included. Bulk stage performance and detail rotor exit radial-circumferential traverse results are presented. These test results demonstrate that the design point stage efficiency of the redesigned compressor turbine is about six percentage points higher than that of the original design.

Introduction

The cooled, single-stage compressor turbine used in a two-shaft industrial gas turbine engine was derived from the first stage of a three-stage turbine designed in the late 1960s. In the new application the stage pressure ratio and loading were increased. In addition, the stator was restaggered closed to provide the correct engine match. This resulted in positive blade incidence and a further reduction in stage efficiency. In order to improve the engine performance it was decided to redesign the compressor turbine. The design objective was to produce a high-efficiency, reliable, long-life compressor turbine suitable for engine application at a firing temperature of 2410 R (1339 K). To achieve the highest possible stage efficiency, advanced technology design methods were employed and performance enhancing design features were incorporated. The radial distributions of airfoil outlet flow angles were optimized to result in hub and tip work unloading and high hub reaction. Denton's three-dimensional time-marching flow calculation program was used to optimize the airfoil surface velocity distributions, stator lean, and stator outer endwall contour. To verify the performance of the new compressor turbine design prior to its introduction into a production engine, an extensive rig test program was carried out. The original compressor turbine design was also rig tested, to ensure the correct assessment of the engine performance improvement with the new compressor turbine. To carry out these tests the cold flow turbine test rig was designed, manufactured, and then installed in the Canadian National Research Council test facility in Ottawa, Canada.

Contributed by the International Gas Turbine Institute and presented at the 33rd International Gas Turbine and Aeroengine Congress and Exhibition, Amsterdam, The Netherlands, June 5-9, 1988. Manuscript received by the International Gas Turbine Institute September 1987. Paper No. 88-GT-74.

Aerodynamic Design

The main objective of the redesign was to produce a high-efficiency, reliable, long-life single-stage compressor turbine, which could be accommodated within the geometric constraints of an existing industrial gas turbine engine (Diakunchak, 1985). To ensure that the high-efficiency objective would be achieved, advanced technology aerodynamic design methods were employed and performance enhancing design features were incorporated. The radial distributions of design point flow conditions throughout the turbine gas path were generated by a streamline curvature-type radial equilibrium program, which incorporated inside-the-airfoil calculation planes. Denton's three-dimensional time-marching channel flow analysis program (Denton, 1979) was used to optimize airfoil surface velocities, the stator outer wall contour, and the stator lean.

The engine design point parameters for the redesigned compressor turbine were as follows:

Total pressure ratio	= 2.79
Speed	= 85 rev/s
Stage inlet temperature, T	= 2410 R (1339 K)
Stage inlet total pressure	= 123.1 psia (8.488×10^5 N/m^2)
Stage inlet mass flow	= 238.6 lb/sec (108.3 kg/s)
Stage work, Δh	= 129.5 Btu/lb (3.0×10^5 J/kg)
Work parameter, $\Delta h/T$	= 0.0537 Btu/lb R(2.247×10^2 J/kgK)
Loading factor, Δh/(mean wheel speed)^2	= 2.024
Flow factor, average axial velocity / mean wheel speed	= 0.712

The aerodynamic design method used in the redesign of the compressor turbine was highly iterative. It consisted of several major design cycles and many minor iterations. Using ap-

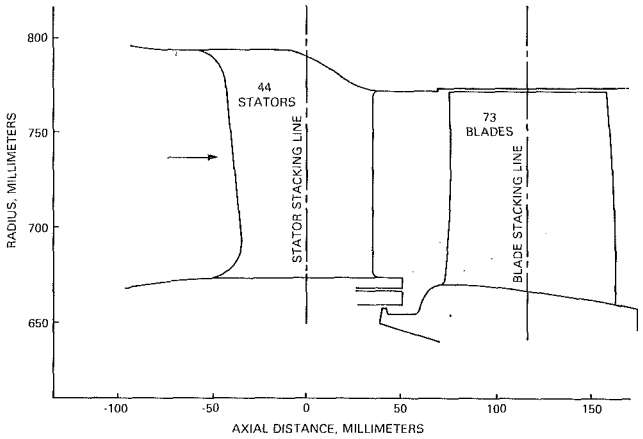

Fig. 1 Compressor turbine hot gas path layout

proximate initial input data, the axisymmetric streamline curvature flow program was used to calculate gas path flow conditions. Based on this preliminary information, airfoil cross sections were designed on cylindrical surfaces. The airfoil section surface velocity distributions were optimized with the aid of a quasi-three-dimensional version of Denton's program. The three design sections were then faired to produce the three-dimensional airfoil, which was analyzed by the three-dimensional version of Denton's program. This version of the program was used to optimize the stator outer wall contour and stator lean. The airfoil geometric data and the airfoil outlet flow angles predicted by the three-dimensional program were then fed back into the axisymmetric flow solution program and the cycle repeated. A boundary layer program was used to analyze airfoil cross-section surface velocity distributions to verify the acceptability of the design. Finally, satisfactory stator and blade designs, which satisfied both the aerodynamic and mechanical design criteria, were achieved.

To maximize the stage efficiency the following design features were incorporated:

1 Radial work distribution was such that hub and tip were unloaded relative to midspan.

2 The hub reaction (based on static pressure) was made as high as possible and the hub-to-tip reaction variation was made as small as possible, in order to reduce stator losses, increase blade hub acceleration, and reduce blade tip leakage.

3 The stator outer wall was contoured as shown in Fig. 1.

4 The stator was leaned so that the angle between the suction surface and the inner wall increased.

5 The axial stator to blade spacing was such that low airfoil losses would result without incurring mechanical problems.

6 The blade tip clearance was kept to a minimum and the blade tip was set at the same radius as the stator outer platform.

7 Blade platform leading edge was rounded out.

8 Stator leading edge ramps and generous airfoil fillet radii were incorporated.

9 Stator and blade trailing edge thicknesses were made as low as was practical for cast airfoils with internal air cooling.

10 Both airfoils were designed with account taken of induced incidence.

11 Stator and blade surface diffusions were less than 15 percent on the suction surface and less than 50 percent on the pressure surface, and aft loading was employed.

12 The gaps between stator platforms were sealed with strip seals and those between blade platforms by pin seals, in order to reduce platform leakage.

The final design of the new compressor turbine achieved most of the aerodynamic design objectives. The 24 percent meridional stator contraction (see Fig. 1) approximately equalled the optimum value given by Deich (1960) for the new

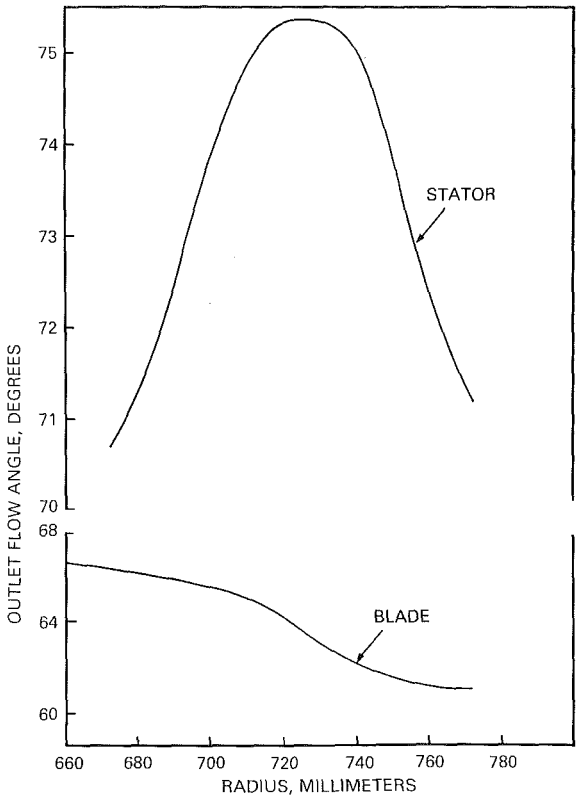

Fig. 2 Stator and blade outlet flow angle distribution

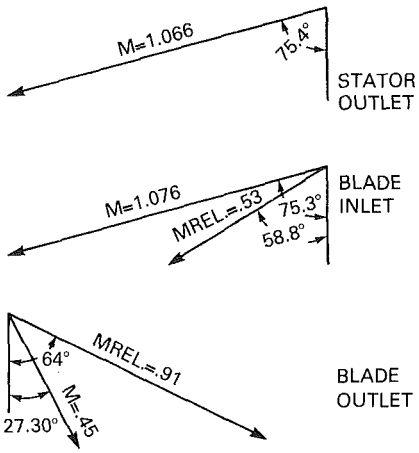

Fig. 3 Midspan velocity triangles

stator aspect ratio. The stator to blade axial gap of 56 percent of stator axial chord was a reasonable compromise between aerodynamic, mechanical, and blade vibration considerations. The hub and tip work unloading were 15 and 8 percent, respectively, the hub reaction was 24 percent, and the hub-to-tip reaction variation was 6 percentage points. To achieve this the stator outlet absolute and blade outlet relative flow angle distributions were designed as shown in Fig. 2. The midspan velocity triangles were as shown in Fig. 3.

Considerable design effort was required to ensure that when the three stator design sections (see Fig. 4) were faired to produce the three-dimensional airfoil, an insert type of cooling scheme could be incorporated. The new stator design had 44 airfoils (compared to 40 in the original design), −10 deg nominal incidence, 4 to 7 deg uncovered turning, about 4 deg trailing edge wedge angle, 0.120 in. (3.05 mm) trailing edge thickness, elliptical trailing edge shape, 0.74 midspan Zweif-

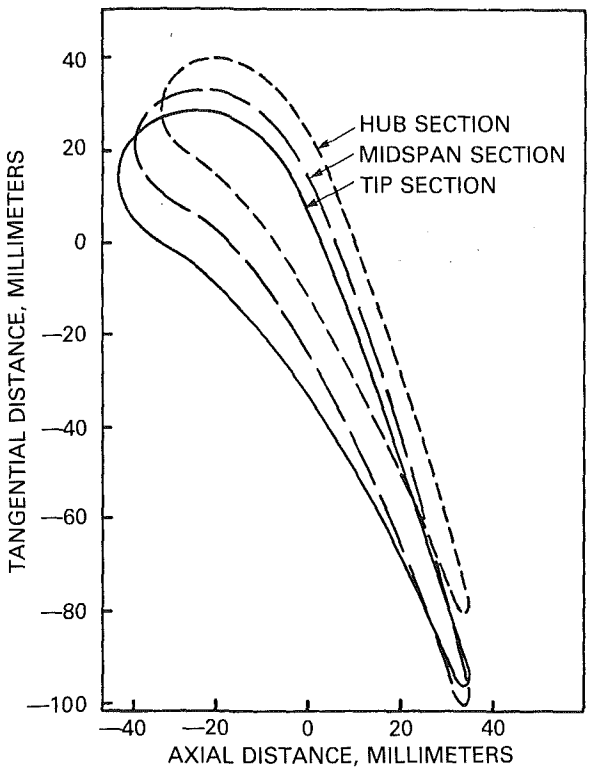

Fig. 4 Final stator design sections

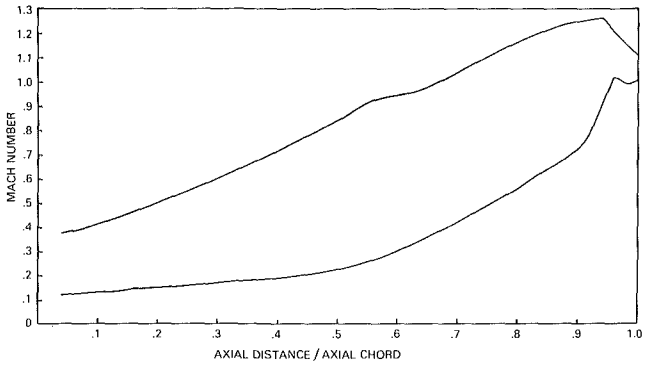

Fig. 5 Stator midspan Mach number distribution

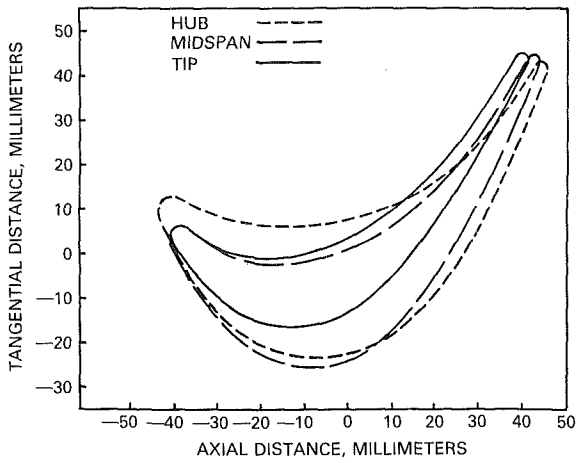

Fig. 6 Final blade design sections

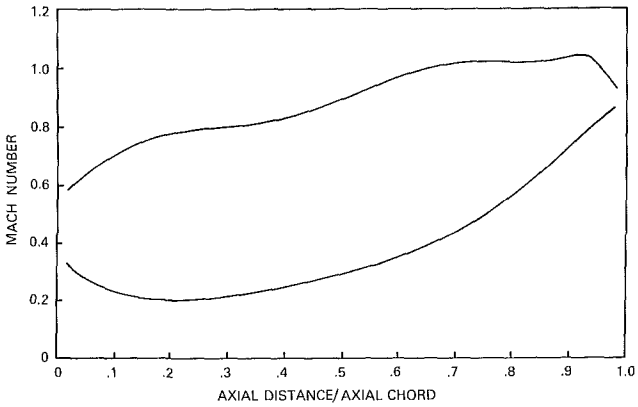

Fig. 7 Blade midspan Mach number distribution

Table 1 Comparison of midspan airfoil design parameters

	STATOR		BLADE	
Parameter	Original	Redesigned	Original	Redesigned
Zweiffel's Coefficient	.58	.74	.74	.9
Aspect Ratio	1.0	1.4	1.2	1.2
Trailing Edge Thickness / Throat Opening	.12	.12	.16	.13

fel's coefficient, and 1.4 axial chord based aspect ratio. The stator had good acceleration on both surfaces (see Fig. 5), 15 percent suction surface diffusion near the trailing edge, and less than 10 percent pressure surface diffusion. The boundary layer analysis indicated that the stator would not have flow separation and that the profile losses would be low.

The three blade design sections (see Fig. 6) of the 73-airfoil design (compared to 80 airfoils in the original design) were stacked so that the desired internal cooling scheme could be accommodated. The new blade had close to zero nominal incidence, 9 to 12 deg uncovered turning, 4 to 6 deg trailing edge wedge angle, 0.127 in. (3.23 mm) trailing edge thickness, 0.9 midspan Zweiffel's coefficient, and 1.2 aspect ratio. At midspan the suction surface had continuous flow acceleration up to almost the trailing edge (see Fig. 7) and only about 13 percent diffusion near the trailing edge. The pressure surface diffusion was about 60 percent, just slightly higher than desired. The rest of the blade had equally good surface velocity distribution, except for the outermost streamline where the suction surface diffusion exceeded the design requirement. The boundary layer analysis confirmed the aerodynamic acceptability of the blade design.

Table 1 compares the important airfoil design parameters of the original and the redesigned compressor turbines.

In the estimation of the redesigned compressor turbine efficiency, the axial turbine loss system based on the modification of Ainley and Matheson's method was used. Corrections were applied for the beneficial design features and for the harmful cooling air and leakage effects. The hot running blade tip clearance was assumed to be about one percent. The resulting design point stage efficiency for the new compressor turbine was estimated to be 87.5 percent.

Test Facility

The turbine test rig was designed to accommodate a range of axial turbines with up to 10 lb/sec (4.54 kg/s) mass flow rate, 4:1 pressure ratio, 117 rev/sec speed, and 600 kW output power (Gosling, 1984). To provide the desired turbine inlet temperature, ambient air was preheated in a combustor burning natural gas. The hot gas leaving the combustor was mixed

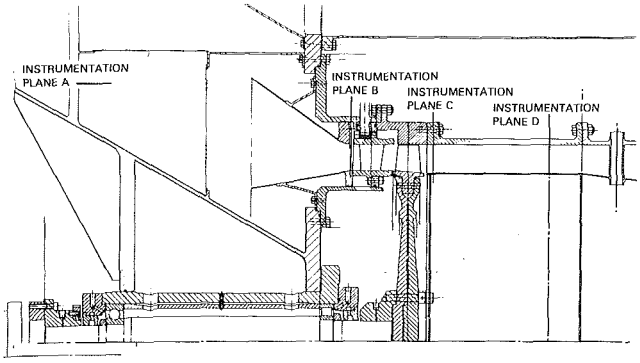

Fig. 8 Test section

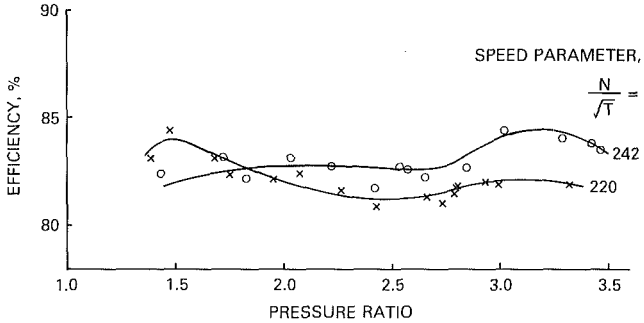

Fig. 9 Variation of efficiency with pressure ratio, original design

with additional ambient air in an arrangement of concentric tubes to provide good mixing at a relatively low pressure loss. The flow then passed into a large chamber fitted with two screens. A conical air meter was located at the end of this chamber. From the flow meter the flow passed through a three-branch manifold into a large plenum via baffles and two screens before entering the test section inlet duct. The screens and the turbine inlet duct were designed to give approximately the correct turbulence level and inlet boundary layer thickness so as to simulate the engine flow conditions. The test section inlet temperature was maintained at a level to give a turbine exit temperature approximately equal to the test cell temperature. After passing through the turbine and the exhaust duct, the flow was discharged through an exhauster. There was no provision made for the simulation of airfoil cooling air flows. The turbine power was absorbed and measured with a standard Froude 600 kW hydraulic dynamometer. The dynamometer electronic control system provided speed measurements and overspeed protection.

In order to simulate the engine aerodynamic operating conditions as closely as possible and stay within the rig limitations, a scale factor of 0.45 was used for the rig hardware. The turbine stator ring was designed so that it could be rotated about the turbine center line. This allowed radial-circumferential traverses to be carried out with relatively simple traverse equipment. The stators were individually cast segments in 410 stainless steel. The blades were machined from solid 6061 T6 aluminum blocks and pinned to a split disk machined out of alloy steel forgings.

The cross section of the test rig working section and the location of the main instrumentation planes were as shown in Fig. 8. The flow meter upstream temperature was measured by an eight-point thermocouple rake, the upstream total pressure by a pressure transducer, and the differential pressure by a very accurate pressure transducer and a backup water tube manometer. The turbine inlet conditions were measured by twelve thermocouples and twelve static pressure taps equally spaced around the inlet plenum (see instrumentation Plane A, Fig. 8). At stator inlet (Plane B) there was provision for radial traverses. Traverses carried out at this location indicated that the inlet radial temperature and pressure profiles were flat and that the endwall boundary layer thickness was approximately 3 percent of annulus height. Four inner and outer wall static pressure taps were also located at stator inlet. The stator inlet static pressure readings were used to estimate the turbine inlet total pressure, which excluded the losses across the upstream screen and the inlet duct. Static pressure taps (four on the inner wall and four on the outer wall) were also located at stator exit, Plane C (on the redesigned stage only), and Plane D. At rotor exit (Plane C) provision was made for radial traverse using United Sensor Type WT wedge probe. This probe, in conjunction with the rotatable stator ring, was used to obtain radial and circumferential distributions of temperature, pressure, and flow angle. At Plane D total pressures and temperatures were measured with 27 Kiel probes, which had thermocouples mounted in their stems. The probes were positioned in the annulus so as to measure a good average of the downstream flow conditions. A well-mixed downstream temperature was measured by three equally spaced six-point thermocouples located farther downstream.

The pressures were measured by pressure transducers and a Scanivalve wafer switch unit. The output from this unit and from the thermocouples was fed into an Auto Data 9 data logging system, which was connected to a KAY PRO II portable computer used for analysis and data storage. The printer in the Auto Data 9 unit provided a hard copy of the test data. The detailed test data analysis was carried out by a computer located in Hamilton.

The rig operation was started by switching on the power and services. The operation of the emergency and vibration monitoring equipment was tested next. When the exhauster had been started, closing the exhauster inlet bleed valve resulted in the rotation of the turbine rotor. The turbine speed was increased gradually to 33 rev/sec and the dynamometer speed control was set to hold this speed. The combustor gas supply valve was then opened and the igniter switched on. After successful ignition, the igniter was switched off. Speed and load were increased as desired by closing the bleed valve further. The exhauster inlet depression was set to give the required stage pressure ratio and the fuel flow was adjusted to give a satisfactory exhaust temperature.

Test Results

Original Compressor Turbine. After the completion of rig commissioning and instrumentation shakedown, a series of tests was carried out to determine the overall performance of the original compressor turbine design with 1.5 percent blade tip clearance. At the end of these tests, radial-circumferential traverses at the rotor exit plane were done at about a dozen operating conditions with different speeds and pressure ratios. The rig was then rebuilt with tip clearance increased to about 3 percent and some of the bulk tests were repeated.

The overall stage efficiencies based on the dynamometer measured power and on the measured temperature drop (between instrumentation Planes A and D) were in excellent agreement (to within 0.5 percent). Since in the rig tests of the redesigned compressor turbine problems were experienced with the dynamometer load cell, the temperature drop based efficiency was used in the comparison of the performance of the original and redesigned turbines. The original compressor turbine stage efficiency based on the measured temperature drop and pressure ratio derived from the calculated total pressure at stator inlet (Plane B) and the average rotor exit pressure measured by the Kiel probes (Plane D) was as shown in Fig. 9. For the highest speed lines tested ($N/\sqrt{T}$ = 220 and 242, where N = rotational speed in rev/min and T = inlet temperature in degrees Rankine) the efficiency first decreased

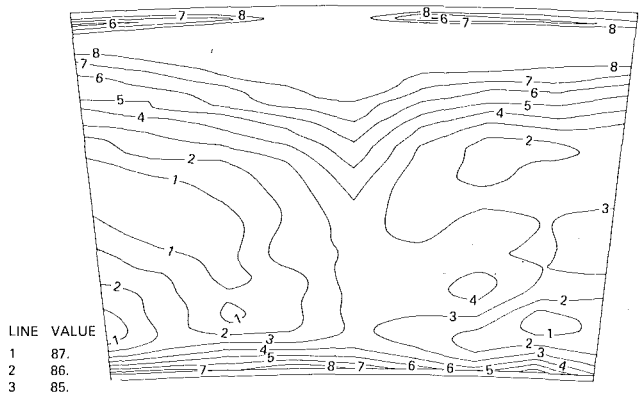

Fig. 10 Streamline efficiency, original compressor turbine

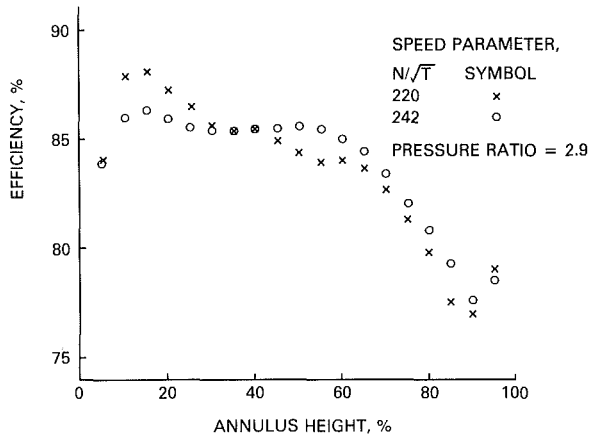

Fig. 11 Efficiency versus annulus height, original design

slightly up to a pressure ratio of about 2.5, then increased slightly up to pressure ratio of about 3, and finally decreased at higher pressure ratios. This efficiency variation, although unusual, has been observed by other researchers (Okapuu, 1974). The improvement in stage efficiency between pressure ratios of 2.5 and 3 was probably due to reduced stator suction surface diffusion as a result of increasing stator exit Mach number and improved rotor acceleration due to increased reaction. The small decrease in stage efficiency at the highest pressure ratio tested indicated that the blade was not near limit loading at that condition. For the two highest speed lines the efficiency ranged between about 81 and 84.5 percent. Detailed analysis of the bulk test results indicated that the blade incidence was highly positive over most of the operating range and that the estimated losses of both the stator and blade were high. The airfoil losses and blade incidence were estimated from the measured annulus static pressures, inlet and outlet total temperatures, outlet total pressure, inlet mass flow, stage work and rotational speed, and using continuity and compressible gas equations.

The test rig measured stage efficiency was lower than that based on previous engine test results. This was an unexpected result, since rig efficiencies are usually higher than corresponding engine efficiencies because of absence of losses associated with airfoil cooling, leakages, etc. This result was partially due to much higher than desired surface roughness of the cast stators (about 300 μin., 7.6 μm, compared to the desired 32 μin., 0.8 μm) and lower airfoil Reynolds numbers in the rig than in the engine (however the rig Reynolds numbers were higher than the critical value). A contributing factor was the pressure loss due to flow mixing and endwall skin friction between rotor exit and the downstream instrumentation Plane D. The last reason was given credibility by the radial-circumferential traverse results, which indicated up to 2 percent higher efficiency for equivalent test points. Therefore, based on the radial-circumferential traverse results, a correction to the average mixed-out rotor outlet pressure was derived and was then used to correct the bulk stage efficiencies. The variation of corrected efficiency with pressure ratio was similar to that in Fig. 9, but with increased efficiency in the higher pressure ratio range. The corrected efficiency was in better agreement with engine test results, keeping in mind the differences in stator surface roughness and Reynolds number between rig and engine.

The rig test results indicated that the swallowing capacity was about 2 percent higher than expected even though the measured geometric throat area of the rig stator was small by 0.8 percent. This result could have been due to instrumentation error (especially in the measurement of mass flow) or leakage around the stator. However it was believed that the leakage was small because of the sealing used around the stator.The nondimensional mass flow was constant above a pressure ratio of about 2.2 and there was little variation with speed. These results confirmed that this was a stator choked design.

The radial-circumferential rotor exit traverses were done at different speeds and pressure ratios covering a wide range of the compressor turbine operating conditions. Each traverse covered approximately one stator pitch. For each condition data were recorded at 10 circumferential and 24 radial locations. Since nulling the probe at each traverse position would have resulted in excessive traverse lines, a calibrated United Sensor WT wedge probe was used to measure the total and static pressure, total temperature, and flow angle. At high stage pressure ratios (i.e., near the design point) the total rotor exit mass flow estimated from the traverse results was up to 10 percent higher than the value measured by the flow meter. This was due to inaccurate estimation of static pressure because the probe calibration data was obtained at lower Mach numbers than were experienced in the rig. Although the probe calibration error affected the static pressure and flow angle, it did not affect the total pressure measurement and hence the estimated efficiency based on the average of the total pressures. The streamline efficiency estimated from traverse results taken over one stator pitch, at a pressure ratio of about 2.9, and $N/\sqrt{T} = 220$, was shown in Fig. 10. These results showed high efficiency cores in the lower part of the annulus, the location of the stator wake, and a severe dropoff in efficiency over the outer 40 percent of the annulus. The latter could be attributed to blade tip leakage effects, since the efficiency exhibited very little circumferential variation. The variation of mass-averaged streamline efficiency with annulus height at 2.9 pressure ratio and two speeds was as shown in Fig. 11.

After the completion of the radial-circumferential traverses, the test section was rebuilt with blade tip clearance increased to about 3 percent of blade height. For the two highest speed lines, the decrease in efficiency was about 1.5 percent compared to previous tests with 1.5 percent blade tip clearance. Thus the decrease in efficiency was about one percent for each percent increase in tip clearance. This variation was much less than was expected for the highly loaded blade design. It is possible that the change in efficiency with tip clearance was obscured by the high blade loss due to highly positive blade incidence.

Redesigned Compressor Turbine. The redesigned compressor turbine rig tests were carried out at the same 1.5 percent blade tip clearance as in the original turbine, although the engine hot running blade tip clearance was expected to be about 1 percent. The variation of stage efficiency based on the measured temperature drop was as shown in Fig. 12. The results exhibited more scatter than in the tests of the original com-

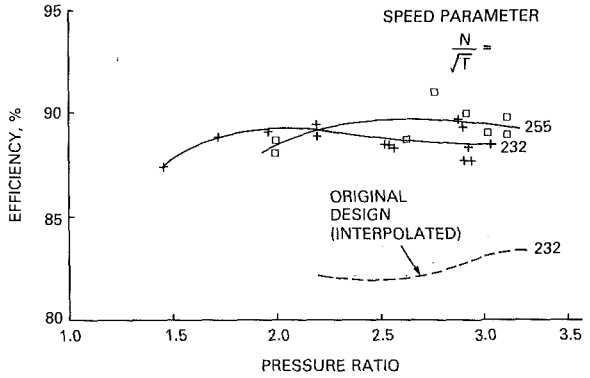

Fig. 12 Variation of efficiency with pressure ratio, redesigned compressor turbine

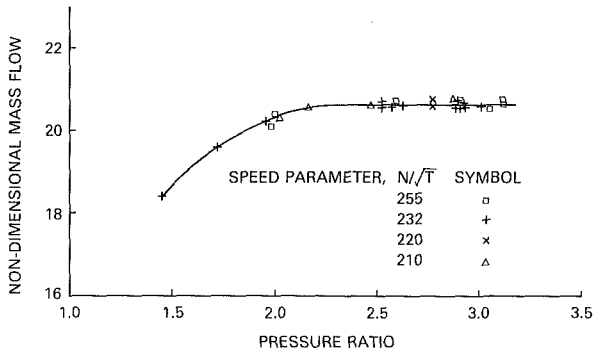

Fig. 13 Nondimensional mass flow versus pressure ratio, redesigned compressor turbine

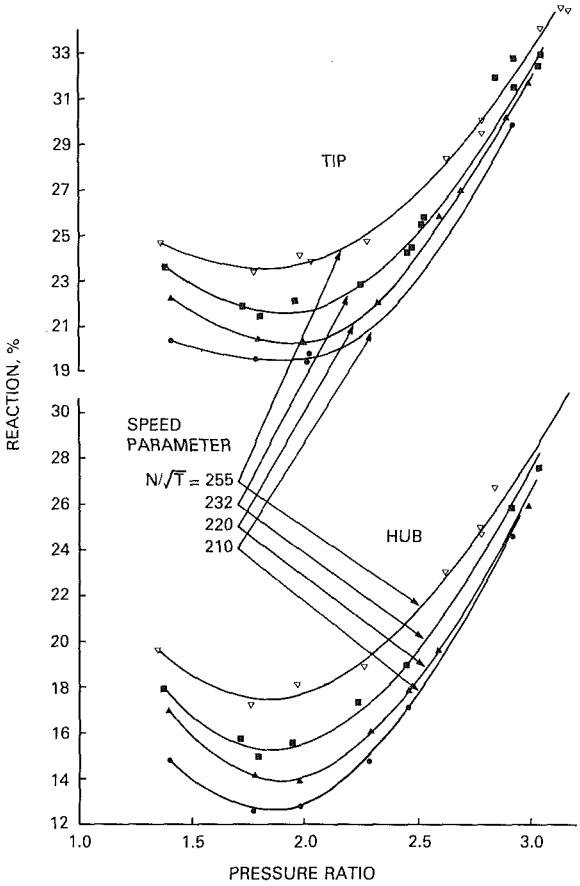

Fig. 14 Reaction versus pressure ratio, redesigned compressor turbine

pressor turbine. The average lines drawn through the points for the two speed lines ($N/\sqrt{T}$ = 232 and 255) did not have the same shape as the two highest speed lines in the original design. This was as expected because of improved airfoil surface accelerations in the new design. At the rig design point pressure ratio of 2.9 and the design speed ($N/\sqrt{T}$ = 232), the redesigned compressor stage efficiency was 88.7 percent, or almost six percentage points better than that of the original design (see the interpolated $N/\sqrt{T}$ = 232 speed line from the original turbine test results, shown on Fig. 12). The detail analysis of the design point test results showed that the blade incidence was close to zero and that both the stator and blade losses were considerably lower than in the original design.

When the previously described outlet pressure correction was applied, the redesigned compressor turbine design point efficiency was estimated to be about 90 percent, or about 6 percentage points higher than that of the original design. The improvement was mostly due to the improved design technique and the performance enhancing features incorporated in the new design, since the positive blade incidence in the original design accounted for only about one percentage point of the improvement. Based on the rig test results it was estimated that the redesigned compressor turbine engine "cooled" efficiency would exceed the 87.5 percent design value by one to two percentage points.

The rig test results indicated that the nondimensional mass flow of the redesigned compressor turbine was about 4 percent too high. This result agreed well with the geometric stator throat area, which was measured too large by 3.85 percent. Beyond a pressure ratio of about 2.3 the nondimensional mass flow was constant (see Fig. 13), as was expected for a choked stator design.

The static pressure based stage reaction variation was shown

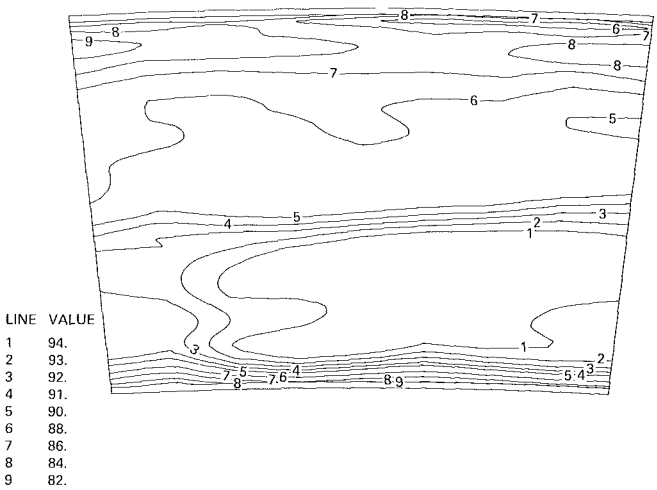

Fig. 15 Streamline efficiency, redesigned compressor turbine

in Fig. 14. The design point hub reaction was 26 percent and the tip reaction was 30.6 percent, compared to design values of 24 and 30 percent, respectively. The mean reaction was therefore slightly higher than design. This could be explained by the larger than required stator throat area. The smaller than expected hub-to-tip reaction variation was perhaps due to airfoil outlet flow angle distributions being different from those assumed in the design or due to a measurement error in the stator exit static pressure.

The streamline efficiency estimated from the radial-circumferential traverse results taken at the design point indicated that the best performance was obtained over the lower half of

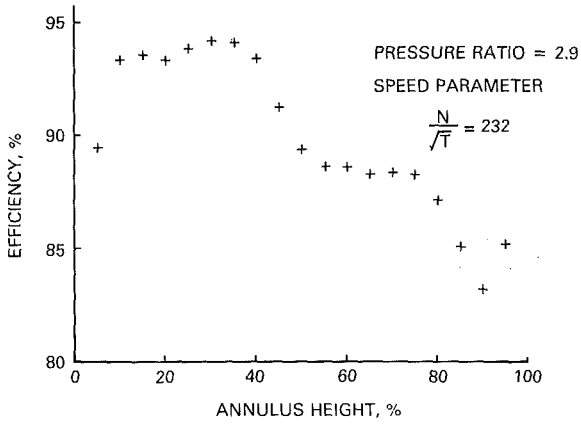

Fig. 16 Efficiency versus annulus height, redesigned compressor turbine

the annulus (see Fig. 15). From about 40 percent of annulus height the efficiency decreased. The tip leakage effect was less pronounced than in the original design and the effect of stator wake was less obvious. The latter effect could be due to reduced stator trailing edge thickness and lower stator profile losses in the redesigned compressor turbine. Based on the inspection of rotor outlet temperature, pressure, and outlet swirl angle distributions, the decrease in midspan efficiency was due to a decrease in temperature drop as a result of flow underturning, and not due to a high pressure loss. Further investigation would be required to determine if the midspan efficiency could be improved by stator or rotor restagger, or by a stator redesign. The radial variation of streamline efficiency with annulus height at about 2.9 pressure ratio was as shown in Fig. 16. The comparison of Figs. 11 and 16 indicated that the efficiency of the redesigned compressor turbine showed a considerable improvement over that of the original design over the complete span.

Conclusions

1 The corrected stage efficiency of the original compressor turbine design was close to the expected value derived from engine results.

2 The redesigned compressor turbine design point rig efficiency, based on measured temperature drop, was about 88.7 percent, or about six percentage points higher than that of the original design.

3 The corrected design point efficiency of the new design was about 90 percent.

4 The swallowing capacity of the new design was higher than expected due to overly large stator throat area.

5 The redesigned compressor turbine design point hub and tip reactions were close to the expected values.

6 The radial-circumferential traverse results showed that the redesigned compressor turbine efficiency was higher across the whole annulus than that in the original design.

Acknowledgments

The author would like to acknowledge the contribution of the following individuals in organizing and carrying out the rig tests, collecting the test data, and analyzing the test results: Mr. G. McQuiggan, Mr. M. Gosling, Mr. A. Rickard, Mr. J. Young, Mr. D. Mekker, Mr. P. Spedaler, Mr. S. O'Neill, and Mr. B. Mendonca.

The rig tests were carried out at the Gas Dynamics Laboratory of the Canadian National Research Council, in Ottawa, Canada. The author wishes to express thanks to Dr. R. G. Williamson, Section Head of the Gas Dynamics Laboratory, and his staff for their cooperation.

References

Diakunchak, I. S., et al., 1985, "Aerodynamic Design of a Highly Loaded, High Efficiency, Cooled Single Stage Compressor Turbine for an Energy Efficient Industrial Gas Turbine," CIMAC International Congress on Combustion Engines, Oslo, June.

Denton, J. D., and Singh, U. K., 1979, "Time Marching Methods for Turbomachinery Flow Calculation," VKI Lecture Series: *Transonic Flows in Turbomachinery*.

Deich, M. E., et al., 1960, "Method of Increasing Efficiency of Turbine Stages With Short Blades," *Teploenergetika*, No. 2, Feb.; Translation No. 2816, Associated Electrical Industries, Manchester, Apr. 1960.

Gosling, M. C., 1984, "The Design, Manufacture and Operation of a Model Turbine Test Rig," ASME Paper No. 84-GT-130.

Okapuu, U., 1974, "Some Results From Tests on a High Work Axial Gas Generator Turbine," ASME Paper No. 74-GT-81.

Turbulence Measurements in a Multistage Low-Pressure Turbine

A. Binder

Th. Schroeder

J. Hourmouziadis

MTU,
Munich, Federal Republic of Germany

The flow in the rotor blades of a five-stage low-pressure turbine was investigated experimentally using hot-film probes. Time averaging, Fourier transforms, and ensemble averaging are applied for data reduction. The techniques prove to be a very helpful instrument for the assessment of the flow characteristics in the relative frame. A strong interaction is identified between two successive rows of rotor blades. A physical model, developed from velocity and turbulence results, gives a comprehensive understanding of the phenomenon. The main parameter is the nonuniformity of the flow entering the downstream blade row. Separation occurs when the wake of the upstream rotor blades enters the blade passage near the leading edge, preferably on the pressure side. The interaction is quasi-steady in the relative frame and rotates with the rotor speed. It was observed only in one of three investigated blade rows. Further studies are necessary to identify the mechanism correlating the nonuniformity to the separation.

Introduction

Subsonic turbomachinery has been developed to extremely high performance levels. Low-pressure turbines for aircraft engines can be designed today with efficiencies well beyond 90 percent for high-altitude, low-Reynolds-number operation. This has become possible with the application of complex numerical prediction systems. The design methodology however is based and still heavily relies on precise and detailed experimental results. Accordingly, development work on test facilities and instrumentation has made a significant contribution to this evolution. A variety of sophisticated and versatile measurement techniques are currently available to the aerodynamicist.

All of these experimental techniques can be easily applied to the flow in stationary parts. Difficulties arise with measurements of the rotor flow. The main problem is the transfer of the signals from the rotating to the stationary frame. These difficulties have been overcome in the low-speed research turbines reported upon by Dring and Joslyn (1981) and Hodson (1985), but they still present a considerable obstacle for investigations in original size, high-speed industrial turbomachinery.

For application in the latter cases two direct methods, measuring the flow within the rotor blade passage, and one indirect, measuring the wake, have emerged from the work of the past several years.

- The use of telemetry to transmit the signals of transducers located on the rotating parts, as discussed by Hourmouziadis and Lichtfuss (1985). Basically all measurements possible in a guide vane can be repeated in a rotor blade. The necessary equipment, however, is very complex and requires an extremely careful calibration procedure. The method is only applied when no alternatives are available.
- Laser anemometry uses a device located on the stationary frame to measure the flow in the rotor blade passage. It has been successfully applied, for example by Binder (1985) in a turbine and by Williams (1987) in multistage compressor investigations. Its application is rather time consuming. The limitations however arise mainly from the "visibility" of the flow to the laser beam, particularly for shrouded blades, commonly used in low-pressure turbines.
- In the indirect method hot-wire probes are used in the stationary frame downstream of the rotor. The unsteady signal is then processed to analyze the rotor wake. This method has been successfully applied by Pfeil and Schroeder (1981) for fundamental research and by Sharma et al. (1985) for low-speed turbine investigations.

These three methods were then considered for application in the five-stage low-pressure turbine shown in Fig. 1. Stage and measuring station numbering is also defined in the figure. The first stage of the low-pressure turbine is the third stage in the engine. Because of the conditions imposed by the turbine design and the test rig, hot-film probes were selected. These special measurements were part of a comprehensive program both for verifying the performance and for detailed flow analysis. It comprised the following:

- performance characteristics,
- Reynolds number variation,
- radial traverses of three- and five-hole probes,
- tangential traverses of complete instrumentation at the exit plane,
- measurement of static pressure distributions on the guide vanes,
- boundary layer investigations using surface hot films on the first and last guide vane and
- hot-film probe measurements behind the second, fourth, and last rotors (Fig. 1).

Some of the results of the hot-film probe measurements

Contributed by the International Gas Turbine Institute and presented at the 33rd International Gas Turbine and Aeroengine Congress and Exhibition, Amsterdam, The Netherlands, June 5–9, 1988. Manuscript received by the International Gas Turbine Institute September 1987. Paper No. 88-GT-79.

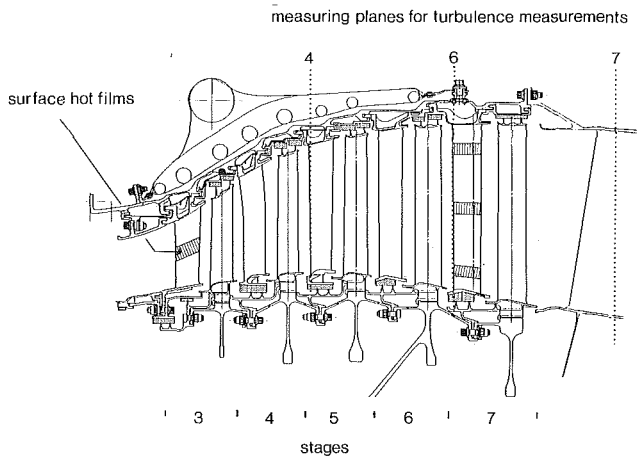

Fig. 1 Low-pressure turbine

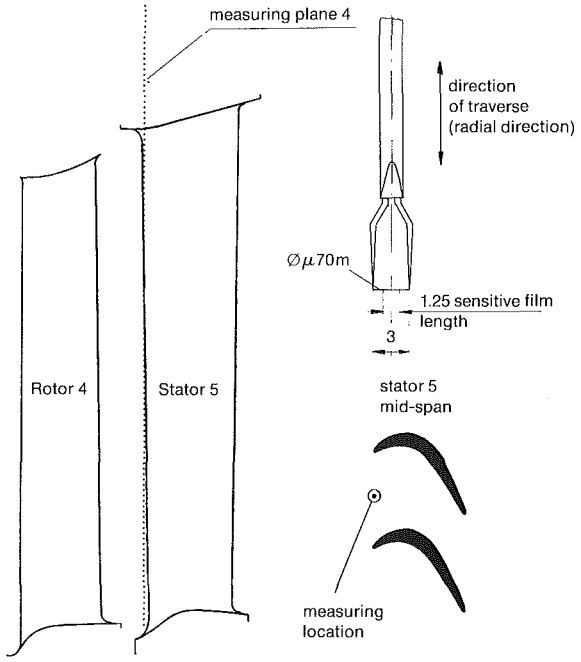

Fig. 2 Location of measuring plane 4 and fiber-film probe (DANTEC 55R01)

downstream of the rotor blades are presented and discussed in this paper.

Experimental Apparatus and Test Conditions

The measurements were made using straight hot-film probes traversed radially through the measuring planes downstream of the stage 4, 6, and 7 rotors (Fig. 1). It was not possible to have more than one probe at each plane. Circumferential traverses and thus measurement of the effects of the stator were not possible. Because of the short axial gaps between the successive rows, the probes at planes 4 and 6 had to be arranged slightly offset toward the next stator stage within the flow passage (see Fig. 2). However, this is of no consequence as far as the results are concerned, since the purpose of this investigation was to look at relative fluctuations in the distributions acquired by the methods used. The representation of the measured data as relative fluctuations was chosen to compare the data obtained at different spans and measuring planes. For technical reasons, plane 7 had to be located far downstream from the stage 7 rotor (Fig. 1). The distance between the measuring planes and the trailing edge of the rotor at midspan is shown in Table 1.

Table 1 Location of measurement stations

Measuring plane	Distance between probe and TE of rotor (in relative flow direction)
4	1.04 x true chord
6	0.80 x true chord
7	4.50 x true chord

All measurements were carried out at design pressure ratio and corrected speeds. The Reynolds numbers used for the tests were Re = 120,000, 170,000, 230,000, and 493,000, where Re = 170,000 corresponds to altitude operation, and the take-off Reynolds number is about 380,000.

Measurement and Instrumentation

The hot-film probes type DANTEC 55R01 (Fig. 2), operated in constant temperature mode, were adjusted at midspan to measure the mean absolute velocity and were kept at that position during the spanwise traversing. The flow angle could not be measured.

This procedure resulted in an error for the mean velocity measurement at off-midspan positions, which however was negligible because of the small spanwise variation of the flow angle. The fluctuating component parallel to the hot-film sensor axis was not measured in accordance with the well known cosine law described by Champagne et al. (1967). For that reason in the velocity fluctuations and turbulence intensities measured only two velocity components are included.

The linearized hot-film probe signals, as well as the trigger signal required for the ensemble averaging (1 pulse per rotor rotation), were recorded using a Honeywell 101 high-performance tape recorder. Analysis was made after the tests had been completed.

Data Reduction

An example of a typical measured velocity distribution is shown in Fig. 3. Because of the superposition of periodic and random fluctuations, direct physical analysis of the distribu-

Nomenclature

A = amplitude of spectral analysis of velocity fluctuation (rms)
c = absolute flow velocity
c' = absolute flow velocity fluctuation (random part)
f = frequency
h = reduced blade span
l = chord length
M = number of sampling points per record
Ma = Mach number
N = number of records for ensemble averaging process
Re = Reynolds number based on exit velocity and chord length, vane 3, midspan
Re_{xxx} = Reynolds number in xxx thousand
rms = root mean square
T = time period of rotor frequency
TE = trailing edge
Tu = turbulence intensity

Superscripts

$\bar{}$ = time-averaged
$\tilde{}$ = ensemble-averaged

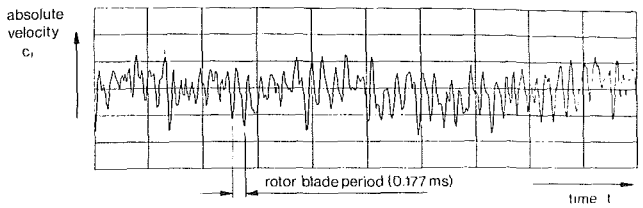

Fig. 3 Typical velocity record behind a rotor (rotor 4, 50 percent span, RE493)

tions is not possible. Therefore, the following three procedures were used for analyzing the velocity behavior:

- Fourier transforms
- Ensemble averaging
- Time averaging

Fourier transforms of the tape-recorded signals were made using an HP 3562 FFT analyzer, where the frequency spectra were obtained from the superposition of 64 individual frequency analyses (free-run mode). In keeping with the frequency limits of the probes and the tape deck, a frequency limit of 20 kHz was selected. The amplitudes (rms values) were plotted linearly over the frequency and normalized with the time-averaged mean value of the velocity $\bar{c}$.

Ensemble averaging was the main data reduction method used. It is particularly suited for the investigation of periodically unsteady flow processes, enabling the periodic fluctuations to be separated from the random fluctuations. This procedure, described for example by Bendat and Piersol (1986), has already been used frequently in hot-wire probe measurements in investigations of unsteady flows in turbomachinery (Lakshminarayana and Poncet, 1974; Evans, 1975; Gostelow, 1977; Lakshminarayana, 1981; Hodson, 1985; Pfeil and Sieber, 1986) as well as in model tests (Pfeil and Schroeder, 1981). The results presented here were obtained using an HP 9000 series 300 computer plus AD converter. The technical details and the parameters used in the ensemble averaging are listed in Table 2.

The rotor wake is seen by the probe in the absolute frame of reference as a periodic fluctuation with a random disturbance superimposed. In the ensemble-averaging technique, data are collected with every rotor revolution, thus separating the periodical from the random fluctuations. The equations for calculating the periodically fluctuating mean velocity $\tilde{c}(t)$ and the periodically fluctuating random unsteadiness (rms value) $\sqrt{\tilde{c}'^2}\ (t)$ given by Bendat and Piersol (1986) are

Ensemble-averaged mean velocity:

$$\tilde{c}_j(t_j) = \frac{1}{N}\sum_{i=1}^{N} c_{ji}(t_j) \tag{1}$$

Ensemble-averaged random unsteadiness:

$$\sqrt{\tilde{c}_j^{12}(t_j)} = \sqrt{\frac{1}{N-1}\sum_{i=1}^{N}[c_{ji}(t_j)-\tilde{c}_j(t_j)]^2} \tag{2}$$

$$t_j = 0 \ldots\ldots T$$

$$j = 1 \ldots\ldots M$$

where c_{ji} represents the jth sample in the ith time record of digitized and stored values.

The time-averaged mean velocity was obtained by integration of the ensemble-averaged $\tilde{c}(t)$. The identical value is obtained from the time averaging of the original velocity $c(t)$ shown in Fig. 3.

Table 2 Ensemble averaging parameters

Throughput	102.4 kHz
Tape speed reduction for ensemble averaging	1:32
Conversion resolution	0.012% (14 bit)
Number M of sampling points per record	2048
Number N of records in ensemble averaging	75 - 200

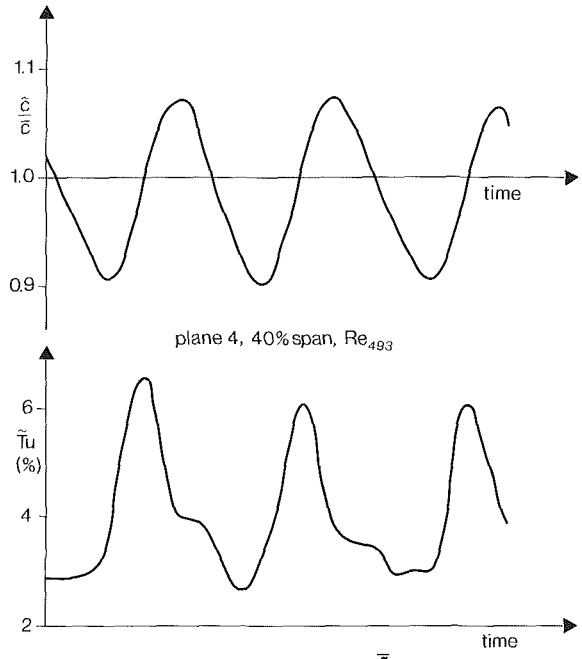

Fig. 4 Absolute velocity $\tilde{c}/\bar{c}$ and turbulence $\bar{\tilde{T}}u$ distributions (ensemble averaged)

Time-averaged mean value:

$$\bar{\tilde{c}} = \frac{1}{T}\int_0^T \tilde{c}(t)dt = \frac{1}{T}\int_0^T c(t)dt; \qquad \text{i.e., } \bar{\tilde{c}} = \bar{c} \tag{3}$$

The time-averaged random unsteadiness $\sqrt{\bar{\tilde{c}}'^2}$, as well as the associated turbulence intensity $\bar{\tilde{T}}u$, do not contain a periodically fluctuating mean velocity component $\tilde{c}(t)$. This is in contrast to the parameters determined with an analog true rms voltmeter from $c(t)$.

Time-averaged random unsteadiness:

$$\sqrt{\bar{\tilde{c}}'^2} = \sqrt{\frac{1}{T}\int_0^T \tilde{c}'^2\ (t)dt} \tag{4}$$

Associated turbulence intensity:

$$\bar{\tilde{T}}u = \sqrt{\bar{\tilde{c}}'^2}/\bar{c} \tag{5}$$

The time-averaged mean value $\bar{c}$ was used for normalizing the ensemble-averaged values to enable the results, obtained at different locations, to be compared with one another.

Normalized ensemble-averaged mean velocity:

$$\tilde{c}(t)/\bar{c} \tag{6}$$

Normalized random unsteadiness:

$$\tilde{T}u(t) = \sqrt{\tilde{c}'^2}\ (t)/\bar{c} \tag{7}$$

The time dependence of the random unsteadiness indicates the variation of the turbulence intensity across the rotor wake.

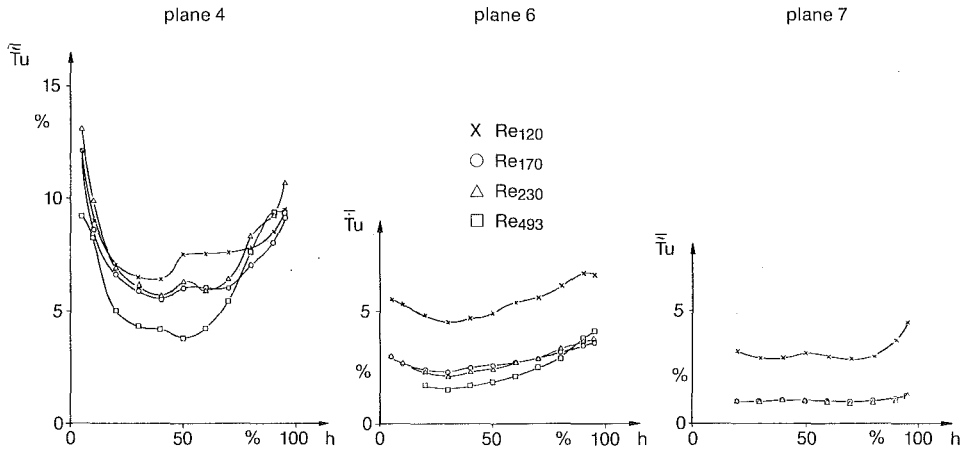

Fig. 5 Radial turbulence distribution $\bar{\tilde{T}}u$

As an example, in Fig. 4 distributions of $\tilde{c}/\bar{c}$ and $\tilde{T}u$ are plotted. In this diagram three rotor blade periods with the maximum wake depth measured are shown. According to the parameters given in Table 2 each period consists of 18 sampling points (intervals).

Discussion of the Results

Time-Averaged Mean Values. An initial survey of the flow conditions at the above-specified measuring planes is given in Fig. 5, which shows the turbulence intensity $\bar{\tilde{T}}u$ versus blade span.

In measuring plane 4 downstream of the second rotor, a pronounced variation in the turbulence over the blade span occurs at all Reynolds numbers, where the high values in the casing and hub areas are probably attributable to the secondary flows encountered at these regions. It is noticeable that these areas exhibit a smaller variation with the Reynolds number than the mainly two-dimensional flow between approximately 25 and 70 percent blade span. To facilitate the physical interpretation of the results, only the midspan region is considered in the following discussion. The marked dependence of turbulence on the Reynolds number near midspan continues up to Re_{493} and presumably does not end there. The overall high level of the turbulence intensity leads to the conclusion either that the probe was located within the wake of the stage 4 stator or that separation occurred on the blade of the stage 4 rotor. A more detailed analysis is given later.

In measuring plane 6 the pronounced radial variation of turbulence, accompanied by the strong increase toward the casing and hub, is no longer recognizable, suggesting that the secondary flows in the rear stages of the turbine are not as strong as in the forward stages. Major differences can be also observed in the midspan region. At Re_{120} turbulence levels are about the same as in plane 4. For higher Reynolds numbers however they drop significantly down to values of only about 2 percent. It should be kept in mind that in both stations the distance of the probe from the trailing edge was approximately the same (Table 1). The Reynolds number does not appear to have a significant influence beyond 170,000. The turbine was designed to perform efficiently down to Reynolds numbers of about 150,000 and this has obviously been achieved in this case. The high turbulence levels at Re_{120} indicate that the flow has started to separate.

Station 7 lies farther downstream of the cascade than planes 4 and 6, limiting the possibility of making a quantitative comparison. Qualitatively, however, the picture is similar to that at plane 6. The turbulence shows an abrupt drop between Re_{120} and Re_{170}, and remains constant up to the highest Reynolds number. Despite limited comparability, the test results indicate that the last stage performs very similar to that upstream of station 6. The lower turbulence levels are probably attributable to the dissipation over the greater distance between the trailing edge and the measuring plane.

Summing up, it may be said that the rotor flow at planes 6 and 7 exhibits similar behavior, but is quite different at plane 4, where generally higher turbulence intensity should be noted. Station 7 will not be included in further analysis.

Frequency Spectra. The frequency spectra at planes 4 and 6 at 40 percent span are presented in Fig. 6. For sake of clarity, only the distributions for Re_{120} and Re_{493} are shown.

One of the conclusions of the discussion of Fig. 5 was that the turbulence intensity was reduced with increasing Reynolds number. This was particularly clear at station 6. This trend can be seen again for the broad band noise in the frequency spectra, which is equivalent to the turbulence intensity. The very low amplitudes at 20 kHz demonstrate that the frequency range of the measurement system used (0–20 kHz) was suitably chosen.

At station 6, it is accompanied by a change in the structure of turbulence. There is a distinct reduction of the lower frequency noise. The experimental results of Hourmouziadis et al. (1987) show that this is an indication of separation for the lower Reynolds number Re_{120}.

Several peaks, which correspond to the blade passing frequencies or their harmonics, rise above this turbulent noise. As can be seen from the diagrams, the higher Reynolds numbers are not only associated with reduced turbulence, but also with a clear reduction in the periodic fluctuations. This indicates that the velocity defect in the wake also greatly depends on the Reynolds number. Here again one is struck by the difference between the two stations. While only a slight drop in the periodic fluctuation with increasing Reynolds number is recognizable at plane 4, the reduction at plane 6 is considerable.

The most important difference in the frequency spectra between the two measuring planes, however, lies in the occurrence of a second peak in addition to that at the blade passing frequency of rotor 4 (f4) at plane 4. This second peak, which is associated with a somewhat lower frequency, corresponds to the blade passing frequency of the stage 3 rotor (f3), which has two blades less. At Re_{493} both have practically the same amplitude. At measuring plane 6 a second peak from the upstream rotor is almost nonexistent. Only a small second peak at Re_{120} can be observed on the right of f6. It belongs to the stage 5 rotor, which has two blades more.

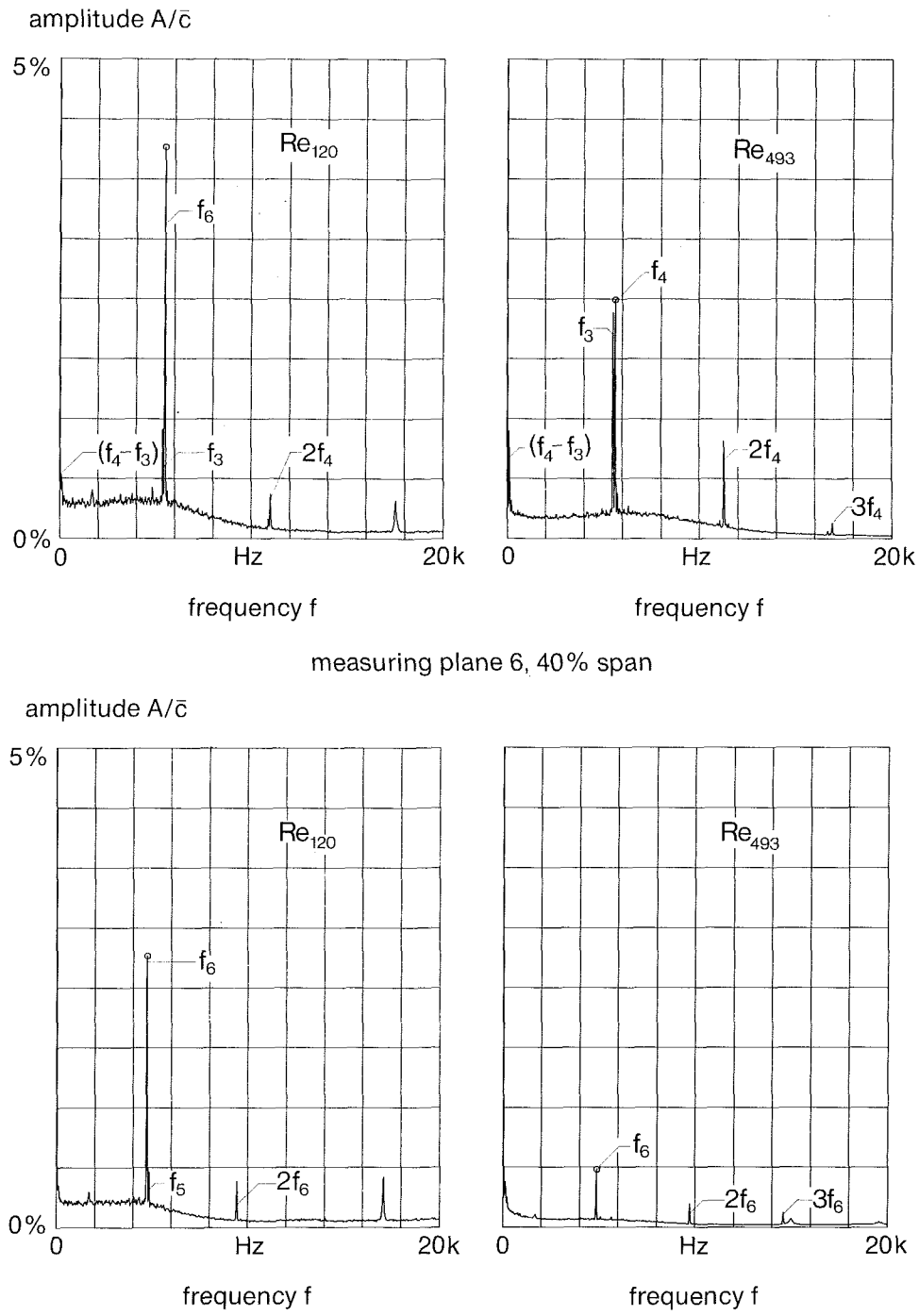

Fig. 6 Frequency spectra (linear)

The results discussed above indicate that the flow through the stage 4 rotor is strongly influenced by the rotor of the upstream stage 3. In fact the wake of rotor 3 can be readily identified in the measuring plane. One could consider separating the two wakes by means of an inverse Fourier transform, to analyze the flow of the upstream rotor blades. This was not attempted, because it is only possible if the superposition of the two flow fields is linear. In reality there is a strong nonlinearity present, particularly when shear layers, such as wakes and boundary layers, interact. The resulting flow behind the second rotor shows only the response to the nonuniform inlet flow.

Ensemble-Averaged Values. For the further analysis of the difference between planes 4 and 6, Figs. 7 and 8 show the distributions of the ensemble-averaged velocity $\tilde{c}/\bar{c}$ and turbulence intensity $\tilde{Tu}$. For easier comparison, the distributions of all four Reynolds numbers are presented in each figure. The abscissa length corresponds to slightly more than one revolution of the rotor (time in the absolute frame or circumferential position in the relative frame).

In the velocity distribution, in the upper part of each figure, each downward pointing peak corresponds to the absolute velocity defect of a wake. The maximum value in between corresponds to the flow velocity in the inviscid core flow be-

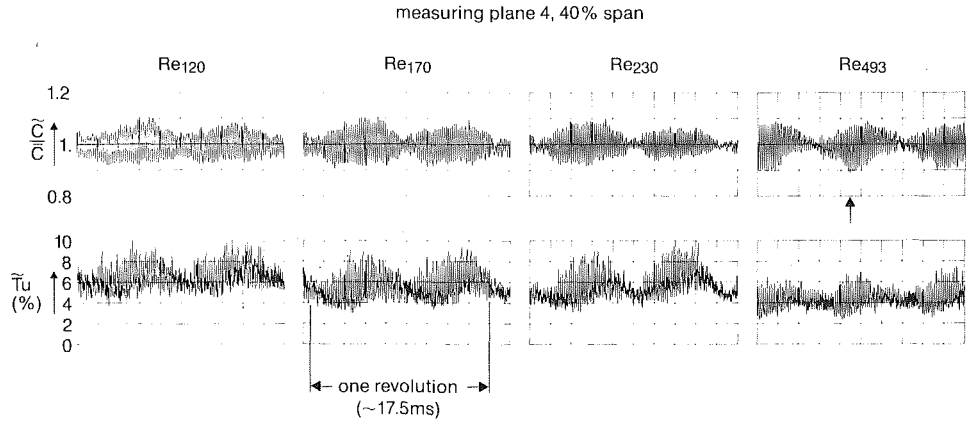

Fig. 7 Absolute velocity $\tilde{c}/\bar{c}$ and turbulence $\tilde{Tu}$ distributions (ensemble averaged)

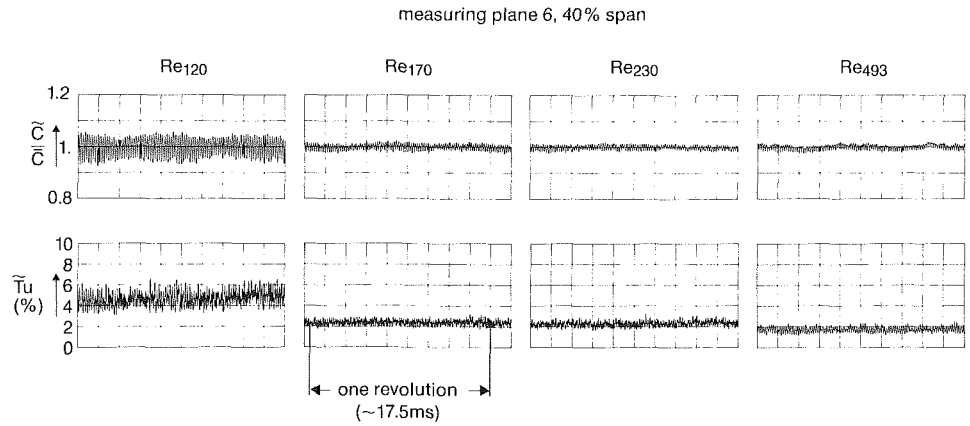

Fig. 8 Absolute velocity $\tilde{c}/\bar{c}$ and turbulence $\tilde{Tu}$ distributions (ensemble averaged)

tween the blades. The arrow in Fig. 7 (Re_{493}) indicates the position of the wakes plotted enlarged in Fig. 4. There is a phase shift in the turbulence fluctuations. The high values indicate the wakes and the minimum turbulence levels the inviscid flow.

Looking at the results of plane 4 (Fig. 7), the most surprising aspect concerning the wake and core flow envelopes is that a marked change in both the velocity and turbulence occurs around the rotor circumference. A beat frequency of 2 can be clearly identified. For example, at Re_{170} the velocity defect of a wake is about 5 percent of the mean value in the node of the envelope, and about 20 percent in the antinode. The minimum increase in the turbulence during a wake passage is about 2 percent in the node and the maximum about 5 percent in the antinode.

Considering the frequency spectra results, it is easy to conclude that the cause of this circumferential periodicity lies in the interaction between the stage 3 and 4 rotors. There is a difference of 2 in the number of blades of the two rotors. If the flow through the stage 4 rotor is affected by the nonuniform flow from the stage 3 rotor, this is reflected in a fluctuation in the envelope with the frequency $f4 - f3 = 2f_{Rotor}$. Consequently, a beatlike distribution with two nodes and two antinodes appears at plane 4 (Williams, 1986; and Epstein et al., 1986). The shift of the relative circumferential position of these nodes at Re_{493} in comparison with the other Reynolds numbers is only caused by a change in the trigger position and is not related to the flow.

The absolute velocity defect in an antinode is largely unaffected by the Reynolds number and amounts to a maximum of 18–20 percent of the mean value. With a distance of the probe from the trailing edge of about one chord length (Table 1), such a wake depth signifies that boundary layer separation has taken place (Hourmouziadis et al., 1986). In contrast, in the region of the nodes the wake depth at Re_{493} is only 3 percent, which indicates that no separation occurs. From Re_{170} to Re_{120} a marked increase of wake velocity defect takes place. It should be noted again that the turbine was designed to perform marginally below Re = 150,000, and this appears to be true only in the node region.

A further indication of separation in the region of the maximum $\tilde{c}$ fluctuations in the antinodes is the turbulence distribution. It exhibits a sharp increase of 4–5 percent at Re_{120} and of about 4 percent at Re_{493} from the core to the wake flow. In the node area, the increase is considerably smaller, amounting to roughly 1.5–2 percent.

The turbulence between the wakes of rotor 4 is given by the minimum values in Fig. 7. This base turbulence is generated by stator 4 and the other upstream blade rows and likewise exhibits a pronounced double period per revolution of the rotor.

Despite the same difference in the number of blades between the stage 5 and 6 rotors, a beatlike distribution of the velocity $\tilde{c}$ and variation in the turbulence extrema do not occur at plane 6 (Fig. 8). However, the interaction between these two rotors is revealed in a slight waviness of the velocity with the frequency (f5–f6), that is with the half period of a rotor revolution. A considerable difference to plane 4 also lies in the maximum velocity defect in the wake. At Re_{120} it is about 11 percent, but has already decreased considerably to about 3.5 percent at Re_{170} followed by only a slight change to about 3 percent at Re_{493}. The turbulence changes similarly between Re_{120} and Re_{170}. The basic (minimum) level drops from approximately 4 to 2 percent and the increase during the wake passage changes

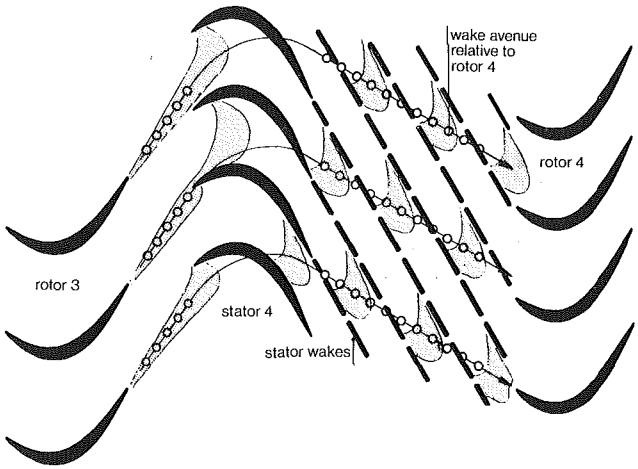

Fig. 9 Rotor 4 inflow conditions (schematic)

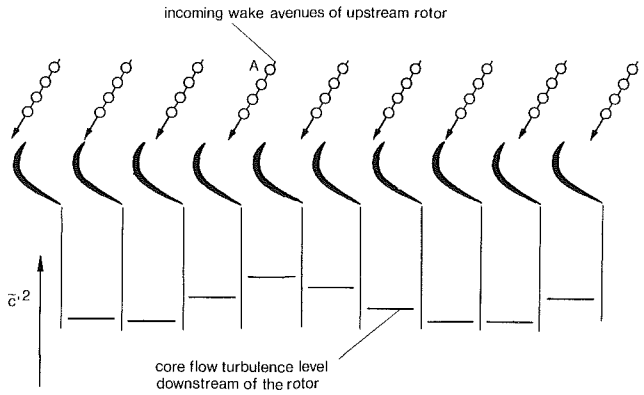

Fig. 10 Rotor 4 inflow and outflow conditions (schematic)

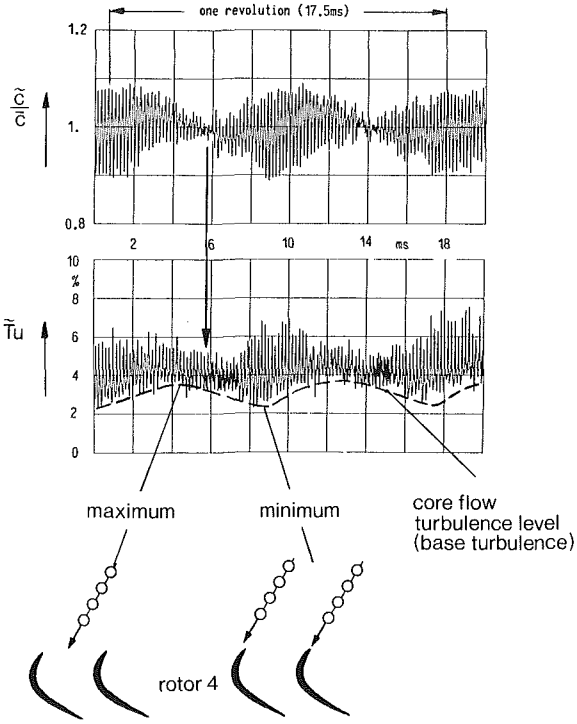

Fig. 11 Regions related to different inflow conditions

from 2.5 percent to less than 1 percent. Considering that the basic level essentially indicates the turbulence generated by the two blade rows upstream of rotor 6, it may be assumed that both the stage 5 rotor and stage 6 stator do not experience any further significant change with the Reynolds number. The turbulence increase during the wake passage reflects the boundary layer flow of the stage 6 rotor only. No Reynolds number effects can be observed beyond Re_{170}.

Comparison of the velocity fluctuations at the two measuring planes reveals similar behavior of the wakes in the nodes at plane 4 and in the distributions at plane 6. For Reynolds numbers of 170,000 and higher the airfoils perform satisfactorily in both cases. At Re_{120} complete separation is about to occur on the blades of rotor 6 and on those of rotor 4 lying in the nodes. It should be pointed out that the ensemble-average technique permits some kind of steady-state evaluation of the flow in the rotating frame. The beat frequency shown in Fig. 7 always involves the same blades. It is always the same airfoil that separates in the antinodes or has attached flow in the nodes. This flow structure rotates with the rotor speed and appears in the manner described here, whenever the blading is located in the same relative position to the stator vanes.

Model for Interpretation of Results

In order to investigate the physical phenomenon more deeply, the following two questions need to be considered in detail:

- What is the reason for the distinct variation of the minimum turbulence envelope?
- Which parts of the upstream rotor wake are responsible for the separation in the stage 4 rotor?

To help answer these questions, the nature of the nonuniform flow to a rotor is shown schematically in Fig. 9. The wakes shedded from the rotor are chopped and distorted by the stator, and are convected downstream in the absolute flow direction (Binder et al., 1985; Hodson, 1985; Joslyn et al., 1986; Tweedt et al., 1985). The thick broken lines indicate the stator wakes, and thus absolute flow direction. Considered from the relative system, the wake segments are arranged in an avenue to the downstream rotor. The relative flow direction of the individual wake avenues is represented by lines and circles. The difference in the number of rotor blades now causes a tangential phase shift of the wake avenues to the blades. For example, the wake avenue at the bottom in Fig. 9 impinges on the leading edge of the rotor blade, while the avenue of wake segments at the top flows into the blade channel. In a straight cascade test section similar flow situations were simulated by Wittig et al. (1987).

This phase shift of the incoming wake segments is illustrated schematically again in Fig. 10. The smaller number of blades of the upstream rotor causes the relative positions of the wakes to shift in the circumferential direction. A wake, flowing for example into the middle of the duct (position A), is followed in the direction of rotation of the rotor by one that has shifted somewhat toward the pressure side. The associated turbulence distribution in the core flow encountered downstream of the rotor is shown in the lower part of the figure, in which the wake areas have been deliberately omitted.

In the core flow, in the almost inviscid region between the blades, the incoming turbulence will change only slightly, since no further turbulence is created and the dissipation at the Reynolds numbers in question is rather low. This means that a highly turbulent inflow is also reflected in the core flow downstream of the blade row and a low turbulence flow remains low passing through the cascade. The wake avenue entering the row between two blades at A in Fig. 10 will result in higher turbulence levels in the core flow downstream of the cascade. Several blades to the left and to the right the wake segments impinge on the leading edge and do not enter the main flow in the blade passage. This leads to lower core flow

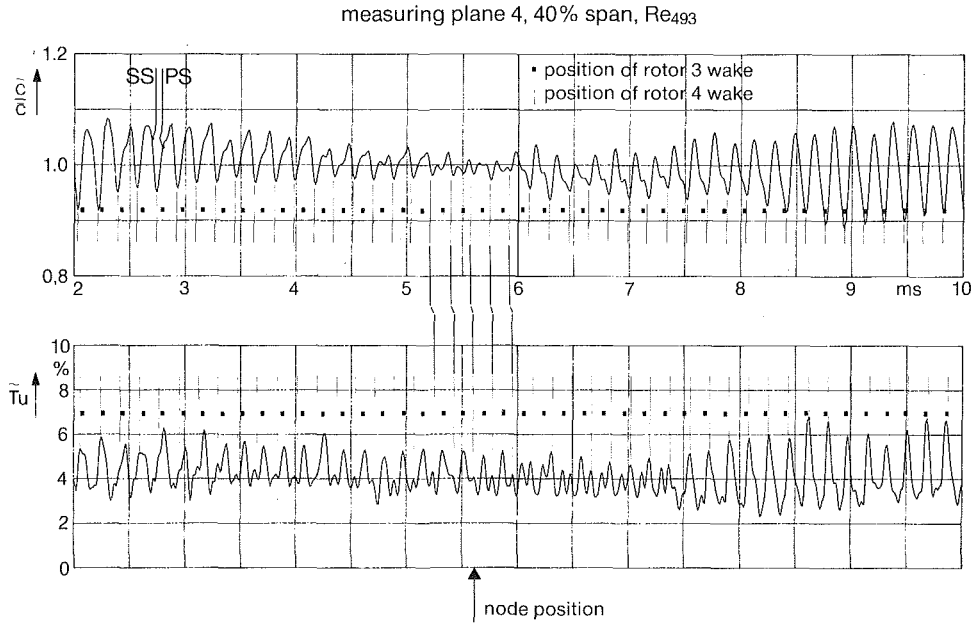

Fig. 12 Absolute velocity $\tilde{c}/\bar{c}$ and turbulence $\tilde{Tu}$ distributions (ensemble averaged)

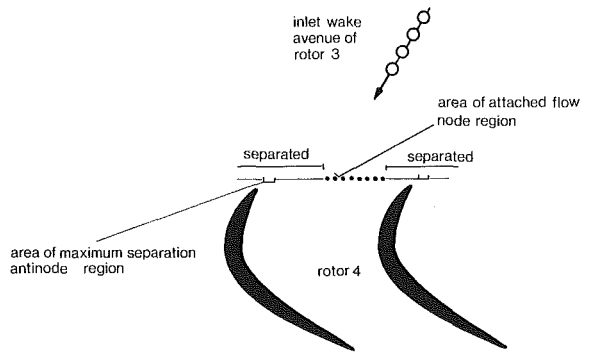

Fig. 13 Inlet flow regions leading to attached or separated rotor flow

turbulence levels at the exit of the cascade. This results in a wavelike variation of the base turbulence. The fact that the turbulence in the wakes is clearly greater than in the inviscid main flow indicates that the waviness should be reflected in the envelope of the minimum values of the turbulence. In the case discussed here, with a difference of 2 in the number of blades between the stages 3 and 4 rotors, there must be two maximum and two minimum values for every revolution of the rotor.

The distributions of the normalized ensemble-averaged mean velocity $\tilde{c}/\bar{c}$ and the corresponding turbulence intensity $\tilde{Tu}$ for station 4 from Fig. 7 are shown again in Fig. 11 for Re_{493}. The waviness in the basic turbulence, mentioned above, is clearly recognizable. The corresponding positions of the wake avenues flowing into the stage 4 rotor are also shown. The position of the node in the velocity distribution, where no separation occurs, is indicated by an arrow. As already described above, the lowest increase in the turbulence in the wake occurs in the vicinity of this node. The node and thus the lowest increases in turbulence occur roughly between the maximum and minimum values of the basic turbulence. A marked reduction in the turbulence increase during wake passage is already noticeable at the maximum base turbulence, and this is maintained until just before the minimum value is attained. Approximately five to ten wake peaks before this, pronounced increases in turbulence during passage of the rotor wakes can be observed. This means that flow separation at the rotor blades does not occur when the wakes from the upstream rotor enter the rotor between the center of the core flow and the suction side of the blades. If the rotor wake impinges at the leading edge of the blade or slightly toward the pressure side, separation will occur.

Further confirmation of these results is provided by the analysis of the individual wakes. For this purpose, Fig. 11 is plotted enlarged in the region 2–10 ms in Fig. 12 to permit their better separation. The periodicity of the stage 4 rotor is marked with dashes to show the minimum velocity and maximum turbulence in each case. The slight displacement between the two is caused by the fact that changes in the relative direction of flow along the wake result in a mismatch between the wake of the absolute and relative velocity (Joslyn et al., 1986; Pfeil and Schroeder, 1986).

The dots in Fig. 12 indicating the periodicity of the stage 3 rotor are arranged such that they correspond with the second peak in the node region (5–6 ms) in both the $\tilde{c}$ (downward pointing peak) and the $\tilde{Tu}$ distributions. This twin peak represents the flow resulting from the response of the rotor 4 to the nonuniformities of the inlet flow. An "intermediate wake" develops and is superimposed onto the main wake.

It can be clearly seen in the velocity distribution $\tilde{c}$ that this "intermediate wake" changes position relative to the main wake according to the different pitches of the two rotors. In the region of 5 ms it is exactly in between the wakes of the stage 4 rotor. Proceeding to the left, it approaches the pressure side of the wake of the stage 4 rotor, and at about 4–3 ms a clear increase in the wake depth and mixing occur with the result that the wake from the stage 3 rotor is recognizable only as a slight pressure side kink on the main wake. Proceeding right from the node at 6 ms, the behavior is similar or even more pronounced, but here the main wake is now approached from the suction side. The wake depths again increase considerably after approximately 7.5 ms reaching a maximum at around 9–10 ms.

The turbulence distribution exhibits a similar behavior. The twin peaks in the vicinity of the nodes are much more pronounced, and without the marked dots and dashes, it would

be impossible to separate the wakes of the stage 3 and 4 rotors. The variation of turbulence intensity, described in Fig. 7 and 11, originates from the two wakes present in the node area with the two peaks being virtually equally pronounced.

The physical model developed for the interaction of two blade rows permits a complete interpretation of the experimental results and gives a comprehensive understanding of the nonuniformity and the Reynolds number effects observed in the rotor 4 wake.

Concluding Remarks

The experimental investigation presented here shows that hot-film probe measurements combined with the ensemble-average technique are a very useful method for the analysis of rotor flow in turbomachinery. Appropriate evaluation of the test results gives a clear indication of the presence or absence of profile separation.

Quite strong interactions between rotating blade rows were identified. They are caused by the wakes of the upstream rotor convected downstream through the guide vanes and generating a nonuniformity at the inlet to the next row of rotor blades. Detailed analysis of the ensemble-averaged velocity and turbulence intensity distributions led to the conclusive results (Fig. 13):

- Separation is triggered when the upstream rotor wake enters the blade passage near the leading edge, preferably on the pressure side.
- No separation occurs when the wake enters with the core flow in the midpassage region.

The phenomenon is quasi-steady in the relative frame and rotates with the rotor speed. The separated or attached flow always involves the same individual airfoils and is repeated periodically whenever their relative position to the guide vanes is the same.

The measurements were carried out only in one circumferential location. Any influence from the stator therefore could not be separated. It is very clear, however, that the main parameter is the nonuniformity of the flow. The interaction was observed only in one of the three rotors investigated. The mechanism leading to the particular interaction cannot be explained at present and further investigations are required.

Acknowledgments

The authors would like to thank J. Reifenschneider and H. Becker from the MTU test group, who carried out the extensive experimental program, R. Goehl for the excellent measurements with the hot-film probes, and W. Voigt and K. Ruoff for the ensemble averaging and the further hot-film data reduction.

References

Bendat, J. S., and Piersol, A. G., 1986, *Random Data Analysis and Measurement Procedures*, Wiley, New York, pp. 425–483.

Binder, A., Foerster, W., Kruse, H., and Rogge, H., 1985, "An Experimental Investigation Into the Effect of Wakes on the Unsteady Turbine Rotor Flow," ASME *Journal of Engineering for Gas Turbines and Power*, Vol. 107, pp. 458–466.

Binder, A., 1985, "Instationary Flow Effects in the Rotor of a Turbine," Ph.D. Thesis, RWTH Aachen, Federal Republic of Germany, ESA-TT-1001.

Champagne, F. H., Sleicher, C. A., and Wehrmann, O. H., 1967, "Turbulence Measurements With Inclined Hot Wires," *Journal of Fluid Mechanics*, Vol. 28, No. 1, pp. 153–182.

Dring, R. P., and Joslyn, H. D., 1981, "Measurements of Turbine Rotor Blade Flows," ASME *Journal of Engineering for Power*, Vol. 103, No. 2, pp. 400–405.

Epstein, A. H., Gertz, J. B., Owen, P. R., and Giles, M. B., 1986, "Vortex Shedding in Compressor Blade Wakes," *Transonic and Supersonic Phenomena*, Propulsion and Energetics 68th Specialists Meeting, Munich, Federal Republic of Germany.

Evans, R. L., 1975, "Turbulence and Unsteadiness Measurements Downstream of a Moving Blade Row," ASME *Journal of Engineering for Power*, Vol. 97, pp. 131–139.

Gostelow, J. P., 1977, "A New Approach to the Experimental Study of Turbomachinery Flow Phenomena," ASME *Journal of Engineering for Power*, Vol. 99, pp. 97–105.

Hodson, H. P., 1985, "Measurements of Wake-Generated Unsteadiness in the Rotor Passages of Axial Flow Turbines," ASME *Journal of Engineering for Gas Turbines and Power*, Vol. 107, pp. 467–476.

Hourmouziadis, J., Buckl, F., and Bergmann, P., 1987, "The Development of the Profile Boundary Layer in a Turbine Environment," ASME JOURNAL OF TURBOMACHINERY, Vol. 109, No. 2, pp. 286–295.

Hourmouziadis, J., and Lichtfuss, H.-J., 1985, "Modern Technology Application to Compressor and Turbine Aerodynamics," 7th ISABE, Beijing, People's Republic of China, Sept. 9–13, Paper No. ISABE 85-7033.

Joslyn, H. D., Caspar, J. R., and Dring, R. P., 1986, "Inviscid Modelling of Turbomachinery Wake Transport," AIAA *Journal for Propulsion*, Vol. 2, No. 2, pp. 175–180.

Lakshminarayana, B., and Poncet, A., 1974, "A Method of Measuring Three-Dimensional Rotating Wakes Behind Turbomachinery Rotors," ASME *Journal of Fluids Engineering*, Vol. 96, pp. 87–91.

Lakshminarayana, B., 1981, "Techniques for Aerodynamic and Turbulence Measurements in Turbomachinery Rotors," ASME *Journal of Engineering for Power*, Vol. 103, pp. 374–392.

Pfeil, H., and Schroeder, Th., 1981, "Decay of the Wake Behind a Cylinder Crossing Rapidly the Flow," AIAA Paper No. 81-0209.

Pfeil, H., and Schroeder, Th., 1986, "Measurements Behind a Cylinder Moving Transverse to the Flow Compared With the Wake Flow Behind a Cylinder at Rest," *Journal of Flight Sciences and Space Research*, Vol. 10, No. 3, pp. 158–167.

Pfeil, H., and Sieber, J., 1986, "Velocity Distribution and Decay Characteristics of Wakes Behind a Compressor Rotor-Blade," ASME Paper No. 86-GT-115.

Sharma, O. P., Buttler, T. L., Joslyn, H. D., and Dring, R. P., 1985, "Three-Dimensional Unsteady Flow in an Axial Flow Turbine," AIAA *Journal for Propulsion*, Vol. 1, No. 1, pp. 29–38.

Tweedt, D. L., Hathaway, M. D., and Okiishi, T. H., 1985, "Multistage Compressor Stator/Rotor Interaction," AIAA *Journal for Propulsion*, Vol. 1, No. 6, pp. 449–455.

Williams, C. M., 1986, "Laser Velocimetry Study of Stator/Rotor Interactions in a Multi-stage Gas Turbine Compressor," AGARD 6th Symposium on Advanced Instrumentation for Aero Engine Components, Philadelphia, PA.

Williams, C. M., 1987, "Inter & Intra Blade Row Laser Velocimetry Studies of Gas Turbine Compressor Flows," ASME Paper No. 87-GT-235.

Wittig, S. L., Dullenkopf, K., Schulz, A., and Hestermann, R., 1987, "Laser Doppler Studies of the Wake-Effected Flow Field in a Turbine Cascade," ASME JOURNAL OF TURBOMACHINERY, Vol. 109, No. 2, pp. 170–176.

Unsteady Interaction Effects on a Transitional Turbine Blade Boundary Layer

D. A. Ashworth
Rolls-Royce plc,
Derby, United Kingdom

J. E. LaGraff
Syracuse University,
Syracuse, NY 13244

D. L. Schultz
The University of Oxford,
Oxford, United Kingdom

Results are presented illustrating the detailed behavior of the suction surface boundary layer of a transonic gas turbine rotor in a two-dimensional cascade under the influence of both free-stream turbulence and simulated nozzle guide vane wakes and shocks. The instrumentation included thin film resistance thermometers along with electrical analogues of the one-dimensional heat conduction equations to obtain wide bandwidth heat transfer rate measurements in a short duration wind tunnel. This instrumentation provides sufficient time resolution to track individual wake and shock-related events and also the turbulent bursts of a transitional boundary layer. Wide bandwidth surface pressure transducers and spark Schlieren photography were used in support of these heat transfer measurements. The results showed a direct relationship between the passage of wake disturbances and transient surface heat transfer enhancements. It was possible to track both wake and transitional events along the surface and to compare these with the expected convection rates. Analysis of the signals allowed direct calculations of intermittency factors, which compared well with predictions. Additional effects due to a moving shock/boundary layer interaction were investigated. These resulted in marked variations in heat transfer rate both above and below the laminar values. These excursions were associated with separation and re-attachment phenomena.

Introduction

The need to understand the processes by which transition takes place in a boundary layer and its susceptibility to disturbance by events occurring in the free-stream have led to a growing amount of research, much of it aimed toward the gas turbine industry. An increase in the level of free-stream turbulence has been shown to encourage the transition process (Blair, 1982; Rued and Wittig, 1984) following the turbulent spot models proposed by Schubauer and Klebanoff (1956). The effects of intermittent changes in flow conditions such as those caused by the Nozzle Guide Vane (NGV) and rotor blade interactions have also been shown to have significant influence on heat transfer rate to the blades, as detailed by Dunn (1985) and Doorly (1985). The tests reported in this paper investigate both the transitional phenomena and the influence of a simulated NGV on a rotor blade suction surface boundary layer. The use of wide bandwidth heat transfer instrumentation enables individual events such as turbulent spots developing in the transitional boundary layer to be easily identified, at free-stream conditions corresponding to the gas turbine environment in terms of Mach number, Reynolds number, and gas-to-wall temperature ratio.

Experimental Approach

The present study was carried out on a transonic gas turbine rotor blade in the Isentropic Light Piston Tunnel (ILPT), as described by Schultz et al. (1977). The ILPT is a short duration facility, which for a typical run time of about 0.5 s gives a gas-to-wall temperature ratio of 1.5. For these tests a five-bladed cascade of 50 mm inlet span was used with a Mach number of 0.38 at inlet and 1.18 at the exit plane with a corresponding Reynolds number of 0.92×10^6. The free-stream turbulence level could be varied from a background level of less than 0.8 percent to a "high" level of about 3 percent by use of a grid of 2 mm bars placed 208 mm upstream of the cascade inlet plane. The operating conditions are detailed in Fig. 1, using the definitions: Re = Reynolds number $= \rho U_2 C_t / \mu$, with viscosity derived from Sutherland's law; M = isentropic Mach number $= U/a_1$, where sound speed $a_1 = \sqrt{\gamma R T_1}$.

The position of the heat transfer instrumentation is also shown in Fig. 1, with the 17 thin film gages spaced around the suction surface. For these tests the gages were spaced 2.5 mm apart from 8 to 50 percent of the surface perimeter of 64.2 mm, with a 5 mm spacing thereafter. The gages were 0.5 mm wide and covered 4 mm of the span, compared with the 10 mm gages used previously in the cascade to enable smaller three-dimensional events to be observed. The gage effectively averages the heat transfer rate along its length, thus reducing the magnitude of any events of size smaller than the film coverage. Heat transfer rate was obtained using a well-established technique (Schultz and Jones, 1973) by using elec-

Contributed by the International Gas Turbine Institute and presented at the 2nd ASME/JSME Thermal Engineering Joint Conference, Honolulu, Hawaii, March 22-27, 1987. Manuscript received at ASME Headquarters June 14, 1988.

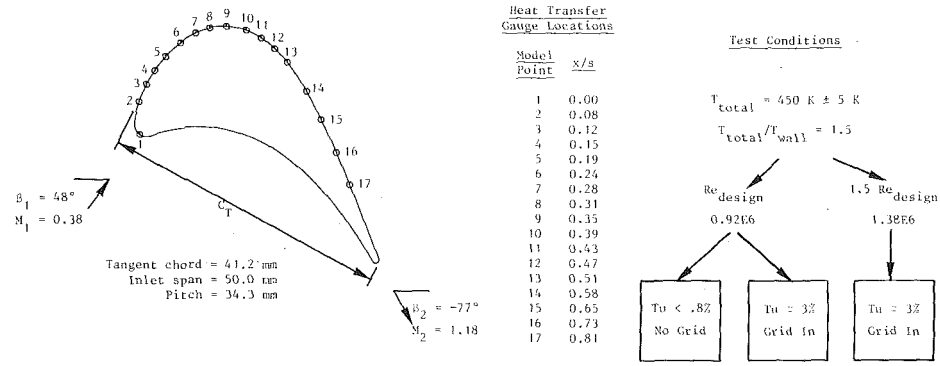

Fig. 1 Instrumented model details and test conditions

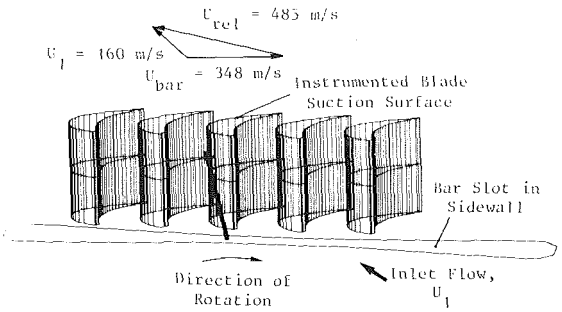

Fig. 2 The cascade with rotating bar configuration

trical analogues of the semi-infinite conduction equation to give a direct measurement of heat transfer rate with a bandwidth of 100 kHz, as described by Oldfield et al. (1984). Wide bandwidth surface-mounted pressure transducers (Kulite type XCQ-062-50D) were used, together with spark Schlieren photographs, in the analysis of the data.

In order further to characterize the free-stream conditions, constant temperature hot-wire anemometer measurements were made at the tunnel centerline at the entrance plane of the cascade leading edge. The probe used was a DISA P11 5 μm platinum coated tungsten wire 2 mm long and connected to a DISA 55D01 constant temperature anemometer bridge tuned to a bandwidth of greater than 50 kHz.

The heat transfer results are presented in Nusselt number form, i.e.,

$$\mathrm{Nu} = \frac{\dot{q}_m}{(T_0 - T_m)} \frac{C_t}{k}$$

with gas conductivity $k = 0.0047 + 7 \times 10^{-5} T_0$ in W/mK.

The effects of the NGV-rotor interation were simulated by 2 mm diameter bars attached to a disk spun upstream of the cascade, as described by Doorly and Oldfield (1985b), and illustrated in Fig. 2. By this means it is possible to simulate the inlet perturbation in the rotor relative frame for the cascade, to give the correct NGV wake orientation and scale. This method was used by Ashworth et al. (1985) for the same profile at an inlet angle of 58 deg with a bar-to-cascade midspan pitch ratio of 1.7 representative of a realistic turbine design. The present study reduced the number of bars to 2 giving a pitch ratio of 13.4 so that individual periodic disturbances could be identified, giving a bar-passing frequency of 740 Hz. In the fast sampling period of 6 ms it was possible to capture 4.4 bar-passing cycles, so that the repeatability of events could be determined.

The data were acquired in several ways:

(*i*) Slow samples were taken at 500 Hz using a 64-channel DataTranslation DT1711 A-D board, with a PDP11/34 controlling this acquisition and the tunnel housekeeping channels establishing the steady flow conditions. From these data mean values of heat transfer rate are deduced by choosing a time interval around a measurement point in the run for which conditions are steady (Oldfield et al., 1978).

(*ii*) A Datalab DL2800 transient recorder was used to acquire 16 channels of 4096 points at a sampling rate of 500 kHz at a time in the run around the measure point. These results form the basis of the transient analysis in this paper.

(*iii*) Schlieren photographs stored a "snapshot" of the flowfield as an aid in interpretation of the surface measurements.

Steady Baseline Flow Conditions

Measurements of the mean aerodynamic and heat transfer properties of the rotor cascade are given in Fig. 3 for the suction surface at the test conditions of the present experiment.

Nomenclature

a = speed of sound
C_t = tangential (or true) chord
k = thermal conductivity, W/mK
K = acceleration parameter = $\nu/U^2(dU/dx)$
M = Isentropic Mach number
Nu = Nusselt number
P = pressure
$\dot{q}$ = heat transfer rate, W/m^2
R = radius of curvature, mm or the gas constant, J/kgK
Re = Reynolds number based on inlet total conditions, isentropic exit Mach number, and tangential chord
s = blade surface perimeter
t = time
T = temperature, K
Tu = turbulence level = u'/U
u' = fluctuating velocity, m/s
U = velocity, m/s
V = voltage
x = surface distance from the leading edge
β = gas angle (measured from the axial direction)
γ = ratio of specific heats
γ = intermittency factor
μ = viscosity, kg/ms
ν = kinematic viscosity = μ/ρ
ρ = density kg/m^3

Subscripts

∞ = free-stream
0 = total
1 = inlet
2 = outlet
m = parameter at the selected measuring instant
rel = condition relative to the rotating bar

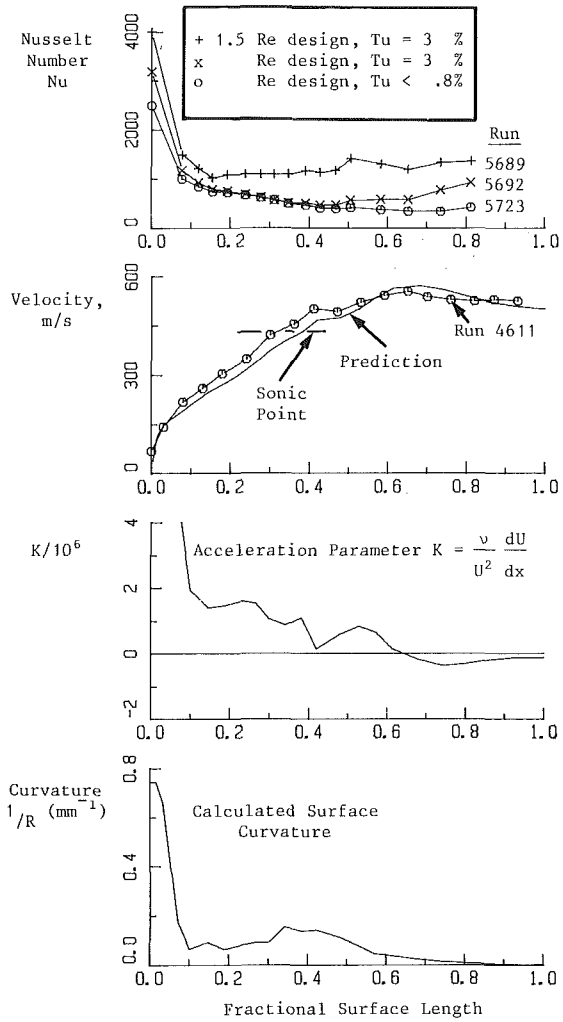

Fig. 3 Baseline surface conditions

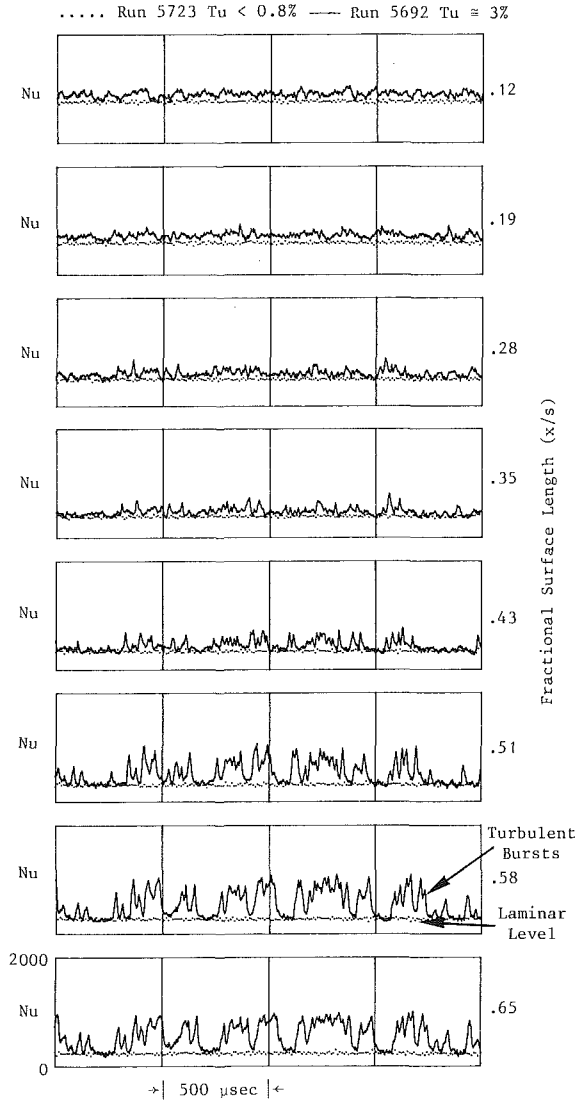

Fig. 4 Measured Nusselt number: the effect of free-stream turbulence on natural transition (the vertical scale for each trace ranges from 0 to 2000 in Nusselt number)

The heat transfer coefficient given as Nusselt number is seen to increase at and near the leading edge as expected with higher free-stream turbulence and blade Reynolds numbers (Lowery and Vachon, 1975). As the boundary layer develops along the surface the heat transfer rates in the high and low free-stream turbulence cases merge together at essentially the laminar level. The low turbulence case heat transfer rate (Tu < 0.8 percent) remains laminar to the x/s position of 0.8 whereas in the high turbulence case (Tu = 3 percent) it begins to increase in proportion (as will be shown in the following section) to increasing levels of turbulent spot intermittency. In the high Reynolds number (and high free-stream turbulence) case the heat transfer rate never comes down to the laminar level and begins climbing due to transitional intermittency soon after the $x/s = 0.15$ location. The free-stream velocity as determined by surface pressure measurements increases gradually along the entire blade surface matching very well the values from a blade-to-blade prediction program. It should be noted that the local flow velocity becomes supersonic by $x/s = 0.34$. The predicted acceleration parameter drops to a very low (favorable) value very early on the blade surface and becomes only slightly adverse beyond the x/s position of 0.63. This is near the rearmost point where wide bandwidth transient heat transfer data are collected and reported on in the following section. It is also near the point where the trailing edge shock wave from the adjoining rotor blade is expected to encounter the suction surface. Transitional high-speed data are not reported past this point, although no significant change in the mean heat transfer coefficient was observed. The calculated surface curvature is also shown to reach a low value a short distance from the leading edge and to remain there to the trailing edge.

Natural Transition on a Turbine Blade Surface Boundary Layer

Wide bandwidth heat transfer signals from surface thin films clearly illustrate the important difference between the low and high free-stream turbulence cases as shown in the transient recorder traces of Fig. 4. The heat transfer rate in the low turbulence case (Run 5723) remains quiet (laminar) throughout the entire measuring range of the transient data (to $x/s = 0.65$). The high free-stream turbulence case, while starting somewhat higher than the laminar case, becomes increasingly dominated by sharp transient events (consistent with turbulent spot development, amplification, and gradual merger), which raise the heat transfer coefficient instantaneously to high turbulent levels until finally the Nusselt number signals become more characterized by the steady turbulent levels. It is clearly seen at the $x/s = 0.65$ point that the flow is at the turbulent level more than half of the time, dropping precisely to the undisturbed laminar values between the

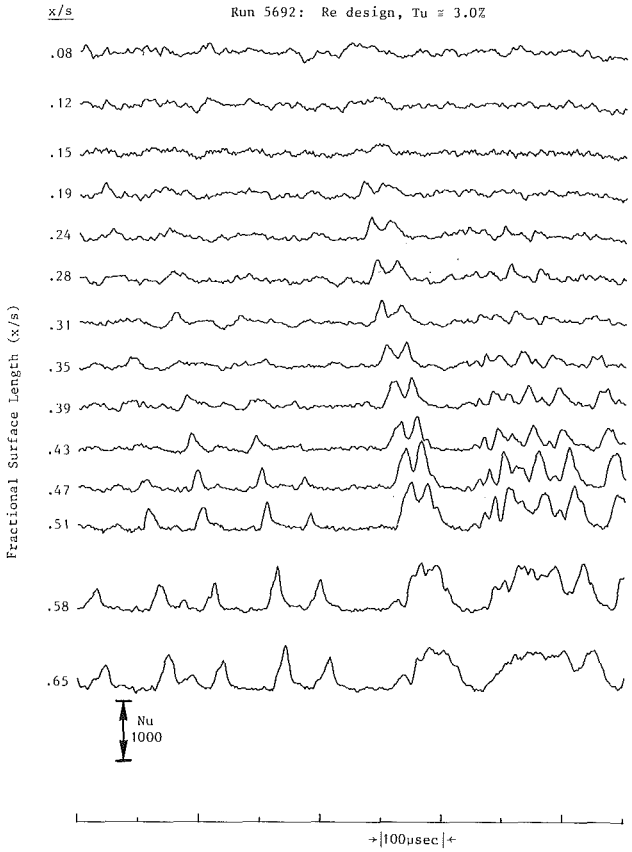

Fig. 5 Natural transition heat transfer progression along the model surface

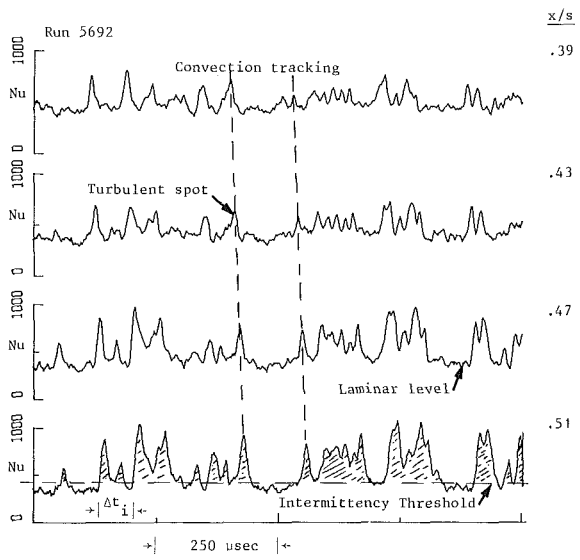

Fig. 6 Turbulent spot convection rate and intermittency calculation

turbulent events. This process starts earlier and proceeds faster for the higher Reynolds number case (not shown here).

The physical process of turbulent spot development growth and merger is dramatically illustrated in Fig. 5 in which a time synchronized overlay of each instantaneous heat transfer record is shown. In this figure the growth and rearward convection of individual turbulent spots are clearly seen as they move along the surface, again with the levels between spots dropping to the laminar values. This growth pattern suggested

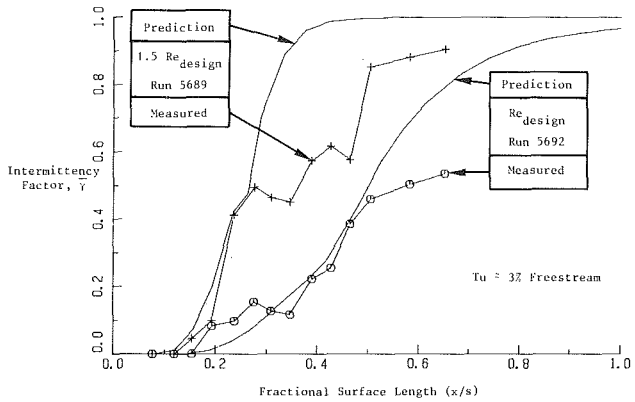

Fig. 7 Intermittency measurements and predictions for natural transition

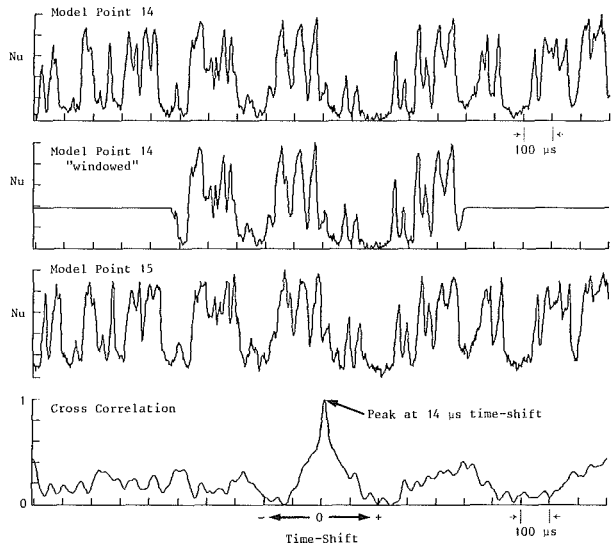

Fig. 8 Example of cross-correlation analysis of adjacent heat transfer signals in a transitional boundary layer (using a program developed by Doorly, 1983)

a procedure for the quantitative analysis of the degree of turbulent activity and the convection rates of individual spots. Figure 6 shows expanded time records of four consecutive positions. By selecting a turbulent threshold level slightly above the laminar value the amount of time that the digital signal is above this value compared to the total time of the trace can be used to define an intermittency value of the boundary layer at any x/s position as

$$\bar{\gamma} = \frac{\sum_{i=1}^{n} \Delta t_i}{t_2 - t_1}$$

between any time interval $t_2 - t_1$. Also clearly seen in Fig. 6 is the regular time delay for the turbulent spot to move from one position to the next. If one were to shift the signals closer together, adjacent heat transfer records would be seen to be nearly coincident except for a very slight but regular displacement in the direction of increasing time. Figure 7 presents the value of the intermittency calculated in this way for the two conditions of design and 1.5 x design Reynolds number each with the turbulence grid in place. The rise of the intermittency above zero and the following rapid rise is seen to follow for some time the predicted values, reaching a value near unity for

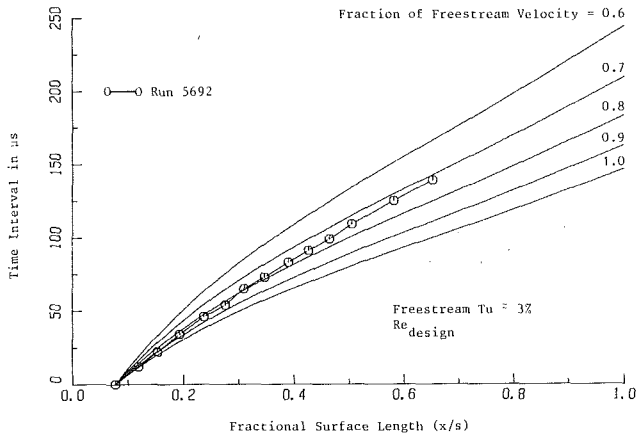

Fig. 9 Measured convection rate of turbulent spots by cross-correlation analysis compared with fractions of the local free-stream velocity

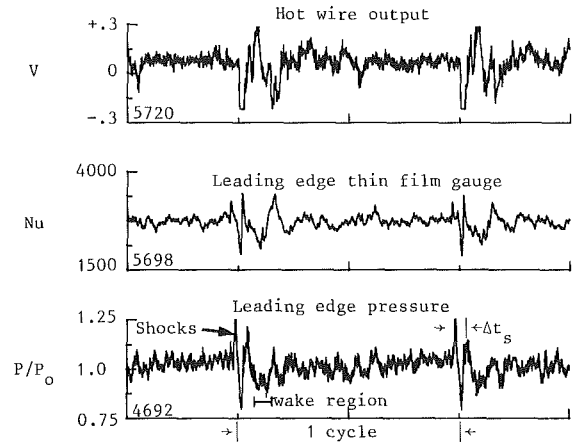

Fig. 10 Comparison of the effect of unsteady wakes and shocks on a free-stream hot-wire output with leading-edge pressure and heat transfer rate measurements

the high Reynolds number case. The prediction code is one developed from the method described in Patankar and Spalding (1970) incorporating a model for mixing in free-stream turbulence into the boundary layer, and allowances for curvature and changes in free-stream conditions during transition, outlined by Forest (1977).

The convection rate for turbulent spots was estimated by measuring time delays for individual well-defined spots and from cross-correlation analysis of adjoining thin film signals. Using a cross-correlation analysis as shown in Figure 8, two signals (each containing 1024 data points) are compared for various values of time delay and the peak value determined. Correlation coefficients of over 0.9 were found for the highly transitional traces late on the blade surface. The time delay was then used with the known film spacing to estimate a mean convection velocity of the discrete events associated with transition. These values are plotted in Fig. 9 assuming a spot origin near the location where the intermittency rises above zero. For comparison, the spot trajectories are compared with curves moving at various fraction of the blade free-stream velocities. The mean convection rates are seen to be between 0.7 and 0.8 of the local free-stream velocity, as observed in low-speed transitional boundary layers.

NGV Wake and Shock Wave Effects

The reaction of an otherwise laminar boundary layer to a higher level of isotropic free-stream turbulence has been detailed above. Clearly transition was induced by these velocity fluctuations of about 3 percent. In this section results are presented of tests at the design Reynolds number (0.92×10^6) with NGV wake and shock structures simulated by the bar-passing apparatus described in the introduction.

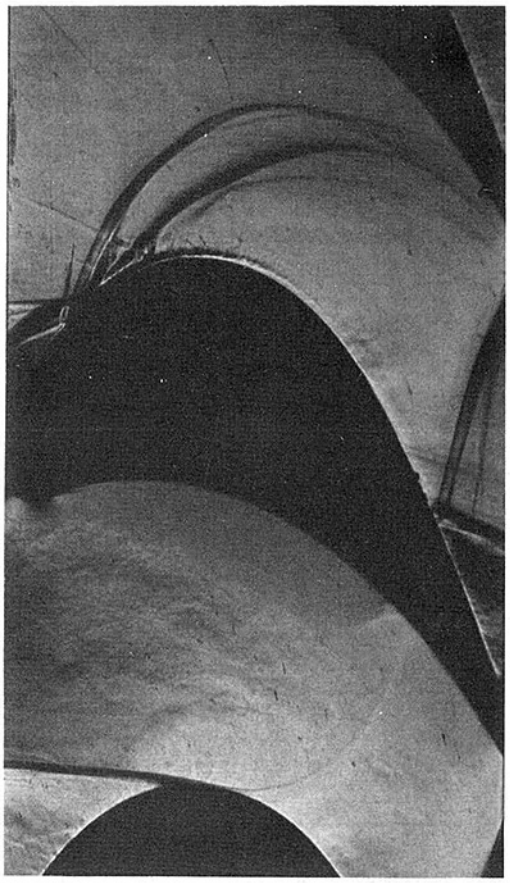

Fig. 11 Schlieren photograph showing the intersection of the moving bar shock waves with the turbine blade suction surfaces

The intermittent perturbations to the inlet flow caused by the simulation are shown in the high free-stream turbulence case in Fig. 10 in terms of hot-wire output from a probe mounted in the free-stream inlet plane at midpassage, and blade surface leading-edge measurements of pressure and heat transfer. These data are normalized with respect to two cycles of the bar-passing event, so that it is possible to relate information from different runs in terms of cycle fraction. The signals show a background turbulent level extending over about 60 percent of the cycle characterized by a similar type of signal to that obtained with no rotating bars. All three signals have a periodic component at bar-passing frequency with two characteristic parts:

(*i*) Over about 6 percent of the cycle rapid changes in level of the order of 5 to 10 μs rise and fall times are observed. The pressure signal varies by ± 25 percent and the heat transfer rate by approximately ± 50 percent. This disturbance is attributed to shock waves generated as the bar sweeps past the cascade. By examination of Schlieren photographs of this flow, an example of which is given as Fig. 11, the nature of the NGV simulated shock structure can be determined. Clearly two shocks are associated with one bar-passing event, the bow and recompression shocks that would be expected at the bar relative Mach number in steady flow. The separation time between these shocks is approximately 75 μs, marked as Δt_s in

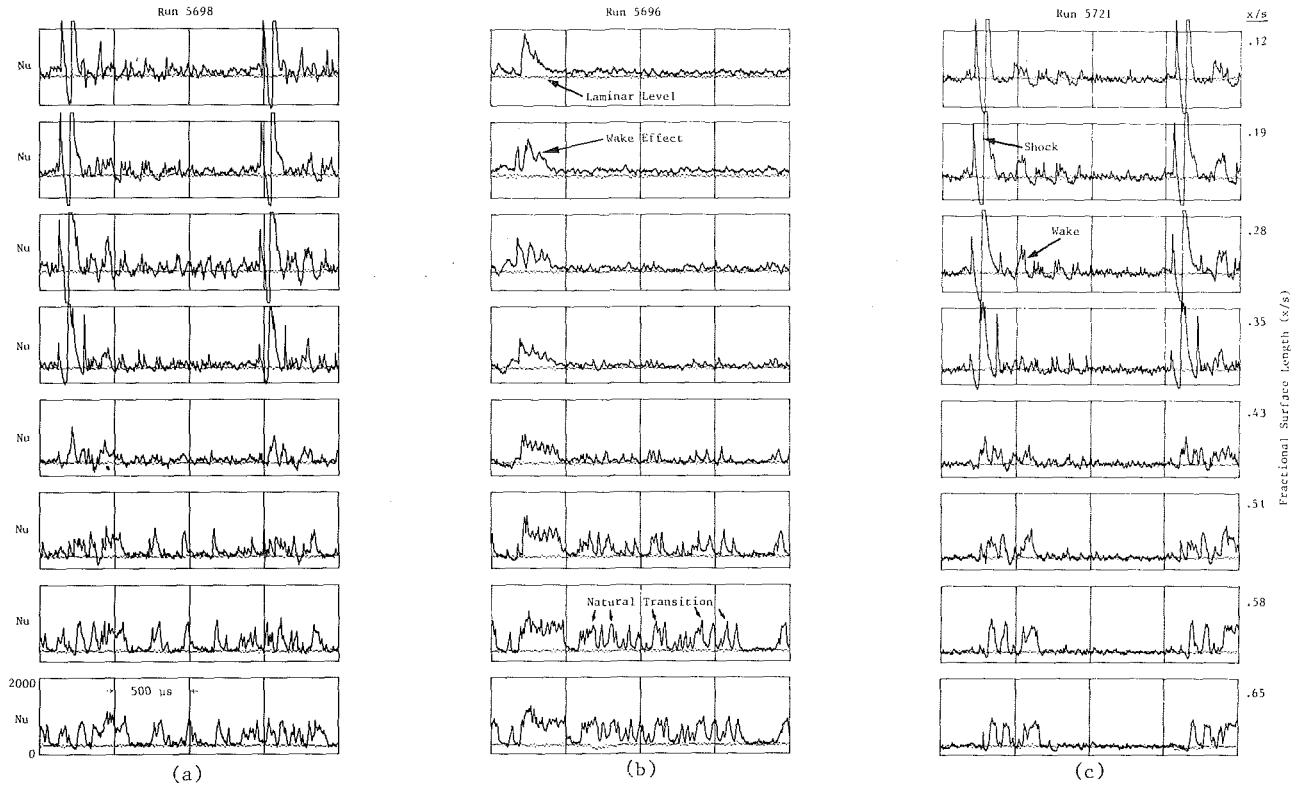

Fig. 12 Comparison of the effects of shock and wake-passing events with undisturbed laminar boundary layer heat transfer

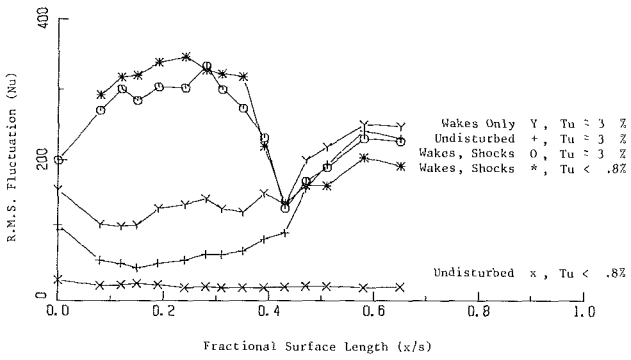

Fig. 13 Comparison of rms Nusselt number fluctuations over the blade surface for various disturbances at the design Reynolds number

Fig. 10, and is seen to correspond to the time interval between the sharp falls in level to the adjacent sharp peak.

(*ii*) Following these rapidly changing events, a second less marked change in level associated with the wake is also visible over about 10 percent of the cycle, denoted as the "wake" region in Fig. 10.

It is possible to analyze the reaction of the blade boundary layer to the wake and shock perturbations by investigation of the sequence of time-resolved Nusselt number plots given in Fig. 12. There is a constant spacing of 5 mm between the thin film gages, starting with gage 3 at an x/s value of 0.12 through to gage 15 at $x/s = 0.65$. The high free-stream turbulence case with wakes and shocks present (Fig. 12(*a*)) is markedly different from the natural transitional boundary layer over the first 35 percent of the surface, with similar rapid rises and falls in Nusselt number due to the perturbations evident in Fig. 10. This shock-related event occurs on the early suction surface due to a shock/boundary layer interaction starting at gage 9, close to the crown of the suction surface. Examination of Schlieren photographs (such as Fig. 11) indicates that the shocks first interact with the boundary layer near to gage 9, the reflection point moving toward the leading edge as the bar moves in the same direction. This is visible on the early gages on Fig. 12(*a*), occurring first on gage 9 then moving gradually through gages 7 and 5 and finally showing on gage 3. The rapid drop in surface Nusselt number is attributed to an unsteady separation and the rise to a turbulent reattachment both caused by the shock boundary layer interaction. The effect of the wake is not clearly discernable in Fig. 12(*a*) and to aid in identification of this the bars were rotated at a lower speed such that the bar relative Mach number was subsonic. The results of this are shown as Fig. 12(*b*) with a much more clearly identifiable enhancement in heat transfer due to this wake. This extends to the later gages of the surface causing the boundary layer to be fully turbulent over the extent of the wake. In Fig. 12(*c*) the background turbulence was reduced to less than 0.8 percent and the periodic disturbances due to the bar-passing events are more clearly evident. The early suction surface has shock-related phenomena extending well into the cycle period but apparent oscillations in Nusselt number moving with the shock. Also apparent from Fig. 12(*c*) is the intermittent nature of the turbulence induced in the boundary layer by the wake and shock interaction, as the boundary clearly returns to its undisturbed laminar value between the periodic events. The heat transfer enhancement due to the wake is clearly evident along the whole surface.

As an aid to quantifying the periodic effects due to wake and shock passing phenomena the rms fluctuations caused by the disturbances in the boundary layer are plotted for each gage in Fig. 13. The baseline run (marked as $\times - \times - \times$) shows a constant low rms level as would be expected, and the higher free-stream turbulent case shows a steady increase following the boundary layer intermittency factor. With just wakes present, as was shown in Fig. 12(*b*), a general enhancement of this rms value is evident over the whole surface, whereas with the shocks present the fluctuation is much enhanced on the

earlier surface but returns to undisturbed values toward the later gages. The values come close together at an x/s of 0.43 for all the bar-passing cases, indicating the extent of the shock interaction region.

Conclusions

It has been established during the course of this study that the Isentropic Light Piston Tunnel facility combined with the wide bandwidth/high sampling rate heat transfer instrumentation has proved capable of tracking very rapidly progressing unsteady events in a transonic boundary layer. Operating under a simulated unsteady gas turbine rotor environment, sensitive detection and precision tracking of transient shock, wake, and boundary layer transitional events was accomplished. Detailed observation of the heat transfer signals confirmed a classical model of the transition process, that is the sudden appearance of sharp spikes of turbulence which multiply, grow, and track downstream at a rate less than the free-stream velocity until gradually merging to form a completely turbulent boundary layer. The tracking of turbulent spots at these high-temperature transonic flow conditions has not been reported before to the best of the authors' knowledge.

A second major finding of this study was the observation that the strong unsteady interaction of a double shock and a simulated NGV wake with the rotor boundary layer did not have any measurable "long term" effects apart from the strong excursion in heat transfer associated with the actual passing of the shocks and wake. The heat transfer fluctuation levels were essentially unchanged far removed from the disturbance (in time) and nearly identical at the rearmost measuring point except for a turbulent patch associated with the shock/wake event itself.

The interaction of the shocks and wake with the rotor establishes in more detail the earlier observation of Ashworth et al. (1985) and Doorly and Oldfield (1985a) of strong changes in local heat transfer coefficient. The tracking of the interaction over the surface could be followed with some precision with the time resolution of the instrumentation used. Further analysis of shock and wake interactions is reported by the authors in Schultz et al. (1986) along with some prediction models of the interaction dynamics.

Acknowledgments

The authors wish to acknowledge the invaluable contributions to this paper made by M. L. G. Oldfield during many discussions throughout the course of the work. We would also like to thank M. J. Rigby and A. B. Johnson for their help in collecting some of the data. Professor LaGraff would also like to acknowledge the financial support for the research given by the US Air Force Office of Scientific Research under grant number 85-0295, Dr. James Wilson, Program Manager. Appreciation is also extended to the Division of International Programs of the National Science Foundation for providing a travel grant (INT-8509407) to facilitate the collaborative research program.

References

Ashworth, D. A., LaGraff, J. E., Schultz, D. L., and Grindrod, K. J., 1985, "Unsteady Aerodynamics and Heat Transfer Processes in a Transonic Turbine Stage," ASME *Journal of Engineering for Gas Turbines and Power*, Vol. 107, pp. 1022–1030.

Blair, M. F., 1982, "Influence of Free-Stream Turbulence on Boundary Layer in Favorable Pressure Gradients," ASME *Journal of Engineering for Power*, Vol. 104, No. 4, pp. 743–750.

Doorly, D. J., 1983, "A Study of the Effect of Wake Passing on Turbine Blades," D.Phil. Thesis, University of Oxford, United Kingdom.

Doorly, D. J., and Oldfield, M. L. G., 1985a, "Simulation of the Effects of Shock Wave Passing on a Turbine Rotor Blade," ASME *Journal of Engineering for Gas Turbines and Power*, Vol. 107, No. 4, pp. 998–1006.

Doorly, D. J., and Oldfield, M. L. G., 1985b, "Simulation of Wake Passing in a Stationary Turbine Rotor Cascade," *J. Propulsion and Power*, Vol. 1, No. 4, pp. 316–318.

Dunn, M. G., 1985, "Turbine Heat Flux Measurements: Influence of Slot Injection on Vane Trailing Edge Heat Transfer and Influence of Rotor on Vane Heat Transfer," ASME *Journal of Engineering for Gas Turbines and Power*, Vol. 107, No. 1, pp. 76–83.

Forest, A., 1977, "Engineering Predictions of Transitional Boundary Layers," *AGARD Conference Proceedings, Laminar-Turbulent Transition*, CP-224, Paper No. 22.

Lowery, G. W., and Vachon, R. I., 1975, "The Effect of Turbulence on Heat Transfer From Heated Cylinders," *Int. J. of Heat Mass Transfer*, Vol. 18, pp. 1229–1242.

Oldfield, M. L. G., Jones, T. V., and Schultz, D. L., 1978, "On-Line Computer for Transient Turbine Cascade Analysis," *IEEE Transactions on Aerospace and Electronic Systems*, Vol. AES-14, No. 5, pp. 738–748.

Oldfield, M. L. G., Burd, H. J., and Doe, H. G., 1984, "Design of Wide Bandwidth Analogue Circuits for Heat Transfer Instrumentation in Transient Tunnels," *Papers from the 16th ICHMT Symposium on Heat and Mass Transfer*, Dubrovnik, pp. 233–258.

Patankar, S. U., and Spalding, D. B., 1970, *Heat and Mass Transfer in Boundary Layers*, 2nd ed., Intertext Book, London.

Rued, K., and Wittig, S., 1985, "Free-Stream Turbulence and Pressure Gradient Effects on Heat Transfer and Boundary Layer Development on Highly Cooled Surfaces," ASME *Journal of Engineering for Gas Turbines and Power*, Vol. 107, pp. 54–59.

Schubauer, G. B., and Klebanoff, P. S., 1956, "Contributions on the Mechanics of Boundary Layer Transition," NACA Report 1289.

Schultz, D. L., and Jones, T. V., 1973, "Heat Transfer Measurements in Short Duration Hypersonic Facilities," AGARDograph No. 165.

Schultz, D. L., Jones, T. V., Oldfield, M. L. G., and Daniels, L. C., 1977, "A New Transient Cascade Facility for the Measurement of Heat Transfer Rates," AGARD Conference Proceedings, *High Temperature Problems in Gas Turbine Engines*, CP-229, Paper No. 31.

Schultz, D. L., Ashworth, D. A., LaGraff, J. E., Johnson, A. B., and Rigby, M. J., 1986, "Wake and Shock Interactions in a Transonic Turbine Stage," AGARD 68th(B) Specialists' Meeting, *Transonic and Supersonic Phenomena in Turbomachines*, Paper No. 3, Neubiberg, Federal Republic of Germany.

earlier surface but returns to undisturbed values toward the later gages. The values come close together at an x/s of 0.43 for all the bar-passing cases, indicating the extent of the shock interaction region.

Conclusions

It has been established during the course of this study that the Isentropic Light Piston Tunnel facility combined with the wide bandwidth/high sampling rate heat transfer instrumentation has proved capable of tracking very rapidly progressing unsteady events in a transonic boundary layer. Operating under a simulated unsteady gas turbine rotor environment, sensitive detection and precision tracking of transient shock, wake, and boundary layer transitional events was accomplished. Detailed observation of the heat transfer signals confirmed a classical model of the transition process, that is the sudden appearance of sharp spikes of turbulence which multiply, grow, and track downstream at a rate less than the free-stream velocity until gradually merging to form a completely turbulent boundary layer. The tracking of turbulent spots at these high-temperature transonic flow conditions has not been reported before to the best of the authors' knowledge.

A second major finding of this study was the observation that the strong unsteady interaction of a double shock and a simulated NGV wake with the rotor boundary layer did not have any measurable "long term" effects apart from the strong excursion in heat transfer associated with the actual passing of the shocks and wake. The heat transfer fluctuation levels were essentially unchanged far removed from the disturbance (in time) and nearly identical at the rearmost measuring point except for a turbulent patch associated with the shock/wake event itself.

The interaction of the shocks and wake with the rotor establishes in more detail the earlier observation of Ashworth et al. (1985) and Doorly and Oldfield (1985a) of strong changes in local heat transfer coefficient. The tracking of the interaction over the surface could be followed with some precision with the time resolution of the instrumentation used. Further analysis of shock and wake interactions is reported by the authors in Schultz et al. (1986) along with some prediction models of the interaction dynamics.

Acknowledgments

The authors wish to acknowledge the invaluable contributions to this paper made by M. L. G. Oldfield during many discussions throughout the course of the work. We would also like to thank M. J. Rigby and A. B. Johnson for their help in collecting some of the data. Professor LaGraff would also like to acknowledge the financial support for the research given by the US Air Force Office of Scientific Research under grant number 85-0295, Dr. James Wilson, Program Manager. Appreciation is also extended to the Division of International Programs of the National Science Foundation for providing a travel grant (INT-8509407) to facilitate the collaborative research program.

References

Ashworth, D. A., LaGraff, J. E., Schultz, D. L., and Grindrod, K. J., 1985, "Unsteady Aerodynamics and Heat Transfer Processes in a Transonic Turbine Stage," ASME *Journal of Engineering for Gas Turbines and Power*, Vol. 107, pp. 1022–1030.

Blair, M. F., 1982, "Influence of Free-Stream Turbulence on Boundary Layer in Favorable Pressure Gradients," ASME *Journal of Engineering for Power*, Vol. 104, No. 4, pp. 743–750.

Doorly, D. J., 1983, "A Study of the Effect of Wake Passing on Turbine Blades," D.Phil. Thesis, University of Oxford, United Kingdom.

Doorly, D. J., and Oldfield, M. L. G., 1985a, "Simulation of the Effects of Shock Wave Passing on a Turbine Rotor Blade," ASME *Journal of Engineering for Gas Turbines and Power*, Vol. 107, No. 4, pp. 998–1006.

Doorly, D. J., and Oldfield, M. L. G., 1985b, "Simulation of Wake Passing in a Stationary Turbine Rotor Cascade," *J. Propulsion and Power*, Vol. 1, No. 4, pp. 316–318.

Dunn, M. G., 1985, "Turbine Heat Flux Measurements: Influence of Slot Injection on Vane Trailing Edge Heat Transfer and Influence of Rotor on Vane Heat Transfer," ASME *Journal of Engineering for Gas Turbines and Power*, Vol. 107, No. 1, pp. 76–83.

Forest, A., 1977, "Engineering Predictions of Transitional Boundary Layers," *AGARD Conference Proceedings, Laminar-Turbulent Transition*, CP-224, Paper No. 22.

Lowery, G. W., and Vachon, R. I., 1975, "The Effect of Turbulence on Heat Transfer From Heated Cylinders," *Int. J. of Heat Mass Transfer*, Vol. 18, pp. 1229–1242.

Oldfield, M. L. G., Jones, T. V., and Schultz, D. L., 1978, "On-Line Computer for Transient Turbine Cascade Analysis," *IEEE Transactions on Aerospace and Electronic Systems*, Vol. AES-14, No. 5, pp. 738–748.

Oldfield, M. L. G., Burd, H. J., and Doe, H. G., 1984, "Design of Wide Bandwidth Analogue Circuits for Heat Transfer Instrumentation in Transient Tunnels," *Papers from the 16th ICHMT Symposium on Heat and Mass Transfer*, Dubrovnik, pp. 233–258.

Patankar, S. U., and Spalding, D. B., 1970, *Heat and Mass Transfer in Boundary Layers*, 2nd ed., Intertext Book, London.

Rued, K., and Wittig, S., 1985, "Free-Stream Turbulence and Pressure Gradient Effects on Heat Transfer and Boundary Layer Development on Highly Cooled Surfaces," ASME *Journal of Engineering for Gas Turbines and Power*, Vol. 107, pp. 54–59.

Schubauer, G. B., and Klebanoff, P. S., 1956, "Contributions on the Mechanics of Boundary Layer Transition," NACA Report 1289.

Schultz, D. L., and Jones, T. V., 1973, "Heat Transfer Measurements in Short Duration Hypersonic Facilities," AGARDograph No. 165.

Schultz, D. L., Jones, T. V., Oldfield, M. L. G., and Daniels, L. C., 1977, "A New Transient Cascade Facility for the Measurement of Heat Transfer Rates," AGARD Conference Proceedings, *High Temperature Problems in Gas Turbine Engines*, CP-229, Paper No. 31.

Schultz, D. L., Ashworth, D. A., LaGraff, J. E., Johnson, A. B., and Rigby, M. J., 1986, "Wake and Shock Interactions in a Transonic Turbine Stage," AGARD 68th(B) Specialists' Meeting, *Transonic and Supersonic Phenomena in Turbomachines*, Paper No. 3, Neubiberg, Federal Republic of Germany.

DISCUSSION

M. L. G. Oldfield[1]

In their paper, Ashworth et al. note the presence, in Fig. 12, of rapid drops in surface Nusselt number, sometimes becoming negative, associated with shock waves passing over the blade surface. They suggest that this is possibly due to a shock-induced unsteady separation and consequent turbulent re-attachment.

More recent work (Johnson et al., 1989) using the same tunnel and blade profile has shown that the rapid compression heating and expansion cooling of the boundary layer by the bar shock waves and expansion fans can cause the observed transient heat transfer peaks and troughs without there necessarily being a separation bubble, although the latter may also occur.

It should be noted that there is an expansion fan generated in front of the trailing edge shock wave of a transonic nozzle guide vane, and so the observed transient troughs are relevant to the full turbine stage.

[1]University of Oxford, United Kingdom.

References

Johnson, A. B., Rigby, M. J., Oldfield, M. L. G., Ainsworth, R. W., and Oliver, M. J., 1989, "Surface Heat Transfer Fluctuations on a Turbine Rotor Blade Due to Upstream Shock Wave Passing," ASME JOURNAL OF TURBOMACHINERY, Vol. 111, this issue, pp. 105–115.

Numerical Simulation of Inviscid Transonic Flow Through Nozzles With Fluctuating Back Pressure

A. Bölcs

T. H. Fransson

Swiss Federal Institute of Technology, Lausanne, Switzerland

M. F. Platzer

Naval Postgraduate School, Monterey, CA 93940

The study presents a numerical method, based on the flux vector splitting approach, to the problem of unsteady one-dimensional and two-dimensional inviscid transonic flows, with emphasis on the numerical determination of the shock position, through nozzles with time-varying back pressure. The model is first validated by comparison with exact (one dimension) and numerical (two dimensions) steady-state solutions. It is thereafter applied to the problem of time-fluctuating back pressure in quasi-one-dimensional and two-dimensional nozzles. The one-dimensional results are validated by comparison with a small perturbation analytical unsteady solution, whereafter a few sample cases are presented with the objective of understanding fundamental aspects of unsteady transonic flows. It is concluded that both the amplitude and frequency of the imposed fluctuating exit pressure are important parameters for the location of the unsteady shock. It is also shown that the average unsteady shock position is not necessarily identical with the steady-state position, and that the unsteady shock may, under certain circumstances, propagate upstream into the subsonic flow domain. The pressure jump over the shock, as well as the unsteady post-shock pressure, is different for identical shock positions during the cycle of fluctuation, which implies that an unsteady shock movement, imposed by oscillating back pressure, may introduce a significant unsteady lift and moment. This may be of importance for flutter predictions. It is also noted that, although the sonic velocity is obtained in the throat of steady-state, quasi-one-dimensional flow, this is not necessarily true for the unsteady solution. During part of the period with fluctuating back pressure, the flow velocity may be subsonic at the throat and still reach a supersonic value later in the nozzle. This phenomenon depends on the frequency and amplitude of the imposed fluctuation, as well as on the nozzle geometry.

Introduction

Unsteady flow is an inherent factor in turbomachines and may have several sources. It can occur because of disturbances from an otherwise uniform inlet or outlet flow (for example due to upstream/downstream blade rows), as self-excited flow phenomena (for example blade flutter), flow separations, fluctuating shock waves, or as pressure fluctuations downstream of, for example, a diffusor.

Many experimental and theoretical investigations have been carried out for the phenomenon of flow unsteadiness introduced by vibrating blades (see for example Bölcs et al., 1987a, 1986, 1987b; Buffum and Fleeter, 1987; Cafarelli and Szechenyi, 1987; Fleeter, 1977; Fransson and Pandolfi, 1986; Gallus, 1984; Gerolymos et al., 1987; Grant and Whitehead, 1980; Joubert, 1984; Pandolfi, 1980; Platzer, 1982; Servaty et al., 1987; Smith, 1972; Szechenyi, 1984; Usab and Verdon, 1986; Verdon, 1977). These investigations show that several physical parameters, such as the flow velocity, blade geometry, reduced frequency, and interblade phase angles play a significant role for the aeroelastic behavior of a blade row. Presently, the most information is available for two-dimensional attached flow, and separated flow phenomena are treated empirically or semi-empirically (Bölcs and Fransson, 1986, 1987a).

Most models for prediction of the two-dimensional attached flow are based on the assumption of small harmonic perturbations of the flow around an otherwise steady-state flow. The most common methods are the linearized sub- or supersonic flat plate theories (for example, Smith, 1972; Verdon, 1977; Namba, 1987; Salaün, 1976). These models have been shown to give good agreement with experimental data, as long as the blade thickness and camber are moderate (Bölcs and Fransson, 1987a). However, they tend to disagree with experimental results for the flow velocities in the neighborhood of the transonic flow regime as well as for the blades with larger thickness and/or camber. In some cases, as long as the flow is shock-free, linearized potential models (for example, Grant and Whitehead, 1980; Verdon, 1977; Usab and Verdon, 1986) can predict experimental results to a high accuracy (Bölcs and Fransson, 1986). Recent results with a linearized

Contributed by the International Gas Turbine Institute and presented at the 33rd International Gas Turbine and Aeroengine Congress and Exhibition, Amsterdam, The Netherlands, June 5–9, 1988. Manuscript received by the International Gas Turbine Institute January 19, 1988. Paper No. 88-GT-287.

potential model, with an explicit unsteady shock-fitting, indicate that the fluctuating shock may have a significant influence on the unsteady response and may, in fact, destabilize an otherwise aerodynamically damped blade row Verdon, 1987.

Cascade experiments in the transonic flow region, under certain circumstances, are known to show relatively large shock fluctuations for small blade amplitudes (see, for example, Bölcs and Schläfli, 1987b), which then brings up the question of when nonlinear effects, especially the shock amplitudes, become so large as to reduce the accuracy of potential small disturbance theories, first of all those with numerically smeared shock waves (for example, Grant and Whitehead, 1980; Newton and Whitehead, 1985) but also the ones with explicit unsteady shock fitting (Verdon, 1987; Usab and Verdon, 1986).

To this end, some recent research has been directed toward the solution of the fully unsteady nonlinear Euler equations in two-dimensional cascades (Gallus et al., 1984; Servaty et al, 1987; Joubert, 1984; Gerolymos et al., 1987; Pandolfi, 1980). These models have been shown to correlate well with the experimental data (Gallus et al., 1984) and with flat plate results (Fransson and Pandolfi, 1986) in the subsonic flow region, but special care has to be taken to reproduce a fluctuating shock wave accurately in order to predict the unsteady lift and moment on the blades.

In the present study, a step toward this problem is shown. The inviscid rotational flow through nozzles is considered. The steady-state transonic shock wave is numerically captured, usually within two cells, whereafter the outlet pressure is imposed to fluctuate (the physical analogy to this can be considered to be, for example, a diffusor with oscillating back pressure). The shock will then move away from its steady-state position and may (in dependence on parameters such as nozzle geometry, pressure amplitude, and frequency) create a flow field different from the steady-state prediction.

Governing Equations and Numerical Method of Solution

Governing Equations. The rotational inviscid unsteady two-dimensional flow (without mass forces, heat transfer, and exchange of energy), considering a perfect gas, can be described in differential, conservative form by the continuity, momentum, and energy equations (see, for example, Zierep, 1976) in the vector form

$$\mathbf{W}_t + \mathbf{F}_x + \mathbf{G}_y = 0 \tag{1}$$

Here, the vectors can be expressed as:

$$\mathbf{W} = \begin{pmatrix} \rho \\ \rho u \\ \rho v \\ \rho e_c \end{pmatrix}; \mathbf{F} = \begin{pmatrix} \rho u \\ \rho u^2 + p \\ \rho uv \\ \rho u h_c \end{pmatrix}; \mathbf{G} = \begin{pmatrix} \rho v \\ \rho uv \\ \rho v^2 + p \\ \rho v h_c \end{pmatrix} \tag{2}$$

and the equation of state of a perfect gas is used for the relation between pressure, density, and temperature

$$\frac{p}{\rho} = RT \tag{3}$$

If all the physical quantities above are made dimensionless with reference values p_{ref}, $x_{\text{ref}} = y_{\text{ref}}$, T_{ref} (and $\rho_{\text{ref}} = p_{\text{ref}} / \{RT_{\text{ref}}\}$, $q_{\text{ref}} = \{RT_{\text{ref}}\}^{0.5}$, $t_{\text{ref}} = x_{\text{ref}}/q_{\text{ref}}$, $e_{\text{ref}} = h_{\text{ref}} = q^2_{\text{ref}}$) the equation system (2) stays the same in dimensionless form.[1] From here on the physical variables are thus dimensionless, unless otherwise stated.

The equation system (1) can be mapped from the physical plane of reference (x, y, t) into a computational plane of reference (ξ, η, τ) with a general transformation:

[1] Note that q_{ref} = velocity of sound/$\sqrt{\gamma}$.

Nomenclature

a = velocity of sound, m/s
A = area, m^2
D = Jacobian determinant
e = internal energy/unit mass, m^2/s^2
e_c = total energy/unit mass $= e + q^2/2 = p[(\gamma-1)/\rho] + q^2/2$, m^2/s
f = frequency, Hz
f = variable, representing any of the physical variables in nondimensional form
$\mathbf{F}$ = flux vector (equation (2))
$\mathbf{G}$ = flux vector (equation (2))
h_c = total enthalpy/unit mass $= e_c + p/\rho$, m^2/s^2
k = reduced frequency based on half chord = $\omega \cdot l_{\text{ref}}/(2q_{\text{ref}})$
l = length, m
M = Mach number
p = pressure, N/m^2
q = velocity vector, m/s
R = gas constant ($\approx$287 for air), m^2/s^{2}K
R^+ = right running Riemann invariant
R^- = left running Riemann invariant
t = time, s
T = temperature, K
u = velocity component in x direction, m/s
v = velocity component in y direction, m/s
$\mathbf{W}$ = flow variable vector (equation (2))
x = coordinate direction, m
y = coordinate direction, m
γ = ratio of specific heats
$\Delta\tau$ = time step
ϵ = small perturbation parameter, equation (34)
η = coordinate direction
λ = eigenvalues
ξ = coordinate direction
ρ = density, kg/m^3
τ = time
ω = circular frequency $= 2\pi f$, rad/s

Subscripts and Superscripts

c = stagnation values
e = values at exit of computational domain
e, amp = amplitude of imposed exit pressure variation
i = computational point in ξ direction
j = computational point in η direction
k = time step
l = length
o = start of oscillation
ref = reference values
s = number of shock
t = thickness
$()_t$ = partial derivatives in time
w = width
x = in x direction
y = in y direction
$()_x$ = partial derivatives in x direction
$()_y$ = partial derivatives in y direction
$-\infty$ = values at infinity upstream
∞ = values at infinity downstream
η = in η direction
ξ = in ξ direction

$$\xi = \xi(x, y, t)$$
$$\eta = \eta(x, y, t) \quad (4)$$
$$\tau = t$$

These equations written in generalized coordinates are solved with a finite difference formulation.

Numerical Grid. For the present application, the numerical grid is chosen such that the grid lines in the y direc

ERRATA

Errata for "Numerical Simulation of Inviscid Transonic Flow Through Nozzles With Fluctuating Back Pressure" by A. Bölcs, T. H. Fransson, and M. F. Platzer, published in the April 1989 issue of the ASME JOURNAL OF TURBOMACHINERY, Vol. 111, pp. 169–180:

Please note the corrected form of the following equations:

Error

$$\mathbf{W}' = D^{-1}\mathbf{W}$$
$$\mathbf{F}' = D^{-1}\{\xi_t\mathbf{W} + \xi_x\mathbf{F} + \xi_y\mathbf{G}\} \quad (6)$$
$$\mathbf{G}' = D^{-1}\{\eta_t\mathbf{W} + \eta_x\mathbf{F} + \eta y\mathbf{G}\}$$
$$D = \xi_x\eta_y - \xi_y\eta_x = 1/\{x_\xi y_\eta - x_\eta y_\xi\}$$

$$\mathbf{F}' = D^{-1}\begin{pmatrix} \xi_x\rho u + \xi_y\rho v \\ \xi_x\{\rho u^2 + p\} + \xi_y\rho uv \\ \xi_x\rho uv + \xi_y\{\rho v^2 + p\} \\ \xi_x\rho u\{e_c + p/\rho\} + \xi_y\rho v\{e_c + p/\rho\} \end{pmatrix}$$

$$= \begin{pmatrix} y_\eta\rho u + x_\eta\rho v \\ y_\eta\{\rho u^2 + p\} - x_\eta\rho uv \\ y_\eta\rho uv - x_\eta\{\rho v^2 + p\} \\ y_\eta\rho u\{e_c + p/\rho\} + x_\eta\rho v\{e_c + p/\rho\} \end{pmatrix} \quad (8b)$$

$$c_1^\xi = \frac{\xi_x}{\sqrt{\xi_x^2 + \xi_y^2}} = \frac{y_\eta}{\sqrt{y_\eta^2 + x_\eta^2}}$$
$$c_2^\xi = \frac{\xi_y}{\sqrt{\xi_x^2 + \xi_y^2}} = -\frac{x_\eta}{\sqrt{y_\eta^2 + x_\eta^2}} \quad (22)$$
$$c_1^\eta = \frac{\eta_y}{\sqrt{\eta_x^2 + \eta_y^2}} = \frac{x_\xi}{\sqrt{x_\xi^2 + y_\xi^2}}$$
$$c_1^\eta = \frac{\eta_x}{\sqrt{\eta_x^2 + \eta_y^2}} = -\frac{y_\xi}{\sqrt{x_\xi^2 + y_\xi^2}}$$

$$R^+ = f(\text{upstream infinity}) = \text{imposed} = \frac{2}{\gamma - 1}a_{-\infty} + q_{-\infty} \quad (29)$$

$$u_{\text{inlet}} = \frac{R^+ - R^-}{2}$$
$$a_{\text{inlet}} = \left\{\frac{R^+ - R^-}{2}\right\} \cdot \left\{\frac{\gamma - 1}{2}\right\} \quad (30)$$

Correction

$$\mathbf{W}' = D^{-1}\mathbf{W}$$
$$\mathbf{F}' = D^{-1}\{\xi_t\mathbf{W} + \xi_x\mathbf{F} + \xi_y\mathbf{G}\} \quad (6)$$
$$\mathbf{G}' = D^{-1}\{\eta_t\mathbf{W} + \eta_x\mathbf{F} + \eta_y\mathbf{G}\}$$
$$D = \xi_x\eta_y - \xi_y\eta_x = 1/\{x_\xi y_\eta - x_\eta y_\xi\}$$

$$\mathbf{F}' = D^{-1}\begin{pmatrix} \xi_x\rho u + \xi_y\rho v \\ \xi_x\{\rho u^2 + p\} + \xi_y\rho uv \\ \xi_x\rho uv + \xi_y\{\rho v^2 + p\} \\ \xi_x\rho u\{e_c + p/\rho\} + \xi_y\rho v\{e_c + p/\rho\} \end{pmatrix}$$

$$= \begin{pmatrix} y_\eta\rho u + x_\eta\rho v \\ y_\eta\{\rho u^2 + p\} - x_\eta\rho uv \\ y_\eta\rho uv - x_\eta\{\rho v^2 + p\} \\ y_\eta\rho u\{e_c + p/\rho\} - x_\eta\rho v\{e_c + p/\rho\} \end{pmatrix} \quad (8b)$$

$$c_1^\xi = \frac{\xi_x}{\sqrt{\xi_x^2 + \xi_y^2}} = \frac{y_\eta}{\sqrt{y_\eta^2 + x_\eta^2}}$$
$$c_2^\xi = \frac{\xi_y}{\sqrt{\xi_x^2 + \xi_y^2}} = -\frac{x_\eta}{\sqrt{y_\eta^2 + x_\eta^2}} \quad (22)$$
$$c_1^\eta = \frac{\eta_y}{\sqrt{\eta_x^2 + \eta_y^2}} = \frac{x_\xi}{\sqrt{x_\xi^2 + y_\xi^2}}$$
$$c_2^\eta = \frac{\eta_x}{\sqrt{\eta_x^2 + \eta_y^2}} = -\frac{y_\xi}{\sqrt{x_\xi^2 + x_\xi^2}}$$

$$R^+ = f(\text{upstream infinity}) = \text{imposed} = \frac{2}{\gamma - 1}a_{-\infty} + q_{-\infty} \quad (29)$$

$$u_{\text{inlet}} = \frac{R^+ - R^-}{2}$$
$$a_{\text{inlet}} = \left\{\frac{R^+ + R^-}{2}\right\} \cdot \left\{\frac{\gamma - 1}{2}\right\} \quad (30)$$

$$\mathbf{F}^\pm = \frac{\rho}{2\gamma}\begin{pmatrix} 2(\gamma-1)\lambda_1^x\lambda_1^{x\pm} & +\lambda_3^x\lambda_3^{x\pm} & +\lambda_4^x\lambda_4^{x\pm} \\ 2(\gamma-1)v\lambda_1^{x\pm} & +v\lambda_3^{x\pm} & +v\lambda_4^{x\pm} \\ (\gamma-1)q^2\lambda_1^{x\pm} & +\left[\frac{\lambda_3^{x2} + v^2}{2}\right]\lambda_3^{x\pm} & +\left[\frac{\lambda_4^{x2} + v^2}{2}\right]\lambda_4^{x\pm} + w^{x\pm} \end{pmatrix} \quad (13)$$

$$\xi = \xi(x, y, t)$$
$$\eta = \eta(x, y, t) \tag{4}$$
$$\tau = t$$

Viviand (1974) has shown that equation (1) can stay in strong conservative form with a transformation of the above type. Equation (1) is then mapped into

$$\mathbf{W}'_\tau + \mathbf{F}'_\xi + \mathbf{G}'_\eta = 0 \tag{5}$$

with

$$\begin{aligned} \mathbf{W}' &= D^{-1}\mathbf{W} \\ \mathbf{F}' &= D^{-1}\{\xi_t \mathbf{W} + \xi_x \mathbf{F} + \xi_y \mathbf{G}\} \\ \mathbf{G}' &= D^{-1}\{\eta_t \mathbf{W} + \eta_x \mathbf{F} + \eta y \mathbf{G}\} \\ D &= \xi_x \eta_y - \xi_y \eta_x = 1/\{x_\xi y_\eta - x_\eta y_\xi\} \end{aligned} \tag{6}$$

where D is the Jacobian determinant of the transformation (4) and the metric terms are related to the derivatives of x, y, and t by (see, for example, Pulliam, 1986, equation (4)):

$$\begin{cases} \xi_x &= y_\eta D \\ \xi_y &= -x_\eta D \\ \xi_t &= -x_\tau \xi_x - y_\tau \xi_y \end{cases} \tag{7a}$$

$$\begin{cases} \eta_x &= -y_\xi D \\ \eta_y &= x_\xi D \\ \eta_t &= -x_\tau \eta_x - y_\tau \eta_y \end{cases} \tag{7b}$$

The Jacobian determinant, in the center of an element, corresponds physically to the inverse of the cell area (Anderson et al., 1985).

In the present study, the interest is focused on unsteady flow phenomena in channels of nonvarying sections in time. The terms ξ_t and η_t are thus zero, wherefore the vectors $\mathbf{W}'$, $\mathbf{F}'$, and $\mathbf{G}'$ can be expressed, in component form, as

$$\mathbf{W}' = D^{-1} \begin{pmatrix} \rho \\ \rho u \\ \rho v \\ \rho e_c \end{pmatrix} \tag{8a}$$

$$\begin{aligned} \mathbf{F}' &= D^{-1} \begin{pmatrix} \xi_x \rho u + \xi_y \rho v \\ \xi_x\{\rho u^2 + p\} + \xi_y \rho u v \\ \xi_x \rho u v + \xi_y\{\rho v^2 + p\} \\ \xi_x \rho u\{e_c + p/\rho\} + \xi_y \rho v\{e_c + p/\rho\} \end{pmatrix} \\ &= \begin{pmatrix} y_\eta \rho u + x_\eta \rho v \\ y_\eta\{\rho u^2 + p\} - x_\eta \rho u v \\ y_\eta \rho u v - x_\eta\{\rho v^2 + p\} \\ y_\eta \rho u\{e_c + p/\rho\} + x_\eta \rho v\{e_c + p/\rho\} \end{pmatrix} \end{aligned} \tag{8b}$$

$$\begin{aligned} \mathbf{G}' &= D^{-1} \begin{pmatrix} \eta_x \rho u + \eta_y \rho v \\ \eta_x\{\rho u^2 + p\} + \eta_y \rho u v \\ \eta_x \rho u v + \eta_y\{\rho v^2 + p\} \\ \eta_x \rho u\{e_c + p/\rho\} + \eta_y \rho v\{e_c + p/\rho\} \end{pmatrix} \\ &= \begin{pmatrix} -y_\xi \rho u + x_\xi \rho v \\ -y_\xi\{\rho u^2 + p\} + x_\xi \rho u v \\ -y_\xi \rho u v + x_\xi\{\rho v^2 + p\} \\ -y_\xi \rho u\{e_c + p/\rho\} + x_\xi \rho v\{e_c + p/\rho\} \end{pmatrix} \end{aligned} \tag{8c}$$

These equations written in generalized coordinates are solved with a finite difference formulation.

Numerical Grid. For the present application, the numerical grid is chosen such that the grid lines in the y direction (= lines of constant η) are situated half a mesh away from the nozzle walls, i.e., the cell center of the numerical grid coincides with the wall.

Numerical Formulation. As the aim of the study is to investigate large-amplitude unsteady shock waves and their influence on the unsteady loading, it is necessary to consider a method that results in fairly sharp definitions of aerodynamic shocks.

See Errata Sheet

In such a case a shock-fitting algorithm would obviously be ideal but cumbersome, especially for turbine flows with merging or crossing shocks. It was thus decided to rely on a shock-capturing algorithm, based on upwinding differences. This is realized with the flux vector splitting technique (Anderson et al., 1985; Steger and Warming, 1981; van Leer, 1982). In this technique the fluxes $\mathbf{F}'$ and $\mathbf{G}'$ from equation (8) above are split into forward and backward contributions according to the sign of the local (one-dimensional) eigenvalues. From the various splittings found in the literature (for example, Anderson et al., 1985; Steger and Warming, 1981; van Leer, 1982; von Lavante and Haertl, 1985) the one proposed by Steger and Warming (1981) was adopted.

The development of the splitting for Cartesian coordinates is given in detail by Anderson et al. (1985) and Steger and Warming (1981) and only the final result is presented here. The eigenvalues of the flux vectors $\mathbf{F}$ and $\mathbf{G}$ in equation (1) can be expressed as

$$\begin{cases} \lambda_1^x &= u \\ \lambda_2^x &= u \\ \lambda_3^x &= u + a \\ \lambda_4^x &= u - a \end{cases} \quad \text{and} \quad \begin{cases} \lambda_1^y &= v \\ \lambda_2^y &= v \\ \lambda_3^y &= v + a \\ \lambda_4^y &= v - a \end{cases} \tag{9}$$

These eigenvalues can be, depending on the magnitude of the velocities u and v ($v \le 0$; $0 < u$, $v \le a$; u, $v > a$), separated into positive (λ_n^+) and negative (λ_n^-) parts so that ($n = 1, 2, 3, 4$)

$$\lambda_n = \lambda_n^+ + \lambda_n^- \tag{10}$$

In the original work by Steger and Warming (1981) this was done by defining

$$\lambda_n^+ = \frac{\lambda_n + |\lambda_n|}{2} \qquad \lambda_n^- = \frac{\lambda_n - |\lambda_n|}{2} \tag{11}$$

With this splitting of the eigenvalues λ_n^x and λ_n^y into positive and negative parts, the flux vectors $\mathbf{F}$ and $\mathbf{G}$ can also be split into two terms $\mathbf{F}^+$, $\mathbf{G}^+$ and $\mathbf{F}^-$, $\mathbf{G}^-$ (Steger and Warming, 1981), with

$$\begin{aligned} \mathbf{F} &= \mathbf{F}^+ + \mathbf{F}^- \\ \mathbf{G} &= \mathbf{G}^+ + \mathbf{G}^- \end{aligned} \tag{12}$$

The split flux vectors can be expressed as (for details of the splitting, see, for example, Anderson et al., 1985):

$$\mathbf{F}^\pm = \frac{\rho}{2\gamma} \begin{pmatrix} 2(\gamma-1)\lambda_1^{x\pm} & +\lambda_3^{x\pm} & +\lambda_4^{x\pm} \\ 2(\gamma-1)\lambda_1^x\lambda_1^{x\pm} & +\lambda_3^x\lambda_3^{x\pm} & +\lambda_4^x\lambda_4^{x\pm} \\ 2(\gamma-1)v\lambda_1^{x\pm} & +v\lambda_3^{x\pm} & +v\lambda_4^{x\pm} \\ (\gamma-1)q^2\lambda_1^{x\pm} & +\left[\frac{\lambda_3^{x2}+v^2}{2}\right]\lambda_3^{x\pm} & +\left[\frac{\lambda_4^{x2}+v^2}{2}\right]\lambda_4^{x\pm} + w^{x\pm} \end{pmatrix} \tag{13}$$

$$\mathbf{G}^{\pm} = \frac{\rho}{2\gamma}\begin{pmatrix} 2(\gamma-1)\lambda_1^{y\pm} & +\lambda_3^{y\pm} & +\lambda_4^{y\pm} \\ 2(\gamma-1)u\lambda_1^{y\pm} & +u\lambda_3^{y\pm} & +u\lambda_4^{y\pm} \\ 2(\gamma-1)\lambda_1^{y}\lambda_1^{y\pm} & +\lambda_3^{y}\lambda_3^{y\pm} & +\lambda_4^{y}\lambda_4^{y\pm} \\ (\gamma-1)q^2\lambda_1^{y\pm} & +\left[\frac{u^2+\lambda_3^{y2}}{2}\right]\lambda_3^{y\pm} & +\left[\frac{u^2+\lambda_4^{y2}}{2}\right]\lambda_4^{y\pm}+w^{y\pm} \end{pmatrix} \tag{13}$$

with

$$w^{x\pm} = \frac{(3-\gamma)(\lambda_3^{x\pm}+\lambda_4^{x\pm})a^2}{2(\gamma-1)}$$
$$w^{y\pm} = \frac{(3-\gamma)(\lambda_3^{y\pm}+\lambda_4^{y\pm})a^2}{2(\gamma-1)} \tag{14}$$

This formulation of splitting the flux vectors means that, for subsonic flow in the direction of investigation (x or y) information is carried from upstream and downstream. However, if the flow becomes supersonic in, say, the x direction all the negative eigenvalues λ_n^{x-} become zero. It is thus seen from equation (13) that $\mathbf{F}^- = 0$; therefore no information is numerically propagated upstream.

The flux vector splitting formulation does therefore reproduce the correct physical domain of influence of propagating signals.

In generalized coordinates the same splitting may be used, as shown by Anderson et al. (1985). For this, they propose to rotate the fluxes locally into a "body-fitted" coordinate system, first for for the $\mathbf{F}'$ flux, while treating the $\mathbf{G}'_\eta$ as a source term, and thereafter the $\mathbf{G}'$ flux, while treating the $\mathbf{F}'_\xi$ as a source term. This procedure is explained in detail by Anderson et al. (1985); therefore only the most important steps are reproduced here.

In order to use the Cartesian splitting as in equation (13), the $\mathbf{F}'$ and $\mathbf{G}'$ fluxes have to be transformed into a form that is identical with $\mathbf{F}$ and $\mathbf{G}$ according to equation (2). This can be achieved by, for the ξ direction, multiplying equation (5) with a transformation matrix $\mathbf{T}^\xi$ from the left:

$$(\bar{\mathbf{W}})_\tau + (\bar{\mathbf{F}})_\xi = -\mathbf{T}^\xi(\mathbf{G}')_\eta + (\mathbf{T}^\xi)_\tau \mathbf{W}' + (\mathbf{T}^\xi)_\xi \mathbf{F}' \tag{15}$$

where

$$\bar{\mathbf{W}} = \mathbf{T}^\xi \mathbf{W}'$$
$$\bar{\mathbf{F}} = \mathbf{T}^\xi \mathbf{F}' \tag{16}$$

Splitting of $\bar{\mathbf{F}}$ into $\bar{\mathbf{F}} = \bar{\mathbf{F}}^+ + \bar{\mathbf{F}}^-$ and multiplication from the right with the inverse of the transformation matrix, $(\mathbf{T}^\xi)^{-1}$, while considering the definition (16), gives

$$\mathbf{W}'_\tau + (\mathbf{F}'^+ + \mathbf{F}'^-)_\xi + \mathbf{G}'_\eta = 0 \tag{17}$$

See Errata Sheet P.171

with the definition

$$\mathbf{F}'^+ = (\mathbf{T}^\xi)^{-1}\bar{\mathbf{F}}^+$$
$$\mathbf{F}'^- = (\mathbf{T}^\xi)^{-1}\bar{\mathbf{F}}^- \tag{18}$$

It should be noted that equation (17) has the same form, if the splitting (12a) is considered, as equation (1), and that the term $\mathbf{G}'_\eta$ has not been affected by the manipulation. It is thus possible to perform a similar transformation procedure also for the η flux, to obtain

$$\mathbf{W}' + (\mathbf{F}'^+ + \mathbf{F}'^-)_\xi + (\mathbf{G}'^+ + \mathbf{G}'^+)_\eta = 0 \tag{19}$$

with

$$\mathbf{G}'^+ = (\mathbf{T}^\eta)^{-1}\bar{\mathbf{G}}^+$$
$$\mathbf{G}'^- = (\mathbf{T}^\eta)^{-1}\bar{\mathbf{G}}^- \tag{20}$$

Note that no assumption has, up until now, been made concerning how the flux splitting should be performed.

If now the rotation matrices $\mathbf{T}^\xi$ and $\mathbf{T}^\eta$ are chosen in a special way, the transformed fluxes $\bar{\mathbf{F}}$ and $\bar{\mathbf{G}}$ can be put into the same form as the expressions for $\mathbf{F}$ and $\mathbf{G}$ in equation (2), whereafter any splitting developed for Cartesian coordinates can be applied directly (Anderson et al., 1985).

To obtain such a form for $\bar{\mathbf{F}}$ and $\bar{\mathbf{G}}$, the rotation matrices $\mathbf{T}^\xi$ and $\mathbf{T}^\eta$ can be expressed, in the case of a nonmoving grid, as

$$\mathbf{T}^\xi = \begin{pmatrix} 1 & 0 & 0 & 0 \\ 0 & c_1^\xi & c_2^\xi & 0 \\ 0 & -c_2^\xi & c_1^\xi & 0 \\ 0 & 0 & 0 & 1 \end{pmatrix} \tag{21a}$$

$$\mathbf{T}^\eta = \begin{pmatrix} 1 & 0 & 0 & 0 \\ 0 & -c_1^\eta & c_2^\eta & 0 \\ 0 & c_2^\eta & c_1^\eta & 0 \\ 0 & 0 & 0 & 1 \end{pmatrix} \tag{21b}$$

with

$$c_1^\xi = \frac{\xi_x}{\sqrt{\xi_x^2+\xi_y^2}} = \frac{y_\eta}{\sqrt{y_\eta^2+x_\eta^2}}$$
$$c_2^\xi = \frac{\xi_y}{\sqrt{\xi_x^2+\xi_y^2}} = -\frac{x_\eta}{\sqrt{y_\eta^2+x_\eta^2}}$$
$$c_1^\eta = \frac{\eta_y}{\sqrt{\eta_x^2+\eta_y^2}} = \frac{x_\xi}{\sqrt{x_\xi^2+y_\xi^2}} \tag{22}$$
$$c_1^\eta = \frac{\eta_x}{\sqrt{\eta_x^2+\eta_y^2}} = -\frac{y_\xi}{\sqrt{x_\xi^2+y_\xi^2}}$$

With these definitions, the flux vectors $\bar{\mathbf{F}}$ and $\bar{\mathbf{G}}$ take the form

$$\bar{\mathbf{F}} = \mathbf{T}^\xi\mathbf{F}' = \sqrt{y_\eta^2+x_\eta^2}\begin{pmatrix} \rho\tilde{u}^\xi \\ \rho\tilde{u}^\xi\tilde{u}^\xi + p \\ \rho\tilde{v}^\xi\tilde{u}^\xi \\ \rho\tilde{u}^\xi(e_c + p/\rho) \end{pmatrix}$$
$$\bar{\mathbf{G}} = \mathbf{T}^\eta\mathbf{G}' = \sqrt{y_\xi^2+x_\xi^2}\begin{pmatrix} \rho\tilde{v}^\eta \\ \rho\tilde{u}^\eta\tilde{v}^\eta \\ \rho\tilde{v}^\eta\tilde{v}^\eta + p \\ \rho\tilde{v}^\eta(e_c + p/\rho) \end{pmatrix} \tag{23}$$

where $\tilde{u}^\xi$ is the velocity normal to a line of constant ξ, representing the scaled contravariant velocity component, and $\tilde{v}^\xi$ is normal to $\tilde{u}^\xi$ (Anderson et al., 1985). Furthermore, $\tilde{v}^\eta$ is the velocity normal to a line of constant η and $\tilde{u}^\eta$ is normal to $\tilde{v}^\eta$, as:

$$\tilde{u}^\xi = \frac{(y_\eta u - x_\eta v)}{\sqrt{y_\eta^2+x_\eta^2}} \qquad \tilde{v}^\xi = \frac{(x_\eta u + y_\eta v)}{\sqrt{y_\eta^2+x_\eta^2}}$$

$$\tilde{u}^\eta = \frac{(-x_\xi u - y_\xi v)}{\sqrt{x_\xi^2+y_\xi^2}} \qquad \tilde{v}^\eta = \frac{(-y_\xi u + x_\xi v)}{\sqrt{x_\xi^2+y_\xi^2}}$$

The expressions for $\bar{\mathbf{F}}$ and $\bar{\mathbf{G}}$ in equation (23) are thus identical to the expressions for $\mathbf{F}$ and $\mathbf{G}$ in equation (2). The splittings expressed in equation (13) can thus be used to obtain $\bar{\mathbf{F}}^+$, $\bar{\mathbf{F}}^-$ and $\bar{\mathbf{G}}^+$, $\bar{\mathbf{G}}^-$ whereafter equation (20) is used to obtain the split vectors $\mathbf{F}'^+$, $\mathbf{F}'^-$ and $\mathbf{G}'^+$, $\mathbf{G}'^-$ necessary for the numerical solution of equation (5), expressed in the split form of equation (19).

Spatial Differencing. In the original work by Steger and Warming (1981) the spatial derivatives were approximated with differences taken "upwind" for both $\mathbf{F}^+$ and $\mathbf{F}^-$, i.e., backward (in the negative x direction) for $\mathbf{F}^+$ and forward (in the positive x direction) for $\mathbf{F}^-$. In the case of generalized coordinates this approach does however not preserve "free stream" values, i.e., it introduces a dependency of the transformation metrics on the result (see, for example, Buning and Steger, 1982). Van Leer proposed instead (see, for example, Anderson et al., 1985) to use a "Monotone Upwind Schemes for Conservation Laws" ("MUSCL") approach, in which the data are first prepared and eventually limited before the numerical differences are performed. The spatial derivatives are here approximated as centered differences, with values at half points

$$\mathbf{F}_x'^{\pm} \approx \Delta \mathbf{F}_i'^{\pm}/\Delta\xi = \{\mathbf{F}'^{\pm}_{i+1/2} - \mathbf{F}'^{\pm}_{i-1/2}\}/\Delta\xi \tag{25}$$

Furthermore, the $\mathbf{F}'^{\pm}_{i+1/2}$ and $\mathbf{F}'^{\pm}_{i-1/2}$ are evaluated with two point "upwind" (i.e., backward for $\mathbf{F}^+$ and forward for $\mathbf{F}^-$) extrapolation (Anderson et al., 1985)

$$\begin{cases} \mathbf{F}'^{+}_{i+1/2} = \mathbf{F}'^{+}(\mathbf{W}'^{-}_{i+1/2}) \\ \mathbf{F}'^{-}_{i+1/2} = \mathbf{F}'^{-}(\mathbf{W}'^{+}_{i+1/2}) \end{cases} \tag{26}$$

$$\begin{cases} \mathbf{W}'^{-}_{i+1/2} = \mathbf{W}'_i + \phi^-_i\{\mathbf{W}'_i - \mathbf{W}'_{i-1}\}/2 \\ \mathbf{W}'^{+}_{i+1/2} = \mathbf{W}'_{i+1} + \phi^+_{i+1}\{\mathbf{W}'_{i+1} - \mathbf{W}'_{i+2}\}/2 \end{cases} \tag{27}$$

In these expressions, the scalar function ϕ is denoted the flux limiter. Its function is to switch from first-order spatial accuracy to second-order at appropriate points. The value $\phi = 1$ gives second-order spatial accuracy while $\phi = 0$ reduces the accuracy to first order.

It has been demonstrated by Anderson et al. (1985) (with an implicit computational code) that, due to the fact that both $\Delta\mathbf{F}^+$ and $\Delta\mathbf{F}^-$ are evaluated at the same computational locations, a method with the "MUSCL" procedure gives smooth results around a sonic rarefaction point.

Integration in Time. With the abovementioned "MUSCL" approach, an explicit second-order numerical scheme can be conceived as a two-step method. This method is modified from the original Steger–Warming model for flux splitting (1981) and can be expressed as (see Grossman, 1986, for one dimension)

First step:

$$\begin{aligned} \mathbf{W}'^{*}_{j,i} = \mathbf{W}'^{k}_{j,i} &- \Delta\tau\{\Delta(\mathbf{F}'^{+}_{j,i})^k + \Delta(\mathbf{F}'^{-}_{j,i})^k\}/\Delta\xi \\ &- \Delta\tau\{\Delta(\mathbf{G}'^{+}_{j,i})^k + \Delta(\mathbf{G}'^{-}_{j,i})^k\}/\Delta\eta \end{aligned} \tag{28}$$

Second step:

$$\begin{aligned} \mathbf{W}'^{k+1}_{j,i} = 0.5\{\mathbf{W}'^{*}_{j,i} + \mathbf{W}'^{k}_{j,i} &- \Delta\tau\{\Delta(\mathbf{F}'^{+}_{j,i})^* + \Delta(\mathbf{F}'^{-}_{j,i})^*\}/\Delta\xi \\ &- \Delta\tau\{\Delta(\mathbf{G}'^{+}_{j,i})^* + \Delta(\mathbf{G}'^{-}_{j,i})^*\}/\Delta\eta\} \end{aligned}$$

where an asterisk indicates values at an intermediate time level and the spatial differences are expressed as centered values according to equation (25).

Boundary Conditions. At the *inlet* boundary a one-dimensional boundary condition with small reflection is introduced by replacing the incoming information (along the characteristics λ_1^x and λ_3^x) by an imposed (at upstream infinity) value of the Riemann invariant such as (Fransson and Pandolfi, 1986)

$$R^+ = f(\text{upstream infinity}) = \text{imposed} = \frac{2}{\gamma - 1}a_{-\infty} + q_{-\infty} \tag{29}$$

The value of the left running Riemann invariant is thereafter determined from the values of the flow variables in the interior of the computational domain, whereafter these two values are combined to yield the inlet flow conditions as

See Errata Sheet P.171

$$\begin{aligned} u_{\text{inlet}} &= \frac{R^+ - R^-}{2} \\ a_{\text{inlet}} &= \left\{\frac{R^+ - R^-}{2}\right\} \cdot \left\{\frac{\gamma - 1}{2}\right\} \end{aligned} \tag{30}$$

An iterative procedure to obtain a higher accuracy can thereafter be performed.

At the *outlet* boundary a similar treatment is made, but the static pressure is instead imposed as a function of time. The boundary will thus reflect disturbances from the inner flow field back into the nozzle (Fransson and Pandolfi, 1986). The Riemann invariant along the characteristic λ_3^x is thus calculated from the inner flow field (R^+) and combined with the value of the entropy along the characteristic λ_1^x to yield

$$\begin{aligned} a_e &= \gamma p_e^{\frac{\gamma-1}{\gamma}} \cdot e^{\frac{s_e}{\gamma}} \\ u_e &= R^+ - \frac{2}{\gamma - 1}a_e \end{aligned} \tag{31}$$

An iterative procedure to determine the points of departure of the characteristics λ_3^x and λ_1^x can thereafter be performed.

Wall Boundaries. As the centers of the numerical cells are situated 1/2 grid from the walls, the cell interface is situated at the wall. Thus, on the *wall boundary* (for example the lower), the spatial derivative $(\mathbf{G}'_j)_\eta$ can be approximated according to equation (25) as

$$(\mathbf{G}'_{j,i})_\eta \approx \Delta(\mathbf{G}'_i)_\eta/\Delta\eta = \{\mathbf{G}'_{j+1/2,i} - \mathbf{G}'_{j-1/2,i}\}/\Delta\eta \tag{32}$$

However, the point $j - 1/2$ coincides now with the lower wall; therefore the boundary condition of no mass flow in the η direction gives

$$\mathbf{G}'_{j-1/2,i} = \begin{pmatrix} 0 \\ 0 \\ p \\ 0 \end{pmatrix} \tag{33}$$

The only flow variable necessary at the wall is thus the pressure, which is determined by extrapolation from the interior of the flow field.

Examples of Application

Two examples obtained with the abovedescribed model will be presented in this section. The first concerns the flow through a quasi-one-dimensional nozzle, and the second the two-dimensional flow through a channel with a 10 percent thick "bump" on the upper wall. In both applications the imposed exit pressure is varied in time, with different amplitudes and frequencies.

Unsteady Quasi-One-Dimensional Transonic Flow. The *first sample case* shown can be considered as a validation of the method. Here, the numerical results are compared to results by Adamson et al. (1976, 1977, 1978a, 1978b, 1978c, 1984, 1986) who have developed analytical small perturbation theories to the problem of oscillating back pressure in tran-

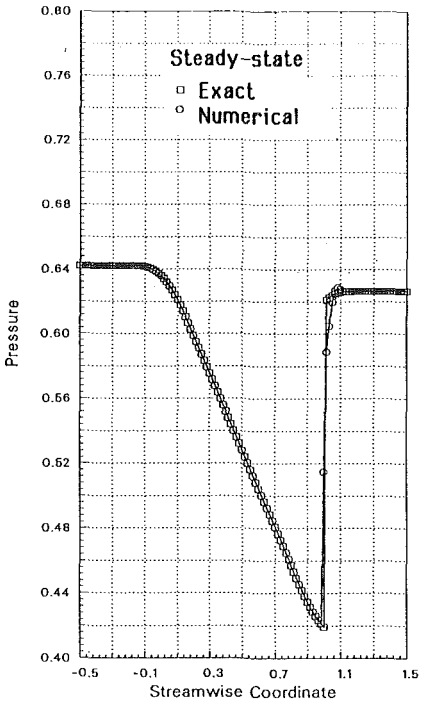

Fig. 1 Exact and numerical steady-state pressure distribution (121 grid points in x direction)

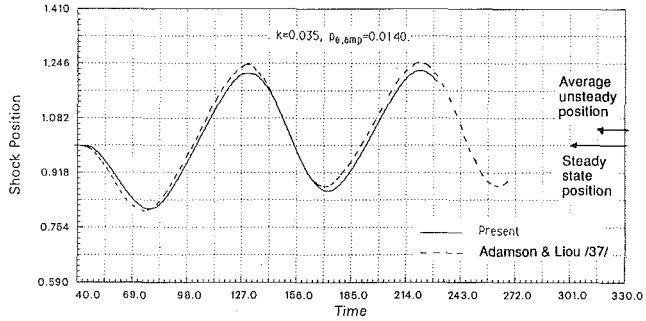

Fig. 2 Comparison of unsteady shock position, as calculated with the present flux vector splitting model and Adamson's (1977) analytical method; Adamson's (1977) second sample case, $k=0.035$, $p_{e,amp}=0.0140$

transonic one and two-dimensional nozzles. Their results indicate that, although the method treats small perturbations, the unsteady shock oscillation amplitude, as well as the time-averaged shock position, depends not only on the steady-state (or average unsteady) back pressure but also on the amplitude of the pressure oscillation and, largely, on the oscillation frequency (as well as, obviously, the nozzle geometry).

As these solutions are of an analytical nature, comparison with the present, fully numerical methodology is of interest. The nozzle area employed for this validation is the one defined by Adamson and Liou (1977), which is given by

$$A(x)=1.+\epsilon^2 f(x) \tag{34}$$

where ϵ is a constant defining the small perturbation and $f(x)$ is a function describing the wall shape

$$f(x)=\begin{cases} 3 & ;-0.5\le x\le -\dfrac{1}{6} \\ \{27[3(x-0.5)+2]^4-48[3(x-0.5)+2]^3\}/13+3 & ;-\dfrac{1}{6}\le x\le \dfrac{1}{6} \\ 18[3(x-0.5)]^2/13 & ;\dfrac{1}{6}\le x\le \dfrac{5}{6} \\ \{27[3(x-0.5)-2]^4+48[3(x-0.5)-2]^3\}/13+3 & ;\dfrac{5}{6}\le x\le \dfrac{7}{6} \\ 3 & ;\dfrac{7}{6}\le x\le 1.5 \end{cases} \tag{35}$$

With this nozzle shape, the inlet is situated at $x=-0.5$, the throat at $x=+0.5$, and the outlet at $x=+1.5$. The area change in the nozzle is 3 percent.

Once the steady-state flow field has been calculated, the unsteadiness is introduced by varying the back pressure according to

$$p=p_e+p_{e,amp}\sin(\omega[t-t_0]) \tag{36}$$

where ω is the circular frequency of the exit pressure fluctuation.

If $p_e=0.6265$ (dimensionless with the steady-state inlet stagnation pressure) the shock in this nozzle is situated at $x=1.0$. This is seen in Fig. 1, where the exact and numerical steady-state positions are presented. It is concluded that the shock position is accurately determined by the numerical model.

If, at a certain time, the imposed back pressure starts to oscillate, disturbances from the outlet will propagate upstream. After a certain time they will reach the shock, which will then be displaced. This is seen in Fig. 2 for a case with $p_{e,amp}=0.0140$ and $k=0.035$ (with a reference velocity $q_{ref}=293$ m/s and a references length of $l_r=0.1$ m, this corresponds to a frequency of $f=33$ Hz). After a certain time the shock has reached its farthest upstream position ($t\approx 77$ in Fig. 2), whereafter the pressure immediately downstream of it starts to move the shock downstream instead. Unless the shock movement is large, the shock will thus exhibit cyclic behavior in time as presented in Fig. 2.

It is concluded that the numerical and the analytical methods (Adamson and Liou, 1977) both predict the same shock oscillation. It is also noted that the average unsteady shock location is not identical with the steady-state position, even though the average unsteady back pressure is the same as the steady-state back pressure.

As the imposed back pressure suddenly changes at a certain time ($t\approx 41$ in Fig. 2), it is obvious that the first cycle will be a transient toward a periodic solution. The experience for flows similar to the sample case above has shown that this transient normally lasts for two cycles and that, thus, the unsteady flow is identical for all the following cycles, as long as the imposed back pressure variation is maintained periodic.

In this sample case, for an imposed back pressure variation of 2.2 percent, the shock amplitude is 18 percent of the distance from the nozzle throat to the nozzle exit, and the average unsteady shock location is 5 percent downstream of the steady-state position ($X_{s,max}\approx 1.23$, $X_{s,min}\approx 0.87$, $X_{s,ave}\approx 1.05$) for the fully developed periodic shock motion.

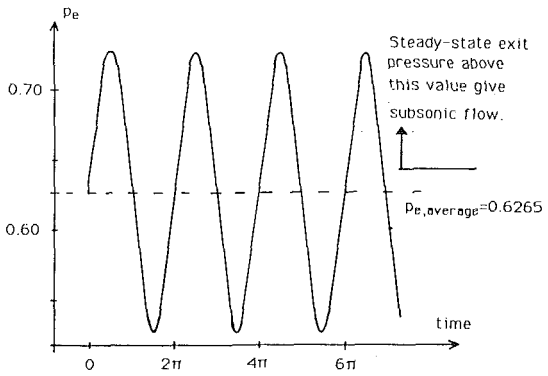

a) Imposed exit pressure variation in time

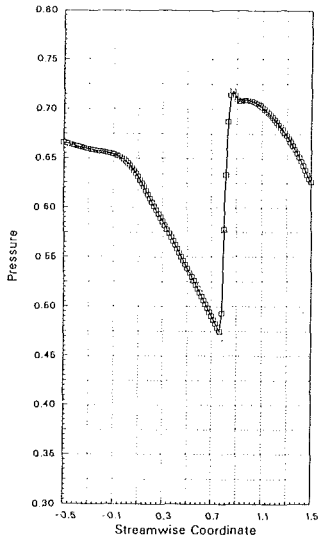

b) Pressure distribution at t = 5π

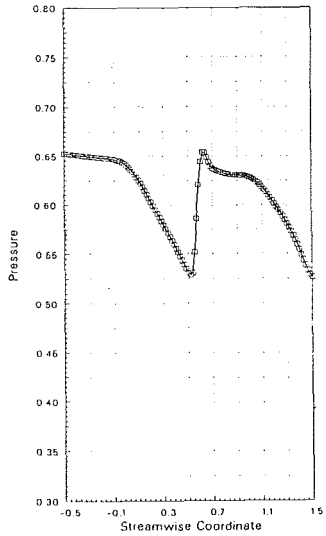

c) Pressure distribution at t = $5\frac{1}{2}\pi$

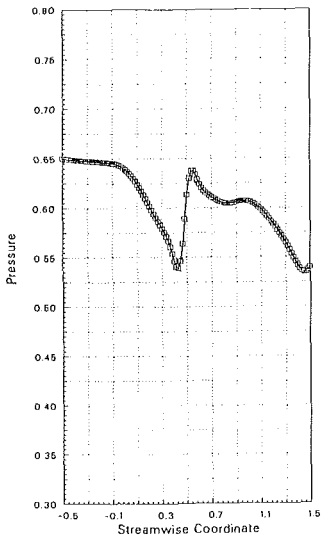

d) Pressure distribution at t = $5\frac{2}{3}\pi$

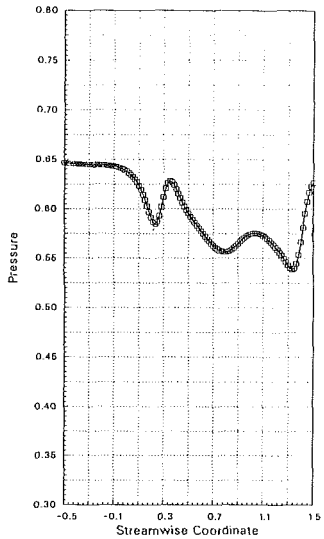

e) Pressure distribution at t = 6π

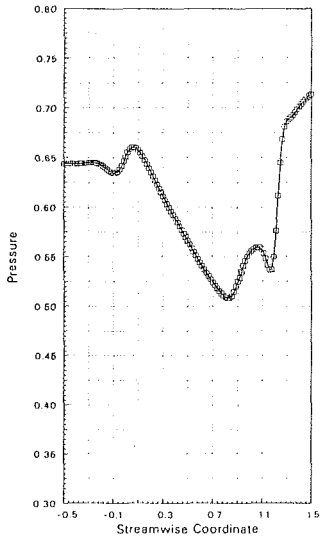

f) Pressure distribution at t = $6\frac{1}{3}\pi$

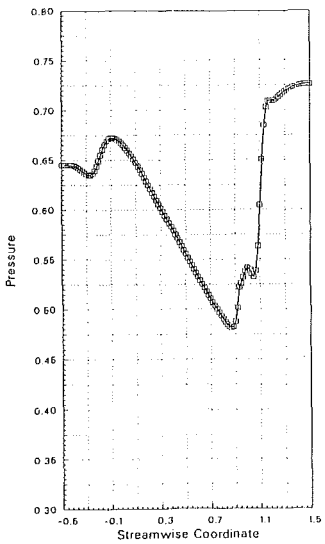

g) Pressure distribution at t = $6\frac{1}{2}\pi$

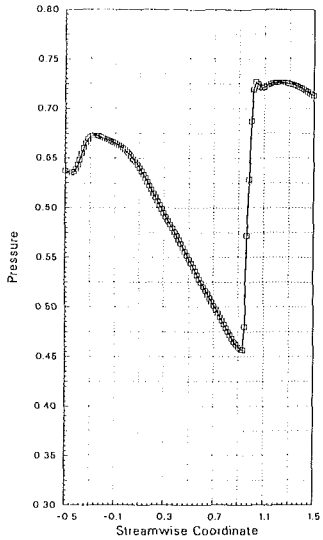

h) Pressure distribution at t = $6\frac{2}{3}\pi$

Fig. 3 Unsteady pressure distribution in a nozzle ($k = 0.318$, $p_{e,amp} = 0.10$, $p_e = 0.6265$, nozzle geometry as in equation (35))

Obviously, the average unsteady shock position and the shock movement will depend on, apart from the nozzle geometry and steady-state back pressure, the imposed back pressure amplitude and frequency.

For the *second sample case* shown here both the frequency and the amplitude of the imposed back presure variation have been modified. The reduced frequency is $k=0.318$ (corresponding to a frequency of $f=300$ Hz with the same reference values as in the first sample case) and the amplitude is $p_{e,amp}=0.10$. The nozzle geometry and the flow values are the same as in the previous case. The steady-state pressure distribution through the nozzle is thus again given by Fig. 1, and the imposed back pressure fluctuation is shown in Fig. 3(*a*) (here the time is referred to the time when the pressure oscillation starts). Only the fully developed periodic solution will be discussed here, and the results from one cycle will be shown ($t=5\pi$ to 7π in Fig. 3*a*).

The pressure distribution throughout the nozzle is shown in Fig. 3 for different time levels. At $t=5\pi$ the instantaneous unsteady back pressure is equal to the steady-state value and the unsteady shock is situated approximately at $x_s=0.78$ (Fig. 3*b*; compare this with the steady-state position at $x_s=1.0$, Fig. 1). Due to the fluctuation of pressure at the outlet, the entire postshock pressure distribution is different at $t=5\pi$ from the steady-state. So is also to some extent the preshock pressure distribution, which will be discussed below.

After $t=5\pi$ the imposed back pressure continues to decrease until $t=5.5\pi$ (Fig. 3*a*). However, the shock still moves upstream, although the entire postshock pressure is decreasing. At this time the exit pressure has reached its minimum value and starts to increase. The instantaneous unsteady pressure distribution then shows that the shock is now just downstream of the throat (Fig. 3*c*). As the exit pressure then starts to increase the disturbances from the outlet will propagate upstream. However, the shock still moves upstream, and passes over into the subsonic part of the nozzle. In the beginning the relative shock velocity is still supersonic, but as the Mach number decreases (as the nozzle cross section is larger farther upstream) the unsteady shock wave will get a subsonic relative velocity and spread out into a compression wave. Simultaneously, the pressure jump over this shock will decrease (Fig. 3*d*, *e*). At time $t=6\pi$ (Fig 3*e*), the flow through the entire nozzle is subsonic.

At the same time the increase in back pressure builds up a compression wave, which steepens later into a shock (Fig. 3*f*). At the time $t=6.5\ \pi$ (Fig. 3*g*), the main expansion through the throat is being built up again, and the flow is supersonic in a small part of the nozzle. However, in contrast to what is expected from steady-state flow, the sonic line does not occupy the throat of the nozzle. At the time under study here, $t=6.5\ \pi$, the sonic line is instead situated approximately at $x\approx 0.66$. As the time increases, this main expansion will build up further, at the same time as the first shock approaches and disappears through the inlet. The shock created by the pressure buildup at the outlet is pushed farther upstream (Fig. 3*g*). The interaction between the expanding flow in the center of the nozzle and this upstream moving shock creates a second small shock at $x\approx 1.0$ (Fig. 3*g*). This is the result of the small pressure wave first appearing at $x\approx 0.9\div 1.0$ at $t=17\pi/3$ and being more accentuated at $t=6\pi$ and $19\pi/3$. Finally, these two downstream shocks merge into one, and a pressure distribution similar to the one at $t=5\pi$ appears ($t=20\pi/3$, Fig. 3*h*). However, it should clearly be stated that, at $t=20\pi/3$, the unsteady flow is still not choked. This also has as a consequence that under no part of the cycle does the maximum flow velocity reach the steady-state preshock flow velocity.

It is also of great interest to compare two parts of the period directly with each other, namely when the imposed exit pressure is at its steady-state value (= average unsteady back pressure). This is the case for $t=5\pi$ (Fig. 3*b*), $t=6\pi$ (Fig. 3*e*) and, obviously, for the steady-state solution at $t=0$ (Fig. 1). From the comparison between $t=5\pi$ and 6π it is concluded that the two pressure distributions are completely different, especially for $x\geq 0.3$. Furthermore, by comparing these results with the steady-state distribution, it is clear that an imposed unsteady back pressure fluctuation can introduce considerable unsteady loads.

Obviously, it is possible to decrease the shock movement by, for example, diminishing the exit pressure amplitude $p_{e,amp}$ or increasing its oscillation frequency. Results similar to the present quasi-one-dimensional flow studies have recently been shown by Allmares and Giles (1987).

Unsteady Two-Dimensional Transonic Flow. One unsteady two-dimensional channel flow sample case will be discussed here. The nozzle geometry consists of a channel with a (nondimensional) length of $l_l=2.0$, a width of $l_w=1.0$, and with a 10 percent thick "bump" ($l_t/l_w=0.10$) on the upper wall. The length of the bump is identical to the channel width and its form is of sinusoidal shape.[2]

The sample case considers the flow with a steady-state (= unsteady average) exit pressure of $p_e=0.7369$, which corresponds to an inlet Mach number of $M_{-\infty}=0.675$.[3] The imposed exit pressure amplitude is $p_{e,amp}=0.12$ ($p_{e,amp}/p_e=16$ percent), with a reduced frequency of $k=0.396$ (corresponding to $f=369$ Hz for a channel width of $l_{ref}=0.1$ m and a referenced velocity of $q_{ref}=293$ m/s). The imposed exit pressure is the same over the width of the channel, and the variation of pressure starts, as in the quasi-one-dimensional cases, with a sinusoidal pressure increase. The presented results start with the steady-state solution and 1.5 cycles of the pressure oscillation will be discussed. The steady-state flow field is given in Fig. 4(*a*) and the unsteady sequence is studied in Figs. 4(*b–p*). The numerical grid used for this computation is uniform, in both the y and x directions, and consists of (14*60) cells. It is concluded from Fig. 4(*a*) that the numerical steady-state solution captures the shock wave within two cells.

As the exit pressure increases, the lines of constant Mach number close to the outlet are pushed upstream, especially at the lower wall (Fig. 4*b*). Up to $t=3\pi/8$ there has been no change for $x\leq 0.7$. At $t=\pi/2$ the exit pressure has reached its maximum value (Fig. 4*c*), whereafter it starts to decrease. The flow does not, however, react instantaneously to this change at the outlet, and the velocity continues to decrease. The signals from the outlet reach farther into the flow field close to the lower wall at a certain time, as here the flow velocity is lower than at the upper wall. The lines of constant Mach number in the flow field are thus still turned more forward, whereas they start to turn backward at the outlet (Fig. 4*d*). Simultaneously, the disturbances propagating close to the upper wall have reached the shock, which then starts to move. The maximum preshock Mach number decreases rapidly as the shock moves upstream (Fig. 4*e*).

At time $t=\pi$ (Fig. 4*f*) the exit pressure has again reached its steady-state level but, due to the finite propagation time of the disturbance signals, the flow velocity in the forward part of the nozzle continues to decrease. The flow is now subsonic throughout the nozzle, although a small unsteady shock wave is still being propagated upstream, in the same manner as the previous one-dimensional sample case, on the upper wall. At a somewhat later time (Fig. 4*g*) the velocity in the nozzle has reached its minimum value and the flow in the upstream part of the channel finally starts to react to the decrease in exit pressure.

[2] This shape, and not the circular arc bump, has been deliberately introduced in order to minimize numerical errors as the unsteady shocks pass over the corners of the bump.

[3] Such steady-state flow fields have been studied, both for circular arc and sinusoidal bumps, by several authors (see, for example, Moretti, 1981, and Ni, 1982).

Mach number in physical plane

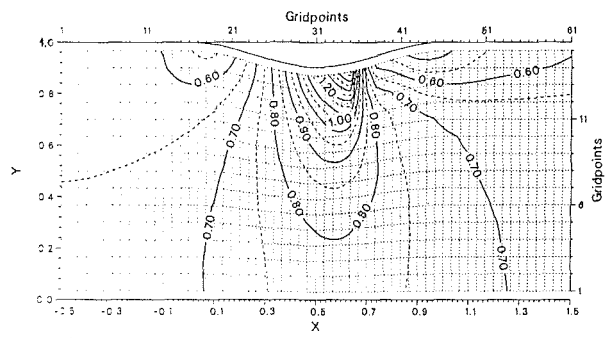

a) t = 0

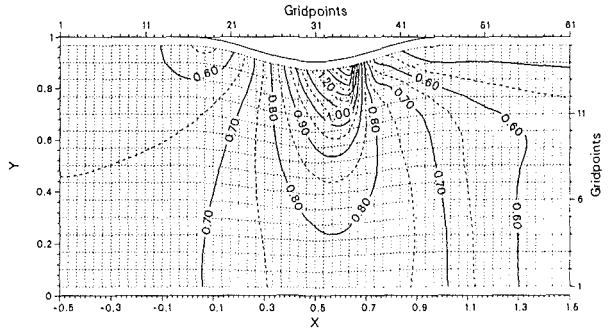

b) t = 3π/8

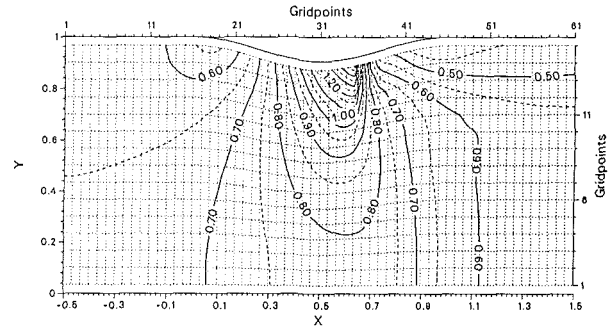

c) t = π/2

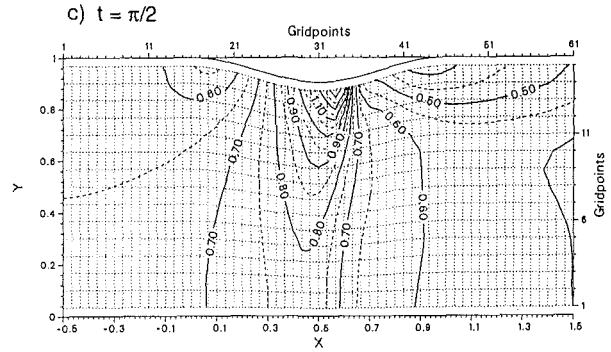

d) t = 3π/4

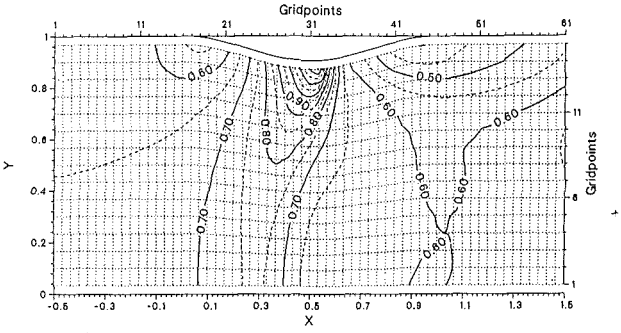

e) t = 7π/8

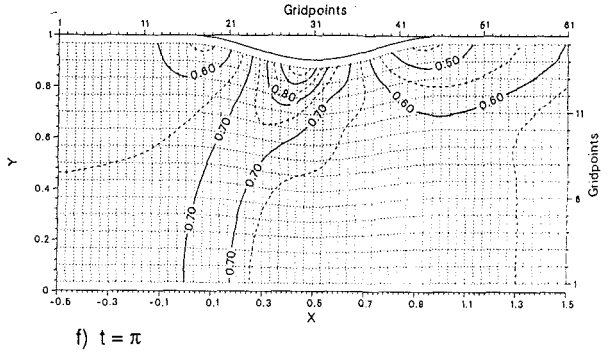

f) t = π

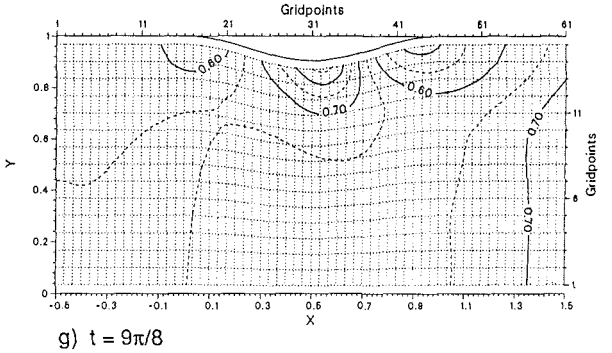

g) t = 9π/8

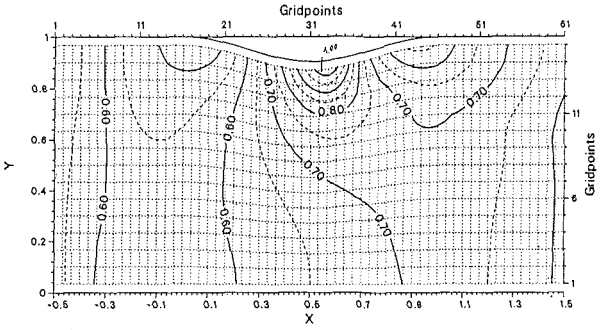

h) t = 11π/8

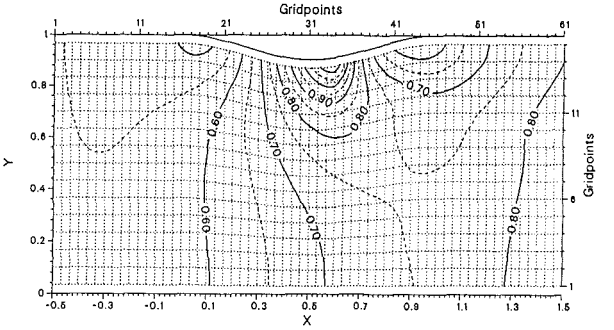

i) t = 3π/2

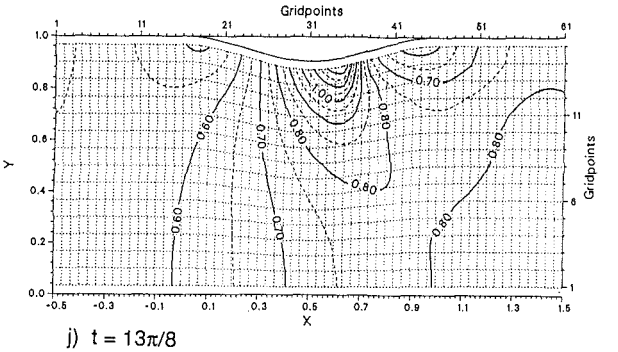

j) t = 13π/8

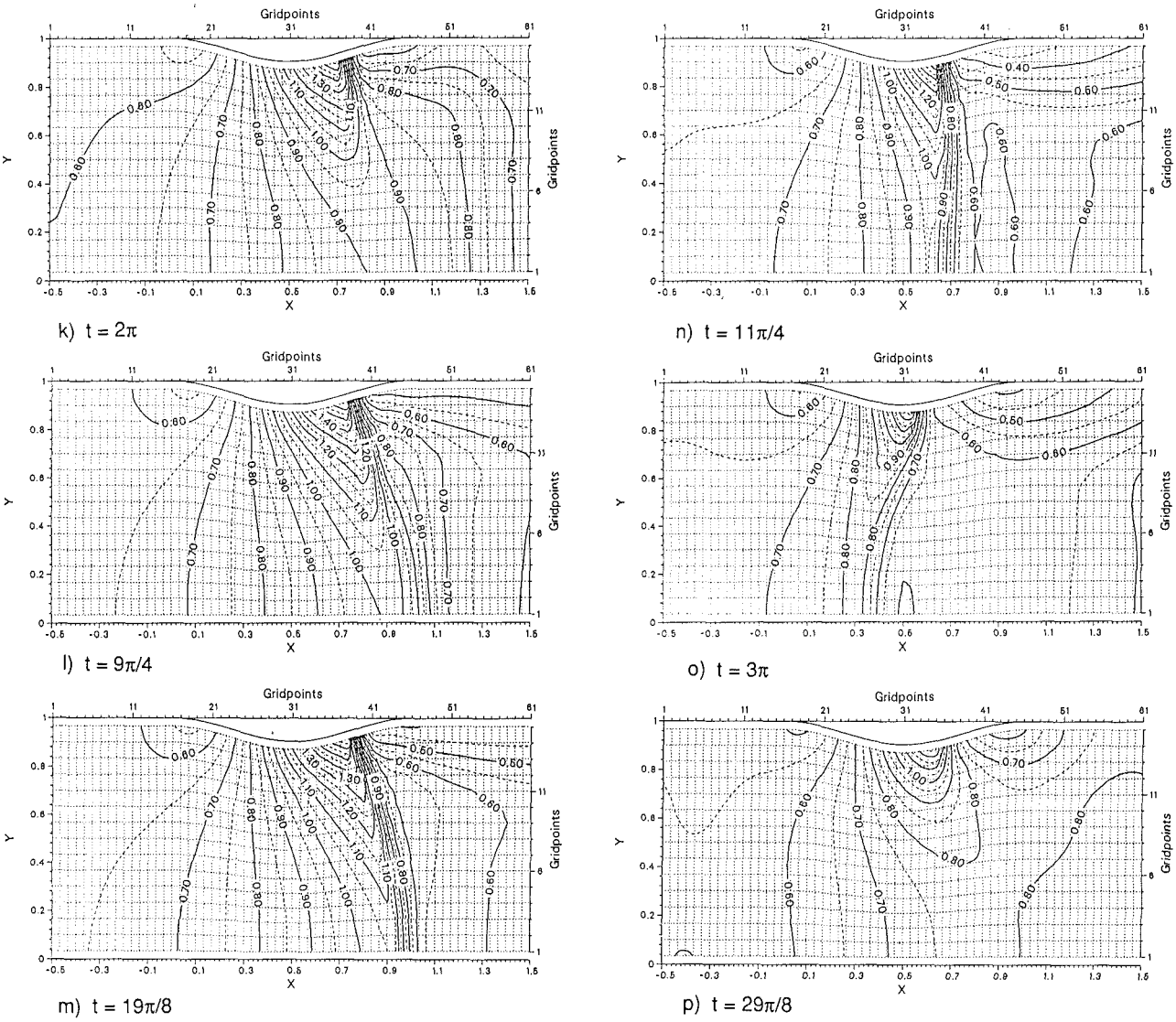

Fig. 4 Sinusoidal "bump" flow. $M_{-\infty} = 0.675$, $p_e = 0.7369$. Unsteady solution for two-dimensional sample case. $p_{e,amp} = 0.12$, $k = 0.369$. Mach number in physical plane.

The increase in flow velocity appears at the whole channel width, but obviously with a larger value at the bump. As the imposed pressure wave train approaches the bump, the flow velocity at the upper wall will again reach a sonic value (Fig. 4*h*) and the shock steepens gradually. At $t = 3\pi/2$ (Fig. 4*i*) the exit pressure has reached its minimum level and somewhat later the shock passes again over its steady-state position (Fig. 4*j*), although with a considerably lower pressure jump than for the steady-state solution (Fig. 4*a*). The pressure at the outlet is now increasing, but the shock is rapidly moving downstream, simultaneously as the flow velocity at the lower wall increases. The flow velocity, on the lower wall, in the forward part of the nozzle increases because of the decrease in the pressure wave train here, and the flow velocity in the aft part decreases because of the increase in pressure at the outlet. The shock at the upper wall is then moved downstream, simultaneously as the compression wave at the lower wall chokes the flow (Fig. 4*k*, $t = 2\pi$; Fig. 4*l*, $t = 9\pi/4$). At the same time the pressure increase at the outlet is moving upstream and this compression wave is slowly building itself up to a shock wave at the lower wall also and, indeed, over the whole width of the channel (Fig. 4*m*, $t = 19\pi/8$). Although the shock at the lower wall is fairly weak, it can still be considered to be captured within two numerical cells.

The shock at the upper wall has now reached its maximum position, with a considerably higher preshock Mach number than for the steady-state flow field, whereafter the whole shock structure is pushed upstream as the imposed pressure wave train from the exit increases the postshock pressure. The part of the shock at the lower wall moves faster upstream than the shock close to the upper wall, and at $t = 11\pi/4$ (Fig. 4*n*) the upper wall shock reaches again its steady-state value. The unsteady lower wall shock is still propagated upstream, but it is now in the subsonic flow field (i.e., $M_{\text{pre-shock}} < 1$). The preshock Mach number on the upper wall is higher than the value for the steady-state solution (Fig. 4*a*) and considerably higher than the value reached during the downward movement of the shock (Fig. 4*j*). Indeed, not only the flow on the upper wall, but the whole flow field is very different for the two time levels having the same shock position (Fig. 4*j*, shock moving downstream; Fig. 4*n*, shock moving upstream).

The shock at the lower wall is pushed farther into the sub-

sonic part of the nozzle and becomes weaker because of the decrease in upstream flow velocity, at the same time as the shock at the upper wall also is moved upstream (Fig. 4*o*). The whole shock structure is turned upstream toward the lower wall, contrary to the earlier position when it was instead turned downstream closer to the lower wall (Fig. 4*m*). The shock, which extended over the whole channel width at $t = 19\pi/8$ (Fig. 4*m*) becomes now so weak as to only be noticed as compression waves, whereafter the flow is again accelerated and the shock on the upper wall slowly starts to appear again (Fig. 4*p*, $t = 29\pi/8$). Although now only the second cycle of the pressure fluctuation is considered, it can be concluded that the flow is building itself up toward a periodic time-varying flow field (compare $t = 13\pi/8$ and one cycle later, $t = 29\ \pi/8$; Figs. 4*j* and 4*p*). The same pattern of shock buildup as seen during the latter part of the first cycle will now be repeated again.

As for the one-dimensional sample case, the large differences in the flow field for identical shock positions (compare Figs. 4*j* and 4*n*) may introduce large unsteady loads, which may be very different from the predicted steady-state lift and moment (Fig. 4*a*).

Obviously, as in the quasi-one-dimensional sample cases shown, the unsteady flow field depends on the imposed exit pressure amplitude and frequency, as well as on the nozzle geometry and the steady-state flow field.

Conclusions

A numerical method for solving the fully unsteady two-dimensional subsonic and transonic inviscid flow has been presented.

- The method gives stationary results that agree well with other numerical and exact solutions for channel flows.
- The unsteady shock movement in a nozzle, as calculated with the present transonic model, agrees well with the one predicted by an analytical small perturbation theory.
- The transonic model has the possibility to capture unsteady shock waves moving into the subsonic part of a nozzle.
- The average unsteady shock position in a nozzle does not, for oscillating back pressure, necessarily agree with the steady-state position.
- The two-dimensional unsteady flow can be very different from the steady-state flow field. It has been shown that the unsteady flow may be choked during some part of the cycle and completely subsonic during some part of the cycle. Furthermore, unsteady shock waves may propagate into the subsonic part of the flow field.
- The pressure jump over the shock, as well as the unsteady postshock pressure, is different for identical shock positions during the cycle of fluctuation, which implies that an unsteady shock movement, imposed by oscillating back pressure, may introduce a significant unsteady lift and moment.
- It is also noted that, although the sonic velocity is obtained in the throat of steady-state quasi-one-dimensional flow, this is not necessarily true for the unsteady flow. During part of the period with fluctuating back pressure, the flow velocity may be subsonic at the throat and still reach a supersonic value farther downstream in the nozzle.

It can be concluded that the present numerical model can predict unsteady wave propagation phenomena in unsteady flows, and can accurately capture moving shock waves. It can be used for investigating unsteady transonic flow, with large-scale shock motions, in nozzles and diffusers.

Presently, experiments with an oscillating shock wave in a converging-diverging nozzle are performed at the EPF-Lausanne. The objective of these tests is to measure the shock oscillations, to compare the numerical results with the data, and to establish the validity of the numerical model.

Acknowledgments

The study was performed while the second author was a Research Associate at the Naval Postgraduate School, and was sponsored by the National Research Council, Washington, DC, USA, with Dr. R. W. Kinney as program administrator. This support is gratefully acknowledged. The authors also present their thanks to Mr. A. Krainer and Mr. P. Ott for their help in preparing the computer graphics.

References

Adamson, T. C., Jr., and Mace, J. L., 1986, "Shock Waves in Transonic Channel Flows at Moderate Reynolds Numbers," *AIAA Journal*, Vol. 24, No. 4, pp. 591–598.

Adamson, T. C. Jr., and Messiter, A. F., 1984, "Forced Oscillations of Transonic Channel and Inlet Flows With Shock Waves," *AIAA Journal*, Vol. 22, No. 11, pp. 1590–1599.

Adamson, T. C., Jr., and Chan, J. S.-K., 1978a, "Unsteady Transonic Flows With Shock Waves in an Asymmetric Channel," *AIAA Journal*, Vol. 16, No. 4, pp. 377–384.

Adamson, T. C. Jr., Messiter, A. F., and Liou, M. S., 1978b, "Large Amplitude Shock Wave Motion in Two-Dimensional Transonic Channel Flows," *AIAA Journal*, Vol. 16, No. 12, pp. 1240–1247.

Adamson, T. C., Jr., and Liou, M. S., 1978c, "Unsteady Transonic Flow in Two-Dimensional Channels," Report No. UM-015411-F, Dept. of Aerospace Engineering, University of Michigan, Ann Arbor, MI.

Adamson, T. C., Jr. and Liou, M. S., 1977, "Unsteady Motion of Shock Waves in Two-Dimensional Transonic Channel Flows," Report No. UM-014534-F, Dept. of Aerospace Engineering, University of Michigan, Ann Arbor, MI.

Adamson, T. C., Jr., and Richey, G. K., 1976, "Analysis of Unsteady Transonic Channel Flow With Shock Waves," *AIAA Journal*, Vol. 14, No. 8, pp. 1054–1061.

Allmaras, S. R., and Giles, M. B., 1987, "A Second Order Flux Split Scheme for the Unsteady Two-Dimensional Euler Equations on Arbitrary Meshes," AIAA Paper No. 87-1119.

Anderson, W. K., Thomas, J. L., and Van Leer, B., 1985, "A Comparison of Finite Volume Flux Vector Splittings for the Euler Equations," AIAA Paper No. 85-0122.

Boelcs, A., and Fransson, T. H., 1987a, "Aeroelasticity in Turbomachines: Comparison of Theoretical and Experimental Cascade Results," *Proceedings Fourth International Symposium on Unsteady Aerodynamics of Turbomachines and Propellors*, Aachen, Federal Republic of Germany.

Boelcs, A., and Schlaefli, D., 1987b, "Experimental Investigation of the Flow Through a Vibrating Annular Turbine Cascade Operating in the Transonic Flow Regime," *Proceedings Fourth International Symposium on Unsteady Aerodynamics of Turbomachines and Propellers*, Aachen, Federal Republic of Germany.

Boelcs, A., and Fransson, T. H., 1986, "Aeroelasticity in Turbomachines: Comparison of Theoretical and Experimental Cascade Results," Communication No. 13 du Laboratoire de Thermique Appliquée et de Turbomachines de l'Ecole Polytechnique Fédérale de Lausanne, Switzerland.

Buffum, D. H., and Fleeter, S., 1987, "The Unsteady Aerodynamics of a Low Solidity Oscillating Cascade," *Proceedings Fourth International Symposium on Unsteady Aerodynamics of Turbomachines and Propellors*, Aachen, Federal Republic of Germany.

Buning, P. G., and Steger, J. L., 1982, "Solution of the Two-Dimensional Euler Equations With Generalized Coordinate Transformation Using Flux Vector Splitting," AIAA Paper No. 82-0971.

Cafarelli, I., and Szechenyi, E. J., 1987, "Aeroelastic Pressure Measurements on a Compressor Blade: Comparison With Straight Cascade Results," *Proceedings Fourth International Symposium on Unsteady Aerodynamics of Turbomachines and Propellors*, Aachen, Federal Republic of Germany.

Fleeter, S., 1977, "Aeroelasticity Research for Turbomachines Applications," AIAA Paper No. 77-437.

Fransson, T. H., and Pandolfi, M., 1986, "Numerical Investigation of Unsteady Subsonic Compressible Flows Through an Oscillating Cascade," ASME Paper No. 86-GT-304.

Gallus, H. E., Holtman, H., and Servaty, S., 1984, "Computation of the Subsonic Flow Field Through Oscillating Compressor and Turbine Cascades," *Proceedings Third International Symposium on Unsteady Aerodynamics of Turbomachines and Propellors*, Cambridge, United Kingdom, pp. 73–92.

Gerolymos, G. A., Quiniou, H., and Joubert, H., 1987, "Aircraft Compressor Flutter Analysis," *Proceedings Fourth International Symposium on Unsteady Aerodynamics of Turbomachines and Propellors*, Aachen, Federal Republic of Germany.

Grant, R. J., and Whitehead, D. S., 1980, "Force and Moment Coefficients for High-Deflection Cascades," *Proceedings Second International Symposium on Aeroelasticity in Turbomachines*, Lausanne, Switzerland, pp. 85–127.

Grossman, B., 1986, "Fundamental Concepts in Computational Gas Dynamics," *A Designer's Tool*, Mar. 10–14, The Polytechnic University, Long Island Center, Farmingdale, NY.

Joubert, H., 1984, "Supersonic Flutter in Axial Flow Compressors," *Pro-*

Ni, R., 1982, "A Multi-Grid Scheme for Solving the Euler Equations," *AIAA Journal*, Vol. 20, No. 11.

Pandolfi, M., 1980, "Numerical Experiments on Unsteady Flows Through Vibrating Cascades," *Proceedings Second International Symposium on Aeroelasticity in Turbomachines*, Lausanne, Switzerland, pp. 211–228.

Platzer, M. F., 1982, "Transonic Blade Flutter: A Survey of New Developments," *The Shock and Vibration Digest*, Vol. 14, No. 7.

Pulliam, T. H., 1986, "Artificial Dissipation Models for the Euler Equations," *AIAA Journal*, Vol. 24, No. 12, pp. 1931–1940.

Salaün, P., 1976, "Instabilité de flottement dans une grille annulaire," *Revue Française de Mécanique, Numéro spécial (Aeroélasticité dans les turbomachines)*, pp. 35–38.

Servaty, S., Gallus, H. E., and Kau, H. P., 1987, "Computation of Aerodynamic Blade Loads Due to Wake Influence and Aerodynamic Damping of Turbine and Compressor Cascades," *Proceedings Fourth International Symposium on Unsteady Aerodynamics of Turbomachines and Propellors*, Aachen, Federal Republic of Germany.

Smith, S. N., 1972, "Discrete Frequency Sound Generation in Axial Flow Turbomachines," Reports and Memoranda No. 3709, United Kingdom, Mar.

Steger, J. L., and Warming, R. F., 1981, "Flux Vector Splitting of the Inviscid Gasdynamic Equations With Applications to Finite Difference Methods," *Journal of Computational Physics*, Vol. 40, No. 2, Apr., pp. 263–293.

Szechenyi, E. J., Cafarelli, I., Notin, C., and Girault, J. P. 1984, "A Straight Cascade Wind-Tunnel Study of Fan Blade Flutter Started Supersonic Flow," *Proceedings Third International Symposium on Unsteady Aerodynamics of Turbomachines and Propellors*, Cambridge, United Kingdom, pp. 447–458.

Usab, W. J., Jr., and Verdon, J. M., 1986, "On the Application of a Linearized Unsteady Potential Flow Analysis to Fan-Tip Cascades," ASME Paper No. 86-GT-87.

Van Leer, B., 1982, "Flux Vector Splittings for the Euler Equations," *Lecture Notes in Physics*, Vol. 170, pp. 501–512.

Verdon, J. M., 1987, "Unsteady Aerodynamic Response to Arbitrary Blade Motions," *Proceedings Fourth International Symposium on Unsteady Aerodynamics of Turbomachines and Propellors*, Aachen, Federal Republic of Germany.

Verdon, J. M., 1977, "Further Development in the Aerodynamic Analysis of Unsteady Supersonic Cascades," ASME Papers No. 77-GT-44, 77-GT-45.

Viviand, H., 1974, "Formes conservatives des équations de la dynamique des gaz," *La Recharche Aerospatiale*, No. 1, p. 229.

Von Lavante, E., and Haertl, A., 1985, "Numerical Solutions for Euler Equations Using Simplified Flux Vector Splitting," AIAA Paper No. 85-1333.

Zierep, J., 1976, *Theoretische Gasdynamik*, G. Braun Verlag, Karlsruhe, Federal Republic of Germany.

Wake-Boundary Layer Interactions in an Axial Flow Turbine Rotor at Off-Design Conditions

H. P. Hodson

J. S. Addison

Whittle Laboratory,
Cambridge University,
Cambridge, United Kingdom

A series of experimental investigations has been undertaken in a single-stage low-speed turbine. The measurements involved rotor blade surface flow visualization, surface-mounted hot-film anemometry, and exit pitot traverses. The effects of varying the flow coefficient and Reynolds number upon the performance of the rotor blade at midspan are described. At the design flow coefficient ($\phi = 0.495$), the rotor pressure surface flow may be regarded as laminar, while on the suction surface, laminar flow gives way to unsteady stator wake-induced transition and then to turbulent flow. Over the range of Reynolds numbers investigated (1.8×10^5–3.3×10^5), the rotor midspan performance is dominated by the suction surface transition process; suction surface separation is prevented and the rotor midspan loss coefficient remains approximately constant throughout the range. At positive incidence, suction surface leading edge separation and transition are caused by a velocity overspeed. Reattachment occurs as the flow begins to accelerate toward the throat. The loss associated with the separation becomes significant with increasing incidence. At negative incidence, a velocity overspeed causes leading edge separation of the pressure side boundary layers. Reattachment generally occurs without full transition. The suction surface flow is virtually unaffected. Therefore, the rotor midspan profile loss remains unchanged from the zero incidence value until pressure side stall occurs.

Introduction

Knowledge of the off-design performance of a turbine is important since it affects the operating costs and component life. In the case of aero-engines, idling, take-off, and cruise will result in very different operating conditions within the turbine, particularly in the low-pressure stages. Similarly, marine and industrial gas and steam turbines and constant pressure turbochargers are often required to operate away from the design point for significant lengths of time. In pulse turbocharging applications, the periodic cycling of the mass flow and pressure also results in large departures from the mean operating condition.

At present, the off-design performance of axial turbines is usually predicted using methods based upon correlations. Cascade testing and computational methods are also employed, albeit to a much lesser extent. In each case, the flow is assumed to be steady, even though it is known that the close proximity of rotating and stationary blade rows and the resulting unsteady flow can have a profound effect upon even the design point performance of turbines (e.g., [1]).

The unsteady flow that occurs as a result of the relative motion of adjacent blade rows gives rise to various interactions. The potential influence of a blade extends both upstream and downstream and decays exponentially with a length scale typically of the order of the chord or pitch. In contrast, the wakes are convected downstream from the blade row and their rate of decay is much less than that of the potential influence. The wake effect will therefore persist even where the blade rows are spaced far apart. In axial turbines, the blade row spacings are typically of the order of one quarter to one half of a blade chord. When this spacing is near the lower limit, it is likely that potential and wake interactions will coexist. In transonic stages, further interactions arise as the direct result of the impingement of the trailing shock waves upon the downstream blade row [2–4]. In low-aspect-ratio turbines [5], the blade row interactions are dominated by the unsteadiness caused by the secondary flows and associated vortices rather than by the wakes. The present paper is specifically concerned with wake interactions in the absence of these other phenomena.

The majority of research concerned with wake interactions, whether in a turbomachine (e.g., [1]) or in a simulation (e.g., [6]) has concluded that the most significant effect is the periodic forcing of the transition of the blade surface boundary layers and the influence this has upon the aerodynamic and thermodynamic performance of the blade row.

The presence of the wake above the blade surfaces causes the formation of a turbulent patch within an otherwise laminar boundary layer (see [1–4, 6]). The leading edge of this

Contributed by the Internal Gas Turbine Institute and presented at the 33rd International Gas Turbine and Aeroengine Congress and Exhibition, Amsterdam, The Netherlands, June 5–9, 1988. Manuscript received by the International Gas Turbine Institute January 13, 1988. Paper No. 88-GT-233.

patch travels with the leading edge of the wake at approximately the free-stream velocity. The rear of the patch travels more slowly, at a rate that is more typical of that observed at the rear of turbulent spots formed by natural transition [6]. Due to the differing leading and trailing velocities, the patches caused by successive wakes merge rapidly and the transition process is complete ahead of the would-be position of the end of natural transition.

Away from the design point little is known about the influence of unsteady flow upon performance. Indeed, reference [8] contains the only detailed investigation of the off-design (reduced flow coefficient) steady-state performance of an axial turbine stage that is known to the authors; while Doorly [3] briefly describes the effects of reduced Reynolds number, albeit from 2×10^6 to 1×10^6, upon simulated wake interactions in a cascade model of a high-pressure turbine.

The present paper is concerned with the mechanisms and relevance of wake interactions in axial turbines. It describes an investigation of the design and off-design performance of a large-scale low-speed single-stage axial flow turbine for which the effects of unsteady flow at the design condition have previously been reported [1, 7, 9]. The effects of changing flow coefficient and Reynolds number upon the performance of the rotor midspan section are considered. The operating range includes values typical of those found in low-pressure turbines.

Experimental Details

Research Turbine. The single-stage turbine used for the present investigation has been previously described [1, 7, 9].

The turbine is a 50 percent reaction, free-vortex design with zero exit swirl. The stage consists of 36 stator blades followed by 51 rotor blades with aspect ratios of 1.5 and 2.0, respectively, and a constant hub–tip ratio of 0.7. The flow at rotor midspan, with which much of the present investigation is concerned, is essentially two dimensional and free from the influences of secondary flow and tip leakage phenomena.

The rotor blade was designed for relative inlet and exit angles of 0 deg and −65 deg, respectively. At midspan, this corresponds to a flow coefficient $\phi = V_{x1}/U_m$ of 0.498 and a Reynolds number, based upon rotor relative exit velocity and chord, of 3.15×10^5. The airflow rate through the turbine and the rotational speed were separately controlled. This enabled the independent variation of flow coefficient and Reynolds number. At the design Reynolds number, the flow coefficient was varied from 0.26 to 0.82, while at the design flow coefficient, the Reynolds number was varied in the range from 1.8×10^5 to 3.3×10^5. Table 1 contains further details of the stage.

Table 1 Turbine midspan section: design conditions

	Stator	Rotor
Flow coefficient, V_{x1}/U_m	0.498	
Stage loading $\Delta h_0/U_m^2$	1.0	
Reynolds number Re	4.2×10^5	3.15×10^5
Rotational speed, rpm	—	530.
Inlet axial velocity V_{1x}, m/s	17.95	—
Blade inlet angle (from axial)	0.0 deg	0.0 deg
Blade exit angle (from axial)	65.0 deg	−65.0 deg
Chord, mm	152.4	114.3
Pitch-chord ratio	0.742	0.698
Aspect ratio	1.5	2.0
Number of blades	36	51
Mean radius, m	0.647	0.647

Table 2 Stator wake measurements

Traverse location (downstream of stator trailing edge)	43 percent C_{xs}	117 percent C_{xs}	
δ^*/stator pitch	0.0080	0.0084	
θ/stator pitch	0.0071	0.0070	
$H=\delta^*/\theta$	1.27	1.20	
Loss coefficient Y_p	0.014	–	
Incidence variation	7.5 deg	5.0 deg	Relative Frame
Mean incidence Δi	2.1	2.0	
Velocity defect $\Delta V/\tilde{V}$	0.105	0.080	
Maximum turbulence intensity	9.5 %	5.5%	
Mean turbulence intensity	4.1%	3.2%	

In previous investigations, the stator–rotor axial gap has been set at 75 and 143 percent of the stator axial chord C_{xs}. For the present investigation, the gap was reduced to a more representative 50 percent C_{xs}. At this spacing, the rotor–stator interactions were still expected to be dominated by wake interactions but the intensity of the interactions was expected to be greater. Table 2 contains details of the rotor midspan inflow obtained in the rotor relative frame and taken from [1].

Turbine Rotor Flow Visualization. One of the few surface flow visualization techniques available for investigations in the rotating frame is that used, for example, by Joslyn and Dring [8]. The rotor blade hub surfaces were coated with Ozalid paper. With the turbine at the desired operating condition, ammonia gas was then ejected through static pressure tappings in the surface of the blades. These tappings were positioned at 10, 30, 50, 73, and 95 percent span on the pressure surface and at 5, 27, 55, 77, and 94 percent span on the suction surface. The typical exit velocity of the ammonia from a tapping was less than 0.01 percent of the free-stream velocity and thus unlikely to affect the main flow. Although ammonia (molecular weight of 17 kg/kmol) is much lighter

Nomenclature

A = anemometer calibration constant
C_x = axial chord
E = anemometer voltage
h_0 = stagnation enthalpy
i = incidence
k = anemometer calibration constant
P_0 = stagnation pressure
Re = Reynolds number
rms = root-mean-square
s = surface distance or blade pitch
T = periodic time
t = time (rotor position)
Tu = turbulence intensity
U_m = mean blade velocity
V = velocity
Y_p = stagnation pressure loss coefficient $= \dfrac{\Delta P_{0\text{rel}}}{\frac{1}{2}\rho V_{3\text{ rel}}^2}$
α = air flow angle (from axial)
δ^* = displacement thickness
θ = momentum thickness
ρ = density
τ_ω = wall shear stress
ϕ = flow coefficient
Ω = rotational frequency

Subscripts

0 = stagnation
1 = stator inlet
2 = stator exit or rotor inlet
3 = rotor exit
rel = relative
s = surface or stator
x = axial

Superscripts

$\bar{}$ = mean phase
$\sim$ = phase-locked average
$'$ = random or nondimensional value

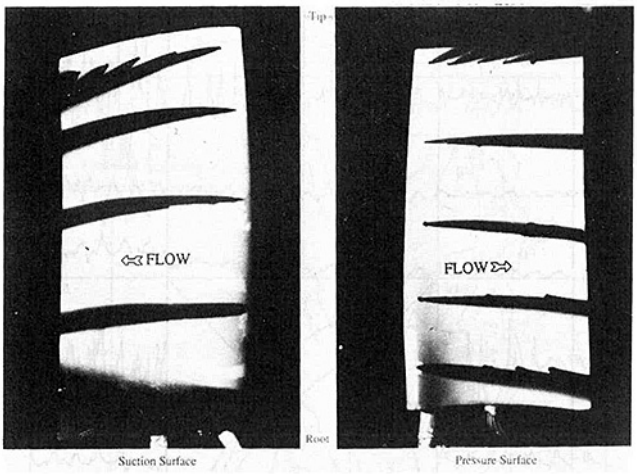

Fig. 1 Rotor surface flow visualization: Re = 3.15 × 10^5, $\phi = 0.498$ ($i = 0$ deg)

than air (29 kg/kmol) experiments by other investigators (see [8]) have shown that the buoyancy effects are negligible.

All the rotor flow visualization experiments were carried out at the design Reynolds number of 3.15×10^5.

Turbine Rotor Exit Traverses. The rotor midspan exit flow was traversed using a fast response pitot probe. The traverse was located at the half an axial chord downstream of the rotor. The rotating frame traverse gear and pitot were the same as those used in previous experiments [1]. The pitot is relatively insensitive to incidence and it was sufficient to align it with the mean outlet flow angle. The probe has an upper frequency limit in excess of 10 kHz.

At each of 64 locations, 256 samples were acquired during the passage of six stator blades. The data were phase-lock averaged over 16 revolutions; increasing this did not give significantly different results.

Surface-Mounted Hot-Film Anemometers. The development of the rotor midspan pressure and suction surface boundary layers was investigated using an array of DANTEC surface-mounted constant temperature hot-film anemometers. The multi-element gage was similar in construction to those used successfully in the Transonic Casade Facility at the Whittle Laboratory [10, 11]. The gages were repositioned several times in order to permit a full investigation of the rotor midspan boundary layers.

The similarity between the velocity and temperature profiles, the latter generated by the hot-film anemometer, leads to a relationship between the rate of heat transfer to the fluid and the wall shear stress of the form [12]

$$E^2 - A^2 = k\tau_w^{1/3}$$

where E is the bridge output voltage and the constant A represents the heat lost to the substrate. In the previous work [1] carried out at low speed, individual hot-film gages have been calibrated. In the present case, however, the calibration of an array would have been both difficult and extremely time consuming. It was therefore decided to adopt a similar procedure to that described in [10, 11]. It is assumed that the constant A in the above equation can be approximated by the bridge voltage measured under zero flow conditions E_0. Furthermore, reducing the data to the form of $(E^2/E_0^2 - 1)$ should suppress the effects of different values of the constant of proportionality k given the assumption that the rates of heat transfer to the air and substrate are similar functions of the same variables. In practice, a further simplification was introduced whereby the data acquired were in the form of voltages.

Due to limitations imposed on the data acquisition rate, the signals from each hot-film could not be acquired simultaneously and so the signals presented are not referenced to the same physical position of the rotor on the same revolution. For each gage, 256 data points were acquired during the passage of six stator blades. The data were phase-lock averaged over 64 cycles.

Phase-Lock Averaging Technique. The use of phase-lock averaging to process periodic data out of raw signals obtained in rotating machinery is a well-established technique requiring little further explanation.

In addition to the ensembled mean voltage

$$\tilde{E}(t) = \frac{1}{N}\sum_{n=1}^{N} E(n, t)$$

which is phase-locked to the rotational frequency of the turbine, the ensembled mean square was also acquired, thus enabling the ensembled root mean square (rms)

$$\text{rms}(t) = \frac{1}{N}\sqrt{\sum_{n=1}^{N}[E(n, t) - \tilde{E}(t)]^2}$$

$$= \frac{1}{N}\sqrt{\sum_{n=1}^{N}[E^2(n, t) - \tilde{E}^2(t)]}$$

to be determined, where $E(n, t)$ is the nth phase locked ensemble of the voltage $E(t)$. The ensembled rms thus contains information only about how the random content of the signal varies with rotor position t.

Results and Discussion

Design Condition. The results of the rotor surface flow visualization study, obtained at the design condition, are presented in Fig. 1. In each of the photographs shown and in subsequent ones, the line of sight is approximately normal to the midspan chord line. Figure 1 shows that on both the suction and pressure surfaces, the flow at midspan is nominally two dimensional. On the suction surface, where three-dimensional effects are usually most evident, the effects of secondary flow are restricted to the outer and inner 20 percent span. At both 27 and 77 percent span on the suction surface, the traces of ammonia emitted from the most upstream holes mask the traces of the downstream holes, indicating that there is little or no radial movement of the flow at these spanwise positions. At midspan, the ammonia traces suggest that the flow vectors near the suction surface point radially outward by a few degrees. Measurements obtained by traversing hot wires positioned near peak suction, albeit at the larger axial gap of 75 percent C_{xs} [13], show that at the surface, the radial flow angle is approximately 7 deg outward at midspan.

The rotor midspan surface velocity distribution, predicted by the method of Whitehead [15], is shown in Fig. 2 together with the velocity data obtained in an equivalent linear cascade [1]. In this figure and elsewhere, the surface distance is measured from the geometric leading edge of the rotor blade. It shows that the profile is moderately aft-loaded, with continuous acceleration on the pressure surface. Peak suction occurs near 45 percent s on the suction surface. The predicted velocity distribution was employed as input data to the boundary layer prediction scheme of Cebeci and Carr [14]. Predictions of the wall shear stress for laminar and fully turbulent flow over the suction surface and laminar flow over the pressure surface are also presented in Fig. 2. On the pressure surface, after an initial decrease, the predicted wall shear stress rises continually as a result of the continuous acceleration on that surface. Transition is not predicted. On the suction surface the wall shear stress in both the laminar and the

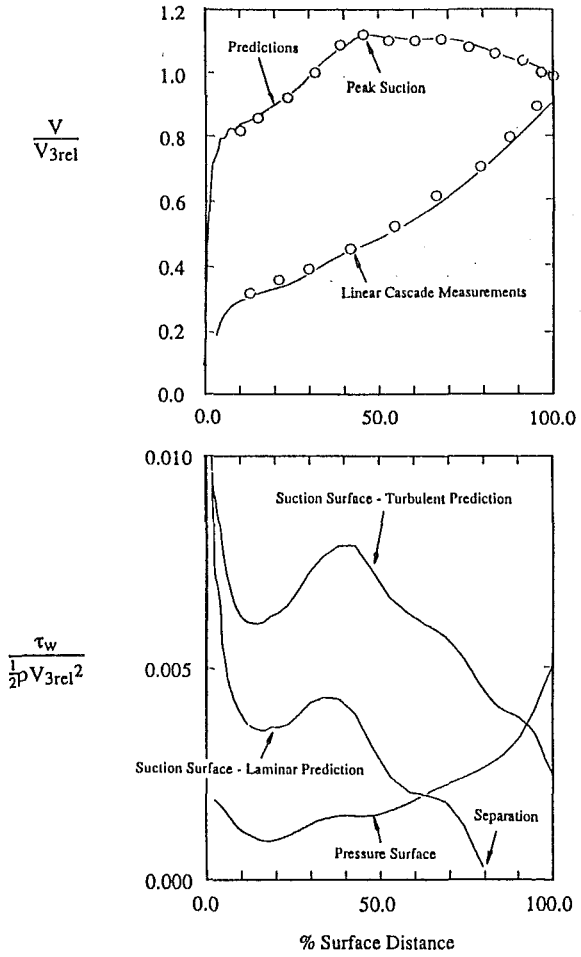

Fig. 2 Rotor midspan isentropic surface velocities and boundary layer predictions: Re = 3.15 x 10^5, $\phi = 0.498$ ($i = 0$ deg)

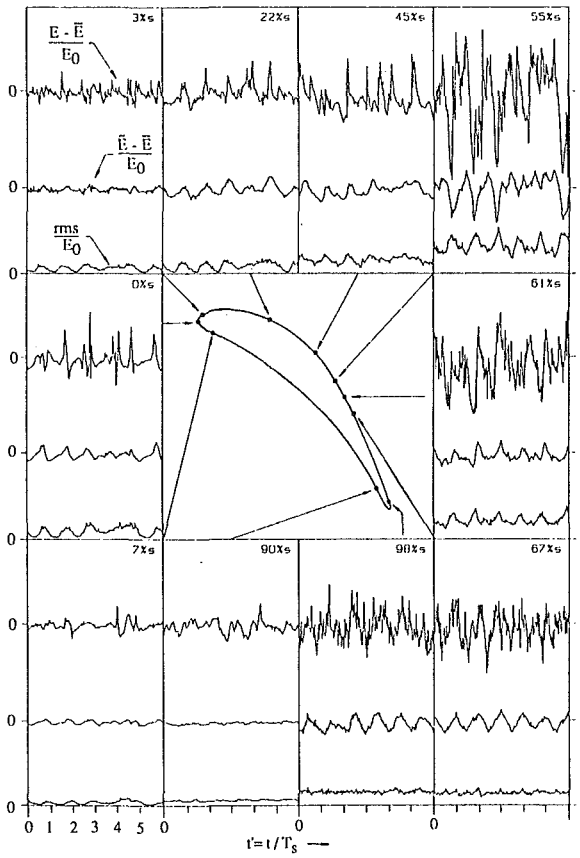

Fig. 3 Rotor midspan hot-film results: Re = 3.15 x 10^5, $\phi = 0.498$ ($i = 0$ deg)

turbulent boundary layers is relatively high until after peak suction. In the laminar case, separation is predicted near 79 percent s.

Examples of the hot-film data obtained at the design Reynolds number are shown in Fig. 3. Each box contains the data from one hot film. For each of the gages, the fluctuating component of the raw signal and the ensembled mean are shown together with the ensembled rms. The vertical scale in this and other figures is the same in all cases. In each of the traces, the time ordinate has been nondimensionalized with respect to the stator wake passing periods, so that $t' = t/T_s$. The reader may notice that in these and other hot-film results, the disturbance caused by each stator wake is not identical. This is due to six support struts, which are equispaced around the circumference in the inlet section of the rig and which shed wakes onto the 36 downstream stator blades. Consequently, every sixth stator blade has an artificially thickened wake. This can be seen, for example, near $t' = 4$ in the rms traces of the leading edge gage (0 percent s) of Fig. 3.

Figure 3 shows that at the geometric leading edge (0 percent s), the continual movement of the instantaneous stagnation "point," which occurs as the stator wakes intersect the leading edge, results in relatively high levels of phase-locked periodic unsteadiness. The raw data are characterized by the periodic occurrence of sharp spikes interspersed by relatively slow variations. These spikes do not appear in the ensembled mean signal. In the presence of the wakes therefore, relatively high levels of random unsteadiness are indicated by the rms traces. These may be a consequence of decelerating the turbulent wake flow toward the stagnation region, cycle-to-cycle variations, or vortex shedding within the stator wakes. Reference to the results from gages adjacent to the leading edge shows that the stagnation region is limited to just a few percent of the surface distance, which is consistent with the relatively small incidence variation that exists within the wake as indicated by Table 2.

Beyond the stagnation region, the results of Fig. 3 show that on the suction surface, there are three distinct regions of flow. The first or laminar region ends before 45 percent s, which corresponds to peak suction. In this region, the raw signals and ensembled mean traces are similar, with only relatively low-amplitude, low-frequency information being present.

The second or transitional region begins near 45 percent s. This is approximately 10 percent s earlier than with a stator–rotor axial gap of 75 percent C_{xs} and 20 percent s earlier than with a gap of 145 percent s [1]. At 45 percent s, Fig. 3 shows that the raw signal contains rapid periodic increases in shear stress followed by short periods of high-frequency fluctuations and then a decay back to the relatively quiescent state. The near-zero values of the rms traces indicate the extent (in time) of the quiescent state. Such traces are typical of those observed in boundary layers undergoing forced transition as a result of the passage of wakes over the blade surface (e.g., [2]). The rapid increase of shear stress in the raw signals signifies a change of state within the boundary layer, that is, from laminar to turbulent flow. The higher frequency fluctuations that follow this increase represent the turbulent fluctuations present within the turbulent patch. The quiescent regions between the turbulent patches therefore correspond to the regions of laminar flow between wakes. As the flow develops further on the suction surface, transition progresses so that by 55 percent s, the rms no longer approaches zero for any part of the wake passing cycle and the regions of higher frequency fluctuations are greater in extent.

At approximately 67 percent s, 15 percent s earlier than at

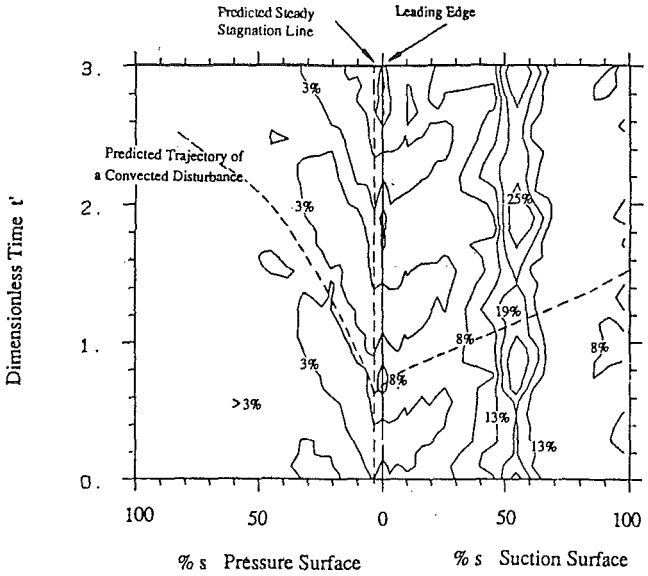

Fig. 4 Surface distance-time plot of hot-film rms: Re = 3.15 x 10^5 and $\phi = 0.498$; contours are of rms/E_0

the larger axial gaps [1], the third or turbulent phase of boundary layer development is entered. In this region, the random and periodic components of the signal are of similar magnitude. The mean level of the rms traces is reduced when compared with those within the transitition region. The variation in the rms is also negligible in the turbulent region. In a transitional boundary layer, the change of state results in a change of heat transfer rate from the hot-film that is much greater than the fluctuations observed in turbulent boundary layers. The raw signals show that this is indeed the case. The periodic variations of the ensembled signal within the transitional boundary layer should also be far greater than those outside the transition region. This does not explain the different amplitudes or mean levels of the rms traces within the transitional and turbulent regions. The rms contains information only about the random content of the traces. Therefore, in the transition region, either the turbulent patch, which develops under a wake, consists of not one but many turbulent spots that occur randomly in the presence of the wake, or the transition process itself is extremely sensitive to any cycle-to-cycle variations that may occur. A much closer inspection of the raw hot-film signal near the start of the transition region shows that separate spots do exist and in some cases, are in the process of merging. This random occurrence of turbulent spots also explains why, in the transition region, the amplitude of the ensembled signal is much less than that of the raw signal.

The occurrence of three distinct phases of boundary layer development noted above is well known in the case of steady cascade flows, where laminar flow gives way to transition and then turbulent flow. In the literature, however, little attention has been paid to the extent of the first of the three regions noted in the presence of wakes. Indeed, in previous investigations [1] of the present turbine, the primary flow regime was believed to be one of a relaminarizing turbulent flow rather than what now appears to be a disturbed laminar boundary layer. A further discussion of these aspects can be found below and in a companion paper to the present work [16].

So far, the discussion has been concerned with the development of the flow on the suction surface. However, Fig. 3 also contains results obtained on the pressure surface at the design condition. Initially, the boundary layer state is similar to that on the suction surface, but whereas transition occurs on the suction surface, the characteristic waveforms associated with transition never materialize on the pressure surface. There is very little evidence of either random or periodic unsteadiness. The raw signals show that the unsteadiness that does exist occurs mainly at relatively low frequencies. The rate of decay of the unsteadiness on the pressure surface becomes evident when it is remembered that the mean shear stress rises continuously on this surface (Fig. 2). A comparison with the results of [1] shows that these results are very similar to those obtained at the larger axial gaps of 75 and 145 percent C_{xs}.

The character of the hot-film signals has been used to identify the state of the blade surface boundary layers. The changes of state are particularly characterized by the rms traces. In view of this, the rms data from each of the hot-film gages have been combined into the surface distance–time plot of Fig. 4. As in previous plots, the time is nondimensionalized with respect to the stator passing period. The contours shown are of the rms levels nondimensionalized with respect to the zero-flow voltage. Figure 4 also contains the predicted trajectory of small disturbances, which are convected with the free stream. The phase of the trajectories has been arbitrarily chosen best to aid the interpretation of the data.

Many of the trends noted in Fig. 3 are summarized in Fig. 4. From the initially high levels of unsteadiness around the leading edge, distinct regions of high and low levels of random unsteadiness emerge. On the pressure surface, these regions simply extend to the trailing edge, since the boundary layer does not undergo a change of state. The regions of high unsteadiness are convected at the local free-stream velocity and must therefore be a direct result of the impingement of the wake on the pressure surface, since the convection rates of small-amplitude disturbances are known to be much less than in the free stream. This means that disturbances present within the boundary layer are very rapidly damped, since individual elements of the boundary layer must experience alternating levels of high and low free-stream disturbances.

On the suction surface, Fig. 4 shows that the development of the boundary layer does indeed consist of the three distinct regions of flow. Over the initial part of the surface, the state is similar to that on the pressure side and the random unsteadiness within the boundary layer is convected with the wake in the free stream. Therefore, although there is undoubtedly an injection of unsteadiness into the boundary layer at the leading edge, it is again the random unsteadiness generated by the wake that dominates the initial development of the suction surface boundary layer. At 45 percent s, transition of the suction surface boundary layer begins. In Fig. 4, this process first manifests itself as an increase in the rms values within the wake affected region. As other experiments have shown (e.g., [2, 6]), the trailing edge of the transitional patch lags behind the free stream so that the turbulent patches caused by successive wakes merge to form a continuously turbulent boundary layer. Downstream of the transition region, the rms levels still vary as a result of the wake interactions, but the levels themselves are much reduced, as has already been discussed above.

Reynolds Number Variation. The relevance of Reynolds number to the performance of steady flow turbine cascades is well known. At Reynolds numbers less than 10^5, many profiles behave in a laminar fashion with profile loss coefficients that vary as $Re^{-1/2}$. At Reynolds numbers above 10^6, many profiles are described as turbulent, with losses that vary as $Re^{-1/5}$. In between these limits, it is impossible to generalize since the process of transition is dependent upon many different parameters. This section reports the effects of changing Reynolds number upon the boundary layer development and consequent profile loss of the turbine rotor midspan section. The Reynolds numbers investigated extend from 1.8×10^5 to 3.3×10^5, which is the range within which many cascades begin to stall.

The midspan section of the rotor has previously been in-

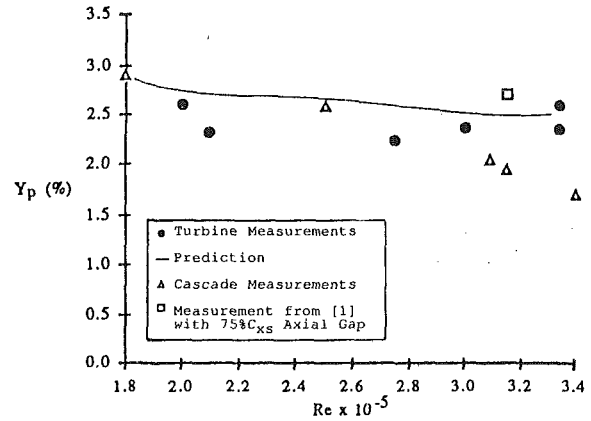

Fig. 5 Variation of rotor midspan profile loss with Reynolds number: $\phi = 0.498$ ($i = 0$ deg)

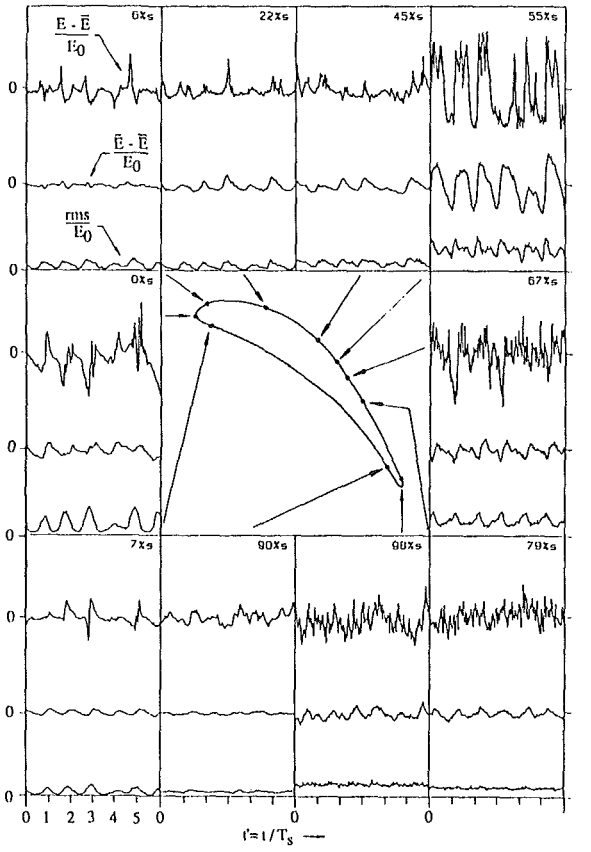

Fig. 6 Rotor midspan hot-film results: Re = 1.80 x 10^5, $\phi = 0.498$ ($i = 0$ deg)

vestigated in a cascade [1] where, at the design Reynolds number, it is known to have laminar boundary layers on both of the blade surfaces. On the suction surface laminar separation occurs at approximately 79 percent s with reattachment not quite occurring by the trailing edge. A laminar vortex street forms downstream of the blade. The area-averaged midspan stagnation pressure loss coefficient, based upon exit dynamic pressure, was equal to 0.0195. Further measurements [17] have since been obtained in the same cascade. At lower Reynolds numbers, gross separation occurs and more loss results, while at a Reynolds number of 3.4×10^5, turbulent reattachment occurs just prior to the trailing edge and the overall loss is slightly reduced.

Figure 5 summarizes the results of the exit traverses carried out behind the turbine rotor at midspan. The profile loss coefficients were obtained by area integration of the measured values. The scatter in the experimental data is most probably because it was necessary to assume that the measured stagnation pressure between the rotor wakes represented the zero loss level. The linear cascade results and the mass-averaged value obtained at the larger axial gap of 75 percent C_{xs} are also shown for reference. The predictions shown in the figure will be discussed below. In the turbine, the profile loss is almost independent of Reynolds number, while in the cascade, it increases significantly as the Reynolds number is reduced. These differences in behavior between the rotor and cascade can be traced, as expected, to differences in the transition process on the suction surfaces, and it is encouraging to note that the apparent working limit of the turbine rotor can be extended to lower Reynolds numbers than cascade tests would suggest.

Hot-film data were obtained at off-design Reynolds numbers of 1.8, 2.4, and 3.3×10^5. On the suction surface, the boundary layers experienced the three phases of development described above at each of the Reynolds numbers investigated. The differences are restricted to differences in the levels of unsteadiness present and the locations of the start and finish of transition. On the pressure surface, the boundary layers are disturbed only by the presence of convected phenomena, the disturbances being least at the highest Reynolds number. This decrease is due to changes in ambient temperature, which affect the sensitivity of the hot-films. In fact, the general level of signals should be higher owing to the increase in heat transfer that occurs in a single state boundary layer as the Reynolds number is increased. The boundary layers are also more susceptible to free-stream disturbances at the higher Reynolds numbers.

Figure 6 shows the traces obtained at the lowest Reynolds number of 1.8×10^5. A comparison of Figs. 3 and 6 confirms that the differences in boundary layer development at the two Reynolds numbers are slight. At the lower Reynolds number on the pressure surface, the boundary layers are again disturbed but laminar in the presence of the wakes. Indeed, it is only in the transition region on the suction surface that any significant differences occur. A comparison of the hot-film traces obtained on the suction surface shows that at the higher Reynolds number, transition is further advanced at 45 percent s than at the lowest Reynolds number, where it has only just begun. As a result of the decreased Reynolds number, transition is largely complete by 79 percent s rather than by 67 percent s.

Previous results [7] obtained in the turbine show that the wake may be modeled as a negative jet. Reference to this model shows that in the free stream, adjacent to the suction surface, the velocity waveform should be characterized by an increase in velocity as the wake approaches, a rapid decrease to below the undisturbed value as the centerline of the wake passes by, and then a rise to the undisturbed value. On the pressure side, this wave form should be inverted. Near the leading edge, the boundary layers are relatively thin so that the ratio of the time required for a disturbance to diffuse across the boundary layer to the periodic time of the wake passing is so low that the response should be quasi-steady. In the vicinity of the leading edge, for example 0 percent s and 7 percent s on the pressure surface, Fig. 6 shows that the wave forms of the ensembled mean hot-film signals are indeed similar to the expected pressure side velocity waveforms. The traces obtained at 6 percent s on the suction side are also similar to the expected form. As the boundary layers develop further along the surfaces, the diffusion time increases so that the response will no longer be quasi-steady and the similarity is no longer clearly observed.

The above discussion has centered largely upon the effects of the random unsteadiness (turbulence) within the stator wakes upon the transition process of the blade surface boundary layers. In correlations of the effects of turbulence

Table 3 Rotor midspan incidence and flow coefficients

Flow coefficient	0.82	0.59	0.54	0.49	0.45	0.41	0.35	0.26
Rotor incidence	+40°	+20°	+10°	0°	−10°	−20°	−40°	−60°

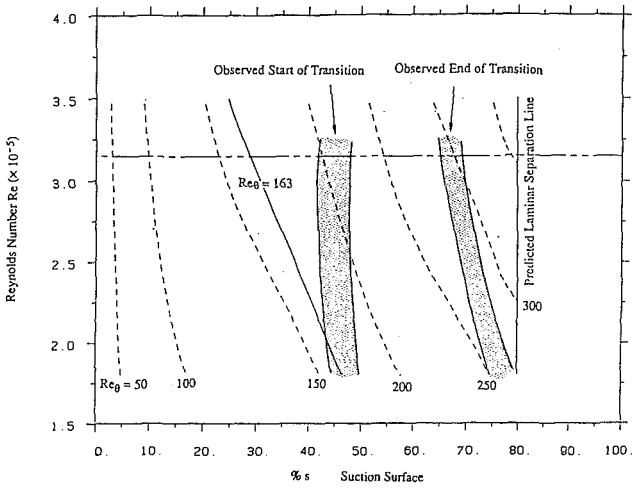

Fig. 7 Variation of predicted suction surface Re_θ and measured rotor midspan boundary layer state with Reynolds number: $\phi = 0.498$ ($i = 0$ deg)

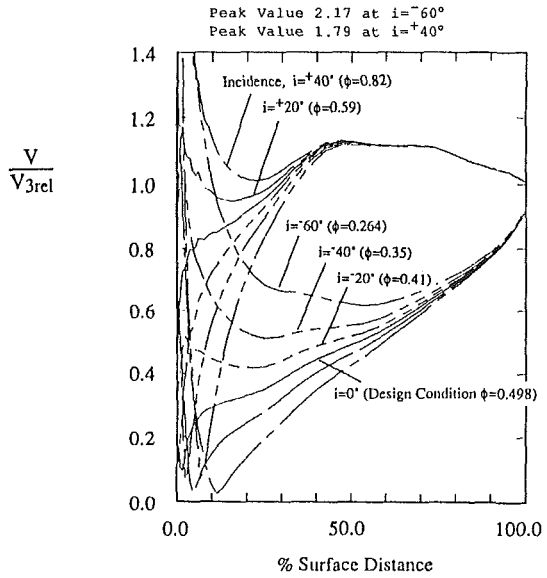

Fig. 8 Variation of predicted rotor midspan isentropic surface velocities with incidence (flow coefficient)

upon transition, the Reynolds number based upon momentum thickness is often of prime importance. In some correlations (e.g., [18, 19]) the effects of the local nondimensional pressure gradient are also included, although as [19] shows, there is little dependence at modest levels (>1.5 percent) of free-stream turbulence intensity, particularly in accelerating flows.

Figure 7 contains a contour map of the predicted variation of momentum thickness Reynolds number Re_θ for laminar suction surface boundary layers as a function of surface distance and chord based Reynolds number. In addition to the contours, the estimated start and finish of transition are also shown. It should be remembered that the contours are of predicted values and that as the measurements of [9] show, the actual values are slightly greater prior to transition.

Figure 7 shows that transition begins when Re_θ reaches a value of between 160 and 205 and that it ceases at a value of between 255 and 300. Transition therefore begins soon after peak suction and ends when the predicted laminar Re_θ would have increased by approximately 95. The correlations of transition in [18–20] suggest that transition will not occur below a value of 163, whatever the external pressure gradient or turbulence intensity. Thus, it is not surprising that laminar flow occurs over the leading portion of the suction surface. Similarly, the pressure side value never exceeds 150, and given the continuous acceleration on that surface, transition should never occur. The correlations and location of the start of transition also suggest that on the suction surface at the higher Reynolds numbers, the free-stream turbulence intensity is approximately 3 percent, whereas at the lowest Reynolds number, it is 5 percent or more. This implies that the stator wake flow and/or the interaction is affected by the changes in Reynolds number, a phenomenon that should be studied in future investigations.

The above conclusions are based upon correlations of steady flow effects. However, given that it is the turbulence in the wakes that appears to cause transition, the use of steady flow correlations might be justified. Indeed, Hart [21] has measured the effects of free-stream turbulence upon a boundary layer typical of that found on a low-pressure turbine suction surface. His results showed that at levels of free-stream turbulence similar to those observed in the present rotor, laminar flow existed in the presence of the turbulence. He observed that although the Reynolds stresses within the disturbed laminar boundary layer were generally insignificant, the nonzero values near the free stream were sufficient to reduce the shape factor below the undisturbed laminar value. Hart's results are therefore consistent with those in [9]. They further support the hypothesis that the flow over the leading portion of the suction surface and over the pressure surface is laminar but disturbed. Figure 7 also shows that as the Reynolds number is reduced, the start and finish of transition move rearward, indicating that at lower Reynolds numbers, laminar separation might not be prevented.

The variation of the average state of the boundary layer within the transition region may be assumed to be approximately linear. Predictions were therefore made of the suction surface momentum deficit by averaging the values obtained from calculations in which transition was specified at the start and end of the measured transition region. This value, together with a prediction of the laminar pressure surface momentum deficit, enabled the profile loss predictions shown in Fig. 5 to be calculated. The agreement between the experimental data and predictions supports the conclusions drawn above regarding the nature of the boundary layer flows. The constancy of the prediction is of course due to the compensating effects of the movement of the transition region and the changes in Reynolds number.

Variation of Flow Coefficient. In this section, the performance of the rotor is investigated over a range of flow coefficients which, as Table 3 shows, covers a range of rotor midspan incidence from approximately −60 deg to +40 deg.

The effect of incidence upon the aerodynamic efficiency of a blade row is primarily related to the extent to which the velocity (or pressure) distribution is modified by a change of incidence. Figure 8 presents predicted rotor midspan velocity distributions, obtained using the method of Whitehead [15], for a range of incidence angles. Joslyn and Dring [8] studied the off-design performance of an axial turbine and showed that providing the blockage from boundary layer separations

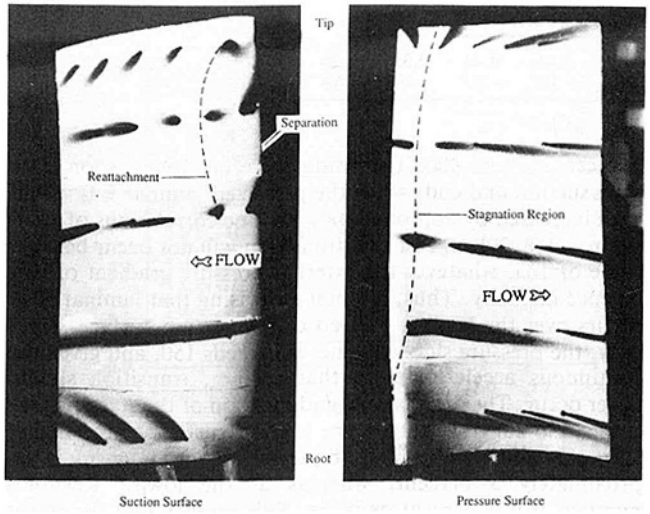

Fig. 9 Rotor surface flow visualization: $Re = 3.15 \times 10^5$, $\phi = 0.82$ ($i = +40$ deg)

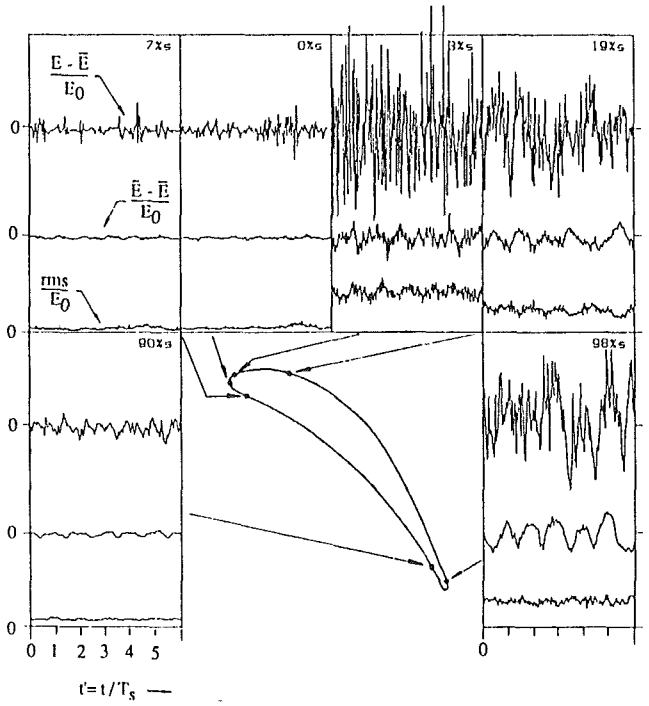

Fig. 10 Rotor midspan hot-film results: $Re = 3.15 \times 10^5$, $\phi = 0.82$ ($i = +40$ deg)

was small, the use of two-dimensional predictions was justified. As in previous plots, the geometric leading edge is the origin of the surface distance coordinate.

Positive Incidence. Figure 9 contains the results of the flow visualization study obtained at a flow coefficient 0.82 ($i = +40$ deg). It should perhaps be noted here that the flow visualization is a time-mean representation of the unsteady flow field. The true stagnation "line" will move backward and forward along the blade surface in response to the unsteady flow. This is thought to explain the bidirectional flows observed in the pressure surface flow visualization near the leading edge at both 30 and 50 percent span. This must also indicate the close proximity of the tappings at 30 and 50 percent span to the stagnation region. At 50 percent span, the flow visualization indicates that the stagnation region occurs near 13 percent s, a value that agrees with that shown in the predictions of Fig. 8 and is consistent with a high angle of incidence.

The velocity predictions also indicate that at $i = +40$ deg, a large leading edge velocity overspeed occurs on the suction surface. As a result of the ensuing diffusion, the flow visualization of Fig. 9 indicates the existence of a leading edge separation bubble over the outermost half of the span. The separation occurs very close to the leading edge while the reattachment "line," also indicated by bidirectional flows, runs from approximately 25 percent s near midspan to 15 percent s near the tip. The reattachment "line" at midspan therefore occurs near to where reacceleration is predicted (Fig. 8). This suggests that reattachment may be due to reacceleration or at least reduced diffusion and not simply transition.

The states of the midspan pressure and suction surface boundary layers have also been investigated with the aid of surface-mounted hot-film anemometers. A selection of traces is shown in Fig. 10. These show that on most of the pressure surface, the development of the boundary layer is similar to that observed at the design condition. The pressure surface boundary layer may therefore be assumed to be in a disturbed but laminar state. A further analysis shows that the pressure side disturbances are again convected at the free-stream velocity.

At the leading edge of the blade (0 percent s), the hot-film traces of Fig. 10 indicate that the suction surface boundary layer is laminar and, compared to other gage locations, virtually steady. The high mean value, when compared with the zero flow voltage, suggests that it is also attached. The rapid acceleration around the leading edge, which is responsible for the presence of this stable laminar boundary layer, must finish soon after, since at the next gage (3 percent s) on the suction surface, very high levels of random, mainly high-frequency unsteadiness exist. The intensity (rms) of the random unsteadiness is affected by the wakes, but is high at all times. The phase-locked periodic unsteadiness is relatively small at this location. These facts suggest that the separation and subsequent transition are dominated by the time-mean flow field but nonetheless affected by the wake passing. At 19 percent s, the raw signal, the ensembled mean, and rms are much more typical of the turbulent boundary layers observed over the rear part of the suction surface at zero incidence. The net heat transfer to the fluid has also increased significantly by this point, a trend that began at 16 percent s, indicating that reattachment is largely complete by 19 percent s. This is slightly upstream of the location indicated by the flow visualization. In contrast to the situation at separation, the traces at 19 percent s show that near the reattachment region, the periodic and random variations are of equal significance. However, it is impossible to determine whether the position of the reattachment "line" is steady or not or, indeed, if the bidirectional spread of the ammonia traces noted above is due to the random (i.e., turbulent) nature of the flow or simply the periodic movement of the reattachment zone. Beyond 19 percent s, the hot-film signals change in magnitude but not significantly in character.

Experiments were also undertaken at a flow coefficient of 0.59 ($i = +20$ deg). At this condition, the flow visualization contained no evidence of a leading edge separation bubble and the stagnation "line" occurred upstream of the most forward pressure side ammonia tappings. As the incidence was reduced, the significance of the tip leakage and secondary flows also decreased. The appropriate velocity distribution of Fig. 8 was again used as input data to the boundary layer prediction method, which predicted that laminar separation should occur near the leading edge of the suction surface at $i = +20$ deg. However, at $i = +18$ deg leading edge separation was not predicted. Given the approximate nature of the incidence calculation and that predicted velocity distributions are being

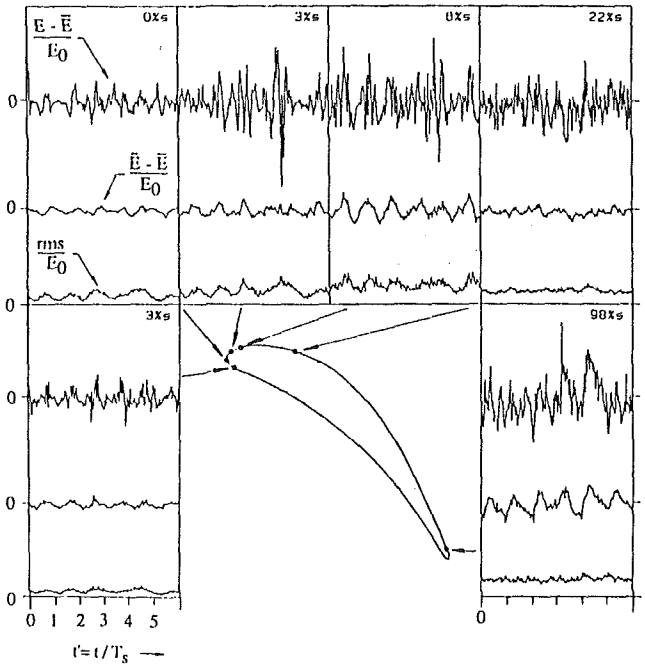

Fig. 11 Rotor midspan hot-film results: $Re = 3.15 \times 10^5$, $\phi = 0.65$ ($i = +20$ deg)

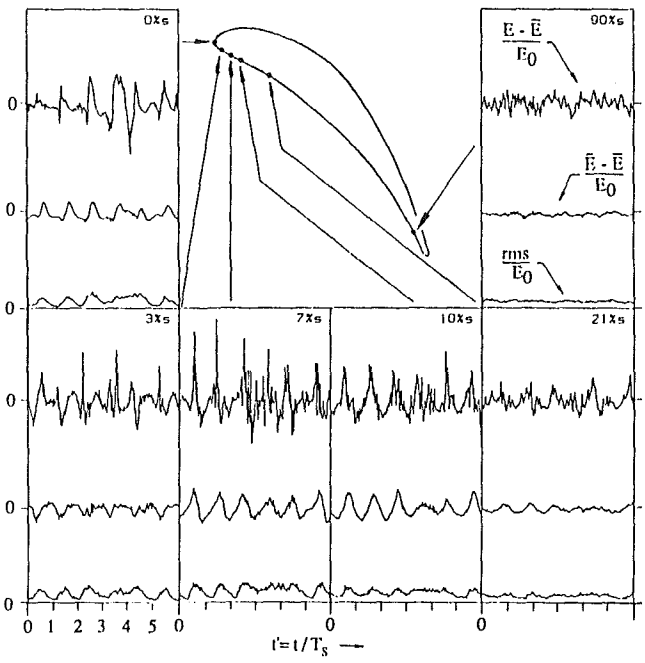

Fig. 12 Rotor midspan hot-film results: $Re = 3.15 \times 10^5$, $\phi = 0.41$ ($i = -20$ deg)

used as input data for the boundary layer code such a discrepancy is not unreasonable. It should however be noted that the boundary layer equations, because there is no upstream influence, tend to predict early separation in regions of very rapid diffusion.

Some of the hot-film data obtained at $i = +20$ deg are shown in Fig. 11. The stagnation region is situated between 0 and 3 percent s on the pressure surface. As in previous cases, a disturbed but laminar boundary layer develops on the pressure surface. On the suction surface, the raw hot-film traces show that transition begins very close to the leading edge. Between 0 and 3 percent s, for example, the intensity of the high-

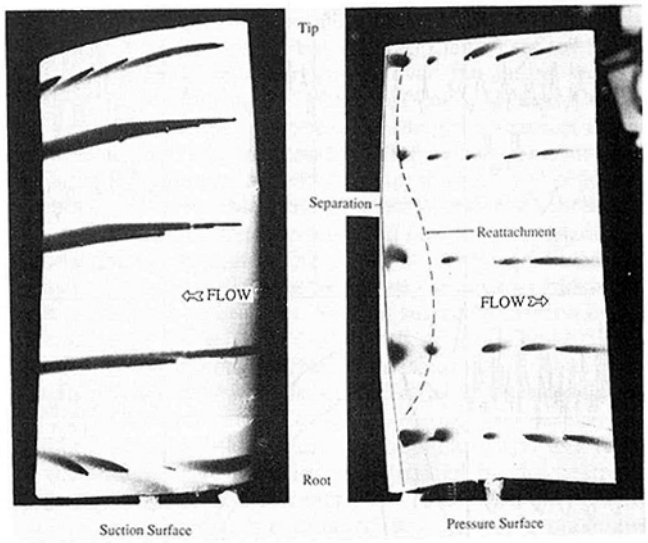

Fig. 13 Rotor surface flow visualization: $Re = 3.15 \times 10^5$, $\phi = 0.35$ ($i = -40$ deg)

frequency random fluctuations increases. At 3 percent s, the regions of low random unsteadiness between the wakes can only just be identified. Given that the velocity distribution at $i = +20$ deg again contains a leading edge overspeed and that separation is predicted to (just) occur, such traces are to be expected. In addition, the raw signals of Fig. 11 at 3 percent s on the suction surface contain many more turbulent spikes than there are wakes (six). This indicates that although transition is, on average, phase locked to the passing of the stator wakes, the process of transition is not simply governed by the presence of turbulence in the wakes. Similar observations have been made regarding the process of transition on the suction surface at the design incidence. Figure 11 shows that by 6 percent s on the suction surface the turbulent spikes have begun to merge with those from adjacent wakes so that a quiescent region between the wakes can no longer be identified in the rms traces. Fully turbulent flow occurs beyond 22 percent s.

Negative Incidence. In this section, the results obtained using the ammonia flow visualization technique and the surface-mounted hot-film gages are presented for a range of reduced flow coefficients. The relevant velocity predictions for the rotor midspan section are presented in Fig. 8.

At $i = -10$ deg of incidence, the predictions suggest that the boundary layers at midspan should be little different to those at the design flow coefficient. The experiments confirmed that this was the case.

At a flow coefficient of 0.41 ($i = -20$ deg), a small amount of diffusion, insufficient to cause laminar separation, is predicted to occur on the pressure surface near the leading edge. The flow visualization experiments confirmed this and showed that the flow is still similar to that which occurs at the design condition. The only differences were the reduced extents of the secondary and tip leakage flow and the slightly greater radially outward shift of the ammonia traces on the suction surface at midspan.

Some of the hot-film data obtained at a flow coefficient of 0.41 ($i = -20$ deg) are presented in Fig. 12. The data obtained on the suction surface were again very similar to those obtained at the design flow coefficient except for a possible but slight movement of the stagnation region onto the suction surface. They are therefore not presented. On the pressure surface however, the initial development of the rotor midspan boundary layer is different to that which occurs at zero incidence. The diffusion that now exists near the leading edge of the pressure surface and is shown in Fig. 8 must explain the ex-

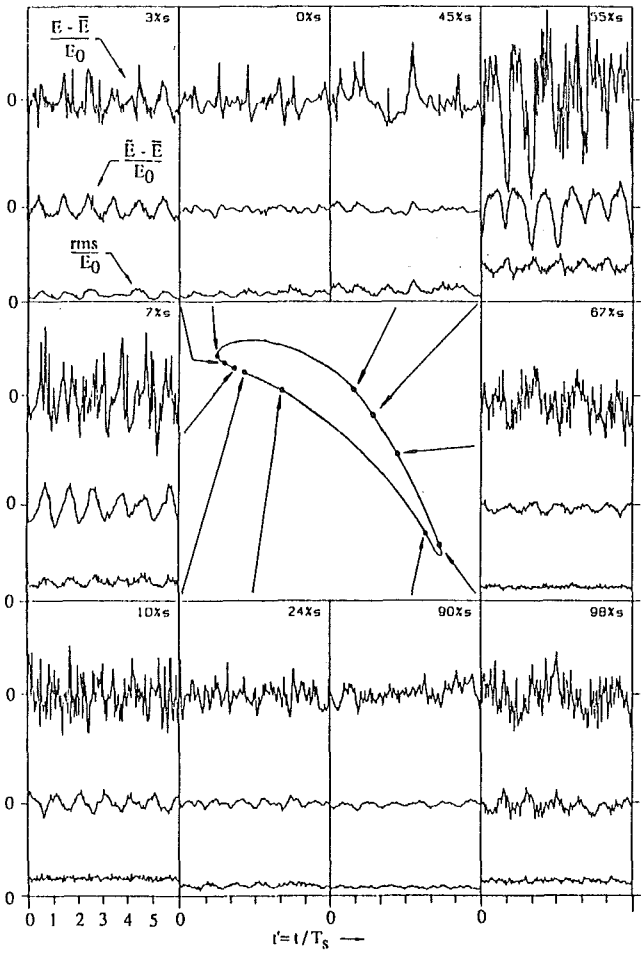

Fig. 14 Rotor midspan hot-film results: Re = 3.15 x 10^5, $\phi = 0.35$ ($i = -40$ deg)

istence of what appear to be the beginnings of turbulent patches at 3 and 7 percent s on the pressure side of the blade. As was the case in the leading edge bubble at +20 deg of incidence, the occurrence of these spikes appears to be random, although on average, they are phase locked to the wake passing. On the pressure surface reacceleration begins near 21 percent s so that the fluctuations are rapidly attenuated and the boundary layer begins to revert to the laminar state.

The flow visualization results shown in Fig. 13 were obtained at a flow coefficient of 0.35 ($i = -40$ deg). At this condition, the pressure surface flow has begun to deteriorate. The reversed flow that occurs over the entire span is due to a pressure side leading edge separation bubble. The position of the separation line near 3 percent s agrees with that predicted for a laminar boundary layer. The sharp cutoff of the upstream movement of the ammonia within the bubble suggests that the position of separation is not influenced by the unsteady inflow. The severity of the pressure gradient is also indicated by the fact that both laminar and turbulent separation are predicted to occur. The apparent reattachment line of this bubble is indicated in the figure. At midspan, reattachment appears to occur near 25 percent s, which is near the point at which the flow begins to reaccelerate.

The hot-film data of Fig. 14 were also obtained at a flow coefficient of 0.35 ($i = -40$ deg). Like the flow visualization, they show that the suction surface flow is little affected by the operation at large values of negative incidence. Transition, for example, still begins near 45 percent s. On the pressure surface, the trends noted above with decreasing incidence continue. At 3 percent s, there is the first occurrence of what again

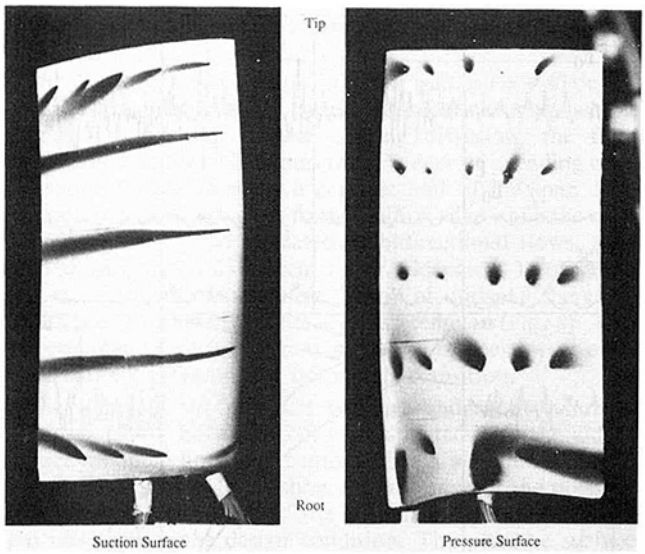

Fig. 15 Rotor surface flow visualization: Re = 3.15 x 10^5, $\phi = 0.26$ ($i = -60$ deg)

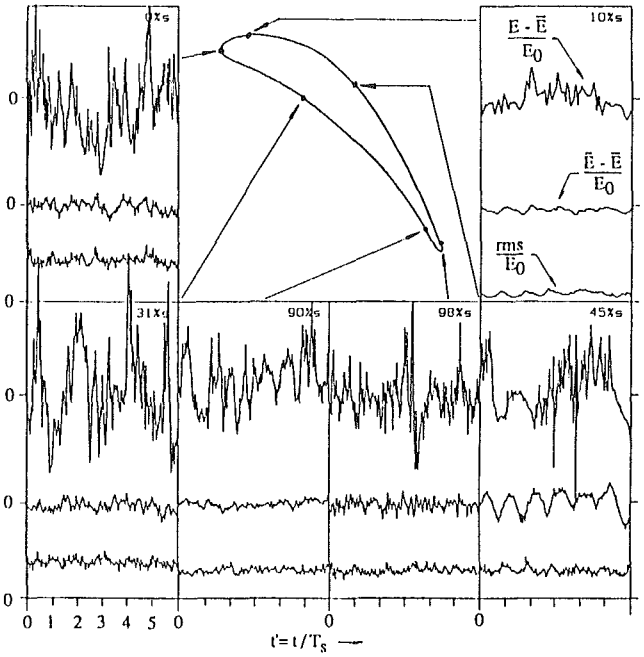

Fig. 16 Rotor midspan hot-film results: Re = 3.15 x 10^5, $\phi = 0.26$ ($i = -60$ deg)

appear to be turbulent spikes or patches. By 7 percent s, many more spikes have formed and there are virtually no quiet periods between the wakes. At 10 percent s, the turbulent patches have merged so that the periodic variation in the rms is reduced and the flow is probably turbulent though separated. Beyond the start of the reacceleration (25 percent s), the pressure surface boundary layer becomes increasingly damped so that by the trailing edge, the higher frequency fluctuations are much reduced in amplitude. Nevertheless, the random levels are greater than at the more positive incidences, suggesting that the pressure surface boundary layer is relaminarizing rather than laminar.

The last set of data was obtained at a flow coefficient of 0.26 ($i = -60$ deg) when, as Fig. 8 shows, there is massive pressure side leading edge diffusion. The appropriate flow visualization is shown in Fig. 15. The pressure side boundary layer has completely separated from the blade surface. The

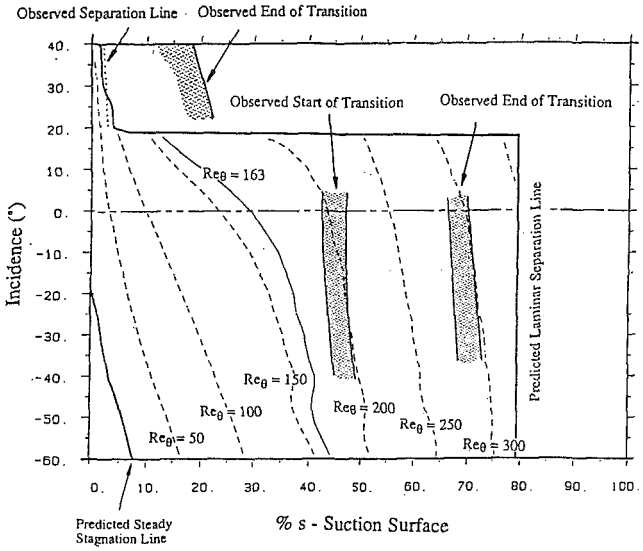

Fig. 17 Variation of predicted suction surface Re_θ and measured rotor midspan boundary layer state with incidence: $Re = 3.15 \times 10^5$

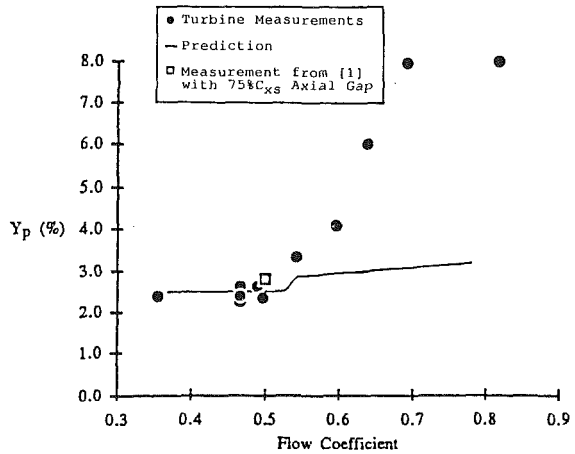

Fig. 18 Variation of rotor midspan profile loss with incidence: $Re = 3.15 \times 10^5$

almost circular traces formed by the ammonia show that diffusion rather than convection dominates the flow near the surface. As a result, the hot-film traces of Fig. 16 show that there is a high degree of random unsteadiness on the pressure surface with very little evidence of any periodic phenomena. The raw signals contain intermittent regions of high frequency, high shear followed by quieter periods of variable length. There is little evidence of phase-locked phenomena. The disturbances occur at a frequency less than that of the wake passing. These and other hot-film traces of Fig. 16 are reminiscent of hot-wire signals observed in stalling axial compressors. Given that there is little if any deflection through the rotor blades at this condition, this may not be surprising. The extent of the pressure side stall is such that for the first time at negative incidence, a significant change in the suction surface boundary layers can be observed. At 45 percent s, which is usually the first gage to show transition, the raw signal appears to contain a patch of laminar flow between two larger bursts of turbulent flow. In contrast to the pressure side results however, the ensembled results at this and other suction side locations contain evidence of wake passing phenomena, although this is less so nearer the trailing edge.

Some of the effects of negative incidence have also been investigated by Joslyn and Dring [8]. In particular, they presented the results of flow visualization experiments and blade surface static pressure measurements. The higher blade loading and differences in hub-tip ratio led to separation of the pressure side boundary layer over the entire span at relatively modest negative incidences (i.e., 15 deg). Nevertheless, their conclusions regarding the gross features of the time mean flow field are broadly in line with the present ones.

Figure 17 contains a contour map showing the predicted variation of Re_θ for a laminar boundary layer as a function of rotor midspan incidence (positive and negative) and blade suction surface coordinate. The positions of the predicted and measured laminar separation lines and the measured locations of transition are also shown. Suction surface transition begins at a value of $Re_\theta = 200$–210 and ends at $Re_\theta = 290$–295 providing that leading edge diffusion does not occur. Thus it appears that the stator wake is little affected by operation at incidence as it is convected through the rotor blade passage. The rapid thickening of the suction side boundary layer as a result of the leading edge diffusion is illustrated by the upstream shift of the Re_θ contours at even $i = +10$ deg. On the pressure surface (not shown), the value of Re_θ reaches a maximum value of 160 near the trailing edge at $i = -20$ deg which, according to available correlations, is still insufficient to cause transition.

Loss Measurements and Predictions. The development of the suction and pressure side boundary layers at midspan has been described above with the aid of flow visualization and hot-film data. In this section, the results of traversing a pitot probe behind the rotor at midspan are presented. Figure 18 summarizes those results. Data were not obtained at the lowest flow coefficient due to the inability of the traverse mechanism to operate under the high centrifugal loads.

The profile loss coefficients of Fig. 18 show that the rotor midspan is virtually unaffected for flow coefficients between 0.35 and 0.49 (-40 deg $\le i \le 0$ deg). Presumably, this would not be the case should pressure side stall occur. The predicted losses, obtained by the method described above, correspond to the measured values for the range of negative incidences shown.

At positive incidence, the existence of suction surface diffusion near the leading edge might be expected to be necessary before the loss is to increase since transition otherwise occurs on the back surface. The predicted loss curve for positive incidence was therefore obtained by specifying transition at the start of this diffusion, should it occur. At a flow coefficient of 0.54 ($i = +10$ deg), the predicted velocity distribution has a very small amount of leading edge diffusion. The reasonable agreement between the measured and predicted loss suggests that the above hypothesis is in fact correct. However, Fig. 18 also shows that the measured loss increases much more rapidly with incidence than does the predicted value. Given that leading edge separation occurs at flow coefficients above 0.59 ($+20$ deg), it is likely that this significant discrepancy can be attributed to the loss generated by the leading edge separation bubble, which is not included in the model.

Conclusions

The midspan performance of a turbine rotor blade has been investigated over a range of flow coefficients and Reynolds numbers.

At the design flow coefficient, the pressure surface boundary layer was found to be laminar. On the suction surface, three different phases of boundary layer development were observed. The initial phase of laminar boundary layer development was followed by transition caused by the wake interactions and then turbulent flow once transition had been completed.

Operation at reduced Reynolds number did not cause the rotor midspan efficiency to deteriorate. On the suction sur-

face, the wake-induced transition prevented laminar separation and the associated loss penalty observed in cascade. Transition moved rearward as the Reynolds number was reduced owing to the increased stability of the boundary layer. This resulted in a near constant loss.

Due to the conservative design of the blading, significant amounts of negative incidence can be withstood before the midspan boundary layers deteriorate. Any disturbances produced in the attached pressure side boundary layer or in a leading edge separation bubble are rapidly damped as the flow accelerates to the trailing edge. The net effect of the wake interactions is small at all negative incidences. Thus, the midspan efficiency remains constant until pressure side stall occurs.

On the suction surface, the interaction of the stator wakes with the boundary layers influences the transition process, but this is only significant when there is no leading edge diffusion ($i < +10$ deg). When there is leading edge diffusion, the wakes affect the transition process, but it is suggested that transition would occur anyway in the presence of leading edge separation. Therefore, operation at positive incidence probably incurs less of a penalty than steady flow cascade measurements would suggest. This is because part of the penalty, in terms of suction surface boundary layer transition, has already been paid at the design condition.

The formation of turbulent patches in the presence of wakes within an otherwise laminar boundary layer has been found to be preceded by the formation of many turbulent spots which then grow to form the turbulent patches.

Acknowledgments

The authors wish to thank the staff of the Whittle Laboratory for their assistance with the work described. They are also grateful to the Central Electricity Generating Board for their support of the flow visualization study.

References

1 Hodson, H. P., "Boundary Layer and Loss Measurements on the Rotor of an Axial Flow Turbine," ASME *Journal of Engineering for Gas Turbines and Power*, Vol. 106, Apr. 1984.

2 Doorly, D. J., and Oldfield, M. L. G., "Simulation of the Effects of Shock Wave Passing on Turbine Rotor Blade," ASME *Journal of Engineering for Gas Turbines and Power*, Vol. 107, 1985, pp. 998–1006.

3 Doorly, D. J., "Modeling the Unsteady Flow in a Turbine Rotor Passage," ASME JOURNAL OF TURBOMACHINERY, Vol. 110, 1988, pp. 27–37.

4 Schultz, D. L., et al., "Wake and Shock Interactions in a Transonic Turbine Stage," *AGARD Conference on Transonic and Supersonic Phenomena in Turbomachines*, AGARD CP-401, Munich, Sept. 1986.

5 Binder, A., "Turbulence Production Due to Secondary Vortex Cutting in a Turbine Rotor," ASME *Journal of Engineering for Gas Turbines and Power*, Vol. 107, Oct. 1985, pp. 1039–1046.

6 Pfeil, H., Herbst, R., and Schroder, T., "Investigation of the Laminar-Turbulent Transition of Boundary Layers Disturbed by Wakes," ASME *Journal of Engineering for Power*, Vol. 105, 1983, pp. 130–137.

7 Hodson, H. P., "Measurements of Wake-Generated Unsteadiness in the Rotor Passages of Axial Flow Turbines," ASME *Journal of Engineering for Gas Turbines and Power*, Vol. 107, Apr. 1985.

8 Joslyn, H. D., and Dring, R. P., "Turbine Rotor Negative Incidence Stall," ASME Paper No. 83-GT-23.

9 Hodson, H. P., "The Development of Unsteady Boundary Layers on the Rotor of an Axial-Flow Turbine," *AGARD Conference on Viscous Effects in Turbomachines*, AGARD CP-351, Copenhagen, June 1983.

10 Hodson, H. P., "The Detection of Boundary Layer Transition and Separation in High Speed Turbine Cascades," presentedat 8th International Symposium on Measurement Techniques in Transonic and Supersonic Flows, Aachen, Sept. 1983.

11 Hodson, H. P., "Boundary Layer Transition and Separation Near the Leading Edge of a High Speed Turbine Blade," ASME *Journal of Engineering for Gas Turbines and Power*, Vol. 107, Jan. 1985.

12 Bellhouse, B. J., and Schultz, D. L., "Determination of Mean and Dynamic Skin Friction, Separation and Transition in Low Speed Flow With a Thin-Film Heated Element," *Journal Fluid Mechanics*, Vol. 24, No. 2, 1966.

13 Hodson, H. P., "Unsteady Boundary Layers on an Axial-Flow Turbine Rotor Blade," Ph.D. Thesis, Cambridge University, Cambridge, United Kingdom, 1983.

14 Cebeci, T., and Carr, W. C., "A Computer Program for Calculating Laminar and Turbulent Boundary Layers for Two Dimensional Time-Dependent Flows," NASA TM-78740, Mar. 1978.

15 Whitehead, D. S., "The Calculation of Steady and Unsteady Transonic Flow in Cascades," Cambridge Univ. Eng. Dept. Report A-Turbo/TR 98., 1980.

16 Addison, J. S. and Hodson, H. P., "A Further Examination of Wake-Boundary Layer Interactions in an Axial Flow Turbine," to be published.

17 Heyes, F. J. G., Whittle Laboratory, Cambridge, private communication.

18 Hall, D. J., and Gibbings, J. C., "Influence of Stream Turbulence and Pressure Gradient Upon Boundary Layer Transition," *J. Mech. Eng. Sci.*, Vol. 14, No. 2, 1972, pp. 134–146.

19 Abu-Ghannan, B. J., and Shaw, R., "Natural Transition of Boundary Layers—the Effects of Turbulence, Pressure Gradient and Flow History," *J. Mech. Eng. Sci.*, Vol. 22, No. 5, 1980, pp. 213–228.

20 van Driest, E. R., and Blumer, C. B., "Boundary Layer Transition; Free Stream Turbulence and Pressure Gradient Effects," *AIAA Journal*, Vol. 1, No. 6, 1963, pp. 1303–1306.

21 Hart, M., "Boundary Layers on Turbine Blades," Ph.D. Thesis, Cambridge University, Cambridge, United Kingdom, 1985.

K. V. Bury
Associate Professor,
Department of Mechanical Engineering,
University of British Columbia,
Vancouver, British Columbia,
Canada V6T 1W5

K. J. W. Spurr
Engineering Consultant,
Vancouver, British Columbia, Canada

Evaluation of Turbine Field Acceptance Tests: a Bayesian Approach

A Bayesian error analysis is developed for treating systematic and random errors of field test data from acceptance tests of large hydraulic turbine installations. A practical procedure is suggested for allocating test points among power levels for a specified statistical precision of efficiency determination.

1 Introduction

The primary purpose of a Field Acceptance Test (FAT) is to decide whether the efficiency of an installed turbine unit falls within a no-payment tolerance band placed about the specified efficiency, or, if not, the amount that must be paid by one contracting party to the other. Recently, a new test procedure was proposed so as to provide a coherent data base from which an error analysis could yield a statistical estimate of the unit's performance at a given precision and confidence level [1]. However, the need for a rational procedure to arrive at a statistically defensible contractual decision still remains.

This paper develops further the work presented in [1], specifically addressing the question of how to combine systematic and random measurement errors. This question is avoided altogether in present Test Codes [3, 4], while the current draft revision of the IEC Test Code [7] suggests, without justification, a root-mean-square combination of these errors. This paper approaches the problem of error combination by treating bias in terms of Bayesian statistics. In addition, a practical procedure is suggested for objectively determining the total number of test points, and their distribution among output levels, in order to obtain a specified precision of efficiency determination at a specified confidence level.

2 Efficiency Evaluation

The efficiency evaluation of an installed turbine compares power output with available power at a number of power levels P_j. The resulting efficiency estimates E_j are typically weighted to provide an overall efficiency estimate

$$E = \sum_{j=1}^{k} a_j E_j \tag{1}$$

where $\sum_{j=1}^{k} a_j = 1$, and the weights a_j are contractually specified. The value E is then compared with a guaranteed (contract) efficiency E_g. Since turbine contracts award large payments to one or the other contractual party as a direct function of both the efficiency deviation $|E - E_g|$ and the experimental error in E, it is of considerable economic significance to estimate that error accurately.

Reference [1] proposes a test procedure by which actual measurements near the required power levels P_j are first transformed to rated head [1, App. 1], and then linearly transformed to P_j [1, App. 2]. The following analysis assumes such transformed efficiencies E_{ij}.

3 Error Analysis

To analyze experimental errors, the ith derived efficiency value E_{ij} (at power level P_j) is expressed as

$$E_{ij} = C \cdot \frac{P_j}{Q_{ij} \cdot H_{ij}} \tag{2}$$

where Q and H are hydraulic discharge and net head. Measurement errors in P_j, Q_{ij}, and H_{ij} translate into an efficiency error with two components: systematic (bias) and random.

3.1 Systematic Errors. After the calibration of all measurement systems there remain residual systematic errors whose magnitude and direction (+ or −) remain unknown. For a given instrument installation the unknown bias magnitude β and its direction are typically fixed. Thus no amount of measurement, short of more precise calibrations, will provide any information regarding the bias. However, *subjective* information is usually available regarding possible values of the bias *magnitude* for a given instrument. This information may have been derived from past experience of more precise calibrations of similar instruments,[1] from instrument calibration statements, or from engineering analysis of the instrumentation system. On the other hand, only rarely can anything be ascertained regarding the *direction* of bias.

Typically, in an engineering analysis of a given instrumentation system, a range of bias values is seen to be possible. Some values in this range are likely to command more confidence (or, conversely, uncertainty) than others in the minds of the engineers doing the analysis. The different "degrees of belief"

Contributed by the Gas Turbine Division for publication in the JOURNAL OF TURBOMACHINERY. Manuscript received by the Gas Turbine Division February 1985.

[1] Reference [5] presents regularly updated calibration limitations associated with specific instrument types. These values may be used as a basis from which to infer the bias magnitude expected of a given instrument.

that express this uncertainty may be quantified by constructing a bona fide probability density function (pdf) for a random variable B, which represents possible values of the (fixed) unknown bias β. In this way valuable (nontest) information regarding bias may be rationally encoded and incorporated into a Bayesian statistical analysis of the overall error in E_{ij}.

In practice the residual bias β (not to be confused with instrument resolution) is expressed as the ratio of measurement bias ΔM to the (unknown) value M of the measured quantity

$$\beta = \Delta M/M. \tag{3}$$

For a given instrumentation system this assessment tends to have the following characteristics:

1 there is a single most likely value for β;

2 the true value β is regarded as equally likely to be greater or smaller than the most likely value;

3 the likelihood of β having a particular value decreases rapidly the farther away it is from the most likely value.

When it is reasonable to attribute the above characteristics to the available bias information, one may assume that the degrees of belief can be encoded by a normal pdf on the random variable B; i.e., $B \sim N(\mu_B, \sigma_B)$. Hence the available bias information need merely be employed to estimate the two bias parameters μ_B and σ_B:

(a) The parameter μ_B is estimated by the most likely value m_B on the basis of instrument calibration statements, etc.

(b) There may be sufficient bias information available to agree on a bias band ($m_B \pm \Delta B$) such that it can be stated to have a 50/50 chance of bracketing the unknown (fixed) bias β. Given m_B and ΔB, the standard deviation σ_B is then estimated by $s_B = \Delta B/0.67$.

An alternative approach is to estimate the "worst-case" bias m'_B and to regard this value as a 99.9 percent confidence limit. Thus σ_B would be estimated as $s_B = |m_B - m'_B|/3$.

In this fashion, a Bayesian normal pdf on bias may be established for each instrumentation system (P, Q, and H). These pdf's are assumed independent of individual measurements.

From the first derivative of (2) the relative efficiency bias β_E is related to the bias in P, Q, and H as

$$\beta_E = \Delta P/P - \Delta Q/Q - \Delta H/H \tag{4a}$$

As a conservative approach to estimating β_E, the terms in equation (4a) may be added

$$\beta_E = \beta_P + \beta_Q + \beta_H \tag{4b}$$

Thus β_E is a normal random variable with mean value μ_{BE} estimated as

$$m_{BE} = m_P + m_Q + m_H \tag{5}$$

and standard deviation σ_{BE} estimated [6] as

$$s_{BE} = (s_P^2 + s_Q^2 + s_H^2)^{1/2} \tag{6}$$

Furthermore, because the relative bias may be assumed independent of power levels P_j, the bias of the weighted average E is unaffected by the weighting scheme (1). Hence, this Bayesian approach yields a normal pdf $N(\mu_{EB}, \sigma_{EB})$ on bias magnitude, with parameters that can be estimated with relative ease, utilizing the available (nontest) information in a statistically defensible way. In contrast to the magnitude of bias, its direction remains unknown. This feature is dealt with in Section 6.

3.2 Random Errors. At a given power level P_j, n_j sets of measurements on Q and H are obtained [1] from which n_j efficiency values E_{ij} are calculated. The random measurement error is defined as the difference between a particular measurement and the long-run average of such measurements. The random error R_{ij} in the corresponding efficiency value is assessed directly from the n_j available calculated values E_{ij}. This error is assumed to be a normal random variable with zero mean and standard deviation σ_j, which depends on the power level P_j. Thus $R_{ij} \sim N(0, \sigma_j)$. The parameter σ_j is estimated at each power level from the data as

$$s_j = \left[\sum_{i=1}^{n_j} (E_{ij} - E_j)^2/(n_j - 1)\right]^{1/2}, \tag{7}$$

where the mean value E_j is obtained as

$$E_j = \sum_{i=1}^{n_j} E_{ij}/n_j$$

3.3 Total Error. It can now be stated that the statistical (Bayesian) model for the calculated efficiency E_{ij} is

$$E_{ij} = \eta_j \pm B_E + R_{ij} \tag{8}$$

Since η_j is constant and both B_E and R_{ij} are normal random variables, it follows that the average efficiency E_j at P_j is also a normal random variable with mean value $(\eta_j \pm \mu_{BE})$ and standard deviation $(\sigma_{BE}^2 + \sigma_j^2/n_j)^{1/2}$ (see [6]). Similarly, from equation (1) the average weighted efficiency E is a normal random variable with mean value

$$\mu_E = \sum_{j=1}^{k} a_j \eta_j \pm \mu_{BE} = \eta \pm \mu_{BE} \tag{9}$$

and standard deviation

Nomenclature

B_E = Bayesian random variable representing β_E
C = dimensional constant
c = estimated in-field cost/test point
E = estimate of η
E_{ij} = ith test point efficiency estimate at P_j
E_j = mean efficiency estimate at P_j (estimate of η_j)
$\pm\Delta E$ = error band on E at confidence α
h = slope of payment function
k = total number of power levels P_j
m_{BE}, s_{BE} = estimates of μ_{BE}, σ_{BE}
n = average number of test points/power level
n_j = number of repeated observations transferred to P_j
P, Q, H = power output, hydraulic discharge, hydraulic head
P_j = contractually defined power level
R_{ij} = random error in E_{ij}
s_E = estimate of σ_E
$s_E(n)$ = estimate of σ_E for n test points
s_j = estimate of σ_j
U = contractual penalty (bonus)
z_γ = standard normal variate at probability level $\gamma = 1 - (1 - \alpha)/2$
β_E = relative bias in E
η = average weighted turbine efficiency
η_j = efficiency at P_j
μ_{BE}, σ_{BE} = mean, standard deviation of B_E
μ_E, σ_E = mean value, standard deviation of E
σ_j = standard deviation of R_{ij}

$$\sigma_E = [\sigma_{BE}^2 \cdot \sum_{j=1}^{k} a_j^2 + \sum_{j=1}^{k} a_j^2 \sigma_j^2 / n_j]^{1/2} \quad (10)$$

This Bayesian model for the quantity E can thus form the rational basis for contract decisions on η. In practice the value μ_E is estimated by the final value E from equation (1), μ_{BE} and σ_{BE} are estimated as outlined in Section 3.1, and σ_j are estimated by equation (7).

4 Assignment of Test Points to Power Levels

One of the practical decisions a test director (impartial third party) has to make in the field is the assignment of the number of test points n_j at each power level P_j. As the weighting scheme (1) suggests, at some power levels the efficiency determination is more critical, requiring relatively more test points, than at other power levels. At the same time, the test director has to plan the test so that the total number of test points $\sum_{j=1}^{k} n_j$ is likely to yield a specified precision ΔE at a given level of confidence α. The following simple distribution scheme is proposed as one meeting the above requirements in an unambiguous way.

Let $n = \sum_{j=1}^{k} n_j / k$ be the average number of valid test points per power level. It is then proposed that the total number of test points kn is to be proportioned among the k power levels as

$$n_j = kna_j \quad (11)$$

This scheme assigns test points to power levels in proportion to the weighting factors a_j, while allowing a prediction of the total test effort kn according to the precision requirement on E as follows.

The Bayesian model of efficiency E is $N(\mu_E, \sigma_E)$, where now

$$\sigma_E^2 = \sigma_{BE}^2 \cdot \sum_{j=1}^{k} a_j^2 + \sum_{j=1}^{k} a_j \sigma_j^2 / kn \quad (12)$$

by substituting equation (11) into equation (10). Since the FAT precipitates only one value of E, it is not possible to use a t statistic for constructing inferences on μ_E with σ_E unknown. However, σ_E can be estimated from (12) as s_E by replacing σ_{BE}, σ_j by s_{BE}, s_j, so that inferences on μ_E can be based on the approximate normal model of E: $N(\mu_E, s_E)$. If the total number of test points kn is at least 25, this approximation is highly accurate. Hence, given a precision requirement on E such that the interval $(E \pm \Delta E)$ is to bracket the (unknown) long-run average of E with statistical confidence α, the total test effort kn can be determined from the relation

$$z_\gamma = \Delta E / \sigma_E$$

as

$$kn = \sum_{j=1}^{K} a_j s_j^2 / [(\Delta E / z_\gamma)^2 - s_{BE}^2 \cdot \sum_{j=1}^{k} a_j^2] \quad (13)$$

Note that in order to evaluate n_j from (11) prior to the FAT, the values s_j must be available as estimates from preliminary tests [1].

In practice equation (13) may not yield a sensible prediction kn if the precision requirement ΔE is too tight with respect to the uncertainty s_{BE} surrounding the bias. Relation (13) may then be used to obtain an alternative, more realistic expectation of precision ΔE for a given bias uncertainty s_{BE} and total test effort kn

$$\Delta E = z_\gamma [s_{BE}^2 \cdot \sum_{j=1}^{k} a_j^2 + \sum_{j=1}^{k} a_j s_j^2 / kn]^{1/2} \quad (14)$$

provided preliminary estimates s_j are available.

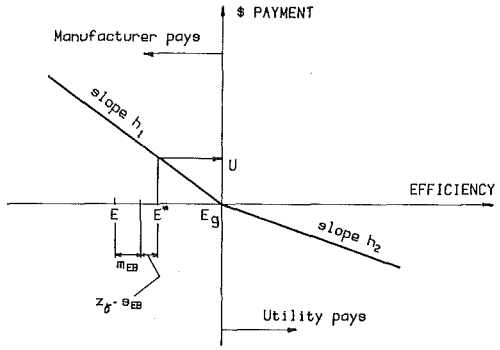

Fig. 1 The payment function and its evaluation for $E < E_g$

From experience [1], the practical limit on the total test effort kn has been found to be around 100 test points, for which equation (14) gives the limiting precision $\Delta E_{\max}$. This limit may be estimated prior to the FAT. If it is found to be unacceptably large, the implication is that it would be worthwhile expending money and effort to reduce the bias standard deviation s_{EB} through better instrumentation.

5 Economics of Additional Test Points

In many cases preliminary estimates s_j are not available, or the turbine contract does not stipulate the confidence level α on the precision ΔE, so that the total test effort kn cannot be planned. In such cases, one may proceed with the FAT in incremental stages until the dollar benefit derived from the improved precision due to additional test points equals the cost of obtaining these points.

If the initial test effort is kn_1 (eg., $kn_1 = 25$ test points), distributed among power levels P_j according to equation (11), then the resulting precision on E is $s_E(n_1)$ from equation (12), where σ_{BE} is estimated as s_{BE} and the σ_j are estimated as s_j from the available data. Next, suppose that additional test points Δn_1 (eg., $\Delta n_1 = 10$) are assigned to power levels P_j so that, cumulatively, relation (11) is satisfied approximately, resulting in the precision $s_E(n_I + \Delta n_1)$ from equation (12). The corresponding improvement in precision is $\Delta s_1 = s_E(n_1) - s_E(n_1 + \Delta n_1)$, and the dollar benefit is $\Delta U = h \cdot \Delta s_1 \cdot z_\gamma$, where h is the slope ($/Δ efficiency) of the payment function (see Fig. 1). The cost of additional test points is $\Delta c = c \cdot \Delta n_1$ where c is the in-field $-cost/test point. Testing then continues in stages until the incremental benefit reaches the incremental cost to within a suitable band of economic indifference, or until a practical limit such as $kn = 100$ is reached.

A running cost-benefit analysis, similar to the one presented, was used by one of the authors during the FAT of a large Canadian turbine installation [1]. This procedure was found to be a highly practical way of rationally deciding the total test effort kn in the field.

6 Contract Decision

Given kn test points, the average efficiencies E_j and the standard deviations s_j of random errors are calculated; see equation (7). The average weighted efficiency E is determined from equation (1), and the standard deviation s_E of the total uncertainty associated with E is estimated; see equation (10).

From equation (9) the decision quantity η may be assessed as $E \pm m_{BE}$. In evaluating the payment function, it is conventional practice to give the benefit of the doubt to the contractual party that is to make payment, by assuming the bias direction in that party's favor. Thus m_{BE} is given the appropriate sign. In addition, an $\alpha/2$-level confidence interval on the random error is used to adjust further the assessment of η in favor of the liable party. Thus, η is assessed as

$$E^* = E + m_{BE} + z_\gamma \cdot s_E \qquad \text{if } E < E_g \quad (15a)$$

Table 1 Cumulative test points and results of test sequence

j	% power level P_j	weighting factor a_j	Stages of Test Sequence 1	2	3	4	5	6
			Cumulative Test Points					
1	100	0.10	3	4	5	6	7	8
2	90	0.25	6	9	11	14	16	19
3	80	0.40	10	14	18	22	26	30
4	70	0.20	5	7	9	11	13	15
5	60	0.05	2	2	2	3	3	4
Total test points per test stage:			26	36	45	56	65	76
Efficiency std.dev. ($s_E \cdot 10^{-4}$)			6.6	6.4	6.0	5.7	5.5	5.4
Payment increment ($\$\Delta U \cdot 10^3$)			--	31.4	62.7	47.0	31.4	15.7
Cost increment ($\$\Delta c \cdot 10^3$)			--	8.0	7.2	8.8	7.2	8.8
Incentive to continue test ($\$ \cdot 10^3$)			--	23.4	55.1	38.2	24.2	6.9

see Fig. 1, and as

$$E^* = E - m_{BE} - z_\gamma \cdot s_E, \qquad \text{if } E > E_g \tag{15b}$$

Hence, the manufacturer pays a penalty

$$U = (E_g - E^*) \cdot h_1, \text{ if } E^* < E_g (\text{or zero if } E^* \geq E_g) \tag{16a}$$

or the utility pays a bonus

$$U = (E^* - E_g) \cdot h_2, \text{ if } E^* > E_g (\text{or zero if } E^* \leq E_g) \tag{16b}$$

where h_1 and h_2 are the slopes of the two segments of the payment function (see Fig. 1).

7 Illustration

For the purpose of illustration, the proposed procedures are applied to the set of actual FAT data described in [1]. However, some of the contractual and other decision quantities, as well as bias estimates, have been chosen arbitrarily.

In this example, the most likely relative bias magnitudes m_B are estimated from instrument certificates and an analysis of signal progression through the instrument system. The extreme (99.9 percent confidence) bias magnitudes m'_B are estimated by analyzing each instrument system under the "worst-case" approach, modified by past calibration experiences. The standard deviations s_B of bias uncertainty are then estimated as $s_B = |m_B - m'_B|/3$:

	m_B	m'_B	s_B
Power	0.0011	0.0020	0.00030
Head	0.0012	0.0020	0.00027
Flow	0.0020	0.0044	0.00080

Hence the most likely relative efficiency bias is $m_{BE} = 0.0043$ from equation (5), and the standard deviation of uncertainty is $s_{BE} = 0.0009$ from equation (6). Assume that the particular turbine contract specifies $k = 5$ power levels at 100, 90, 80, 70, and 60 percent of design output, with corresponding weighting factors $a_1 = 0.10$, $a_2 = 0.25$, $a_3 = 0.40$, $a_4 = 0.20$, and $a_5 = 0.05$. Suppose that the precision ΔE is not specified in the contract, but that preliminary estimates s_j for random efficiency errors are available from exploratory testing: $s_1 = 0.0030$, $s_2 = s_3 = s_4 = 0.0025$, $s_5 = 0.0010$. From relation (14) the limiting precision $\Delta E_{\max}$ for a maximum test effort of $kn = 100$ points is obtained, with α at the conventional 95 percent level ($z_\gamma = 1.96$), as 0.00104. That is, for $kn < 100$ test points, the 95 percent confidence band on E is predicted to be wider than ± 0.00104.

Assuming that the above limitation on ΔE is acceptable to both contractual parties, the FAT may be begun. An initial assignment of $n_I = 26$ points is selected and distributed as per equation (11); see Table 1. The FAT is conducted as described in [1], generating efficiency values from which standard deviations (7) are calculated. The standard deviation of uncertainty on E is calculated from equation (10) as $s_E(26) = 0.00066$. At this point the 95 percent precision is $1.96 \cdot s_E(26) = 0.00129$.

The test continues by assigning a further 10 test points according to equation (11); see Table 1. The resulting standard deviation of E, based on the 36 accumulated test points, is calculated as $s_E(36) = 0.00064$. In this example the weighted efficiency E is found to be less than the guaranteed efficiency E_g, so that the payment slope h_1 applied (see Fig. 1) with the value \$800,000/0.1%E. Thus, the benefit of the decreased value S_E is $\Delta U = 8 \times 10^8 \cdot 0.00002 \cdot 1.96 = \$31{,}400$. The cost coefficient c is \$800, based primarily on the cost of the test crew per average time required for measuring a test point. Thus the cost of decreased s_E is $800 \times 10 = \$8{,}000$, and the incentive to continue testing is \$23,400 at this point. See Table 1 for a continuation of the procedure. After 76 test points the incentive of \$6900 is deemed insufficient, and the test series is terminated. Note that the rate of change of s_E from stage to stage is not smooth, as it depends on the random outcome of each test point.

The assessment of the decision quantity η is according to equation (15a), with $m_{BE} = 0.0043$, $z_\gamma = 1.96$, and $s_E = 0.00054$. In this example, the manufacturer is assessed the penalty $U = (E_g - E - 0.0043 - 1.96 * 0.00054) * 8 \times 10^8$ by relation (16a), where E is the final derived weighted efficiency, based on the 76 test points.

8 Conclusions

A Bayesian treatment of measurement bias has been presented that yields a normal distributional model for the total measurement error in turbine efficiency evaluation. This model allows for a statement of statistical precision on the efficiency value. Nontest information is used in a simple way to quantify uncertainty regarding the magnitude of bias error, in terms of estimating two bias parameters. These estimates may be based on the specific instrument calibration statements relevant to the FAT, or on systematically compiled and updated published information for instrument classes. The normal model of efficiency error allows the total test effort to be chosen in accordance with a requirement of statistical precision, or in accordance with the economics of continuing the test effort incrementally.

A practical scheme has been proposed for sensibly distributing field test points among required power levels such that the highest precision is obtained at the most frequently used operational power levels, consistent with the intent of the contractually defined weighted efficiency.

The proposed analyses are equally applicable to field acceptance tests of turbines or pumps, provided a coherent data base exists, as may be obtained by the test procedures proposed in [1].

References

1 Bury, K. V., Spurr, K. J. W., and Lang, J. H., "Recent Developments in the Field Testing of Large Turbines," ASME JOURNAL OF ENGINEERING FOR POWER, Vol. 107, July 1985, pp. 555-559.

2 Moffat, R. J., "Contributions to the Theory of Single Sample Uncertainty Analysis," ASME *Journal of Fluids Engineering*, Vol. 104, 1982, pp. 250-260.

3 "Power Test Code," ASME, 1949, No. 18.1.

4 "International Code for the Field Acceptance Tests of Hydraulic Machines," Central Bureau of the Electrical Commission, Publication No. 41, Geneva, Switzerland, 1963.

5 "Directory," British Calibrations Service, Teddington Mddx, England, 1983; published quarterly.

6 Bury, K. V., *Statistical Models in Applied Science*, Wiley, New York, 1975.

7 "Draft Revision of IEC Publication 41," Central Bureau of the Electrical Commission, Geneva, Switzerland, 1980.

H. Kodama

S. Nagano

Research and Development Department,
Aero-Engine and Space Operations,
Ishikawajima-Harima Heavy Industries,
Tokyo, Japan

Potential Pressure Field by Stator/Downstream Strut Interaction

The potential pressure field caused by stator/downstream strut interaction is investigated analytically and experimentally. It is shown that the small disturbance theory using an actuator disk model gives a good prediction of the forward propagation of downstream pressure perturbations. The calculation method of stator tailoring to shield the upstream field from the effect of downstream struts is also shown and verified by experiments.

Introduction

The interaction between rotor blade and potential pressure field propagating from the downstream stator and strut is a matter of increasing concern, especially because of the effect on turbomachinery noise. Many investigations on the tone noise generated by rotor/stator/strut interaction have been done using a test engine (Woodward and Balombin, 1984) and a model fan rig (Ho, 1981; Nakamura et al., 1986). In addition, detailed unsteady pressure field caused by the interaction on the rotor blades was also investigated (Ng et al., 1987).

The usual design procedure to reduce the influence of downstream pressure distortion on rotor blade is to increase the axial spacing betwen rotor blade and strut. However, this adds unnecessary weight to the engine. Consequently, it is required to make an effort to understand the manner of propagation of downstream distortion and tailor the flow to shield the rotor blade from the effect of downstream strut.

The most widely used method to predict the potential pressure field due to stator downstream strut interaction is the Douglas–Neumann singularity superposition method (Barber and Weingold, 1978; O'Brien et al., 1985). The method is also applied to the design of stators to block the strut thickness effect (Rubbert et al., 1972). In the method, the boundary of each body is approximated by a large number of line-segment elements and the strengths of singularities distributed over a line-segment element are calculated to satisfy the zero through-flow condition along the body surfaces. This leads to a set of linear algebraic equations and the number of equations is related to the total number of line-segment elements. In the case of stator downstream strut interaction, all stator vanes existing in one cyclic circumferential distortion have to be treated in the calculation. It sometimes happens that, because of a large number of stator vanes, the calculation requires unsatisfactory computing time or unacceptable capability of computer storage. On the other hand, an analytical method using a small disturbance theory (Kodama, 1986) replaces the stator row by an actuator disk and reduces the problem of determining the disturbance flow quantities to that of solving a small number of linear algebraic equations for each harmonic component of the distortion. By combining the actuator disk model with the singularity superposition method in the analysis of stator downstream strut interaction, the computing time can be significantly reduced and its applicability can be also extended within a restricted computer storage.

The objective of the present paper is first to provide an assessment of the accuracy of an actuator disk model by making detailed comparisons between calculated and measured results for the case of stator interaction with downstream strut, and secondly to show the method, using an actuator disk model, of stator tailoring to screen the effect of downstream strut. Verification of the method with experimental data is also included.

Potential Pressure Field Calculation Method

An actuator disk model assumes that the circumferential wavelength of disturbances is much larger than the vane spacing. Further it is assumed that the flow turning, streamline contraction, and total pressure losses occur suddenly at the actuator disk plane. In the theory, the governing equations for an ideal, inviscid, isentropic (but not homoentropic) compressible fluid are linearized using the assumption that the perturbation quantities are sufficiently small compared to the mean quantities. The linearized equations are applied to the upstream and downstream flow field of the actuator disk separately. In order to join the separate flow fields, the physical boundary conditions are introduced at the actuator disk plane. They are the conservation of mass, the conservation of energy, the change in total pressure loss due to circumferential variation in inlet flow, and the specified flow direction at the trailing edge plane of the cascade. Appropriate detailed description of the theory is given by Kodama (1986). Because of the linearized nature of the solution, the circumferential profile of the perturbation can be decomposed into pure harmonic components, and the analysis is carried out for each harmonic perturbation. There is no total pressure or total temperature distortion upstream of the stator. For simplicity, the variation of stator pressure loss due to circumferential variation in inlet flow direction is neglected. Consequently, the vorticity and entropy waves disappear in the present analysis, so that all

Contributed by the International Gas Turbine Institute and presented at the 33rd International Gas Turbine and Aeroengine Congress and Exhibition, Amsterdam, The Netherlands, June 5-9, 1988. Manuscript received by the International Gas Turbine Institute September 11, 1987. Paper No. 88-GT-54.

perturbations are composed of the two waves related to an irrotational field, in which one is attenuated in the upstream direction and the other in the downstream direction. The perturbation components of pressure, velocities, and density are expressed by

$$\frac{p}{p_0} = \left\{C_1\exp(\lambda_1 x) + C_2\exp(\lambda_2 x)\right\}\exp(iky) \tag{1}$$

$$\frac{u}{a_0} = \left\{ -\frac{1}{\kappa}\frac{\frac{\lambda_1}{k}}{M_x\left(\frac{\lambda_1}{k}\right) + iM_y} C_1\exp(\lambda_1 x) \right.$$

$$\left. -\frac{1}{\kappa}\frac{\frac{\lambda_2}{k}}{M_x\left(\frac{\lambda_2}{k}\right) + iM_y} C_2\exp(\lambda_2 x) \right\} \times \exp(iky) \tag{2}$$

$$\frac{v}{a_0} = \left\{ -\frac{1}{\kappa}\frac{i}{M_x\left(\frac{\lambda_1}{k}\right) + iM_y} C_1\exp(\lambda_1 x) \right.$$

$$\left. -\frac{1}{\kappa}\frac{i}{M_x\left(\frac{\lambda_2}{k}\right) + iM_y} C_2\exp(\lambda_2 x) \right\} \times \exp(iky) \tag{3}$$

$$\frac{\rho}{\rho_0} = \frac{1}{\kappa}\left\{C_1\exp(\lambda_1 x) + C_2\exp(\lambda_2 x)\right\}\exp(iky) \tag{4}$$

where

$$k = \frac{2\pi n}{L} \tag{5}$$

$$\lambda_1 = \frac{k}{1-M_x^2}\left\{iM_xM_y + \sqrt{1-M_x^2-M_y^2}\right\} \tag{6}$$

$$\lambda_2 = \frac{k}{1-M_x^2}\left\{iM_xM_y - \sqrt{1-M_x^2-M_y^2}\right\} \tag{7}$$

In the upstream flowfield of the stator, there is no pressure perturbation that propagates from the upstream ($C_{2u}=0$), and the pressure perturbation due to downstream strut and pylon is given (C_{1d} is given). Thus two unknowns (C_{1u}, C_{2d}) should be determined from the following boundary conditions at the actuator disk:

- Conservation of mass flow through the actuator disk
- Specified flow direction at the actuator disk exit

Experiment

Model Rig. The test of stator downstream strut interaction was carried out using an annular model rig. As shown in Fig. 1, the rig consists of a bellmouth entry, a preswirl unit designed to simulate the stator entry flow, and a working section consisting of a model of the stators, struts, pylons, and annulus passage. The air then enters a section of parallel annulus, in which both top and bottom pylons are maintained at constant width and height. The model test was performed on the suction facility.

The top pylon has a 28-deg wedge blending into a 94-mm-wide slab-sided structure, and the bottom pylon starts with a similar wedge but blends into a narrower 39-mm slab-sided structure. In each case the leading edge of the pylon is swept at 7.5 deg.

There are eight struts in addition to the top and bottom pylons. Each strut has the same uncambered profile with a chord length of 43.5 mm and a thickness/chord ratio of 22.5 percent. Leading edges of the struts are swept at 7.5 deg and lie in approximately the same axial position as the pylon leading edges. The struts are staggered by rotating them about an axis parallel to the strut leading edges, and the axes are located at 30 percent chord from the leading edges. The circumferential position of the struts is defined by placing the pivot axes at equal intervals of 36 deg around the duct.

The stator ring consists of 60 aerofoils at an equal pitching of 6 deg. The aerofoils have a chord length of 18 mm and the shape has no radial variation. The leading edges of stator are also swept at 7.5 deg.

The circumferential arrangement of pylons, struts, and stator vanes is shown in Fig. 2.

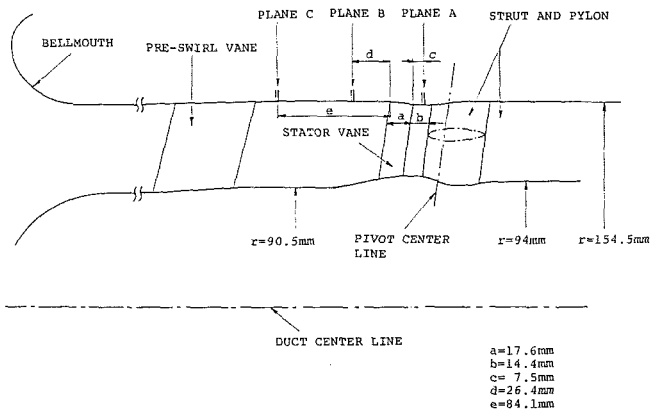

Fig. 1 Schematic of model rig

Nomenclature

a_0 = velocity of sound
C_1, C_2 = complex coefficient of the pressure perturbation
C_p = static pressure coefficient defined by equation (8)
C = airfoil chord
i = $\sqrt{-1}$
k = parameter defined by equation (5)
L = periodic length scale of cascade
M = Mach number of mean flow
n = circumferential harmonic number
P_0, P = mean and perturbation components of static pressure
r = coordinate in radial direction
U, V = x, y components of mean velocity
u, v = x, y components of velocity perturbation
x = coordinate in axial direction
y = coordinate in circumferential direction
β_0, β = mean and perturbation components of flow angle
κ = ratio of specific heats
λ = eigenvalues of perturbation quantities
ρ_0, ρ = mean and perturbation components of density

Subscripts and Superscripts

0 = mean component of flow quantity
d = downstream of trailing edge plane
u = upstream of leading edge plane
x = x component
y = y component
$'$ = mean value plus perturbation

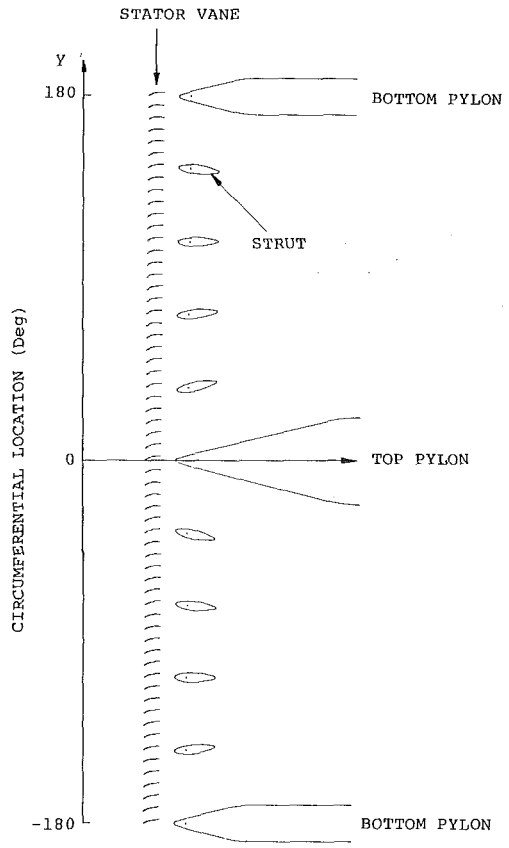

Fig. 2 Circumferential arrangement of strut and pylon

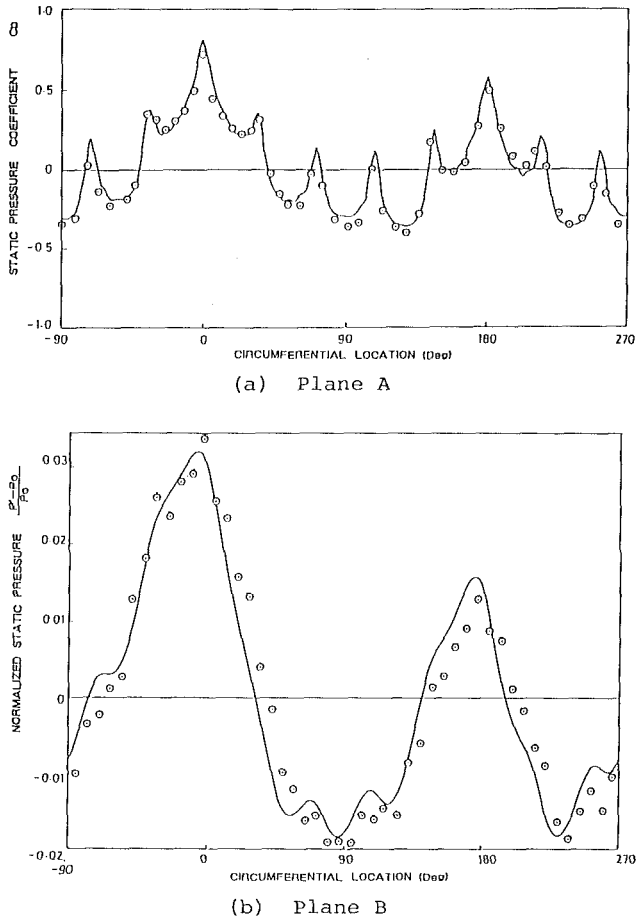

Fig. 3 Comparison of measured and calculated static pressure perturbation (Case 1, M = 0.39): —— calculation; ⊙ measurement

The preswirl unit consists of 13 vanes. The vanes were designed to give a swirl angle of 35 to 37 deg at the stator inlet.

Instrumentation. The instrumentation planes for static pressure distortion measurement are shown in Fig. 1. Plane A was approximately 0.5 stator chord downstream of the stator trailing edge, and approximately midway between stator trailing edge and pylon/strut leading edge at the tip. Plane B was approximately 1.5 stator chords upstream of the stator leading edge. Plane C was approximately 5 stator chords upstream of the stator leading edge.

In order to isolate the effects of the stator and struts from the distortions naturally present in the duct, the pressure coefficients measured in the baseline configuration with no struts or pylons fitted, and with the stator ring fitted, were averaged over the range of flows, and subtracted from the pressure coefficients measured for the various stator/strut/pylon geometries. This has the effect of removing the pressure field downstream of the preswirl unit.

The overall mass flow through the model was measured by an airmeter bellmouth at the entry to the rig, which sucks air from ambient conditions. Four static pressure taps on the wall of the bellmouth, together with a theoretical estimate of the boundary layer growth around the bellmouth and inlet ambient pressure, were used to derive a mass flow. An average Mach number was estimated using the overall mass flow, circumferentially averaged static pressure, and swirl angle.

Comparison Between Calculation and Experiment

The comparisons of calculated and measured results were made in the following strut configurations:

Case 1: Eight struts are all axial.

Case 2: Eight struts are staggered to reduce the induced distortion, but not minimized yet.

Case 3: Relative to Case 2, the stagger angles of the struts adjacent to the top and bottom pylons are increased to minimize the induced distortion.

The comparisons were made at different flows for Cases 1 and 2. All calculations were done at the tip section so as to compare with the outer wall static pressure measurements. Mean components of flow quantities appearing in equations (1)–(4) were estimated from the measurements.

In the analysis, the pressure perturbations due to downstream strut and pylon (C_{1d}) were obtained by the incompressible singularity superposition method. Corrections were made on the strut circulations considering the viscous effect. It should be noted that the stator vanes were not included in this cal-

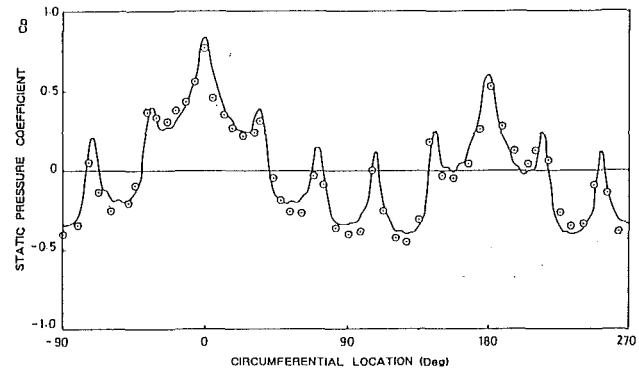

(a) Plane A

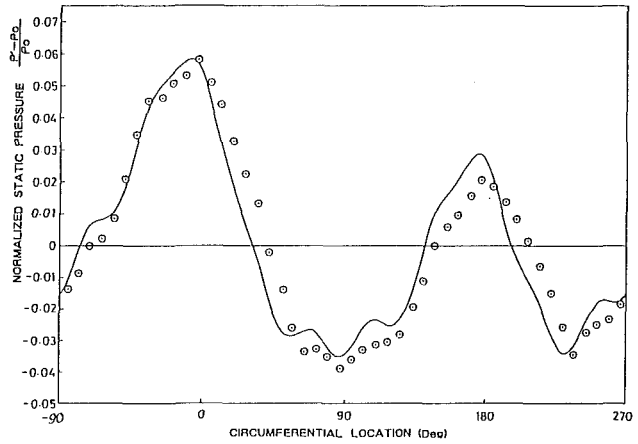

(b) Plane B

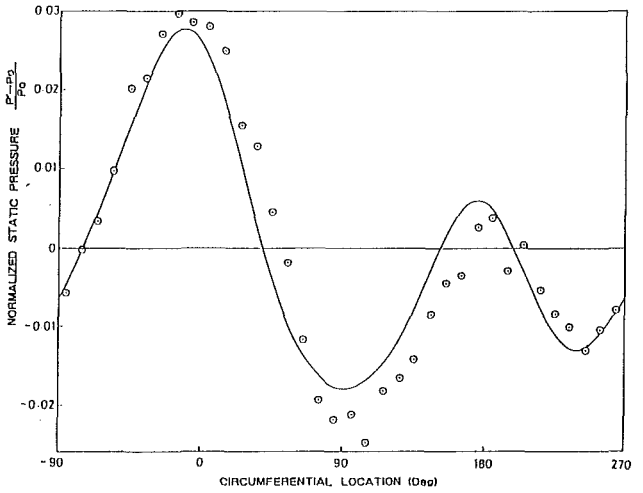

(c) Plane C

Fig. 4 Comparison of measured and calculated static pressure perturbation (Case 1, M = 0.53): —— calculation; ⊙ measurement

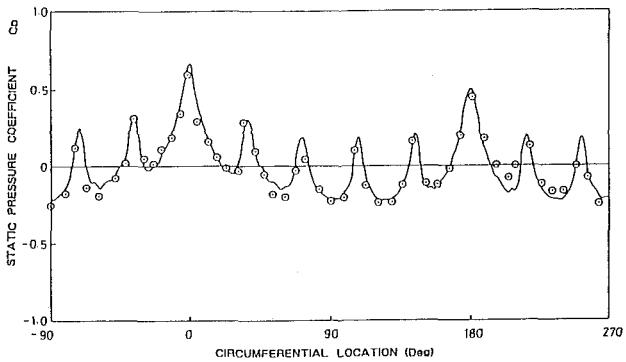

(a) Plane A

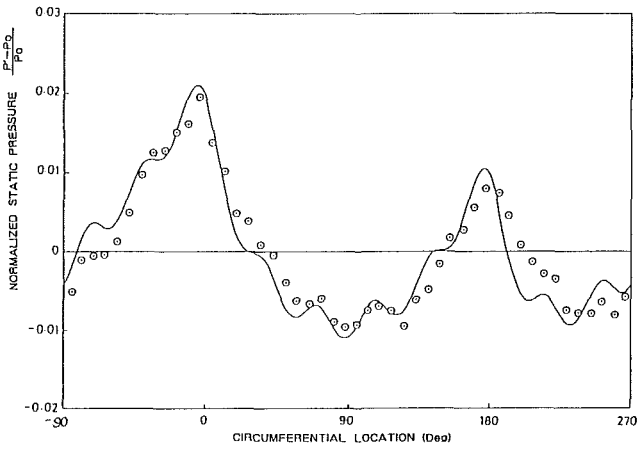

(b) Plane B

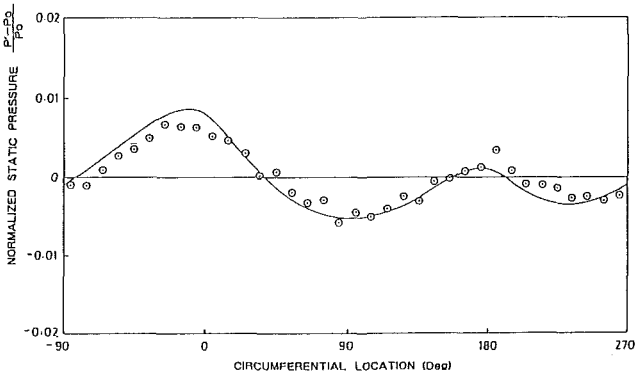

(c) Plane C

Fig. 5 Comparison of measured and calculated static pressure perturbation (Case 2, M = 0.39): —— calculation; ⊙ measurement

culation. The compressibility was taken into account by the Prandtl-Glauert transformation. The results are shown in Figs. 3 to 7. In these figures, Ma denotes the average Mach number at Plane A. The pressure perturbations at Plane A are represented by static pressure coefficients, defined by

$$C_p = \frac{p' - p_0}{\frac{1}{2}\rho_0(U^2 + V^2)} \tag{8}$$

The prediction showed generally good agreement with experimental results.

Calculation Method of Stator Tailoring

This method is another application of a two-dimensional actuator disk model. A circumferential profile of the flow angle at the stator exit to shield the upstream from the downstream pressure perturbation is calculated.

When the upstream of the stator is completely shielded from the effect of downstream strut and pylon, no pressure perturbation exists in the upstream flowfield ($C_{1u} = C_{2u} = 0$). This means that there is no pressure disturbance to cause an interaction with upstream rotor blades. Therefore, it can be assumed that there is no total pressure and total temperature variation in the upstream of the stator. For simplicity, the variation of stator pressure loss due to circumferential differ-

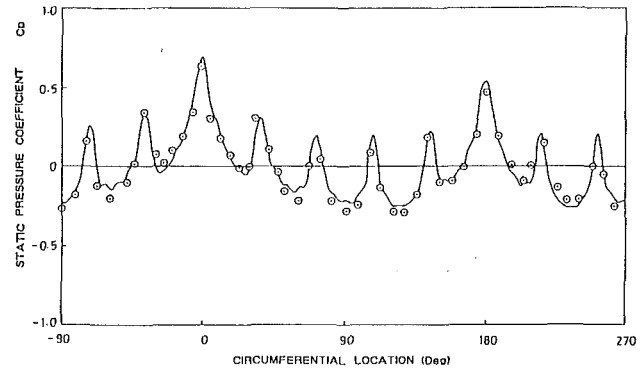

(a) Plane A

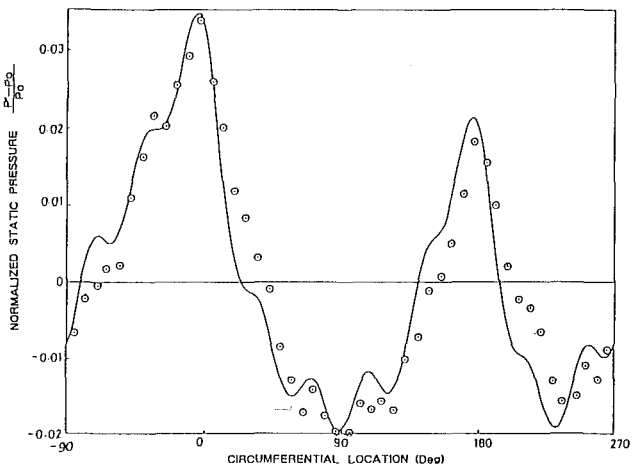

(b) Plane B

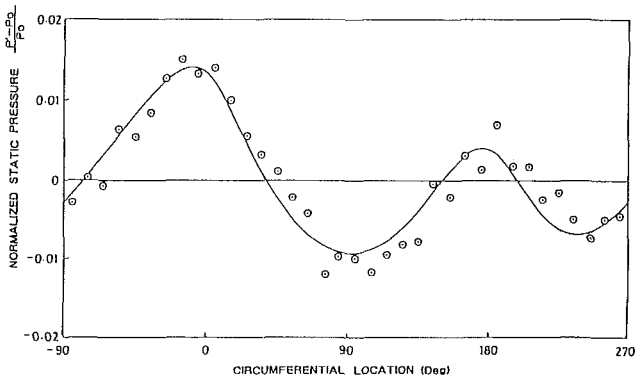

(c) Plane C

Fig. 6 Comparison of measured and calculated static pressure perturbation (Case 2, M = 0.51): —— calculation; ⊙ measurement

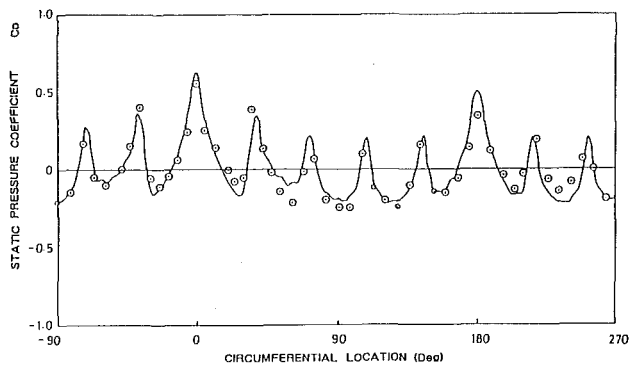

(a) Plane A

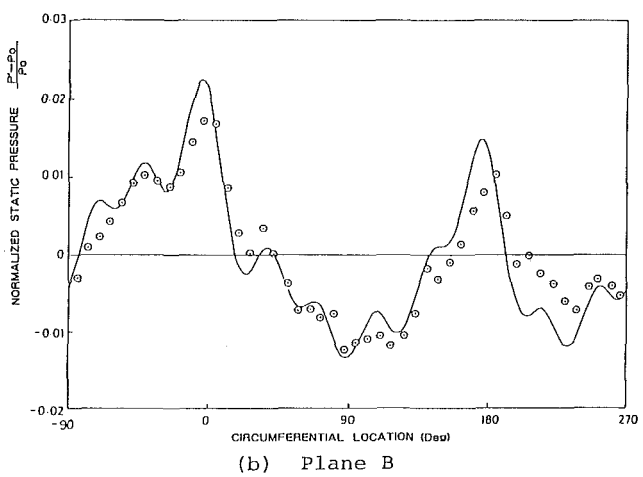

(b) Plane B

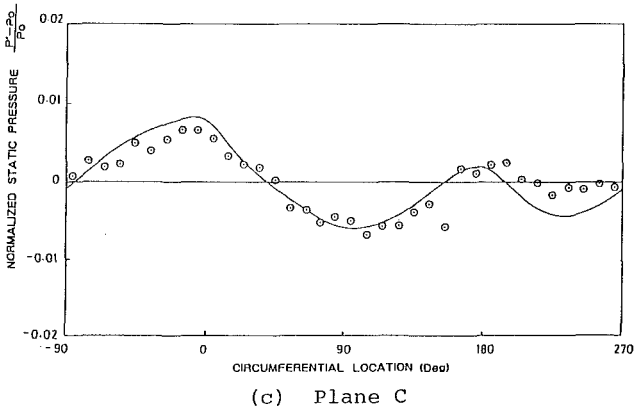

(c) Plane C

Fig. 7 Comparison of measured and calculated static pressure perturbation (Case 3, M = 0.47): —— calculation; ⊙ measurement

ence in the stator load is neglected. The same assumption can be applied to the downstream flowfield. The pressure perturbation due to downstream strut and pylon is given (C_{1d} is given). Consequently we have only one unknown (C_{2d}), and this should be determined from the condition of mass flow conservation through the actuator disk. Since the upstream of the stator has entirely no perturbation, the expression for the mass flow conservation becomes as follows:

$$\rho_{0d}u_d + \rho_d U_d = 0 \quad \text{(at the stator trailing edge)} \tag{9}$$

Substitution of equations (2) and (4) into equation (9) yields the following expression:

$$\alpha_1 C_{1d} + \alpha_2 C_{2d} = 0 \tag{10}$$

where

$$\alpha_1 = -\frac{1}{\kappa}\frac{\dfrac{\lambda_{1d}}{k}}{\mathrm{M}_{xd}\left(\dfrac{\lambda_{1d}}{k}\right) + i\mathrm{M}_{yd}} + \frac{\mathrm{M}_{xd}}{\kappa} \tag{11}$$

$$\alpha_2 = -\frac{1}{\kappa}\frac{\dfrac{\lambda_{2d}}{k}}{\mathrm{M}_{xd}\left(\dfrac{\lambda_{2d}}{k}\right) + i\mathrm{M}_{yd}} + \frac{\mathrm{M}_{xd}}{\kappa} \tag{12}$$

Thus C_{2d} can be obtained from

$$C_{2d} = -\frac{\alpha_1}{\alpha_2} C_{1d} \tag{13}$$

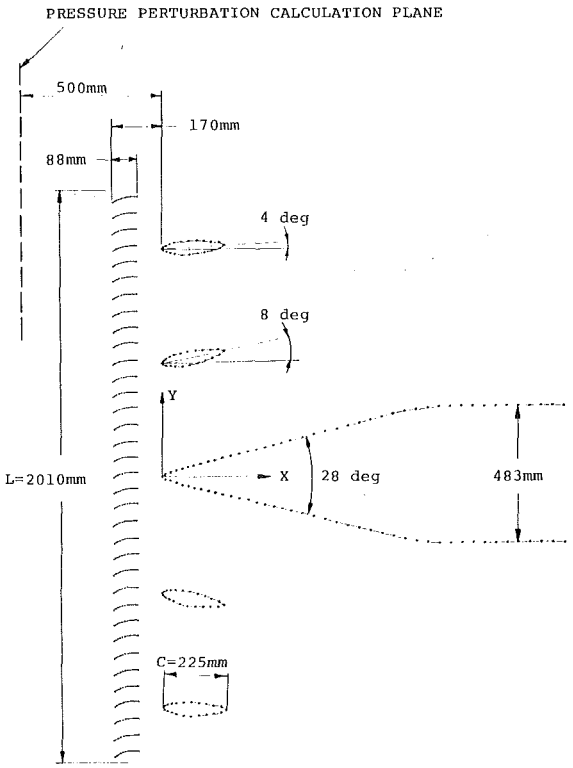

Fig. 8 Calculation model for stator tailoring

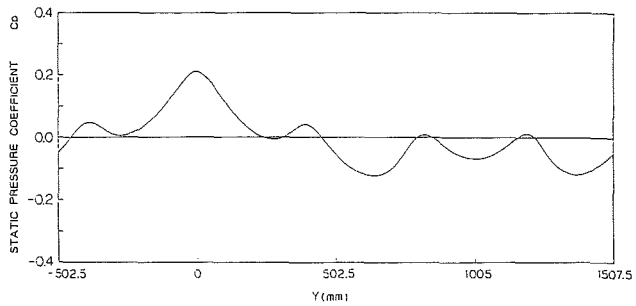

Fig. 9 Static pressure perturbation due to downstream strut and pylon for the calculation model shown in Fig. 8

As the velocity perturbations in the downstream of the stator can be calculated using C_{1d} and C_{2d}, the flow angle at the stator trailing edge can be determined from

$$\tan(\beta_{0d}+\beta_d) = \frac{M_{yd}+\left(\frac{v}{a_0}\right)_d}{M_{xd}+\left(\frac{u}{a_0}\right)_d} \tag{14}$$

The above circumferentially varied flow angle should be achieved by the stator in order to block the effect of downstream strut and pylon.

Analytical Verification of Stator Tailoring Method. The Douglas–Neumann singularity superposition method was used to verify the stator tailoring method developed in this paper. The calculation model is shown in Fig. 8. There are 35 stator vanes, four struts, and one pylon. First of all, the pressure distortion due to downstream strut and pylon (C_{1d}) was calculated using the singularity superposition method, and the result is shown in Fig. 9. It should be noted that the stator vanes were not included in this calculation. C_{2d} was calculated from equation (13), and subsequently, the profile of flow angle

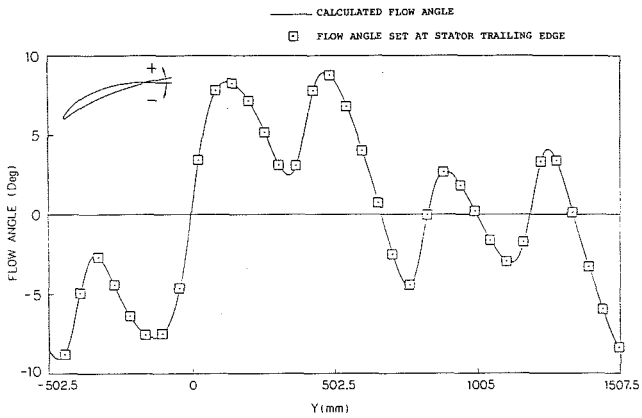

Fig. 10 Calculated flow angle by stator tailoring method for calculation model shown in Fig. 8

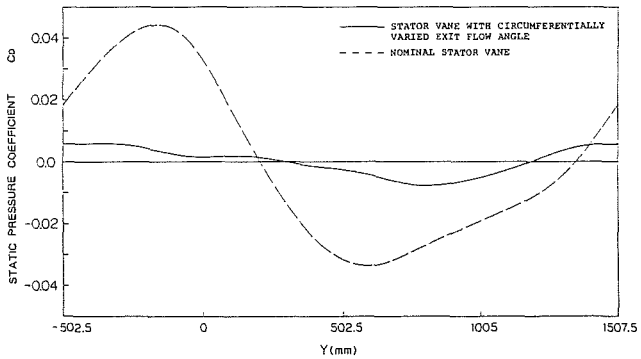

Fig. 11 Calculated static pressure perturbation at upstream of the stator for calculation model shown in Fig. 8

that should be achieved at the stator trailing edge plane to block the effect of downstream strut and pylon was obtained. The result is shown in Fig. 10. Finally, this result was applied to the stator vanes in the calculation using the singularity superposition method. The stator vanes were differently cambered from vane to vane so that the imposed flow angles at the stator trailing edge became the calculated flow angles at the corresponding circumferential positions. The result of the upstream pressure perturbation is shown in Fig. 11, and in this figure, the calculation result using nominal stator vanes with axial exit flow angles is compared. It is found that the pressure perturbation is considerably reduced in the upstream flowfield, but not perfectly reduced. This imperfection is mainly attributed to the assumption of infinitely small pitch used in the actuator disk model.

Experimental Verification of Stator Tailoring Method. The experiment was carried out on the same rig previously described. The strut configuration of Case 3 was selected for the stator tailoring calculation. The pressure perturbation due to downstream strut and pylon (C_{1d}) was obtained by the same procedure used when the upstream pressure perturbation was predicted. The calculation was done at tip section and the resultant flow angle is shown in Fig. 12.

In order to achieve the calculated flow angle at the stator trailing edge plane, another stator ring was designed with circumferentially varied stagger and camber of the vanes. The nine kinds of stator vane already available with different design exit flow angles were used. These vanes were set at different stagger angles from the designs to give desired exit flow angles. Ideally, each vane should have had a different stagger angle, so as to produce different exit flow angles, but this was not practical from a manufacturing point of view. Thus exit flow angles were grouped in 11 kinds as shown in Fig. 12. The

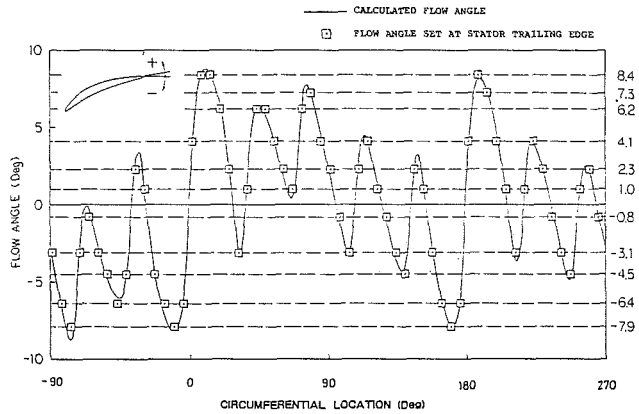

Fig. 12 Calculated flow angle by stator tailoring method for the model test, Case 3

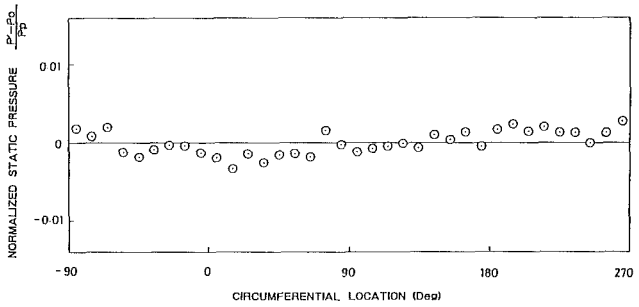

(a) Stator vane with circumferentially varied stagger and camber (M_a=0.43)

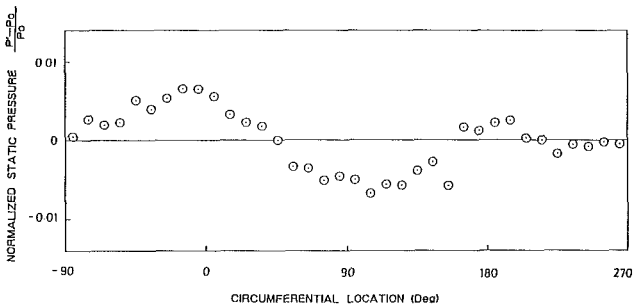

(b) Nominal stator vane (M_a=0.47)

Fig. 13 Measured static pressure perturbation at Plane C (Case 3)

Table 1 Design exit flow angle and change in stagger angle

STATOR VANE NO.	1	1	2	3	3	4	5	6	7	8	9
DESIGN EXIT FLOW ANGLE	7.3	7.3	4.3	3.2	3.2	1.7	-0.4	-2.9	-4.1	-4.4	-6.5
CHANGE IN STAGGER ANGLE	1.1	0	1.9	0.9	-0.9	-0.7	-0.4	-0.2	-0.4	-2.0	-1.4
RESULTANT EXIT FLOW ANGLE	8.4	7.3	6.2	4.1	2.3	1.0	-0.8	-3.1	-4.5	-6.4	-7.9

(deg)

information on the design exit flow angle and the change in stagger angle is supplied in Table 1, and the circumferential arrangement of the vanes is found in Fig. 12.

The experimental result measured at Plane C is shown in Fig. 13. The results of the case for nominal stator vanes are also shown for comparison. The effect of circumferentially varied stagger and camber of the vanes on the upstream pressure perturbation is easily found.

Conclusion

A two-dimensional actuator disk model led by a small perturbation theory was used to predict the pressure perturbation due to stator/downstream strut interaction. The analysis was verified by the experimental measurements carried out on a model rig, and good agreement was obtained.

The stator tailoring method, which is another application of an actuator disk model, to block the effect of downstream strut was also shown. The method was verified analytically and experimentally. Good practical results were obtained.

References

Barber, T. J., and Weingold, H. D., 1987, "Vibratory Forcing Functions Produced by Nonuniform Cascades," ASME *Journal of Engineering for Power*, Vol. 100, pp. 82–88.

Ho, P. Y., 1981, "The Effect of Vane-Frame Design on Rotor-Stator Interaction Noise," AIAA Paper No. 81-2034.

Kodama, H., 1986, "Performance of Axial Compressor With Nonuniform Exit Static Pressure," ASME JOURNAL OF TURBOMACHINERY, Vol. 108, pp. 76–81.

Nakamura, Y., Isomura, K., and Kodama, H., 1986, "Rotor-Strut Interaction Noise of a Model Fan," AIAA Paper No. 86-1871.

Ng, W. F., O'Brien, W. F., and Olsen, T. L., 1987, "Experimental Investigation of Unsteady Fan Flow Interaction With Downstream Struts," *Journal of Propulsion*, Vol. 3, No. 2, pp. 157–163.

O'Brien, W. F., Ng, W. F., and Richardson, S. M., 1985, "Calculation of Unsteady Fan Rotor Response Caused by Downstream Flow Distortions," *Journal of Propulsion*, Vol. XX, No. 6.

Rubbert, P. E., Boctor, M. L., Cowan, S. J., and LaPrete, R. D., 1972, "Concept and Design of Stators Tailored to Shield a Fan From Pressure Disturbances Arising in the Downstream Fan Duct," AIAA Paper No. 72–84.

Woodward, R. P., and Balombin, J. R., 1984, "Tone Generation by Rotor-Downstream Strut Interaction," *Journal of Aircraft*, Vol. 21, pp. 135–142.